A Study of High Transverse Momentum Direct Photon Production in Interactions of 500 GeV/c π^- and Proton Beams on a Beryllium Target

by

Brajesh Chandra Choudhary

Submitted in Fulfillment

of the

Requirements for the Degree

of

DOCTOR OF PHILOSOPHY

Department of Physics and Astrophysics

University of Delhi

Delhi

October 1991

DECLARATION

This thesis presents the direct photon production mechanism and results in interactions of 500 GeV/c π^- and proton beams on beryllium target.

Most of the work presented in this thesis has been published or is in the process of publication.

This work has been done under the supervision of Dr. R. K. Shivpuri. The work has been done by the candidate himself and, to the best of his knowledge, no part of this work has earlier been submitted for any degree or diploma of this or any other university.

(Brajesh Chandra Choudhary)
Candidate

(R. K. Shivpuri)
Supervisor

Head, Dept. of Physics and Astrophysics
University of Delhi, Delhi 110007, India.

In memory of my
Grandparents

Acknowledgements

Every human failure is self-inflicted. Every success has to be nurtured through the caring hands of many people one meets on his way to ones goal. In my opinion, E706 is a very successful experiment and anyone who has ever been involved in this experiment in any capacity, has my most sincere appreciation.

First and foremost, I would like to express my gratitude to my thesis advisor Dr. R. K. Shivpuri, who provided me the opportunity to do research work at Fermi National Acceleartor Laboratory. His guidance over the years has proved most valuable for my shaping as a scientist. I would also like to thank Mr. P. C. Gupta and Mr. Prem Dhingra for taking care of details at Delhi, during my stay at Fermilab.

I would like to thank Prof. Paul Slattery for his leadership to the experiment, his wit and humour and the ideas he provided to the whole group. Prof. Tom Ferbel deserves special thanks for his critical comments on this thesis and also providing me with opportunities to attend summer schools. For my knowledge of the hardware of the experiment, I am thankful to Prof. Eugene Engels, Prof. Carl Bromberg and Dr. Win Baker.

Two persons who deserve special mention for this work are Dr. Marek Zielinski and Dr. George Ginther. Their careful guidance, consultation and ideas at different stages helped to shape this thesis. It was a pleasure to work with my fellow scientists Dr. Phillip Gutierrez, Dr. John Mansour, Dr. Dane Skow, Dr. Carlos Yosef and Dr. Keith Hartman, from our direct photon analysis group. During my four years of stay at Fermilab, I have made many friends and some of those whose company made life more hospitable in the prairie, are Dr. Sudhindra Mani, Dr. Sajan Easo, Dr. Subramaniyam Kartik, Mr. Dhammika Weerasundara and Dr. Phil Cole. I shared house for two and half years with Mr. Rob Roser and if I ever need to do so again, I will always prefer you Rob. My thanks to Mr. Steven Blusk for playing ping-pong and tennis with me.

My existence is the manifestation of my parents love for me. I am and will be always indebted to them for all the sacrifices they have made for me. My sincere thanks are also to my brother and sister for their constant encouragement and confidence in me. My family is my first love.

At last, I would like to thank the taxpayers of India and USA, whose silent commitment to the cause of science and knowledge made this experiment possible through the grants from UGC (India), DOE (USA) and NSF (USA).

Abstract

This thesis presents the measurement of inclusive direct photon production cross section for experiment E706* for the data accumulated during 1987-88 fixed target run at Fermilab.† The experiment employed a large liquid argon sampling calorimeter for electromagnetic particle detection with an energy resolution of approximately $15\%/\sqrt{E}$. The spectrometer was exposed to incident π^- and proton beam interacting with Beryllium (Be) target. The spectrometer triggered on high transverse momentum (P_T) electromagnetic showers.

The incident π^- beam was employed to measure the inclusive direct photon production cross sections from Be target in the P_T range $3.5<P_T<10$ GeV/c. The incident proton beam was used to measure the inclusive direct photon production cross-sections from Be target in the P_T range $4<P_T<8$ GeV/c. The cross sections are presented as a function of P_T averaged over the rapidity ranges $-.7<y<-.2$, $-.2<y<.2$, $.2<y<.7$ and $-.7<y<.7$, as well as a function of rapidity integrated over P_T range of 4 to 8 GeV/c. The ratio of direct photon production to π^0 production (γ/π^0) is also presented. The γ/π^0 ratio for π^- and proton beam on Beryllium target is compared to leading log Quantum Chromodynamics (QCD) predictions. The direct photon cross sections are compared to next to leading log QCD predictions. Results are also compared to previous experiments.

⋆ E706 stands for Experiment number 706 at Fermilab. The experiments at Fermilab are designated in this fashion based upon a number assigned to the proposal when submitted.

† Fermi National Accelerator Laboratory is situated in Batavia, Illinois, USA.

List of Publications

1. G. Alverson *et al.*, "Direct Photon Production at High-p_T in π^-Be and pBe Collisions at 500 GeV/c", Fermilab-Pub-91/212 (submitted to Phys. Rev. Lett.).

2. G. Alverson *et al.*, "Production of π^0Mesons at High-p_T in π^-Be and pBe Collisions at 500 GeV/c", Fermilab-Pub-91/211 (submitted to Phys. Rev. Lett.).

3. J. P. Mansour *et al.*, "Inclusive Production of π^0Mesons and Direct Photons at Large Transverse Momentum" *Proceedings of the DPF meeting, Vancouver, August 1991*, (submitted for publication).

4. James M. Dunlea *et al.*, "Production of Jets Recoiling from Direct Photons" *Proceedings of the DPF meeting, Vancouver, August 1991*, (submitted for publication).

5. C. Bromberg *et al.*, "Design and Operation of Large Straw-Tube Drift Chamber Planes" (submitted to *Nucl. Instr. and Meth.*).

6. B. C. Choudhary *et al.*, "Inclusive Production of $\pi^0$and Direct Photons at Large P_T" Paper presented at the *APS Spring Meeting, Washington, D.C. April 22-25, 1991.*

7. K. Hartman *et al.*, "Hadronic Production of Direct Photons at Large Transverse Momentum" in *Proceedings of the XXVIth Rencontres de Moriond, Les Arcs, Savoie, France, March 11-17 1991*, (submitted for publication by Editions Frontières).

8. V. Abramov *et al.*, "Properties of J/Ψ Production in π^--Be and p-Be Collisions at 530 GeV/c", FERMILAB-Pub-91/62-E.

9. E. Engels *et al.*, "Direct Photon Production in Hadron-Hadron Collisions at 530 GeV", in *Proceedings of the XXV International Conference on High Energy Physics, Singapore, Aug 2-8, 1990*, (submitted for publication).

10. P. Gutierrez *et al.*, "Inclusive Production of π^0, $\eta$and Direct Photons at Large P_T" in *Proceedings of the XXVth Rencontres de Moriond, Les Arcs, Savoie, France, March 11-17 1990*, (submitted for publication by Editions Frontières).

11. S. Mani *et al.*, "Event Structure and Cross Sections for Single Photon Production at 530 GeV/c" in *Proceedings of the Rice Meeting, Houston, Texas, 3-6 Jan 1990*, edited by Billy Bonner and Hannu Miettinen (World Scientific, Singapore, 1990), pp. 564-568.

12. E. Engels Jr., *et al.*, "Performance Characteristics and Radiation Damage Results from the Fermilab E706 Silicon Microstrip Detector System", *Nucl. Instr. and Meth.* **A279** (1989), 272.

13. G. Ginther *et al.*, "Preliminary Results from Fermilab Experiment E706 A Study of Direct Photon Production in Hadronic Interactions" in *Proceedings of the XXIVth Rencontres de Moriond - New Results in Hadronic Interactions, Les Arcs, Savoie, France, March 12-18 1989*, edited by J. Tran Thanh Van, (Editions Frontières) 181-186.

14. C. Johnstone *et al.*, "A-Dependence of Leading Particle Production by 800 GeV Protons" in *Proceedings of the DPF meeting, Storrs, Aug 15-18 1988*, World Scientific, 666-668.

15. P. Lukens *et al.*, "Preliminary Results from Fermilab Experiment E-706 - A Study of Direct Photon Production in Hadronic Collisions" in *Proceedings of the DPF meeting, Storrs, Aug 15-18 1988*, World Scientific, 683-684.

16. C. Yosef *et al.*, "A Study of Direct Photon Production in Hadronic Collisions" in *Proceedings of the Second International Course on Particle Physics, Bogata, Columbia, August 1988* (submitted for publication).

17. G. Alverson, *et al.*, "Preliminary Results from Fermilab Experiment E-706 - A Study of Direct Photon Production in Hadronic Collisions", in *XXIVth International Conference on High Energy Physics*, R. Kotthaus

and J.H. Kühn, eds., (1988), 719.

18. W. F. Baker *et al.*, "A-Dependence of Leading Particle Production by 800 GeV Protons", *ibid.*, p. 1400.

19. G. Ginther *et al.*, "Current Status of Fermilab E-706 A Direct Photon Study" in *New Data and Theoretical Trends - Proceedings of the XIXth International Symposium on Multiparticle Dynamics 1988, Arles, France, June 13-17 1988*, edited by D. Schiff and J. Tran Thanh Van, (Editions Frontières) 217-222.

20. T. Ludlam, *et al.*, "Particle identification for Beauty Physics", *Proc. of the Workshop on High Sensitivity Beauty Physics*, Fermilab, Nov 11-14, (1987), 447-462.

21. G.K. Fanourakis, *et al.*, "Direct Photon Studies: Current Status of Experiment E706 (Fermilab)", *Proc. of the Advanced Research Workshop on QCD Hard Hadronic Processes*, St. Croix, (1987) (in press).

Table of Contents

FIGURE CAPTIONS

TABLE CAPTIONS

1. Introduction

1.1 Introduction to Parton Model

Experimental studies over last two decades have demonstrated that nucleons are not fundamental in structure. Beginning with the deep-inelastic scattering in late 1960's at SLAC,* it has been confirmed that nucleons are composed of constituents, called 'partons'. These experiments provided the experimental proof of the compositeness of nucleons, an idea first proposed by Gell-Mann[1] and Zweig[2]. The partons have been classified in two groups: the quarks which have spin 1/2, fractional charge and can carry flavor (properties such as strangeness, etc) and the gluons which have spin 1, are chargeless and do not carry flavor. Gluons are vector bosons and are identified as the mediators of the strong interaction. Quarks and gluons carry a charge called 'color' and interact with each other through the color charge. There are three types of color charges, often represented by the color red, green and blue. Hadrons, such as baryons, are formed by the combination of quarks of three different colors and have no net color. Mesons are also colorless and are formed by the combination of a quark and an anti-quark of the same color(anti-color). A list[3] of various types of quarks and their quantum numbers is given in Table 1.1.

The theory of the strong interaction among the partons is called Quantum Chromodynamics or QCD. In this theory, the force acts between color charges. The magnitude of the force between the two color charges is proportional to the product of the charges. The intrinsic strength of the interaction is defined by a dimensionless coupling constant α_s. The coupling constant α_s is much larger than the constant of electromagnetism ($\alpha = 1/137$).

There are eight massless gluons in QCD and they carry color charges. The gluons not only transmit the strong force but also change the color of the quarks. In group-theoretical formalism, this property of QCD is defined by SU(3) symmetry, where 3 refers to the three colors that are transformed into one another by the eight

* Stanford Linear Accelerator Center, Palo Alto, California, USA.

QUARKS							
Flavor	**Mass Gev/c^2**	**Q**	**I_z**	**S**	**C**	**B**	**T**
up u	$\simeq 0.35$	+2/3	+1/2	0	0	0	0
down d	$\simeq 0.35$	-1/3	-1/2	0	0	0	0
Strange s	$\simeq 0.55$	-1/3	0	-1	0	0	0
charm c	$\simeq 1.8$	+2/3	0	0	+1	0	0
bottom b	$\simeq 4.5$	-1/3	0	0	0	-1	0
top t	>90	+2/3	0	0	0	0	+1

Table 1.1: The quantum number of quarks. Q, I_z, S, C, B, T are charge, z-component of isospin, strangeness, charm, bottom and top. Free quarks have not been observed in the nature and the mass presented above be taken as indicative only.

massless gluons and S indicates that the sum of the color charges in each SU(3) family is zero.

There is one important consequence of the gluons carrying color charges, which distinguishes QCD from QED (Quantum Electrodynamics). In close analogy to the electromagnetic effect, a quark in a vacuum becomes enveloped in a cloud of virtual gluons and quark-antiquark pairs. The cloud of virtual quark and anti-quark gets polarized, with anti-quarks clustered near the color charge of the source and tending to screen it. The predominant color charge of the gluons near the quark is the same as the charge of the quark itself. Since there is more virtual gluons than the virtual quarks, in the cloud, the influence of gluons is stronger.[4] The charge of the quark becomes spread out in the space, and its effective charge decreases at short distance. As a result, the coupling constant of QCD decreases when distance gets smaller. This property of the QCD is called asymptotic freedom.[5–7] The behaviour of the strong coupling constant between quarks at large distances (comparable to the hadron size) is not very well understood. It is believed that the force may remain constant regardless of the distance between the quarks. This property is called confinement and explains why free quarks have not been seen in nature.

1.2 QCD Phenomenology of High P_T Inclusive Processes

Parton-parton interaction can be well understood by large transverse momentum (P_T) inclusive particle production. Particles produced at large P_T are well described by QCD.[8-11] In parton-parton collisions, high P_T mesons are produced by the fragmentation of partons into hadrons. These mesons come out as a jet in the parent parton direction. To study the characteristics of these hadrons one will have to rely on parton-parton scattering, as well as on parton fragmentation function. An alternative way to study the elementary process is to investigate the production of direct photons at large P_T. The term 'direct photon' means a photon originating from the hard scatter of partons and not from the electromagnetic decays of a hadron. Clearly, by studying direct photons, one has a more direct probe of the interaction. Furthermore, because of the electromagnetic nature of the interaction, direct photon production yields information that is complementary to information obtained from hadron and jet production. Although the direct photon production is suppressed relative to the jet production by the ratio of the electromagnetic to the strong coupling constant α/α_S, as the dominant subprocess for the direct photon production are the same as jet production, except that a gluon is replaced by a photon, it is still considered a better tool to study the parton-parton scattering. Also, as the P_T increases direct photon production and single hadron production rate become comparable to each other because the former arises from the parton-parton hard scattering while the latter is the product of parton fragmentation.

The asymptotic freedom allows one to apply the perturbative technique for calculating cross section at high energies for processes that are dominated by short distance interactions. The QCD coupling constant α_s, which is a function of momentum transfer Q^2 and is called a 'running coupling constant' is given to the leading log in Q^2 as:

$$\alpha_s(Q^2) = \frac{\alpha_s(\Lambda^2)}{1 + \frac{\alpha_s(\Lambda^2)}{4\pi}(11 - \frac{2}{3}n_f)log(Q^2/\Lambda^2)} \tag{1.1}$$

where Λ is the QCD scale parameter, required by the theory and sets the scale for

Q^2 dependence, and n_f is the number of quark flavor kinematically available at the collision energy. The above equation shows that as Q^2 increases, $\alpha_s(Q^2)$ decreases and at $Q^2 \to \infty$, $\alpha_s(Q^2) \to 0$. This means that at high momentum transfer, confinement can be neglected, that the constituents are essentially free in the hadrons and the hadron-hadron interaction may be simply considered as a parton-parton interaction. For $Q^2 \geq 10(\mathrm{GeV}/c)^2$, α_s is relatively small and perturbative techniques can be applied for calculating cross sections.

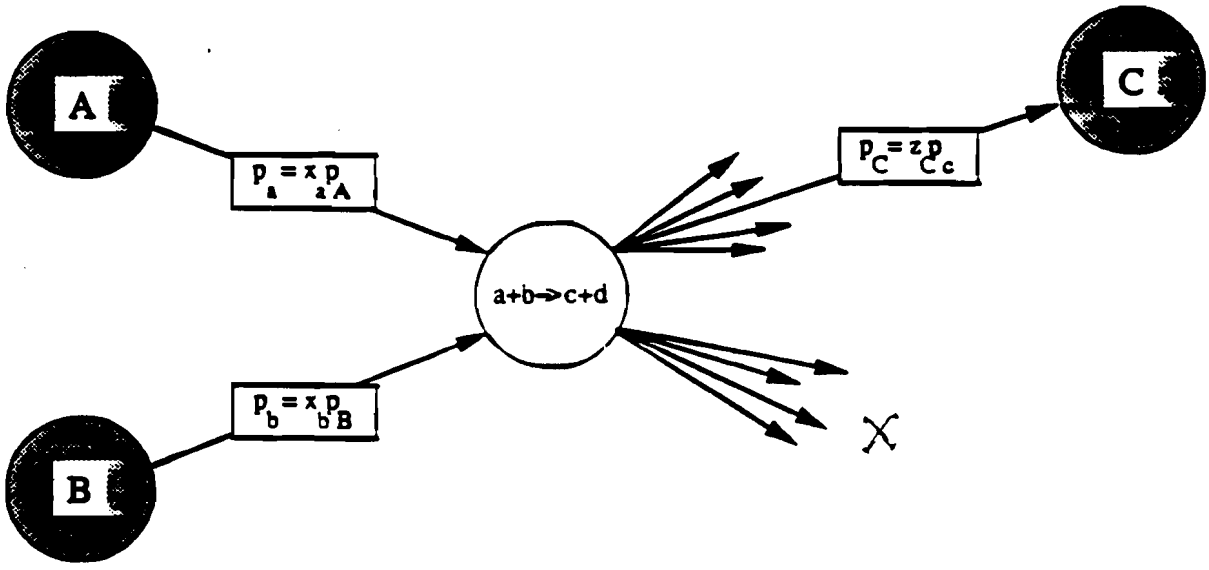

Figure 1.1: Schematic representation of a high P_T reaction.

Let us consider a basic diagram for hadronic interactions AB → CX as shown in Figure 1.1. A and B are interacting hadrons, C is the hadron with large P_T, and X represents all other particles in the final state. The incoming particles A and B contain partons 'a' and 'b' respectively, which scatter, producing partons labelled 'c' and 'd' which have a large transverse momentum component q_t. Subsequently hadron C is produced from parton 'c' via the fragmentation process. Since q_t is the

conjugate variable to the impact parameter of the parton scattering process, large q_t implies that partons have scattered at a small distance where α_s is small and Q^2 is large. Hence perturbation theory can be applied. One can express the invariant cross section for AB $\rightarrow$ CX as the weighted sum of the differential cross section, of all possible parton scattering that can contribute,

$$E_C \frac{d\sigma}{d^3p_C}(AB \rightarrow CX) = \sum_{abcd} \int dx_a dx_b dz_c G_{a/A}(x_a, Q^2) G_{b/B}(x_b, Q^2) D_{C/c}(z_c, Q^2) \times \frac{\hat{s}}{z_c^2 \pi} \frac{d\sigma}{d\hat{t}}(ab \rightarrow cd) \delta(\hat{s} + \hat{t} + \hat{u}) \tag{1.2}$$

where $\hat{s}$, $\hat{t}$, and $\hat{u}$ are the Mandelstam variables for the massless parton parton subprocess, x_a and x_b are the fractions of the longitudinal momentum carried by partons 'a' and 'b' of hadrons A and B, z_c is the fraction of the 'c' parton's longitudinal momentum carried by hadron C. The probability of finding a parton in the interval between x_a and $x_a + dx_a$ is denoted by the distribution function $G_{a/A}(x_a)$. $D_{C/c}(z_c)$ is the probability that hadron C carries a momentum fraction between z_c and $z_c + dz_c$ of the parent parton's (c) momentum and is referred to as the fragmentation function. Structure and fragmentation functions can not be calculated using perturbation theory and must be obtained from data from various hard scattering processes. One can predict the cross section if the structure functions, fragmentation functions and the cross sections for all the parton subprocesses are known. In equation 1.2 the partons have been assumed massless and the initial and final state partons are collinear with the corresponding hadrons i.e the partons have no intrinsic transverse momentum (k_T).

1.3 Direct Photon Production

Direct photon production as a subject has been studied extensively on both the theoretical and experimental level. Several excellent reviews[12-18] can be found on the subject. The reasons for the continuing interest in the study of direct photon physics are:

1. Simplicity: As photons do not carry electric charge they can not interact directly with each other. This greatly reduces the number of subprocesses which contribute to the direct photon production process. As shown in figure 1.2, Compton and annihilation diagrams are the only two subprocesses which contributes to the first order direct photon production. There are only 18 diagrams for three quark flavors for these two subprocesses, compared to 127 separate two-body scattering diagrams for three quark flavors for single particle hadroproduction. Also, because the photons do not carry color charge they do not hadronize removing the inherent ambiguities present in the case of jets which can be either quarks or gluons. Experimentally, it means that it is easier to reconstruct the four vectors of a photon than a jet.

2. Gluon Physics: As shown in figure 1.2, gluons are involved in both the Compton and the annihilation diagram. In the Compton diagram, the gluon is involved in the initial state whereas in the annihilation diagram, the gluon appears in the final state. By separating the contributions from the Compton diagram to the direct photon production process one can measure the gluon structure function of the colliding hadrons. The gluon fragmentation function can be measured by isolating the contributions from the annihilation diagram.

3. QCD tests: The next to leading log[19] (NLL) predictions for direct photon production are available. The theory can be more reliably compared with the data over a wide kinematic range.

To first order, the invariant inclusive direct photon cross section, $A+B \rightarrow \gamma+X$

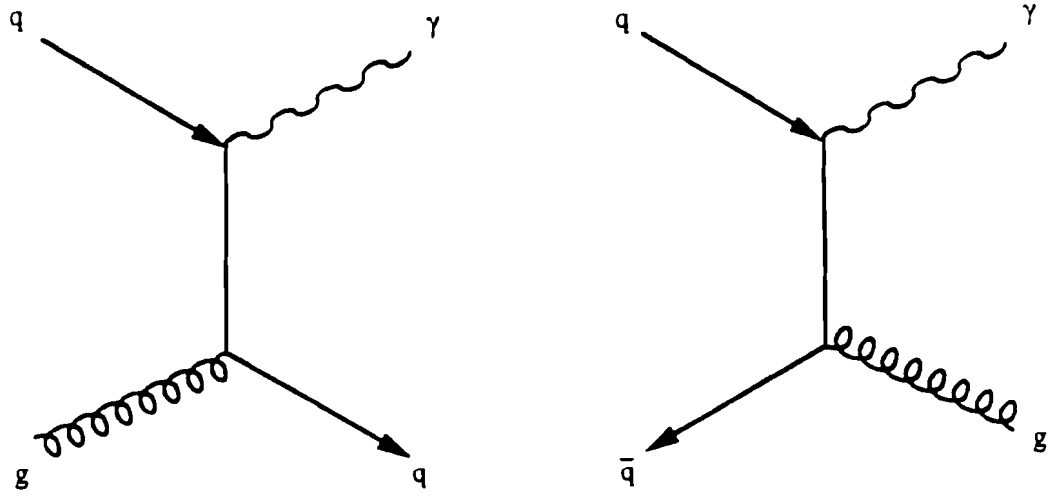

Figure 1.2: Representative lowest order diagrams for direct photon production process.

can be written as:

$$E_\gamma \frac{d\sigma}{d^3p_\gamma}(AB \to \gamma X) = \sum_{ab} \int dx_a dx_b G_{a/A}(x_a, Q^2) G_{b/B}(x_b, Q^2) \times \frac{\hat{s}}{\pi} \frac{d\sigma}{d\hat{t}}(ab \to \gamma d)\delta(\hat{s} + \hat{t} + \hat{u}) \tag{1.3}$$

where we see that the fragmentation term of equation 1.2 has vanished. At lowest order, the constituent cross sections are given by[20]

$$\frac{d\sigma}{d\hat{t}}(qg \to q\gamma) = -\frac{\pi\alpha\alpha_s}{3\hat{s}^2} e_q^2 \frac{\hat{u}^2 + \hat{s}^2}{\hat{u}\hat{s}} \tag{1.4}$$

$$\frac{d\sigma}{d\hat{t}}(\bar{q}q \rightarrow g\gamma) = \frac{8\pi\alpha\alpha_s}{9\hat{s}^2} e_q^2 \frac{\hat{u}^2 + \hat{t}^2}{\hat{u}\hat{t}} \tag{1.5}$$

1.4 Higher Order Corrections

In QCD perturbation theory, higher order corrections (processes not shown in figure 1.2) must be taken into account. When higher order processes are considered, a variety of singularities arise from soft gluon emissions from both the incoming and outgoing partons. One must take care to obtain finite results. Figure 1.3 (Ref. 12) shows the diagrams for direct photon production at leading order and next to the leading order.

The direct photon diagrams that contribute to the various $O(\alpha\alpha_s^2)$ subprocesses are shown in the Figure 1.3(c)-1.3(e). The eight diagrams in Figure 1.3(c) arise from having an additional gluon present in the final state of the first order Compton scattering in Figure 1.3(a). If a gluon is emitted from the incoming quark leg of the Compton process as shown in first graph of Figure 1.3(c) and if the initial quark and the emitted gluon become collinear, then the internal quark line to which the gluon are connected becomes 'on-shell'. In QCD, when the partons are treated as massless, then the invariant mass corresponding to the internal quark line becomes zero and the logarithmic term for the radiative correction becomes infinite. This leads to what is called mass singularity. But the factorization theorem[21-23] allows one to separate the mass singularity and absorb it in the uncalculable portion of the distribution and fragmentation functions. Diagrams in 1.3(e) lead to ultraviolet singularity associated with one loop graph. These are regulated by dimensional regularization and then subtracted. The remaining infrared or soft singularities cancels out when the results of all of the loop graphs and tree graphs are added together. Thus the results for NLL calculations become finite.

Also, the study done by P. Aurenche et al. (Ref. 19) suggested that the direct photon cross section for the next to leading log calculation becomes less sensitive to the choice of the momentum scale compared to the leading log calculation. This was possible because the contribution to the cross section from the leading log term

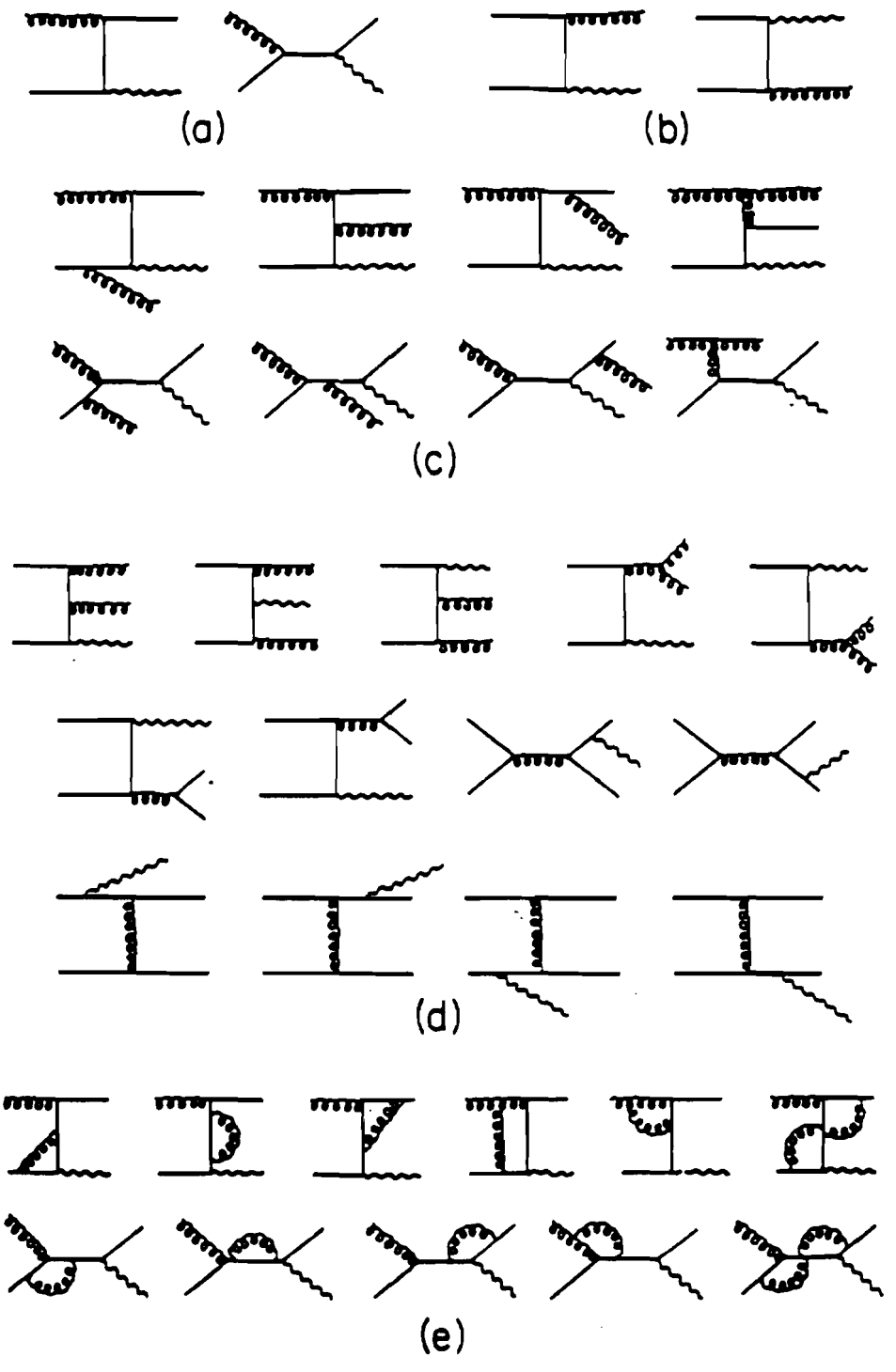

Figure 1.3: Feynman diagram for leading order $O(\alpha\alpha_s)$ and next to leading order $O(\alpha\alpha_s^2)$ direct photon production processes.

decreases with increasing Q^2, while the contribution from the higher order terms increases with Q^2, thus diminishing sensitivity to the choice of the Q^2 scale.

1.5 Background to Direct Photons

π^0's and η's constitute the major source of background to the direct photon signal. Other neutral mesons ($\eta' \rightarrow \gamma\gamma$, $\omega \rightarrow \pi^0\gamma$, $K_s^0 \rightarrow \pi^0\pi^0$) contribute to the background in much smaller quantity. In hadronic interactions π^0's are copiously produced and approximately 99% of time they decay into $\gamma\gamma$.[24] The η's are produced at a rate almost half that of the π^0 and 39% of the time they decay into $\gamma\gamma$ pair (Ref. 24). Contributions from η', ω, K_s^0 etc are usually calculated either from directly measured individual meson yields, or using known relative ratios, such as η'/π^0, ω/π^0, K_s^0/π^0etc, coupled with measured π^0yield. The η' decays only 2% of the time in $\gamma\gamma$ pair (Ref. 24), which can contribute a high P_T photon. ω decays only about 9% of the time into a $\pi^0\gamma$ pair (Ref. 24) from which an energetic photon can be expected. K_s^0 decays 31% of the time into $\pi^0\pi^0$ pair (Ref. 24). These π^0's have to be very energetic to contribute a decay photon as background to the direct photon sample. Nonetheless, in order to precisely measure the direct photon cross section these backgrounds must be understood very well, and the π^0cross section must be measured precisely. Other sources of background at the P_T scale of this experiment are negligible, either due to the low production cross section, or small branching ratio into mode which can provide high energy photons or because of unfavourable decay mode.

Misidentified hadrons can also be a source of background to direct photons. The hadrons can interact and produce showers in the electromagnetic shower detector. Charged hadrons can be rejected by requiring that no charged track be present in the immediate vicinity of the detected shower. This can be accomplished by having charged particle detectors and projecting the charged tracks to the face of the calorimeter, to confirm that the shower deposited in the calorimeter is not coming from charged particles. Neutral hadrons like the neutron and the K_L^0 can be more problematic. These backgrounds can be reduced based on the characteristics

of the longitudinal and transverse shower development inside the calorimeter, and the residual contribution can be estimated using Monte Carlo simulations.

Muons can be a major source of background for the fixed target experiments. Usually a large number of muons are produced due to decay of beam particles while they are being transported to the experimental area. These muons will travel more or less parallel to the beam pipe. These muons can occasionally deposit large amount of energy in the calorimeter. The background from muons can be reduced by studying the time profile of the arriving particles using veto walls, the direction of the arriving particles and the longitudinal shower development inside the calorimeter.

The background subtraction at high P_T, where the direct photon and π^0 production rates are comparable, may not be a very serious problem. As shown by earlier fixed target experiments (Ref. 12 and 13), at low P_T, especially for $P_T <$ 5 GeV/c the background subtraction becomes very sensitive. This requires that the π^0 cross section and the background from the π^0's to the direct photon must be understood very well. This also necessitates a very good understanding of the electromagnetic showers deposited in the detector as well as the reconstruction of the neutral mesons.

1.6 k_T Smearing

In the naive parton model, partons are assumed to be travelling collinear with their parent hadron with no transverse motion. Because the partons are confined within the radius of the hadron (typically of the order of 0.5fm) and so by uncertainty principle they must have a momentum spread (Fermi motion) of the order of 0.4 GeV/c, transverse to the hadron's direction. Thus the P_T of the observed particle produced, will be in part due to the partons already having a net transverse motion, even before scattering occurred. Consider the case when the initial partons have some transverse momentum k_T relative to the beam and the target axis. As part of the P_T comes from the initial quark, the amount of the P_T from the hard scattering will be smaller. The partons also may acquire transverse momentum by

parton emission before scattering, for example the 'effective' k_T due to various 2→3 subprocesses given by the QCD (gluon emission or bremsstrahlung). The effect of the bremsstrahlung contribution can be calculated using perturbative QCD, but only at large k_T. Theoretically, it is difficult to separate the intrinsic k_T from the radiative corrections, since they ultimately come from the same source, quark and gluon interactions.

Because of the smearing, at small P_T, where k_T will be a comparatively larger fraction of the P_T than that at higher P_T, the cross section increase would be relatively higher. So the observed P_T distribution of the particle would have contributions from the intrinsic motion of the partons in the colliding hadrons that supply a part of the total P_T. The steeply falling P_T spectrum in the hard scattering (where the invariant cross section falls at the rate of an order of magnitude per GeV in the P_T range of 3 to 10 GeV/c) tends to shift the effective yield to smaller P_T.

The lowest order analysis of high mass lepton pair production gives the value of $<k_T>$ as 864 MeV[25] but if the next order terms are included the value drops to 600 MeV. In general, as more calculable QCD terms are included, the size of the deduced intrinsic term is reduced.

In addition to theoretical difficulties of defining intrinsic transverse momenta there are also ambiguities in how one incorporates the distributions into a specific calculation. The choice of various assumptions introduces a certain amount of model dependence into the calculation.

In some experiments[26–29] where the data were compared to the leading log calculation, it was found that there is reasonable agreement with the data at the upper end of the P_T spectrum, but for P_T below 6 GeV/c, the data points were higher than the leading log calculations. When smearing term with $<k_T^2>$=0.95 GeV^2 were included in the leading log calculation, the cross section increased by about a factor of 1.6 at P_T = 3 GeV/c and the theory and data merged smoothly. For experiments NA24[30] and NA3,[31] the same kind of effect was found with k_T smearing term. The value of the k_T term for different experiments were different,

depending on the model used. This shows that single photon invariant cross section can be described within the leading log approximation, suitably augmented by the model dependent k_T smearing.

In next to leading-log calculation using optimized PMS scale (Principle of Minimum Sensitivity, PMS scale has been discussed in chapter 6) the theoretical cross section values were compared with direct photon results from experiments NA24 and NA3. The theoretical predictions are in good agreement with data from both the groups. It suggests that for next to leading-log calculation a large k_T smearing term is not needed. The 2→3 subprocess contribute some of the smearing effect. In principle there could be a small k_T contribution. The average value of the k_T would be much less than the leading log calculations. But WA70[32] in their study of double prompt photon production at high transverse momentum by π^- on protons at 280 GeV/c reported that a k_T of 0.9 GeV/c is needed with NLL calculations for a reasonable agreement with the data. The Drell-Yan process $\bar{q}q \rightarrow l^+l^-$ suggests[33,34] a k_T of 0.34 GeV/c. The Drell-Yan data was compared with NLL calculations with k_T of 0.34 GeV/c and k_T of 0.9 GeV/c and the χ^2 per degree of freedom obtained were respectively 28 and 14, thus favoring a higher value of k_T, although, with NLL calculations, a residual k_T of 0.34 GeV/c would have been expected. These conclusions are dependent on the shape of the background which was determined from the data with limited statistics. This indicates that still higher order QCD diagrams (beyond NLL calculations) must be taken into account as in the case of Drell-Yan reactions.[35]

1.7 Nuclear Dependence of Direct Photon Production

Interactions of hadrons with nuclear targets could provide insight into the nuclear characteristics that would not be possible in hadron-hadron interactions. Nuclear targets were used to measure the cross sections for the experiment E706 and the results were divided by the atomic weight of the target to obtain the cross section per nucleon. E706 is one of the very few direct photon experiments (others are E629, NA3 and E705) to use nuclear targets and it is the first experiment to

use different nuclear targets (Copper and Beryllium) in the same experiment. Nuclear targets are easy to use and one can study the space time development of the hadronic process in the nuclear matter. The ratio of the cross section per nucleus for the different targets a and b is often parametrized as

$$\frac{\sigma_a}{\sigma_b} = \left(\frac{A_a}{A_b}\right)^{\alpha} \tag{1.6}$$

where σ_a and σ_b are the cross section per nucleus for target a and b and A_a and A_b are the the atomic numbers. As the relative cross section is determined by the number of the nucleons in each nucleus, α should be close to 1 if the hard scattering process is responsible for the direct photon production. But if that is not the case and if the nucleus is shadowed then the cross section will be proportional to the area of the nuclei and α should be close to 2/3. For high atomic number nuclear targets, where one may expect multiple scattering, the cross section should scale as α>1. Studying the behavior of α with target type, P_T etc. will be interesting. Although the data available may not be sufficient to study the variation of α with P_T in finer bins and does require more data at higher P_T, it does gives us a flavor of nuclear effect on direct photon production. In Chapter 6, is presented the A dependence of cross section from Be and Cu targets.

1.8 Beam Dependence of Direct Photon Production

As we have seen, in the leading log process there are only two hard-scattering subprocesses for producing direct photons, Compton and annihilation diagrams. If only the Compton diagram contributed, the ratio of the π^- and π^+ cross section would be constant at one. However, the presence of a $\bar{u}$ quark in the π^-, as opposed to a $\bar{d}$ quark in the π^+, means that the annihilation subprocess will make a relatively larger contribution in the π^- case. This follows from the larger charge of the $\bar{u}$ quark and also from the fact that the valence u quark distribution in a proton is larger than that of the valence d quark, and the proton does not have valence antiquarks. Thus one can use different beam types to separate the contributions from the diagrams and study them to find the gluon structure and fragmentation function. Also, one

can study the characteristics of quark and gluon induced jets from the separation of diagrams.

Berger et al.[36] have shown that at different $\sqrt{S}$, as P_T increases the annihilation term becomes dominant and the ratio of direct photon production cross section for π^-p/π^+p and $p\bar{p}/pp$ increases. The increase in ratio is larger for π^-p/π^+p compared to $p\bar{p}/pp$. In $p\bar{p}/pp$ process as $\sqrt{S}$ increases, the ratio does not increase so fast.

NA24[37] has shown that for $\sqrt{S}$=23.7 GeV, the ratio $\pi^-p\rightarrow\gamma X/\pi^+p\rightarrow\gamma X$ increases with P_T. The ratio which is close to unity at P_T = 3 GeV/c rises to about 3 at P_T of 6 GeV/c. This is in agreement with QCD predictions[38,39] . For NA3[40] at $\sqrt{S}$=19.4 GeV, the ratio of π^-p/π^+p increases with P_T and is in agreement with the theory.

WA70[41,42] has compared the direct photon production for proton, π^- and π^+ beams. The results were also compared with second order QCD calculations. The results show that $\pi^+p\rightarrow\gamma X/pp\rightarrow\gamma X$ increases with P_T and is in agreement with Duke-Owens Set 1 (DO1) structure function. The comparison was also made for π^- and π^+ beams. The ratio $\pi^-p\rightarrow\gamma X/\pi^+p\rightarrow\gamma X$ increases with P_T and is in agreement with predictions of second order QCD calculations using optimized scales with DO1 and DO2 structure functions.

1.9 Other Direct Photon Experiments

The field of direct photon physics has been studied thoroughly and extensively. The first of the experiments R412[43], R107[44] and CCOR[45] were performed at the CERN* ISR, and demonstrated the evidence for direct photons. Although the results were limited due to systematic and statistical uncertainties, several later experiments at the CERN ISR, fixed target programs at CERN and Fermilab and collider experiments at Sp$\bar{p}$S and at Fermilab (Tevatron) have published results for center of mass energy ranging from $\sqrt{S}$=19.4 GeV to $\sqrt{S}$=1.8 TeV. Table[46]

* European Organization for Nuclear Research.

Collaboration	P_{beam} GeV	$\sqrt{S}$ GeV	Beam	Target	x_T range ($= 2P_T/\sqrt{S}$)
E95	200,300		p	Be	$x_T < .45$
E629	200		p, π^+	C	$.22 < x_T < .45$
NA3	200		$p, \pi^\pm$	C	$.26 < x_T < .62$
NA24	300		$p, \pi^\pm$	H_2	$.23 < x_T < .59$
WA70	280		$p, \pi^\pm$	H_2	$.35 < x_T < .61$
E705	300		$p, \bar{p}, \pi^\pm$	Li_7	$.33 < x_T < .59$
E706	500,800		$p, \pi^\pm, K^\pm$	H_2,Cu,Be	$.18 < x_T < .65$
UA6		24.3	$p, \bar{p}$	p	$.28 < x_T < .58$
R108		62.4	p	p	$.17 < x_T < .42$
R110		63.0	p	p	$.14 < x_T < .29$
R806		63.0	p	p	$.12 < x_T < .38$
R808		63.0	p	p	$.15 < x_T < .33$
AFS		53.0	$\bar{p}$	p	$.11 < x_T < .23$
UA2		546,630	$\bar{p}$	p	$.04 < x_T < .32$
UA1		546,630	$\bar{p}$	p	$.05 < x_T < .32$
UA1		630	$\bar{p}$	p	$.02 < x_T < .13$
CDF		1800	$\bar{p}$	p	$.018 < x_T$
D0		1800	$\bar{p}$	p	$.018 < x_T$

Table 1.2: Above table presents a summary of the direct photon experiments. Fixed target experiments have their incident beam energy shown whereas center of mass ($\sqrt{S}$) energy is shown for collider experiments. Beam type and target type are also evident from the table. Limit on x_T is also shown for all the experiments.

1.2 gives a summary of the experiments. Most of the fixed target experiments were in the energy range $\sqrt{S}$=19.4 GeV to $\sqrt{S}$= 24.3 GeV. The ISR experiments were mostly at $\sqrt{S}$=44 GeV and $\sqrt{S}$=62.4 GeV. The Sp$\bar{p}$S were at $\sqrt{S}$=530 GeV and $\sqrt{S}$=640 GeV whereas CDF and D0 at Fermilab are at $\sqrt{S}$=1.8 TeV. E706 with incident beams of energy 500 GeV (1987-88 run) and 800 GeV (1991 run) which corresponds to $\sqrt{S}$=30.6 GeV and $\sqrt{S}$=38.7 GeV will be able to fill the gap that existed between earlier fixed target experiments and ISR results. Also E706 can study nuclear dependence of direct photon production which has not been studied so far. At present, other than collider experiments, E706 is the only running fixed target direct photon experiment. It is hoped that E706 will provide a better understanding of direct photon production and add further to the knowledge of QCD and hadronic structure.

2. Apparatus

2.1 Overview

This chapter describes the Meson West beamline, the beam composition, target selection and the different components of the spectrometer for experiment E706. The experimental area is located at the end of the Meson West (MWEST) beam line. Figures 2.1 and 2.2 respectively, show the schematic layout of the spectrometer with respect to the MWEST hall and the target. Figure 2.1, also shows the muon detectors for experiment E672[†], which is an experiment using the same beam line, target material and the spectrometer as E706. The detectors, which were built by different collaborating institutions, were optimized to handle a large trigger rate in order to extract the relatively small direct photon cross section. As labelled in figure 2.1 the spectrometer consists of :

- Hadron Shield
- Veto Wall
- Target
- Silicon Strip Detector (SSD)
- An Analysis Magnet
- MultiWire Proportional Chambers (MWPCs)
- Liquid Argon Calorimeter (LAC) consisting of both electromagnetic (EM-LAC) and Hadronic (HALAC) sections
- Forward Calorimeter
- E672 MWPCs, Toroid and Muon Chambers.

† E672 is aimed to study the high mass di-muon production.

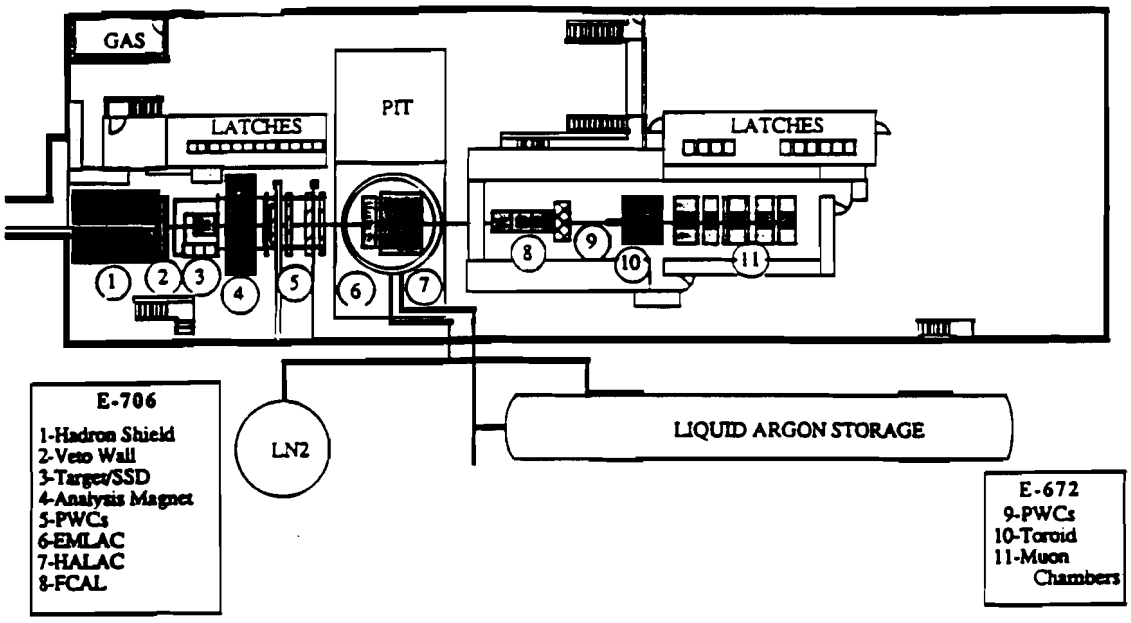

Figure 2.1: MWEST Detector Hall

2.2 Beamline, Cherenkov Counter, Hadron Shield and Veto Wall

Beamline

During the 1987-1988 run, positive and negative secondary beams of momenta 500 GeV/c were transported to MWEST. The Fermilab main accelerator, called the Tevatron, operated with a 57 second cycle, taking the first 34 seconds for various stages of injection, accelerating protons up to 800 GeV, followed by a 23 second extracted spill, during which the primary protons were transported to various fixed target beamlines. The primary protons were bunched in $1ns$ beam bucket, each bucket spaced about $20ns$ apart. The 800 GeV/c primary protons interacted with a 0.75 interaction length aluminum target to produce secondary beam.

Cherenkov Counter[47]

Figure 2.3 shows a helium gas filled differential Cherenkov counter used in the beamline for tagging the beam particle types (π,K,p). It is located 98m upstream

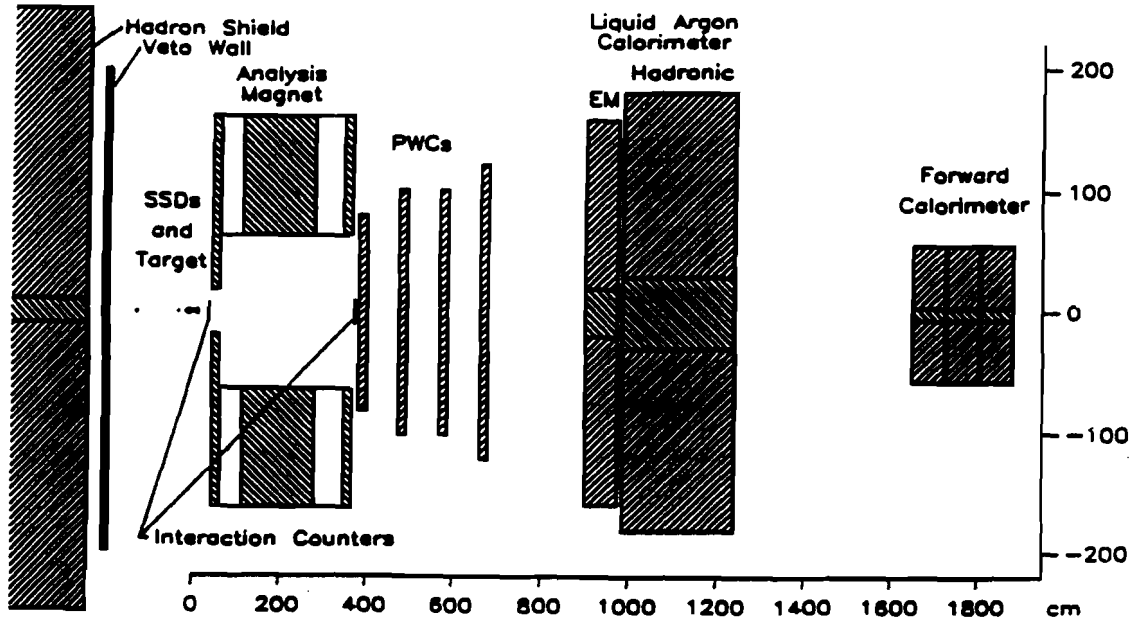

Figure 2.2: Schematic Layout of MWEST Spectrometer

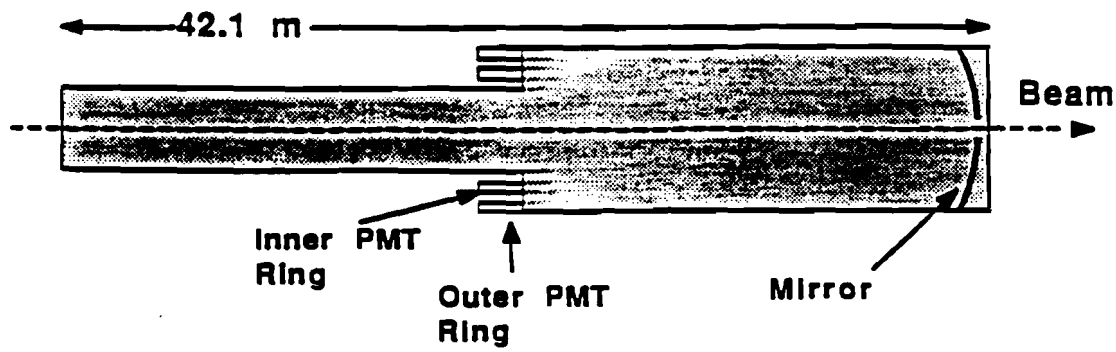

Figure 2.3: E706 Cherenkov Counter

of the secondary target. It has a total radiation length of 42.1 m and an average

Cherenkov angle of 5.217 *mrad* for pions at a pressure of 6.0 psi.[48] To make sure that beam particles did pass through the entire counter; scintillation counters were positioned at each end of the Cherenkov counter. There was a spherical mirror at the downstream end of the Cherenkov counter. The mirror reflects the Cherenkov light back to a light cone and photomultiplier tubes near the upstream end of the counter. During the run, the operating pressure was set between 4 and 7 psi of helium. For negative and positive beam running, the helium pressure in the Cherenkov counter was set to tag to K^- and π^+ peak. The beam composition was determined using the response curve* and is listed in table 2.1.

Negative Beam			Positive Beam		
$\pi^-(\%)$	$K^-(\%)$	$\bar{p}(\%)$	$\pi^+(\%)$	$K^+(\%)$	$p(\%)$
96.9 ± 0.2	2.9 ± 0.2	0.2 ± 0.01	7.2 ± 0.1	1.7 ± 0.1	91.2 ± 0.1

Table 2.1: Beam Composition.

The production angle for negative and positive polarity beam were chosen to be respectively, 0 *mrad* and 1.4 *mrad*. The non-zero production angle for positive beam was chosen to minimize the possibility of transporting the primary beam to the experimental hall. The positive beam had an intensity of $7 * 10^7$ particles/spill and the negative beam had an intensity of $4 * 10^7$ particles/spill.

Hadron Shield

A large number of hadrons are produced during the transport of the beam down the beam line. These hadrons tend to form a halo around the beam pipe. To remove this halo, a 20 foot thick steel shield, is placed at the downstream end of the beamline. Its function is basically to remove the hadrons travelling parallel to the beam. The beam pipe passes through a vertical removable blade in the hadron shield. This blade was removed at the end of the run to calibrate the LAC.

* The beam composition at 500 GeV/c was determined by fitting the monte carlo pressure curve (with known amount of particle composition in positive and negative beam) to the experimental pressure curve, for different coincidence requirements.

Veto Wall

As shown in the Figure 2.4, the veto wall system consists of two overlapping planes, approximately $3m * 3m$ in size. Located downstream of the hadron shield, each of these planes are made of 32 scintillation counters. The scintillation counters are $50cm * 50cm$ in size. The veto wall planes are divided into quadrants with a $10cm * 10cm$ hole at the center, aligned with the beamline. The veto wall was primarily used to detect muons from the beam halo. Muons can deposit electromagnetic showers of energies high enough to create fake high P_T signals in the EMLAC. The coincidence between signals from counters in the two veto walls was used to veto the event at the trigger selection level. The veto wall information was also used during the offline analysis to detect fake photons.

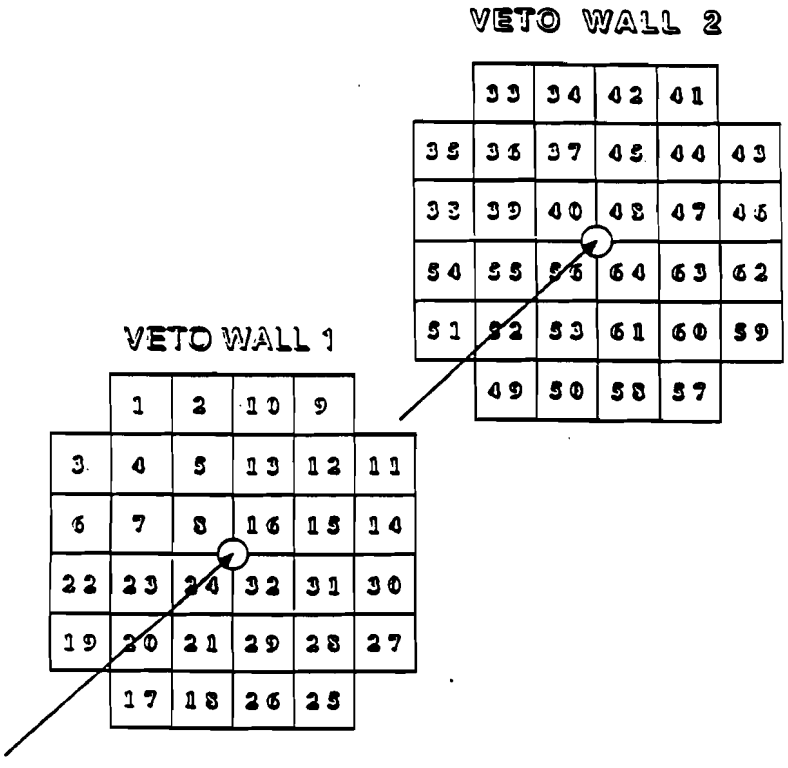

Figure 2.4: Two overlapping veto wall planes. Each plane is made of 32, $50cm * 50cm$ scintillation counters. The arrow indicates the beam direction.

2.3 Target

The target[49] used during most of the run was Beryllium, although Copper was also used along with Beryllium for a part of the run. The target consisted of two copper pieces and twenty beryllium pieces. The copper pieces were $0.8mm$ thick and $1.6mm$ apart followed by twenty pieces of beryllium, each being $2mm$ thick and $1.6mm$ apart. The downstream Beryllium target was separated from the upstream Copper target by $3.2mm$. Each individual target piece was $2cm * 12cm$ in cross sectional area. The target assembly was placed in the SSD box after 3 silicon modules and was followed by four more silicon modules. The target was positioned between sets of Silicon planes, to use upstream planes for proper beam tracking and downstream planes for vertex finding.

Parameters	Be	Cu
Length(cm)	4.0	0.16
Atomic Number	9.01	63.54
Density (g/cm^3)	1.85	8.96
Radiation Length(%)	11.33	11.19
π interaction length(%)	6.90	0.83
p interaction length(%)	9.24	1.03
K interaction length(%)	6.25	0.77

Table 2.2: Target parameters.

Most of the data were taken with Beryllium target (low Z atomic number material and longer radiation length) to minimize photon conversion as well as to minimize secondary interactions. But high Z material like Copper was also used for part of the run to study the A-dependence of direct photon production. Data were also collected with target removed, to study the nature of background tracks in the SSD system. Table 2.2 lists some of the properties of the target materials.

2.4 The Tracking System

The primary purpose of the tracking system was to locate the event vertex, proper beam direction and to measure the momentum of the charged particles. This is very important for the study of jets associated with direct photon candidates as well as to identify the showers deposited in the EMLAC coming from charged particles. The tracking system consists of a set of Silicon Strip Detectors (SSDs), an Analysing Magnet and a set of MultiWire Proportional Chambers (MWPCs).

Silicon Strip Detector

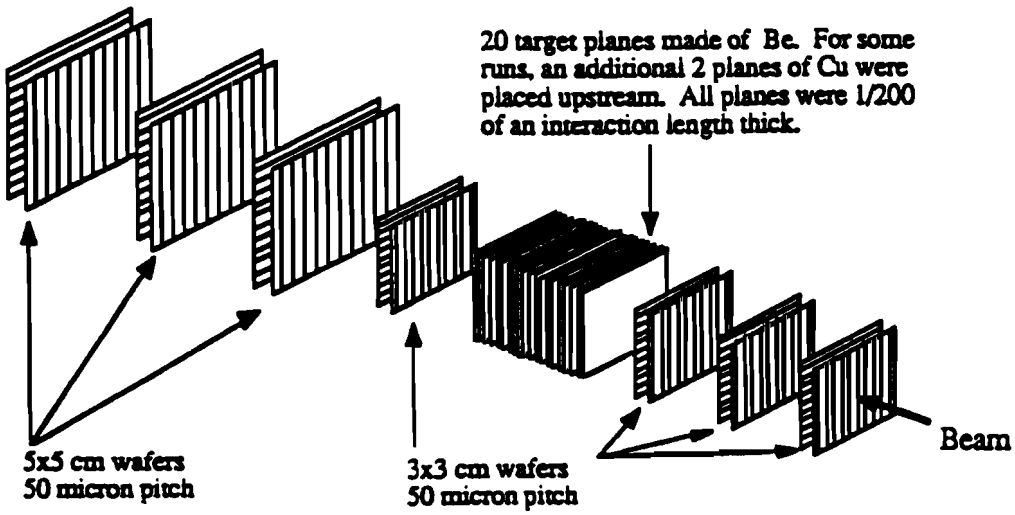

Figure 2.5: The SSD System

The design consideration for the SSD system required that it must be compact along the beam axis and the angular resolution of the SSDs must match that of the MWPCs. The SSD system shown in fig 2.5, consists of 14 planes of SSDs constructed of seven X-Y modules, with two planes per module and a total of 7,120

instrumented channels.[50] Out of the seven modules of the SSD system, three modules are located upstream of the target for beam tracking and are made of $3cm * 3cm$ wafers. The module just downstream of the target is $3cm * 3cm$ in size while the rest of the downstream modules are $5cm * 5cm$ in size. The pitch of the SSD planes are $50\mu m$ and the thickness is $250\mu m$ to $300\mu m$. The planes of the SSD system are essentially PIN diodes. A charged particle passing through these planes will create electron-hole pairs, their number depending on the thickness of the wafer. When a minimum ionizing particle passes through one of these planes, it generates between $2.0 * 10^4$ to $2.4 * 10^4$ electron-hole pairs. The charge is collected in about $20ns$. The signals from the strips are fed into charge sensitive preamplifiers. The output from these preamplifiers are amplified again, discriminated and stored as output.

Analysis Magnet

The analysis magnet is located between the SSD planes and the MWPC planes. It is a vertical dipole magnet with its center located $2m$ downstream of the target. Although the magnet is not a perfect dipole, the field approaches a nearly uniform dipole shape when $20cm$ thick mirror plates are placed on both ends. The geometrical acceptance defined by the hole dimension in the two mirror plates are $35.6cm * 25.3cm$ at the upstream end and $127.0cm * 91.4cm$ at the downstream end over a length of $3.9m$. The magnet has a vertical field of 6.224 KG. The magnetic field was measured using the ZIPTRAK[51] system developed at Fermilab. The magnet was operated at a current of 1050 amps which corresponds to a transverse momentum impulse of 450 MeV/c.

MultiWire Proportional Chambers

There are four multiwire proportional chambers, consisting of four planes (X, Y, U and V) each and is located downstream of the analysis magnet. The wires in the anode planes are equally spaced. The wires in X, Y, U and V planes are oriented to 0^0, 90^0, 36.87^0 and -53.13^0 with respect to the vertical (Y) direction. There are total of 13,440 channels in the 16 planes of the MWPC[52] connected to the data acquisition system. Figure 2.6 shows the various planes in the chamber.

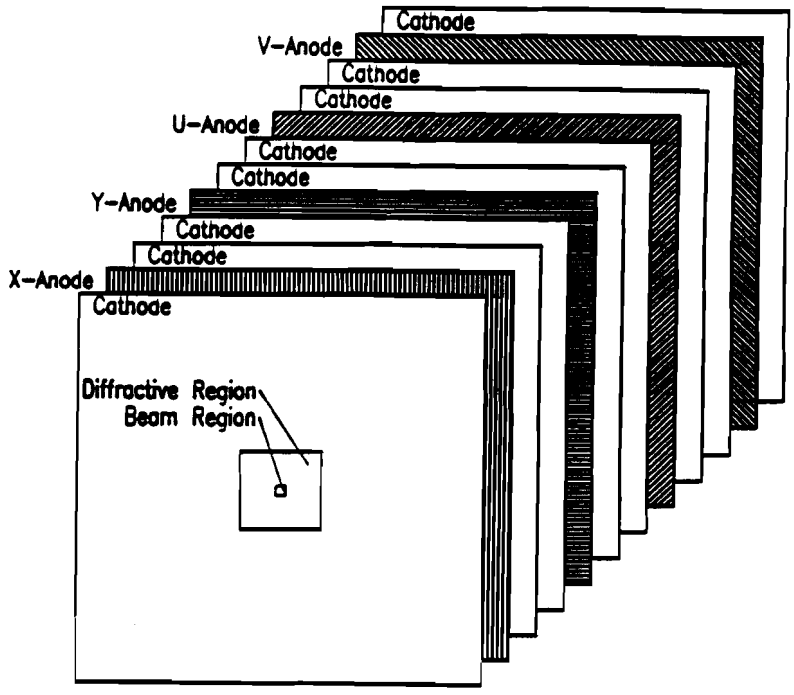

Figure 2.6: The MWPC System

The sense wires in the anode planes are made of gold plated tungsten of diameter $0.02mm$. The wire spacing is $2.54mm$ and the angular resolution of the track is 0.03 $mrad$. The anode planes are surrounded by graphite coated mylar ($0.0254mm$ thick) cathode planes. The cathode planes are segmented into two regions. The graphite coating and segmentation facilitates independent high voltages for different segments of the cathode, so that the region near the beam could be desensitized selectively during high intensity running. The four MWPC modules are of different sizes and the active area increases for the downstream modules. The active area for the four modules are $1.63m * 1.22m$, $2.03m * 2.03m$, $2.03m * 2.03m$ and $2.44m * 2.44m$. The dimension was chosen to maintain approximately constant acceptance for charged tracks, for all the four modules. The MWPC gas mixture is 80.2% argon, 18% isobutane, 1.1% isopropyl alcohol and 0.1% freon. The electronics readout system for the SSDs and the MWPCs were identical, except that there were no preamplifier boards for the MWPCs.

2.5 Liquid Argon Calorimeter

For E706, the Liquid Argon Calorimeter is the most important part of the detector system in order to study the direct photon physics. The LAC consists of mechanically independent, separate electromagnetic and hadronic sampling sections residing in a common cryostat. The calorimeter, which is about $3m$ in diameter, was designed to measure the position and energy of photons, electrons and hadrons as well as to trigger on events with high transverse momentum electromagnetic showers. A brief description of the LAC[53] is given below.

Design Criteria for the LAC[54]

1. The calorimeter should have as large an acceptance (solid angle coverage) as possible.
2. For a reasonable measurement of the comparatively small direct photon cross section, the calorimeter should be capable of running at very high interaction rate of about 1 MHz/sec.
3. The calorimeter should have the ability to distinguish between photons and neutral hadrons.
4. The calorimeter should also be able to trigger efficiently to precisely measure the cross section. This requires that the lateral segmentation of the EMLAC should be such that a trigger based on the transverse momentum (P_T) of the electromagnetic shower can be easily formed, so that the events can be selected and stored for analysis.
5. To properly measure the falling direct photon cross section the background must be understood very well. The primary source of the background is photons from decays of neutral mesons like π^0 and η. The calorimeter must be able to resolve these photons and also distinguish single showers from overlapping showers. The calorimeter should also be able to detect high energy as well as low energy photons so that π^0's and η's could be readily reconstructed. This requires that in addition to large acceptance the calorimeter should have linearity, good energy resolution and fine lateral segmentation.

6. A good gain stability over time is necessary for stable output and to avoid the frequent calibration of LAC which would be required due to large number of readout channels associated with fine segmentation and large acceptance of the calorimeter.

Cryostat and Gantry

As shown in figure 2.7, the LAC system consisting of both an electromagnetic section (EMLAC) and a hadronic section (HALAC) reside in a large stainless steel cryostat, supported by a gantry structure made of steel I shaped beams. The gantry structure can be moved in a direction transverse to the beam axis. Inside the cryostat, the electromagnetic section is placed in front of the hadronic section.

The cryostat is a cylindrical device, $5m$ in diameter and $9m$ high. It is bolted to a cover plate and a 'top hat' made of carbon steel which are part of the gantry. The calorimeters are suspended within the cryostat from steel rods attached to the gantry. The cryostat wall is made of $1.43cm$ thick stainless steel and covered on the outside with approximately $25cm$ of fiberglass and foam for thermal insulation. Dry nitrogen gas flows through the insulation to maintain its integrity. To reduce the amount of the passive material and thus the number of interactions as the beam goes through the cryostat, on the upstream side of the cryostat there is a beam window of diameter $5.08cm$ made with two thin layers of stainless steel sheets with a small gap between them. The beam is adjusted so that it points in the beam window of the cryostat.

To replace liquid argon with lower density material two additional vessels are used inside the cryostat. The first one, placed directly upstream on the EMLAC, is an argon excluder vessel filled with low density Rohacell foam. The second vessel is the beam pipe of diameter $40cm$ which passes through both the calorimeters and is filled with helium gas. The forward calorimeter covers the beam hole region which is $40cm$ in diameter.

The Electromagnetic Calorimeter(EMLAC)

The EMLAC is situated roughly 9m downstream of the experiment target. It is

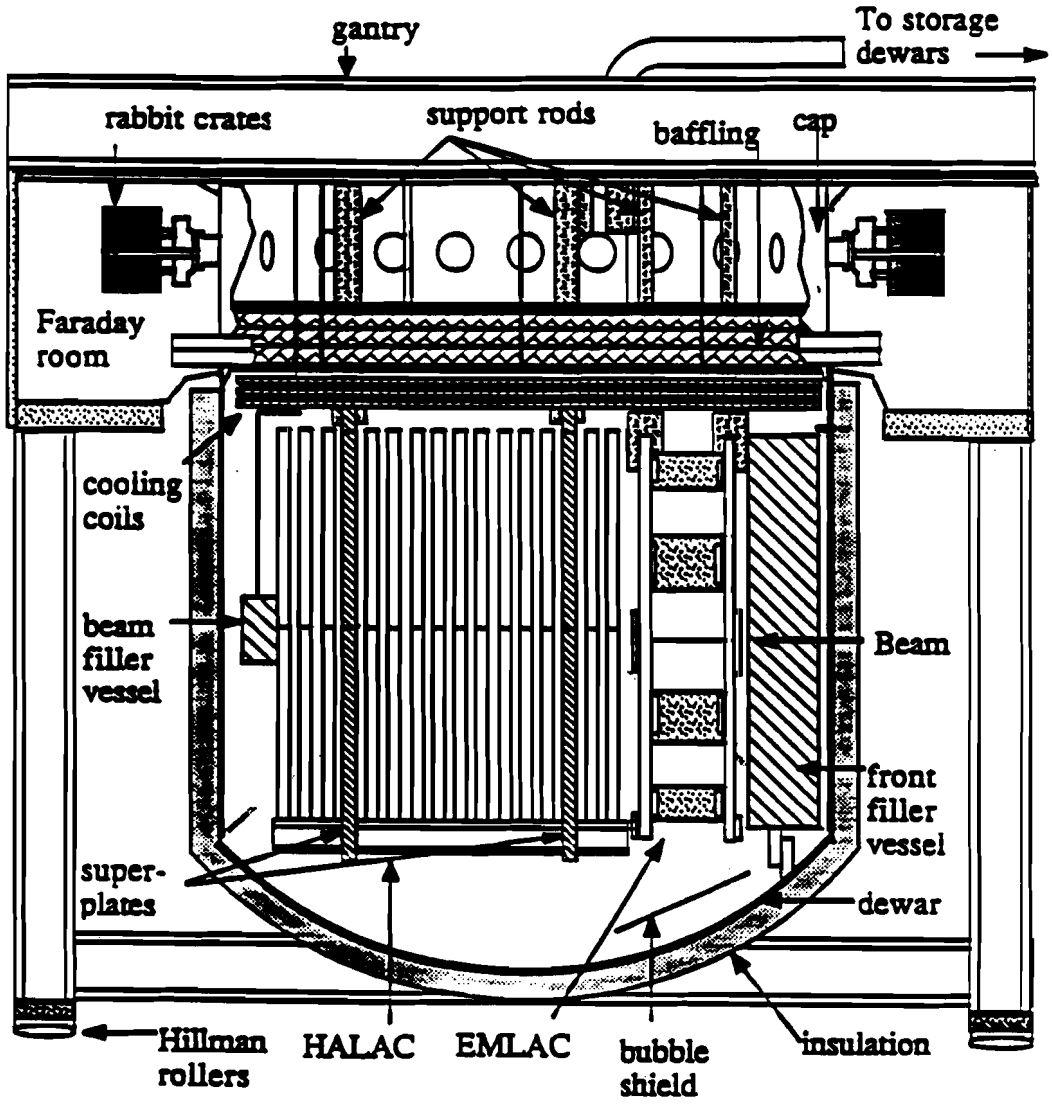

Figure 2.7: LAC gantry and cryostat. Suspended within the cryostat are the EMLAC, HALAC, filler vessel and beam pipe. The cryostat is supported by the gantry.

cylindrical in shape with an inner radius of $21cm$ and outer radius of $160cm$. In the laboratory frame this corresponds to an angular coverage of $21mrad<\theta<173mrad$. A hole of diameter $40cm$ goes through the EMLAC. Figure 2.8 shows the exploded view of the EMLAC. The EMLAC was assembled from four mechanically independent quadrants. An independent support structure holds these quadrants together. Each quadrant is divided into 66, $0.8573cm$ thick layers. In each of these layers, $2.54mm$ of liquid argon separates the $2mm$ thick lead sheet from the octant sized copper clad G-10 anode board. The cross section for a single cell is shown in Figure 2.9. Lead was chosen as the absorber material in order to distinguish between electromagnetic and hadronic showers. Lead has a small radiation length (X_o) of $0.56cm$ and a large interaction length (λ_I) of $17.1cm$. An electromagnetic shower will deposit its energy in a very short distance whereas a hadronic shower will not develop quickly. The EMLAC is 30 radiation lengths in depth and has a total of 6,264 channels.

The octant sized anode board are of R/Φ (radial/azimuthal) geometry and are read out independently. The R/Φ geometry of the anode board was chosen based on the characteristics of the electromagnetic showers. As the electromagnetic showers are limited in their natural width, the R/Φ geometry was used to get good position resolution and also to trigger events of interest, based on deposition of high P_T transverse momentum showers.

The R-view board consists of 256 concentric strips numbered from 0 to 255. The copper on the board is etched in such a fashion that all the strips are focussed on the target, $9m$ upstream of the LAC. As the corresponding strips from the different boards are supposed to subtend the same solid angle at the target, the width of the corresponding strips in R-view boards is a function of the distance from the target in the beam direction. The strips on the first R-view layer are $0.5466cm$ wide. The Φ-view boards are split into inner and outer regions which are read out independently. The inner Φ view consists of 96 strips and each strip subtends an azimuthal angle of 16.36 *mrad*. The outer Φ view consists of 192 strips and each strip subtends an azimuthal angle of 8.18 *mrad*. The inner/outer Φ split occurring

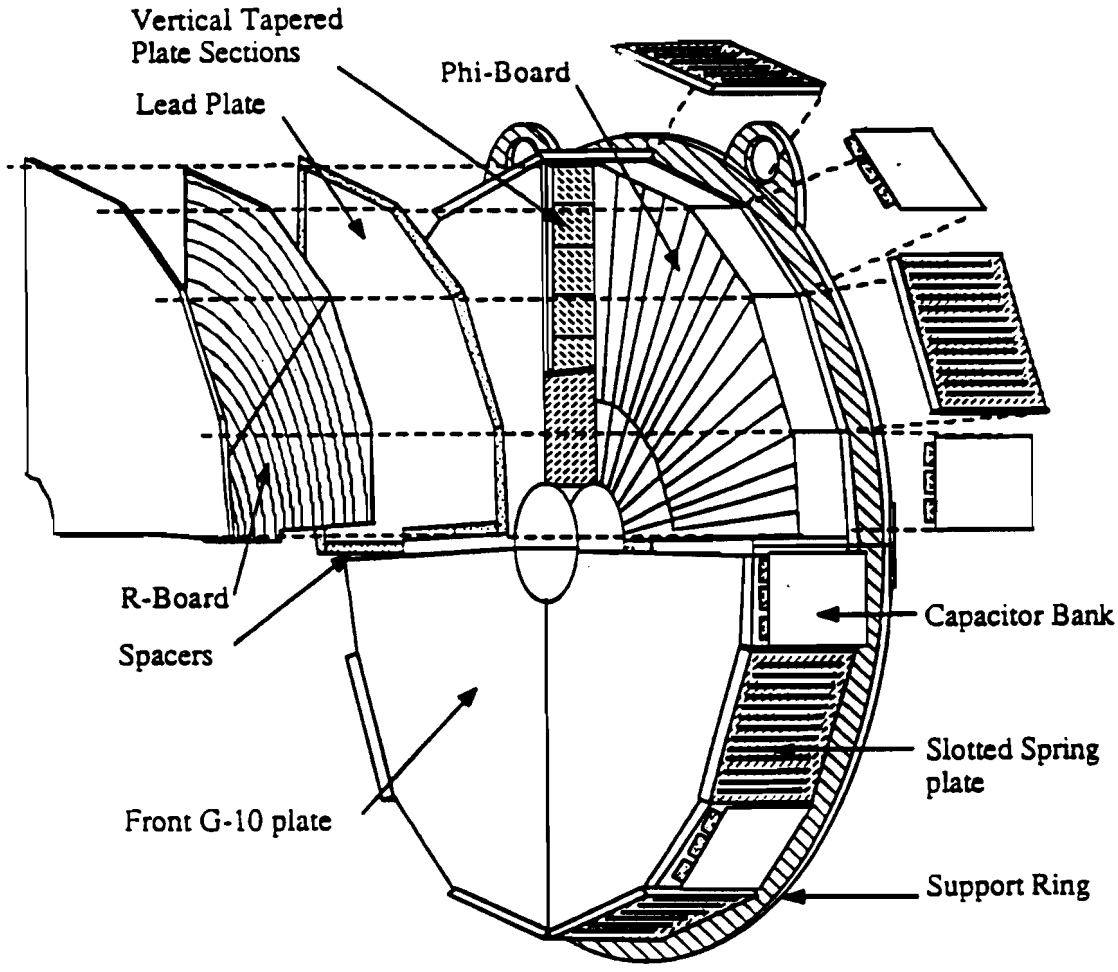

Figure 2.8: The Electromagnetic Calorimeter. The radial and azimuthal geometry of EMLAC is explicitly shown here.

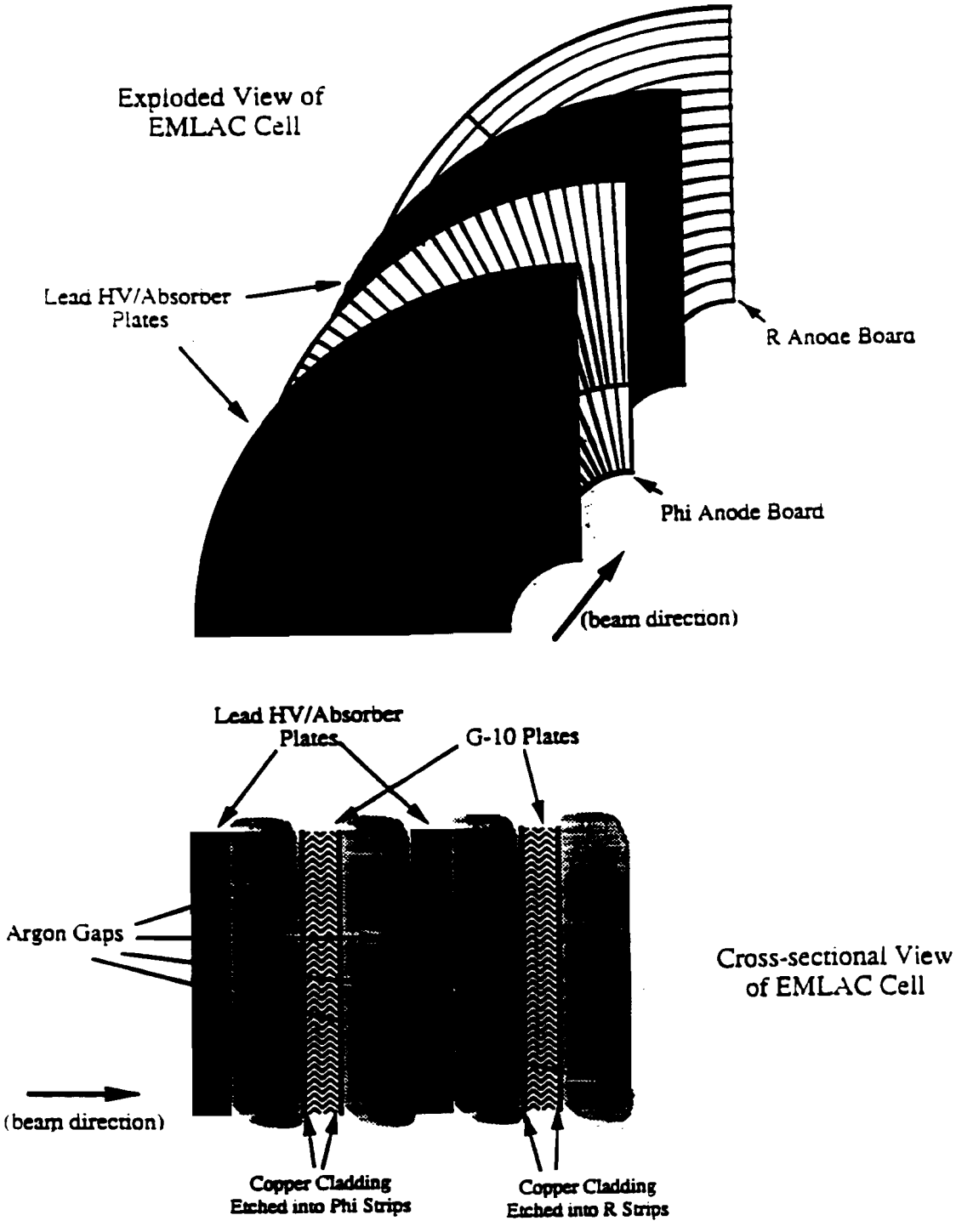

Figure 2.9: Exploded view of single EMLAC cell. Geometrical design for the EMLAC radial and azimuthal anode boards are also visible.

at a radius of $40.2cm$, improves the position resolution at large radii by increasing the number of outer strips. The inner/outer Φ boundary position at $40.2cm$ is also focussed on the target.

Each EMLAC quadrant is made of alternating layers of R and Φ views. The first layer in the beam direction is one of the R views. For the purpose of electronics read out, the calorimeter is divided into two sections longitudinally. The front section which is 22 layers, is approximately 10 radiation lengths thick. The back section, which is 44 layers, is approximately 20 radiation lengths thick. The calorimeter was divided into front and back sections so that one can easily discriminate between electromagnetic and hadronic showers. The electromagnetic showers will be mostly confined in the front section of the EMLAC while the hadronic showers will deposit most of its energy in the back section.

Since anode boards are octant sized each quadrant has two R signal boards and two Φ signal boards, each covering a nominal azimuthal angle of 45^o. The signals from the corresponding strips in the R and Φ views are added together and taken out to a readout board. An example of a readout board is shown in figure 2.10. The front and back sections are read out separately.

During operation, the lead plates are maintained at a high negative voltage of approximately 2.5 kV, so the lead must be kept from coming in contact with the anode boards. Small G-10 buttons are placed on anode boards to prevent it from coming in contact with the cathode. Also two G-10 plates support the quadrants on both sides. The two G-10 plates are connected to each other at the outer edge of the plate. Two high compression washers are used to support the rectangular steel plates to apply uniform pressure to the plates when the detector cools at the low temperature.

The Hadronic Calorimeter(HALAC)

Hadron Calorimeter is a sampling calorimeter eight interactions length in depth. It is designed to fully contain the energetic hadron showers and is centered on the beamline positioned directly behind the EMLAC. The HALAC is used to detect both neutral and charged hadrons. Since hadronic showers have a much wider lateral

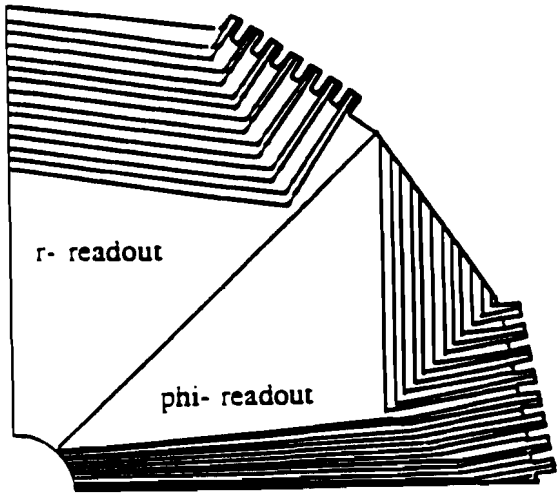

Figure 2.10: EMLAC Readout Boards.

profile than the electromagnetic ones, a very fine segmentation is not required. The HALAC has the same acceptance as the EMLAC. The principle of operation is the same for both the calorimeters. Figure 2.11 shows the structure of the HALAC.

The HALAC[55] is made of 52 layers of steel plates. Each of these absorber plates are $2.54cm$ thick. Between each pair of these absorber plates are readout modules, called 'cookies'. All together there are 53 cookies, including the one in front of the first steel plate and the one in the back of the last steel plate. The steel absorber plate and the readout cookie are separated by $3.2mm$ liquid argon gaps. The calorimeter is divided into front and back sections. The front section consists of 14 cookies and 13 absorber plates (approximately 2 interaction lengths) and the back section consists of 39 cookies and 39 absorber plates (approximately 6 interaction lengths). The absorber plates are octagonal in shape. Two of the 52 steel plates, referred to as super plates support the HALAC. These two super plates are connected to four support rods by means of large clevises. The support rods

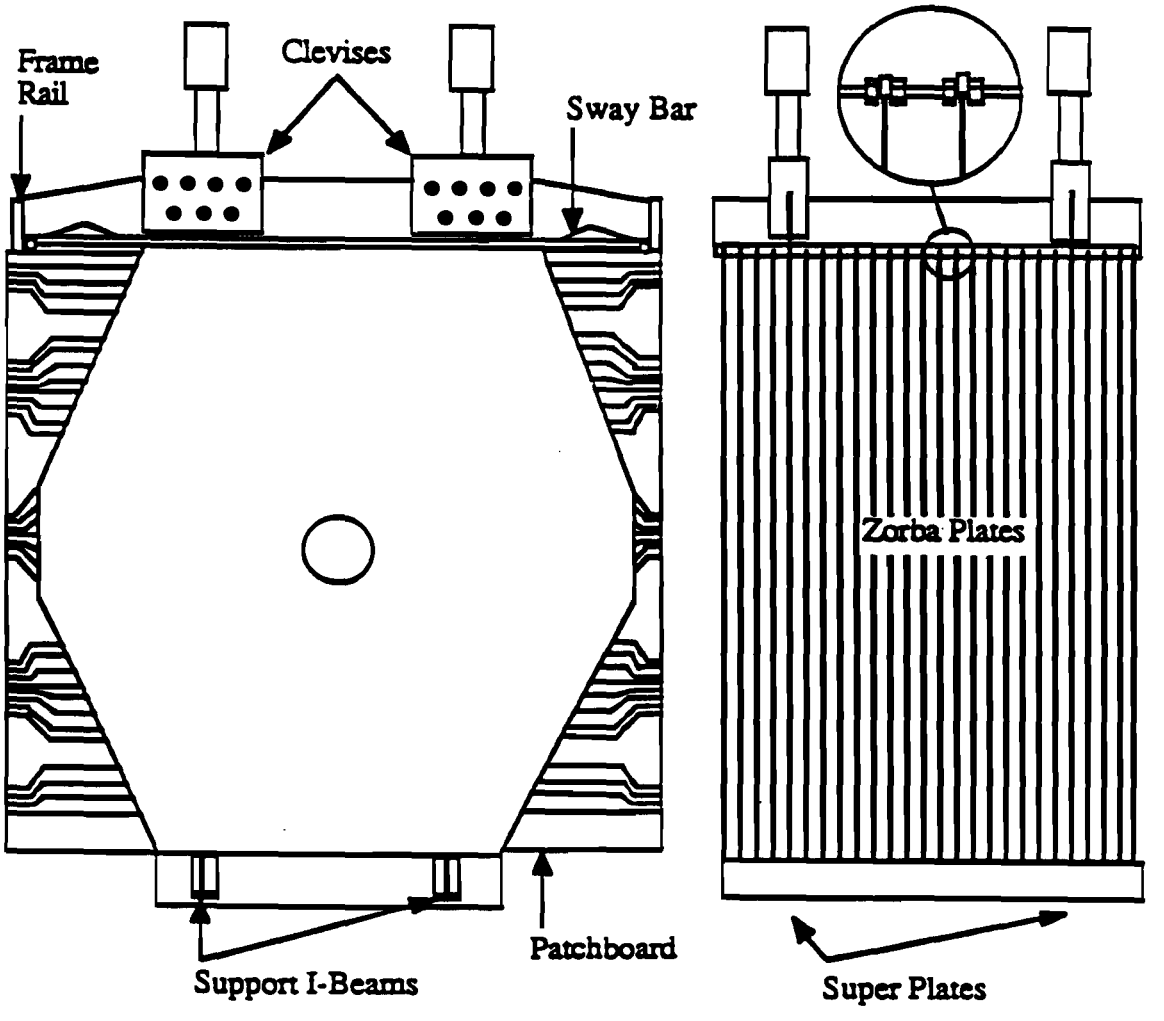

Figure 2.11: The Hadronic Calorimeter. Steel plates acted as absorber material. Noninteracting beam passed through the beam hole, shown in the front view (left picture).

are connected to the gantry. At the bottom of the super plates are two I-beams. These I-beams form the support for the remaining 50 plates. The super plates and I-beams are made of better quality cryogenic stainless steel whereas the remaining plates are made of structurally sound steel which needs only to support their own weight.

Because of hadron shower characteristics, pad-type readout was chosen over strip type readout, thus reducing the channel noise contribution. As shown in figure 2.12 the readout pads are triangular in shape. The smallest pads, near the center, are approximately $30cm^2$ where as the largest ones, at the outer edge are approximately $150cm^2$. Approximately 93% of the hadronic shower energy will be contained in a hexagon formed from six triangular pads. The pads and the readout lines are routed on $0.8mm$ thick copper clad G-10 readout boards. Each of these G-10 readout boards instruments one half of the detector.

Each cookie is divided into two halves, which combine together to cover the whole HALAC. Each cookie consists of seven layers of copper clad G-10, glued together into an octagonal unit. Each cookie also contains the high voltage planes, argon drift gaps and detector pads. Similar to EMLAC, the readout pads in front and back sections of the HALAC were ganged separately to form triangular towers which focussed at the target.

2.6 The Forward Calorimeter (FCAL)

Figure 2.13 shows the forward calorimeter used in the experiment. Situated $17m$ downstream of the target, it consists of three independent cylindrical modules. The whole system is mounted on a rail which allows the FCAL to be moved transverse to the beam direction and cover the beam jet region. FCAL[56] is a total absorption calorimeter consisting of 10.5 interaction length of the material and covers the beam hole region of the LAC. The FCAL is used to study the total P_T of the beam jet which arrives at a very small angle with respect to the incident beam direction due to the beam particle fragmentation in the very forward direction.

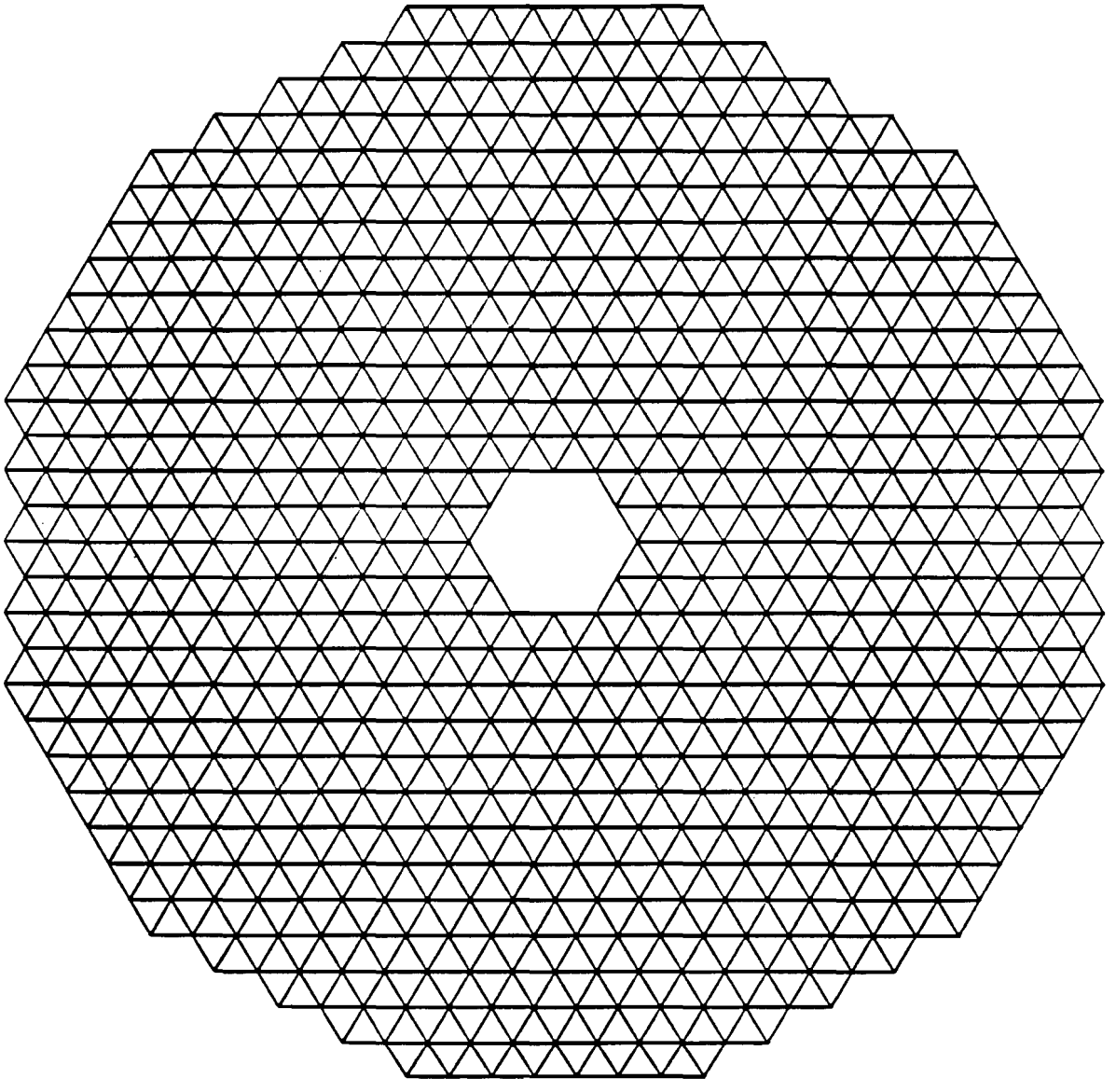

Figure 2.12: Triangular Pad Geometry of a Cookie in HALAC.

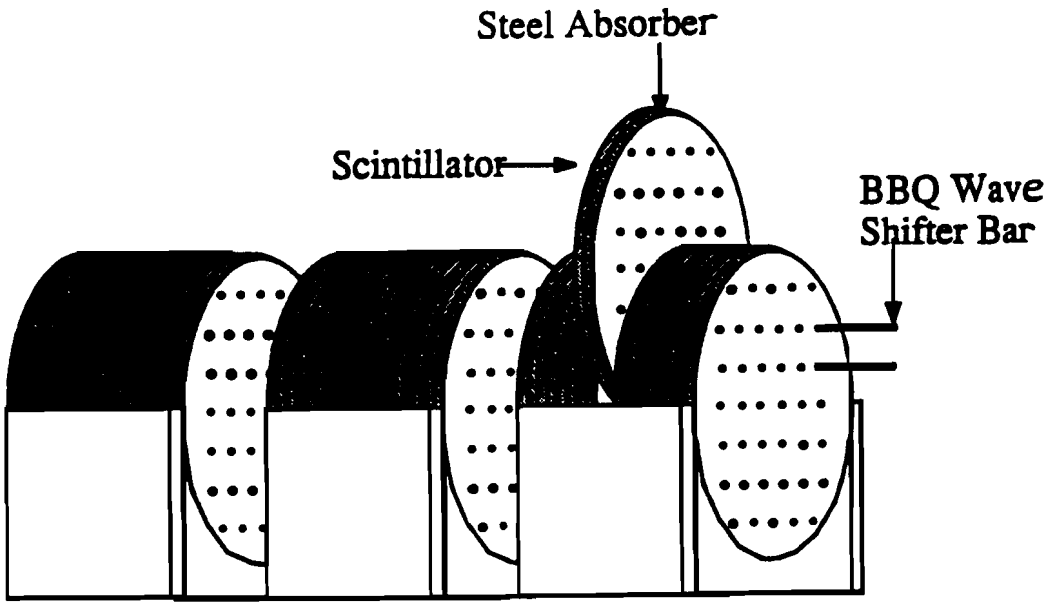

Figure 2.13: The FCAL System

The first two modules of the FCAL contain 28 layers of iron and 29 layers of acrylic scintillator while the third module contains 32 layers of iron and 33 layers of scintillator. The iron layers are $1.905cm$ thick, $114.3cm$ in diameter and separated by gaps of $0.635cm$. The scintillator layers are $0.46cm$ thick. To facilitate the passage of non interacting beam, a hole of diameter $3.18cm$ is made in scintillator and plastic layers. 76 holes, each of diameter $1.12cm$, are also drilled through iron and scintillator plates in which $86.4cm$ long wave shifter rods are placed. Each of these rods are silvered at one end and a photomultiplier tube (PMT) is attached at the other end. These wavelength shifter rods are also doped with BBQ and also contain agents which absorb ultraviolet rays. This was done to minimise the effect of Cherenkov light produced by particles passing through the rod. The light guide absorbs the scintillation light. The blue light emitted by the particles passing through the rod is converted into the green light which travels to the PMT. The light signals are amplified and from these signals one can determine the total energy and transverse momentum deposited in the FCAL.

3. Data Acquisition System and Trigger

3.1 Overview

This chapter describes the data acquisition system as well as the trigger implemented during the 1987-88 data run, necessary for the physics of the experiment. Brief descriptions of the data acquisition system and trigger[57] implementation are presented below.

3.2 Data Acquisition System

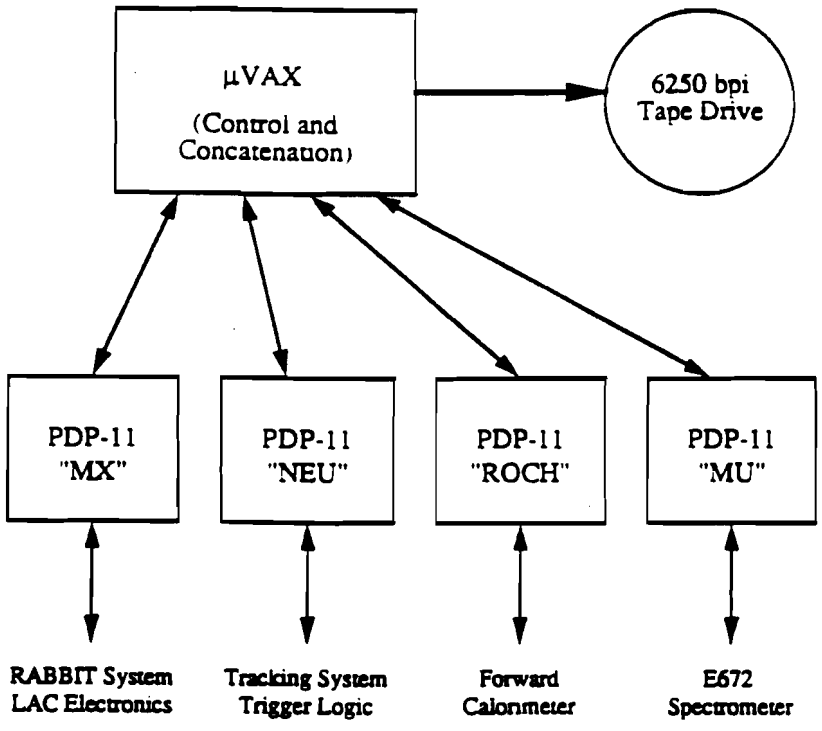

Figure 3.1: Data Acquisition System Diagram

Figure 3.1 shows a block diagram of the data acquisition system. The system consisted of one MicroVax 2000, four PDP-11s and two output 6250 bpi tape drives. The VAXONLINE[58] data acquisition software runs on the MicroVAX. The data

from the different parts of the spectrometer were collected by the PDP-11s, referred to as 'MX', 'NEU', 'ROCH' and 'MU'. The 'MX' was used for reading out the data from LAC via the Redundant Analog Bus Based Information (RABBIT) system. The E706 RABBIT system consists of four components, namely liquid argon calorimeter amplifiers (LACAMPs), the crate controllers (EWEs), the before after time modules (BATs) and the data aquisition sequencers (MXs). The 'NEU', 'ROCH' and 'MU' computers were instrumented with CAMAC system. They were readout using standard parallel and serial links. NEU is used to read out the data from the SSD/MWPC tracking system. It also monitors the condition of the Cherenkov detector and controls the trigger logic. ROCH reads out data from the forward calorimeter. MU read out data from the E672 dimuon system. Experiments E706 and E672 shared the same data acquisition system.

Once the trigger requirements were satisfied, all four PDP-11s received a signal directing them to read out the part of the spectrometer for which they were responsible. The data readout by these four PDP-11s were concatenated by a MicroVax II computer. The MicroVax acted as the on-line data acquisition system driver which controlled the data taking and monitoring. Once the information from all four PDP-11s were concatenated, the final event was sent to the memory known as the event pool and then written out to a magnetic tape.

The main components of the VAXONLINE software package used for the data acquisition system are:

1. GLOBAL MENU is a menu driven routine which contains a database of all the programs in the VAXONLINE system. It also allows programs in the system to operate simultaneously while sharing a single terminal in an organized fashion.

2. EVENT BUILDER is the software which controls the collection of data from different computers, concatenates them into a complete event, and then writes them out to the event pool. A Hydra-scaler which stores an event number that could be read by all the PDP-11s was used for identifying the information from the same event, read by the different PDP-11s. This event number was

initialized by NEU PDP-11, and was automatically incremented with each successive trigger. This unique event number was included with the rest of the information within each PDP-11. The Event Builder program used this number match for event concatenation.

3. BUFFER MANAGER gets events from the event pool and sends them, via the CDLINK* to an EVENT BUILDER.
4. DAQ manages the event pool.
5. RS232† allows communication between PDP-11 and VAX/VMS.
6. RUN CONTROL controls the beginning and end of a run.‡
7. CONSUMER is a program which accesses user code to extract events from the event pool, histograms them, and stores the histograms on disk. This is done to monitor online the spectrometer performance.
8. DISPLAY is a program which allows users to examine histograms generated by CONSUMER program. It can display and manipulate histograms from any histogram area, or set of histograms stored on disk.
9. OUTPUT is the routine that writes out the events from the event pool to the data tape. With OUTPUT, several output tape drives can be used. OUTPUT can switch from one tape drive to another, thus eliminating the dead time in tape rewinding and mounting.
10. COURIER is the central error and information message handler/router. Messages can be sent to the user's terminal and/or to displays controlled by the

---

⋆ It is a DR11-W link between a PDP-11 and the VAX. It is also used to refer to a 'virtual' link within the VAX used for transferring data between processes on the VAX.

† The RS-232 communication system provides the user a means of communicating between a VAX/VMS program and multiple RT-11 front-end systems, over a VAX/VMS RS-232 terminal line.

‡ A data run for the high energy physics experiments may extend from few weeks to many months i.e. the entire period of data taking, as is evident from the word 1987-1988 run. But the big run is divided into many small runs, depending on the need/capability of the experiment. During 1987-1988 data collection, one small run was limited by the capability of a 6250 bpi tape to hold the data or if we decided to perform cold start, which performed several initialization tasks within the system before we filled a 6250 bpi tape. One tape at maximum can hold around 13,000 events and thus we had to start new run almost every half an hour.

router. The user can also generate his own message.

11. STATUS MANAGER makes information available to other processes, thus making inner communication among different processes much easier.

3.3 Trigger

The trigger system was designed to select events triggering on high transverse momentum ($P_T > 3$ GeV/c) electromagnetic showers. It was designed to perform at rates up to 10^6 interactions per second. Since the direct photon production cross section falls approximately exponentially with P_T, the trigger system was designed to select events with at least one high P_T shower. Different trigger combinations were implemented to study the characteristics of the electromagnetic showers. Pulser† triggers were available to test the trigger and the data acquisition system. The trigger selection was done in three steps: beam and interaction definition, preselection of the interaction and final selection of the event.

Beam and Interaction Definition

To define a beam particle, three scintillation counters called BA, BB and BH were used. As shown in figure 3.2, the counters were located in the beam line just downstream of the veto wall, approximately $1.5m$ upstream of the target. Two of the counters BA and BB were, $2.54cm * 2.54cm$ each in area and BB was completely shadowed by BA. The third counter, BH was $12.7cm * 12.7cm$ in area with a hole of $0.95cm(3/8in)$ in diameter. The hole in the BH counter was centered on the beam line. A beam signal was defined as the coincidence of the signals in BA and BB and no signal in BH. If there was no signal in the BH, it meant that the particle went through the $3/8in$ hole.

There were four other scintillation counters (SW1, SE1, SW2 and SE2) located downstream of the target. SW1 and SE1 were placed upstream of the analysis magnet whereas SW2 and SE2 were placed downstream of the analysis magnet.

† In a pulser trigger, a pulse is generated which mimics the r-f clock of the accelerator. It also sends pulse through the trigger.

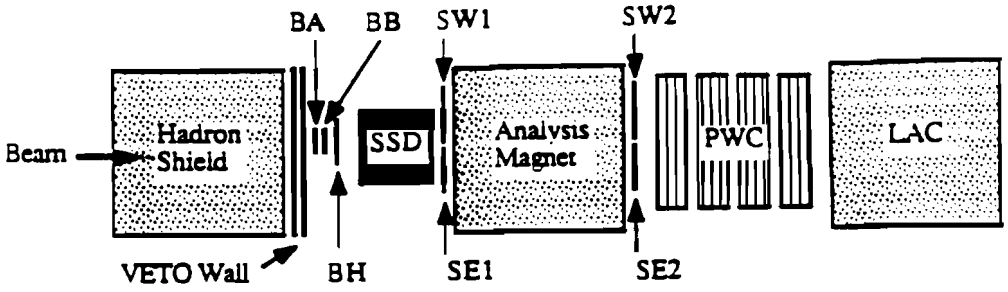

Figure 3.2: Scintillation counter configuration used to define beam. Here the counters have been shown enlarged with respect to other detectors.

The logical OR of the discriminated signals from these four scintillation counters in coincidence with a beam signal was used for defining an interaction trigger. It was also required that no other interaction occurs within $\pm 60ns$ of the present interaction. This was important in order to prevent the overlapping of signals from different events due to insufficient time resolution of the detectors (pile-up of interactions). If all these conditions were satisfied, an interaction strobe signal was produced.

Preselection of an Interaction

The pretrigger was defined in order to quickly reject events which were of no interest to the experiment. Only events with large P_T deposition in any octant of the EMLAC were triggered on. The P_T deposited in the EMLAC was defined as $P_T = E \times \sin(\theta)$, where E is the energy of the shower as measured in the EMLAC and θ is the angle between the beamline and a line from the target to the point where shower energy was deposited.

The R-Φ geometry of the EMLAC was used for the online measurement of the P_T. A Global P_T signal was generated for each octant of the EMLAC. The Global

P_T of the octant was defined as the total P_T deposited in that octant. For an event to be preselected, signals from an octant were required to satisfy the following conditions:

- The innermost 96 R-strips or the next 128 R-strips must have a P_T deposition of at least 1.7 GeV/c. The P_T deposited should also correlate in time with the present interaction.
- The rise time for the LAC signals were of the order of 300ns. If two low P_T showers get deposited in the 300ns prior to the present interaction then the global P_T signal can be faked. To avoid this possibility of early P_T deposition, it was required that the total P_T deposition in the octant within the previous 300ns interval be less than 1.5 GeV/c.

Once the above conditions were satisfied, a corresponding octant pretrigger logic signal was generated. This was done by putting the octant Global P_T in coincidence with the interaction trigger and in anticoincidence with the early P_T signal present within the preceding $300ns$. The logical OR of all octant pretrigger signals was put in coincidence with the interaction strobe and in anticoincidence with the two veto wall signals[†] and SCRKILL.[⋆]

The event gets preselected if the pretrigger signal is generated with the above configuration. This signal was used as a LOAD signal to latch the SSD/MWPC and the FCAL information and also in the formation of the LAC trigger. When there are only beam and interaction signals, then each was prescaled and divided by 10^6 and used as both pretrigger and final trigger.

Final Selection of the Event

Once the events are preselected, the final selection of the event is done on the basis of signals from the LAC. For each octant of the LAC, two signals called Local P_T and Global P_T were generated. The Global P_T could also be generated by

† The two veto wall signals were placed with each other in logical AND combination.

⋆ The SCRKILL signal is a $30\mu s$ wide-pulse generated by noise spikes produced by the 400 Hz power supplies.

coherent noise (noise common to all channels) or from multiphoton events, in which each photon only contributed a small fraction of the total P_T. Fine granularity of the EMLAC was used to reject noisy events, by requiring a Local P_T deposition. Local P_T deposition meant that a substantial fraction of the Global P_T had to be deposited within 16 adjacent radial strips of the calorimeter, roughly the size of an average electromagnetic shower in our energy range. These two P_T signals from each octant were discriminated using different nominal thresholds, in coincidence with the pretrigger strobe. Using the combinations of the two P_T signals and the different thresholds, four LAC triggers were formed. The threshold settings for these four triggers are shown in table 3.1.

Trigger Threshold Settings				
Logic Signal	**runs: 1811-2292**	**2293-2310**	**2311-2904**	**2905-3036**
Local_P_T_Low	1.2			
Local_P_T_High	4.2	3.6		3.0
Global_P_T_Low	2.5			
Global_P_T_High	4.0		3.6	

Table 3.1: Trigger Threshold Settings in GeV/c by run number.

The final LAC triggers are:

- Local_Global_Hi: This trigger was generated if in one or more of the octants of the EMLAC, the P_T deposition was such that the Local P_T signal satisfied the Local_P_T_Low threshold and the Global P_T satisfied the Global_P_T_High threshold.
- Local_Global_Lo: This trigger was similar to Local_Global_Hi trigger, except that here the Global P_T had to satisfy the Global_P_T_Low threshold. This requirement of having two triggers, differing in threshold setting only was done to study the efficiency of the trigger required to satisfy the higher threshold. Since the Local_Global_Lo trigger would have dominated the event selection,

it was prescaled by a factor of 10 to have better trigger acceptance at higher P_T value.

- Single_Local: This trigger required that one or more octants had a Local P_T signal which satisfied the Local_P_T_High threshold. This meant that a large amount of P_T was deposited in a small region (4-8 cm in R). This was very efficient in detecting single photons and photons from $\pi^0$and η decays.
- Two_Gamma: This trigger required that if an octant satisfied the threshold for Local_P_T_Low signal then one of the remaining three octants on the opposite side also must satisfy the threshold for the Local_P_T_Low signal. This trigger was designed to study events having two large electromagnetic showers in the opposite direction.

For the final selection of the trigger, each of these four LAC triggers required that both the pretrigger signal as well as octant pretrigger signal had been generated. If no LAC trigger was selected, a reset signal was sent out to the electronics and the system was readied within $5\mu s$ for the next event. If a trigger was satisfied, then an INTERRUPT signal was sent out to the data acquisition system to readout the stored data from the spectrometer. When the data collection was completed from the spectrometer, a reset signal was sent to the data acquisition system and the trigger system was reset to process the next event.

4. Event Reconstruction

4.1 Overview

Event reconstruction for the experiment is done using an offline software package written in FORTRAN. The driver code for the event processing is called MAGIC. It reads in the raw, unpacked or the reconstructed data; unpacks the raw data; calls the reconstructor needed for the detector required, and outputs the raw, unpacked or the reconstructed data. A tape or disk can be used for both the input and the output. User control cards are used to determine the reconstructors to be used, the number of events to be processed and the error handling during the event processing. The analyzed data is written to the Data Summary Tapes (DSTs). In addition to experiment specific code, MAGIC mainly uses routines developed and maintained by FNAL and CERN. The list includes:

1. ZEBRA[59,60] memory management routines (including I/O)
2. PATCHY[61] code management routines
3. FFREAD[62] control card processing
4. DI-3000[63] graphics routines
5. CERNLIB general utility routines : HBOOK[64]/HPLOT[65]/PAW[66]/HIGZ[67] for plotting and histogramming
6. GEANT3[68] Monte Carlo (GEANT3 is not part of MAGIC. It was used to generate Monte Carlo events to compare with data.)
7. The VAXONLINE data acquisition software, which writes the raw data tapes.

ZEBRA is a CERN developed, FORTRAN set of routines, which allows the creation of data structures at execution time and memory management. It also provides methods for manipulating these structures. The data structure can also be written to a storage medium (tape or disk) and retrieved.

PATCHY is a code management program, developed by CERN. It allows one to change and update the program and the card file. It also allows one to break the

program into many sections, called patches. These patches are divided into several smaller sections, called decks. Changes can only be made into the card files. The card file is used to generate the FORTRAN file. Also, by selecting specific switches, certain patches and decks can be included in the FORTRAN file. Switches also allow one to make files which can be executed on different computers. This feature allowed us to use the VAX, ACP and AMDAHL computers to write raw data, process raw data to write out the DSTs, and to analyse those DSTs for physics.

Variables must be stored in free format way to be read independent of the computer hardware. FFREAD, which is a set of FORTRAN-77 subroutines, provides this facility. It also allows for user to manipulate certain actions. In high energy physics it is very important to have software which displays two or three dimensional graphics images. DI-3000 is a machine and device independent integrated system of graphics software tool which provides this facility. It is a set of FORTRAN-77 routines written in ANSI FORTRAN. It can be run either interactively or in the batch mode.

HBOOK is a subroutine package to handle statistical distributions. The output of HBOOK on devices other than the line printer is produced by HPLOT. It is used to produce drawings of presentable quality. HIGZ stands for High level Interface to Graphics and ZEBRA. This is a part of a larger system called PAW (Physics Analysis Workstation). HIGZ has been implemented to provide a graphics interface to PAW. PAW is a software package used in the analysis and presentation of data.

The design and performance of the detectors and the reconstruction and analysis programs have to be simulated to have better understanding of the detector or to efficiently interpret the results. GEANT3 is a CERN developed system of detector description and simulation tools which provides these facilities.

The machines used for data processing are:

- VAX : used for program development and debugging,
- ACP (Advanced Computer Project) : pattern recognition and event reconstruction,

- AMDAHL : splitting the processed data into different streams to study different physics possibilities.

Code development was done on several VAX computers, and the resulting code was converted to run on the ACP for the first pass data processing. The ACP system is a parallel processor, designed to process individual events in individual CPU systems. A more complete description of the ACP system is given in the next section.

4.2 ACP

The ACP[69-71] system was designed at Fermilab, with the focus on event oriented multiprocessing. In the production environment, the ACP system consists of a single host processor (usually a MicroVAX) and a large number of processing nodes(25-100) in parallel, which are based upon 32 bit Motorola 68020^{TM} microprocessor chips, as shown in figure 4.1. The high speed 32-bit ACP Branch Bus, connects up to 16 crates of Single Board Computers (SBCs) per branch to each other and to the host computer. The SBCs are single-board computers with a CPU and up to 16kbytes of memory. The ACP boards include two/six Mbytes of memory and the Motorola 68882 floating-point coprocessor(FPU). The capacity of each node is approximately equivalent to 0.8 VAX780.

To run the program on the ACP system, the user must divide the application program into two parts: a host part, which runs on the VAX host containing all input/output, and a node part which runs in parallel on all the nodes and will contain the time consuming unpacking of the raw data, event reconstruction and histogramming. All communications between the two pieces of the program will be through the Branch Bus and calls to standard ACP subroutines, which automatically downloads the nodes with the user's code, starts up the nodes, and monitors their performance.

There is an event loop which reads events from the tape or disk and writes output to a tape or disk surrounding a call to a processing subroutine which does the analysis. The host sends raw data to the node and gets output from the node. The

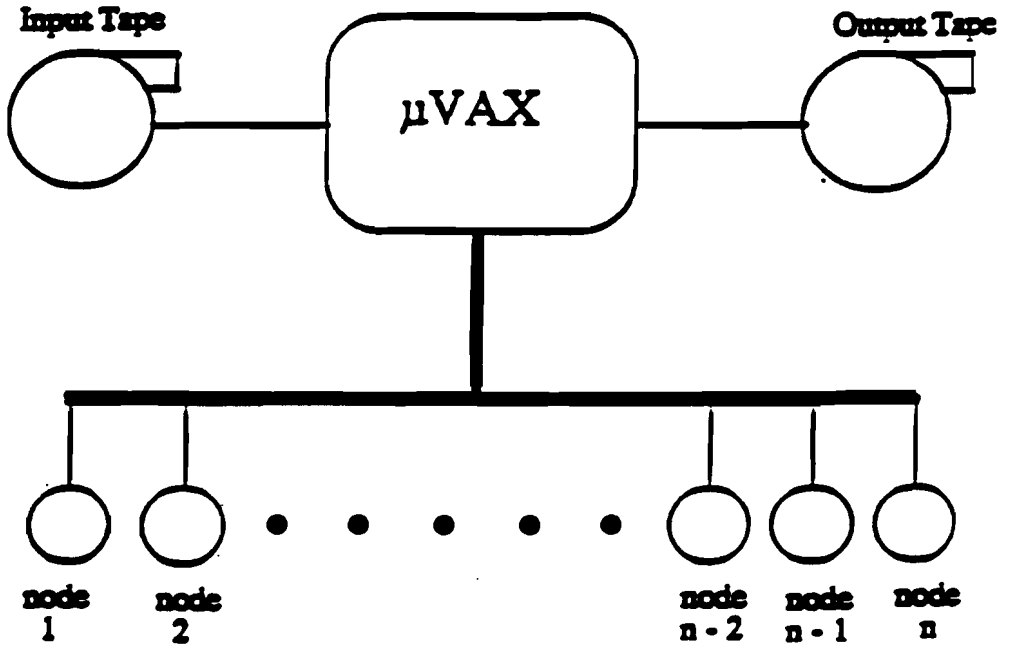

Figure 4.1: Block diagram of ACP Computing System

ZEBRA memory management package and the HBOOK histogramming package, are also implemented on the ACP system. Parameters are passed to the nodes through defined data blocks from the event processing section of the code. This section of the code has to be in pure FORTRAN-77. Also, all data passing between the host part and the node part of the code goes through data blocks. The three basic modes of passing data between the host and node part are:

1. Event processing mode: The individual events are passed from the host to the individual nodes, where they are unpacked and put in working common blocks, processed and then packed from working common blocks to the output common blocks. The output common blocks are returned to the host which

writes the data to the tape or disk. Figure 4.2 illustrates the concept.

2. Constant broadcast mode: In this mode, the experimental constants are passed from a file to all the nodes at the beginning of the run. The same constants are used to process all the events till the host decides to broadcast new constants to all the nodes.

3. Statistics collection mode: Statistics or histograms from all the nodes are collected into the summed data blocks on the host.

Stages of Software Development

The stages of software development for the ACP system are:

1. Write, debug and run the program on a single-processor (VAX780, 3200, 8800 etc).

2. Separate the code into HOST and NODE pieces, run on the ACP Simulator where both the host and the node program runs on a VAX as separate subprocesses. Test the split and event transfer logic and debug it. Usually major debugging is done on simulator because it is much easier to diagnose the problem there.

3. Run the same host and node program on real microprocessor nodes on a software development system, using only one node to begin with and then employing more nodes to check for host and multi-node communication problems.

4. Submit batch jobs to the production ACP system with large number of processing nodes.

In stages 2, 3 and 4 we have a HOST fortran file, a NODE fortran file and a UPF file. (User parameter file - This is a text file with the name of the program and extension UPF. This compiles, links and runs the program, by selecting various options, system, number of nodes, how to transfer data etc.)

E706 and ACP: For our 1987-88 run, we accumulated around 500, 6250 bpi tapes, representing a sensitivity of one event per picobarn. To process one of these tapes

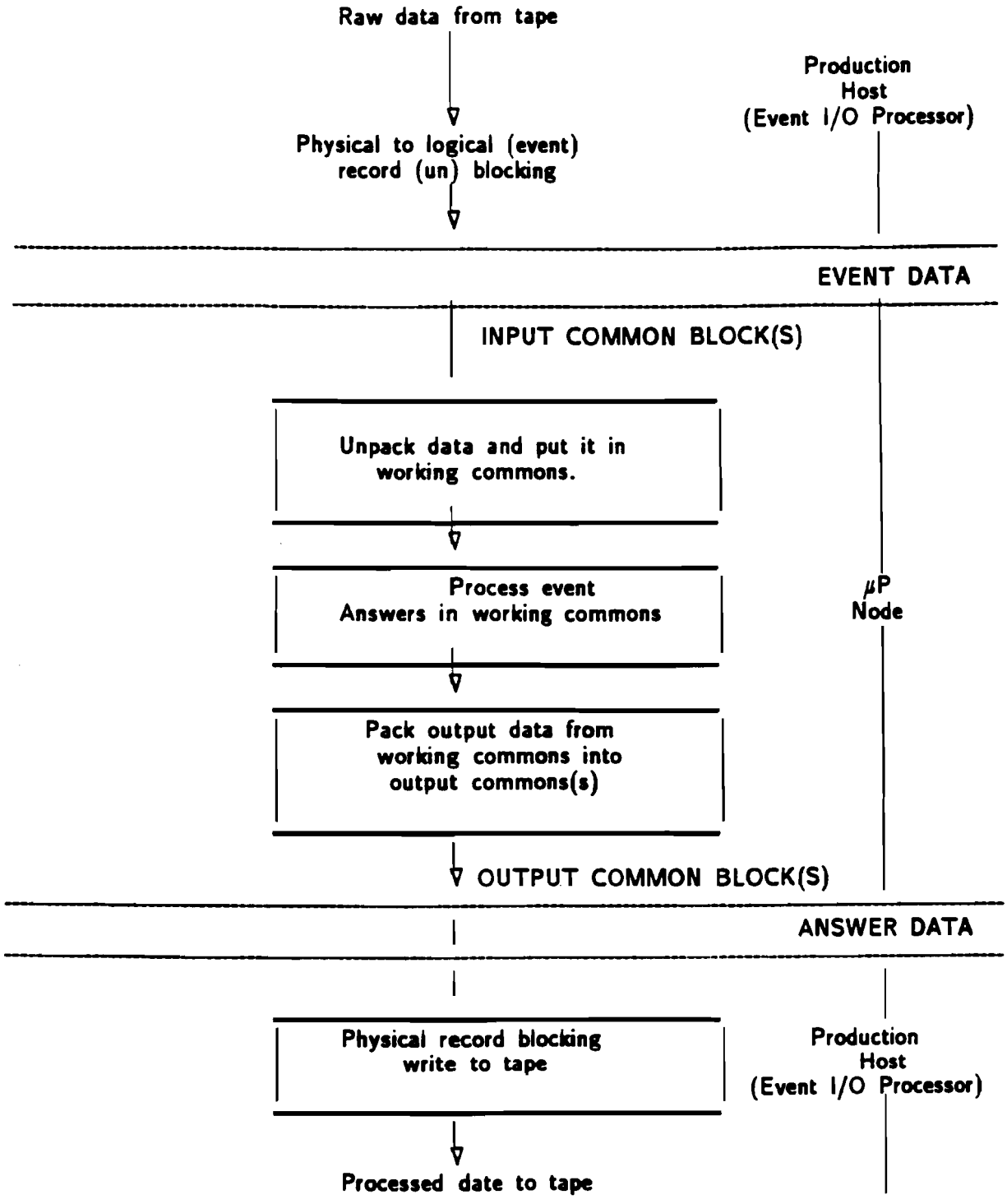

Figure 4.2: Event Processing Mode.

on a VAX780 required around 70 cpu hours. As the capacity of each 32 bit 68020 Motorola microprocessor is around 0.8 VAX780 unit, a machine with 65 nodes is comparable to 50 VAXes. I/O limitations of our program were such that we were able to efficiently use almost all the nodes in any system with up to 65 nodes. Usually one input 6250 bpi tape was analyzed in little more than 2 hrs. There is also the provision to stop individual nodes if they get bogged down in analysing some monstrous event or somehow goes into an infinite loop.

4.3 Charged Particle Reconstruction

The charged particle tracking system consisted of silicon strip detectors, multiwire proportional chambers and a dipole magnet. The tracking system was designed and used to study jets, associated with direct photon production. It was used to locate vertices* within the target region and to find whether the shower deposited in the EMLAC was due to a charged particle or a neutral one. This was done by projecting a charged track to the face of the EMLAC and if the shower was within one cm of the track then it was associated with a charged particle, otherwise it was considered to be coming from a neutral particle. Only showers coming from neutral particles were used in this direct photon analysis.

The software reconstruction package used for the tracking system is called PLREC.[72] The tracking algorithm uses informations from the Silicon Strip Detectors(SSD's) for vertex finding, beam tracking and upstream tracking. It also used informations from MultiWire Proportional Chambers(MWPC's) for the downstream tracking and a dipole analysing magnet for momentum determination. Using the magnetic field of the dipole magnet, the upstream and downstream tracks are matched to make the full trajectory, and the relevant information for each track such as momentum, charge, direction cosine are then stored in the proper data banks to be written out to DSTs. The tracking reconstruction was done by using two types

* The term 'vertex' refers to point of origin of a group of particles. The point where the beam particle interacts within the target is referred to as the primary vertex. A secondary vertex in this kind of experiment can arise either from the decay or interaction of particles produced at the primary vertex.

of tracks, view and space tracks. There are four different views (X,Y,U,V) for the MWPC's and two views (X,Y) for the SSD's.

Downstream tracking: First, tracks are found independently in each of the four views of the MWPC's. A view track is the least squared straight line fit to three or four points from the four planes of each view. These two-dimensional view tracks are then matched among the different views to identify straight line segments in 3-dimensional space. These matched straight lines in 3-dimensions are referred to as space tracks.

View tracks are formed in two passes by searching through the hits.† In the first pass, the first and the fourth plane in the view are chosen as seed¶ planes. The second and third plane, the two planes in the middle are taken as search planes. A hit from each of the seed planes is selected to determine the slope and intercept of a candidate view track. Candidate view tracks are formed with all possible combination of hits from the seed planes. Once candidate view tracks are made, then the search planes are looked for possible hits within ± 1.5 wire spacing of the projected track. If hits are found in both of the search planes, then a four hit view track is formed. If hit is found in only one of the two search planes then it forms a three hit view track. If no hits are found in the search planes then no track is stored for that particular seed pair. Least-squared fits are done for all the candidate tracks, using all the possible combinations of the selected hits. If a four hit track candidate fails to meet the χ^2 criterion, then the fit is redone after removing the hit with the worst residual.

In the second pass, the whole procedure is repeated again with the two inner planes being the seed planes and the two outer planes becoming the search planes. Only those hits were used which did not belong to the original four hit tracks. This pass also creates three-hit tracks which missed either of the two outer planes. The three hit tracks are also required not to share more than two hits with any four hit

† A hit is described as the coordinate of a wire in a plane which registers a signal when a charged particle passes by it.

¶ A seed pair is a pair of hits in which one hit is from one seed plane and the other hit is from the other seed plane.

track. Once all the view tracks are found then the four hit tracks are compared among themselves for shared hits. The tracks with least χ^2 and least shared hits are kept and the others dropped. The same procedure follows for three-hit tracks.

Once view tracks are found, they are matched to form space tracks. The algorithm used for the space track reconstruction is similar to the view tracks finding algorithm. In the first pass, X and Y views are taken as seed view where as U and V views form the search view. In the next pass, U and V views form the seed view while X and Y views form the search view. A 'track seed'[§] which is a candidate for a space track is projected onto the planes of the search view, and hits in the search view are compared to the projected hits of the space tracks. All the hits forming the seed track along with the hits falling within ± 1.5 wire spacing are kept. The stored hits must satisfy the following conditions to form a space track:

- There should be at least two hits from each search view.
- There should be at least a total of four hits from both the search views.
- There should be at least six hits from the track seed planes.
- There should be at least thirteen hits in total.

After candidate space tracks are created from both passes, a track cleanup is performed. If two space tracks share six or more hits, then the one with fewer hits is dropped. If they share the same number of hits then the one with larger χ^2 value is dropped. Any track with nine or more hits not shared by any other track, out of thirteen or more hits which form the space track, is always kept.

Upstream tracking: Upstream of the magnet and downstream of the target there are four SSD modules each with a set of two orthogonal planes. Using these planes, view tracks are formed for both X and Y views. No space tracks are formed for the upstream tracking system due to lack of diagonal planes. The algorithm used for the SSD view tracks are identical to the one used for the MWPC system. If hits are registered in two adjacent strips of a plane then the charge is shared by

§ A 'track seed' is a pair of view tracks in which one of the tracks is from one seed view and the other track is from the second seed view.

these adjacent strips. In such cases these strips are clustered into a single strip to minimize the CPU time. A track is required to have at least three hits out of a total of four possible hits.

Beam tracking: Three SSD beam planes each with two orthogonal (X,Y) views are located upstream of the target. For both the views, a least squared fit is used to find all the three hit beam tracks. Two hit beam tracks are formed from the hits not already used in forming the three hit beam tracks. At a later stage, after the vertex was found (vertex finding is discussed later in this chapter), ambiguities arising from multiple beam tracks are resolved by the vertex location. The track closest to the vertex in transverse direction and within $50\mu m$ of it, is considered as the beam track associated with the vertex. If there are no beam tracks within the $50\mu m$ distance, then no beam track is associated with the vertex.

Linking at the Magnet: The upstream and downstream tracks are linked with each other by projecting these tracks to the center of the magnet. For downstream space tracks, all the upstream tracks are projected to the center of the magnet and the algorithm looks for the upstream view tracks which project to match it within $0.7cm$ in each view. The upstream view tracks are also corrected for the effects of the magnetic field in the X-view. Because the tracks bent primarily in the XZ-plane, an additional cut is required to account for the difference in the Y-slope due to the magnetic field between the upstream and the downstream tracks. Usually, each downstream track[‡] can link with more than one candidate upstream track. The angular difference for each pair is compared to find the best match. If the best match, passes the predetermined cut, then this is selected as a linked or physics track. The charge and momentum of the physics track is calculated from the magnetic field and the angle of the particle trajectory relative to the Z-axis in the YZ plane and the angle relative to the Z-axis at the exit and entry point in the magnet region in the XZ plane.

Vertex finding: The primary vertex is determined from the tracks reconstructed in

‡ There were no upstream space tracks, so in a given view, any upstream track can link to any downstream track, without any constraints from the other view.

the two views of the SSD system. The vertex candidates are found separately in each of the two views and then they are matched to get the three dimensional position of the vertex.

The algorithm looks for four or more, four-hit tracks that also links to downstream tracks. If it finds more than four such tracks, then only those tracks are used for view vertex reconstruction. If the above condition is not satisfied, then if there are more than three four-hit tracks, all of them are used for vertex reconstruction. If this condition is not satisfied, then all three-hit tracks which are linked with downstream tracks are used for vertex reconstruction.

The individual tracks selected for the vertex reconstruction must intersect within the dimension of the target when projected to the target region. If at least three tracks do not project to that region, then the vertex reconstruction is declared a failure.

The vertex position was determined by χ^2 minimization , defined as

$$\chi^2 = \sum b_i^2/\sigma_i^2 \tag{4.1}$$

where b_i is the impact parameter of the ith track and σ_i is the uncertainty in the projection of the ith track.

Only those vertex positions are kept for which the average impact parameter is less than $20\mu m$ or the largest impact parameter is less than $50\mu m$. If the above conditions are not satisfied then the track with the largest impact parameter is not used in the vertex finding algorithm and the process is repeated till either of the above conditions are satisfied or only one track is left, at which point the algorithm stops looking for a vertex and the event is deemed to have no vertex.

The same process is repeated for the other view. After the vertex location is found in both views, refitting of vertices are done by using the tracks in one view and the vertex Z position in the other view. The best X and Y view vertex combination is chosen as X and Y view vertex. The Z position of the vertex found in each view is then weighted with σ_z^2, where σ_z is the error in the Z position. The final matched

vertex Z position is calculated, using the weighted average, of the Z position of the two views. The vertex resolution along the beam direction is about $600\mu m$, and along the transverse direction is about $20\mu m$.

Relinking: For every event, once the vertex is found, the tracks are linked again. If the links are not well defined then the upstream tracks originating from the vertex are given preference. If relinking changes the best link for space track then the physics track is also redefined. Also, the momentum and charge of the physics tracks are recalculated. Space tracks for which no links were found earlier are used to form physics tracks. The momentum for these physics tracks are calculated assuming that the downstream track comes from the vertex.

4.4 Electromagnetic Shower Reconstruction

The software reconstruction package used for the electromagnetic section of the LAC is called EMREC.[73] The EMLAC (described in chapter 2) is divided into front and back sections, which are read out independently. The reconstruction for each quadrant of the EMLAC is done separately and independently. Each quadrant has four views (left R, right R, inner Φ and outer Φ). Left R and right R are the radial readout sections corresponding to $\Phi < 45^o$ and $\Phi > 45^o$. Inner and outer Φ are azimuthal readout sections corresponding to R $<$ 40 cm and R $>$ 40 cm. The shape of the shower depends on its longitudinal origin. Depending on where the shower originated, the amount of energy deposited in the front and back section of the EMLAC will vary. To avoid the dependence of the shower shape on its longitudinal origin, a software summed section was used for the reconstruction, where the corresponding strips from the front and the back section were added. If not otherwise mentioned, the pattern recognition code operated on these summed sections. The reconstruction process involves:

- Unpacking: Conversion of raw data to the deposited energy
- Finding groups of channels (strips) that have significant energy deposition

- Reconstruction of GAMMAS* from the energy peaks found in each view
- Correlation of GAMMAS from different views to form the photons, and
- Determining the time of arrival for the photon

Unpacking: First, the unpacking routine converts the raw ADC data from each strip to the deposited energy E_i, using the relation

$$E_i = A_i G_i (N_i - N_{oi}) \tag{4.2}$$

where
A_i is the conversion constant between ADC counts and energy,
G_i is the relative gain for the channel,
N_i is the digitized value of the pulse height in the channel,
and N_{oi} is the pedestal offset.

The value of A_i was determined from the electron beam data and it was found to be about 3.1 MeV per ADC count. A correction is applied for known insensitive strips. These insensitive strips are due to bad connection or dead amplifier channels. These dead strips are assigned a value equal to the average of the two adjacent strips.

Group and Peak Finding: A set of consecutive strips in a particular view forms a group, if all the strips have energy above a certain minimum value. To be called a group, a continuous set of strips must fulfill the following criteria:

- For left R, right R and inner Φ views, there must be at least three strips above the threshold of 150 MeV. For outer Φ view, it must have at least two strips above the threshold. The requirement is reduced for the outer Φ view because the strips in this view are wider then in other views at large radius.
- The total group energy must be greater than 750 MeV.
- The average energy per strip in a group must be at least 150 MeV.

---

* The GAMMAS are the single view showers. When GAMMAS from both the views, R and Φ correlate, they form a photon.

- The strip with maximum energy must have at least 300 MeV.

After all the groups were found the software started looking for the peaks. A peak is the strip where the energy derivative of the distribution changes its sign. There are two valleys associated with each peak. A peak is found separately for the front section to ensure that the peaks are not lost because of the summing of front and back sections. If a peak is found in the front section, its standard deviation is given as:

$$\sigma = \sqrt{(0.145)^2\,\mathrm{E} + (0.1)^2} \tag{4.3}$$

where
E is the energy in the peak strip,
σ is the estimate of the standard deviation for that energy,
$0.145\sqrt{\mathrm{E}}$ is the intrinsic energy resolution of the EMLAC due to shower sampling fluctuations,
and 0.1 is the incoherent noise contribution to the total resolution.

If the energy difference between the peak strip and its valley on either side is more than 2.5σ, then this peak is considered a significant peak rather than an energy fluctuation.

If a peak is found in the radial view, then the front radial position is calculated and a search is made for a corresponding peak in the back section, to find the back radial position. The difference between the back radial position projected to the front and the front radial position, is known as directionality.

GAMMA Reconstruction: Once the peaks are found, the GAMMAS are reconstructed, depending on the group from which the peaks comes. The reconstruction of single-peak group is the simplest case and involves fitting a parametrized[§] shower

§ The parametrization of the energy independent shower shape was arrived at by using the GEANT3 based E706 Monte Carlo program. The parametrization, given as a function of the radial distance from the center of the shower, is given separately for the front and back sections because the lateral spread of the shower is wider in the back.

shape to the peak and finding the energy. But a multiple-peak group must first be split into several one-peak group, before the positions and energies of the GAMMAS can be calculated. First, the approximate position of each GAMMA is found based on the energy distribution in 3 strips, the peak strip and its two adjacent strips. Then, the following function is minimized with respect to the true GAMMA energy E_k for the kth GAMMA

$$\chi^2 = \sum_{i=1}^{N_s} \frac{1}{{\sigma_i}^2} \left(e_i - \sum_k E_k z_k^i \right)^2 \tag{4.4}$$

where

N_s is the number of strips,

e_i is the energy in strip i,

z_k^i is the fraction of energy from the kth shower in the ith strip,

and σ_i is the standard deviation of the energy for the ith strip.

The minimization is explicitly solved for individual shower energies. Once these energies are found, the energy distribution for each individual shower is found by subtracting the contributions from all other showers in the group. The resulting distribution is used to calculate the new position of the showers. Using the new position, the final GAMMA energy is recalculated using the same algorithm. The radial and azimuthal position of the GAMMA using the middle of the peak strip is given by

$$R_i = (20.2233 + i * 0.5466)cm + \delta R \tag{4.5}$$

$$\phi = (i - 1) * 0.0164 + (q - 1) * \pi/2 + \delta\phi \tag{4.6}$$

where

R_i is the radial position of the strip,

ϕ is the azimuthal angle of the strip,

δR and $\delta\phi$ are corrections based on energy in the three strips,

i is the strip number,

and q is the quadrant number of the EMLAC.

Correlating GAMMAS into Photons: The next stage in the reconstruction process, is to correlate the reconstructed GAMMAS from different views, to form the final photons. As described in chapter 2, in the EMLAC, the G-10 readout boards alternate between radial (R views) and azimuthal (Φ views) boards. This leads roughly to the shower having the same longitudinal energy deposition in R and Φ views, i.e a photon will deposit almost an equal amount of energy in both views. Therefore, both the total energy, and the E_f/E_t* should be very close in the two views. The correlation algorithm tries to match a GAMMA from one view with a GAMMA from another view that has approximately the same energy and E_f/E_t ratio. It is also required that the inner Φ GAMMAS only correlate with R GAMMAS with radius less than 40 cm and outer Φ GAMMAS only correlate with R GAMMAS with radius more than 40 cm. This is called one to one correlation. A more complicated situation arises if the positions of the two photons in either view are so close that their respective GAMMAS cannot be resolved or if a photon fell near the octant boundary. Then the following cases may arise

- one R view GAMMA can be correlated with two Φ view GAMMAS
- one Φ view GAMMA can be correlated with two R view GAMMAS
- two R view GAMMAS can be correlated with two Φ view GAMMAS

The correlation is first done for the boundary GAMMAS. Once this is finished, the code then proceeds with correlating GAMMAS located away from the boundaries. For the off boundary GAMMAS, the correlations attempted are one R to one Φ, one R to two Φ and one Φ to two R.

After correlation, Φ view GAMMAS are reconstructed again, using the information about their R positions obtained during the correlation. This is done because the Φ strip width varies with radial position, introducing some uncertainty in the first stage shower fitting. A known radial position yields a more accurate energy measurement. The correction term obtained is applied to the final photon energy.

---

* E_f/E_t is the ratio of the energy deposited per photon in the front section of the EMLAC to that of the total energy deposited in the EMLAC.

Photon Arrival Time: Each photon has associated with it a time of arrival based upon the strip TVC information. This is useful for rejecting muons. Since the TVCs were fired by the differentiated signals from the LAC, high frequency noise caused random firing of the TVCs. This was eliminated during the software reconstruction stage by associating the energy in the strips with that in the TVCs. The high frequency noise blocked some of the true signals and this resulted in some inefficiency for the TVCs. Another problem was to assign a pedestal* value to each channel.

Pedestal values were determined by calibrating the TVC readings for several values of time interval between a calibration pulse and a trigger signal. The calibrated values of the TVCs which best duplicated the TVC values observed in the data was used as the pedestal value. Due to noise, the TVC efficiency never reached above 90% even for strip energies above 4 GeV. Information from the TVC's were accepted only if the total unpacked energy from the four amplifiers of a particular TVC were at least 4 GeV. The TVC data were also corrected for the pedestal shifts. Each photon, GAMMA or group was associated with a time of arrival from the EMREC timing algorithm.

To find the time associated with an EMREC group, all sets of TVCs which fall within 3 standard deviations($45ns$) of each other were found. Next, using the energy weighted time of arrival, a unique time was associated with each set. The set which has the maximum number of pedestal corrected TVCs get the best timing† associated with it. If two sets have the same number of TVCs then the set having the largest associated energy is defined as the set with the best timing information. The sets with best and second best timing found were stored in the data bank. For each time a quality factor was calculated using the relation, Quality Factor = 1000 * (# of TVCs) + (TVC Group Energy).

As GAMMAS and peaks have one to one correspondence, the timing associated with GAMMAS can be found by the timing of the peak from which it originated.

⋆ Pedestals for the TVCs are not the value when there is no signal, but are the TVC values when energy is deposited for an in-time event.

† Best timing is the time of the most common occurrence, of the time value weighted by the energy.

Since photons can be constructed from as many as four GAMMAS, the photon timing is found by using the best time for each GAMMA.

4.5 Hadron Shower Reconstruction

The software reconstruction package used for the hadronic section of the LAC is called HCREC.[74] The basic purpose of the hadron reconstructor is to find hadrons and to calculate their energy and position. HCREC reconstructs both neutral and charged hadrons and the distinction between them is done only when the LAC reconstructed data are compared with reconstructed tracks from the magnetic spectrometer, projected to the LAC.

The reconstruction program searches the hadron calorimeter for the cluster of pads, with each pad having a minimum of 2 GeV of energy. A cluster can be formed of at least two pads, one of which must have at least 5 GeV of energy. If a given cluster has less than twelve pads and if no more than three pads contain more than 40% of the maximum pad energy, then one hadron is reconstructed. If the cluster has more than twelve pads and other conditions are met then it is assumed that the cluster contains more than one hadron. As the hadrons can start showering in electromagnetic calorimeter itself, the final correction to the hadron energy is applied based upon EMREC results, using showers that correlate in position with hadronic showers.

5. Data Analysis

5.1 Overview

The 1987-88 data run for E706 lasted about 4 months. During this period about 6.4 million events were written on 800 6250-bpi magnetic tapes. The entire data was divided into eight sets, depending on beam polarities, target type, and experimental considerations, like the functionality of the different sections of the spectrometer. These sets were designated A through H (Table 5.1). Out of these 800 tapes, about 500 were processed on ACP system using the MAGIC driver code. At this stage, the variables useful for the understanding of the hardware and the software of the experiment were written to the tape. Table 5.1 shows the details of the data written on the tape. For runs with more than one target, the reconstructed vertex position in conjunction with the known Z-coordinate position of the targets was used during the analysis to find out the target producing the event.

Set	Beam Polarity	Target	Triggers	Run Number
A	Negative	Cu + Be	786K	2852-3036
B	Positive	Cu + Be	440K	2588-2670
C	Positive	Cu + Be	1,225K	2387-2586
D	Negative	Be	1,247K	2062-2382
E	Positive	Be	1,508K	1728-2007
F	Positive	C	161K	1672-1719
G	Negative	C	688K	
H	Negative	C	333K	

Table 5.1: Breakdown of the E706 data sample.

The above table does not include data from the calibration run and also data written without electromagnetic triggers. The data was reconstructed on the ACP,

and afterwards it was split into different analysis streams on the VAX and AMDAHL. The results presented in this thesis were arrived by studying data which satisfied the Single-Local trigger. Data from sets F, G and H were not used in this analysis because these data sets were written before the Single-Local trigger was implemented. One of the chambers in the MWPC system had the high voltage turned off while data for set B was taken. But the data from set B has been corrected for the missing information and has been included in this analysis.

The LAC triggered events were split into three streams, depending on the maximum P_T measured in each event, for single reconstructed photon and for the vector sum P_T of every photon pair. If the highest P_T for the single reconstructed photon or vector sum for the photon pair was less than 3 GeV/c, then the events were rejected. The output streams were divided into three sets depending on their P_T. These streams were called 'PT3', 'PT4' and 'PT5' depending on their minimum P_T of 3 GeV/c, 4 GeV/c and 5 GeV/c respectively. The 'PT3' stream data was used for set A only, because the Single-Local threshold was lowered for runs after 2904. All other sets used have data from 'PT4' and 'PT5' streams only.

The selected streams were also checked for unreliable data. About five percent of the data was rejected based on unreliable trigger behaviour (such as a run with anomalously large percentage of a single type trigger) and improper functioning of a part of the spectrometer/detector. For part of the run, one or more of the EMLAC octants were not functioning properly. For those runs, only data from the functional part of the detector was used and an acceptance correction was applied. After these rejections, the total number of the events left from different streams, available for the analysis is shown in Table 5.2.

Set	A	B	C	D	E
Number of Events	314781	95297	198551	162554	149642

Table 5.2: Events from different sets available for direct photon analysis.

5.2 Data Selection

Muon Rejection

To insure the quality of the data, some cuts were imposed on the events earlier selected for the analysis. One of the major sources of background to the direct photon signal in fixed target experiments is muon generated showers, arising from muons in the beam halo. These muons can be a source of non-target originated off-axis LAC showers which mimic high P_T signals in the EMLAC. During data acquisition, the veto walls were used to reject these muons. Only those events were rejected for which both the veto wall planes registered a hit within a period of 35ns before the interaction and 100ns after the interaction. During offline analysis it was found that some of the events which should have been vetoed, were not vetoed with the above requirement, because the trigger was found to be sensitive to the muons coming 20ns before the interaction. To reduce this contamination, studies were done with photon information from EMREC. The information from the Minnesota latches, which keeps a 300ns wide window around the interaction time, was used to reject the additional muons. A logical software condition was generated between the information from the hit in the veto wall plane to the hit in the corresponding triggering octant. If for a photon a hit was found in the veto wall within this 300 ns window then that photon was rejected. It was also found that some gaps existed between the scintillation counters forming the veto walls. As no coincidence existed, the veto wall did not veto the events for which a muon went through one of such gaps.

To reject these muons, three parameters, time of arrival, directionality and longitudinal profile were used in the offline analysis. The photon arrival time was calculated from the time to voltage converter (TVCs) information. The in-time events were associated with the photons whereas out-of-time events were associated with muons. Figure 5.1 shows the time profile of the highest P_T electromagnetic shower in each event. Figure 5.1(a) shows the arrival time distribution for events where there was no signal in either veto wall plane, in the quadrant corresponding to the triggering octant, within $\pm$ 150 ns of the interaction. Figure 5.1(b) shows

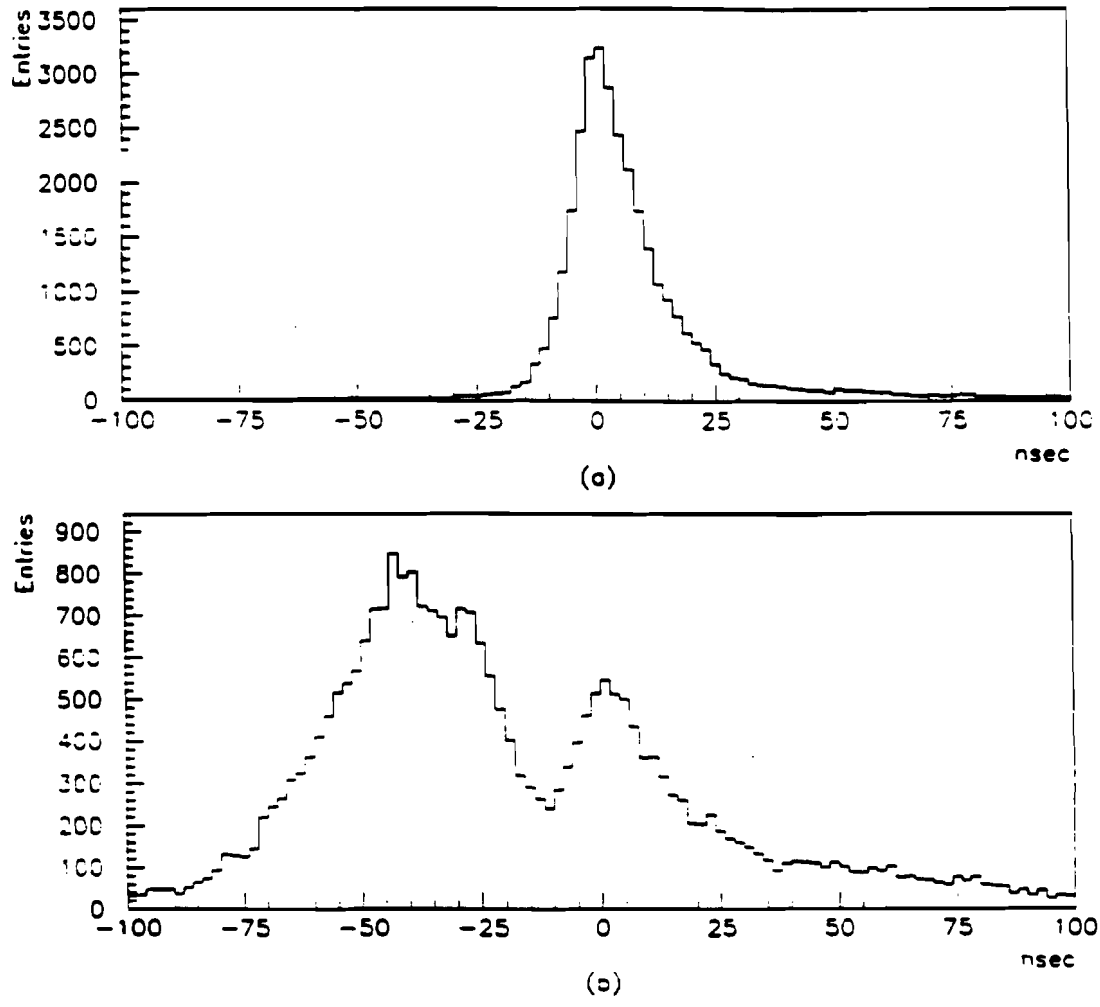

Figure 5.1: Time profile of the highest P_T electromagnetic shower. (a) Events for which there was no signal in either veto wall plane in the quadrant corresponding to the triggering octant. (b) Events for which a veto wall hit was recorded.

the time distribution for those events for which a veto wall hit was recorded. The large peak present in Figure 5.1(b) for times earlier than 25 ns is not apparent in Figure 5.1(a). This shows that out-of-time showers were responsible for a sizeable number of experimental triggers. The early muons can be seen from the peak around 35ns before the interaction time. The distribution seen at the positive arrival time represents the inefficiency resulting from the condition requiring a coincidence between the two veto wall planes to veto the event at the pretrigger level. Photons were rejected if they had a time more than 15 ns earlier or 40 ns after the nominal zero time, as recorded by the TVCs.

As most of the muons are produced during the in-flight decay of the beam particles, they come more or less parallel to the beam direction. To distinguish these muons from the particles originating in the target, another parameter called directionality δ was used. Directionality of a particle is measured from the position of the shower deposited in the front and back section of the EMLAC. It is a measure of the photon trajectory and is defined as:

$$\delta = r_{front} - \frac{Z_{front}^{LAC}}{Z_{back}^{LAC}} r_{back} \tag{5.1}$$

where r_{front} and r_{back} are the reconstructed front and back radial positions of the shower centroids. Z_{front}^{LAC} and Z_{back}^{LAC} are the longitudinal positions of the front and back sections of the EMLAC with respect to the target position. Z_{front}^{LAC} and Z_{back}^{LAC} are respectively, 900 cm and 918.5 cm.

The concept of directionality is shown in Figure 5.2. From figure 5.2 and equation 5.1, it is clear, that for a particle travelling parallel to the beam direction, the directionality will be positive. For particles coming from the target region the directionality will be centered around zero. Figure 5.3 shows a scatter plot of directionality vs P_T of the highest P_T photon in the triggering quadrant when the triggering octant had a veto wall hit during the $\pm$ 150 ns window. The plot shows a clear enhancement in the positive directionality for high P_T objects. Figure 5.4 shows a scatter plot for directionality vs P_T of the highest P_T photons when there

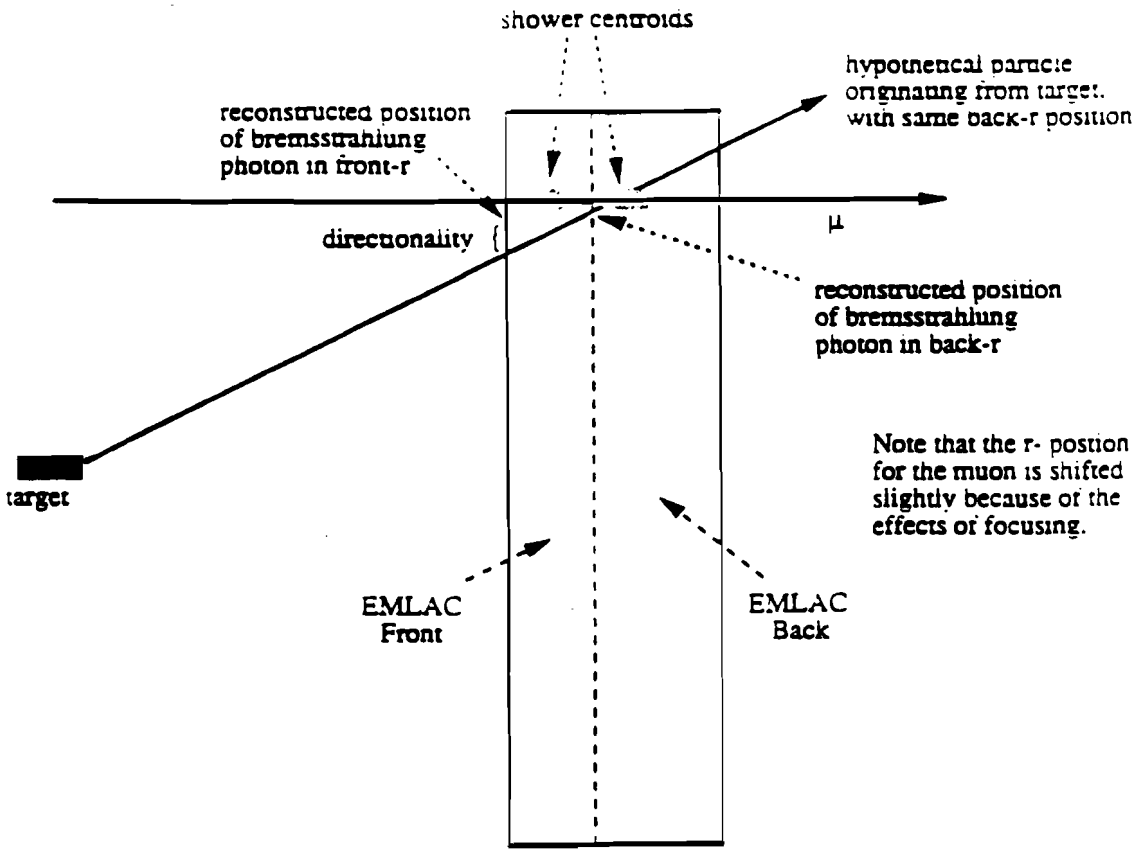

Figure 5.2: Concept of directionality. A particle travelling parallel to the beam will have a larger directionality than a photon which originates from the target.

are no veto wall hits. From these two plots it is clear that no veto wall hit requirement removes most of the high P_T particles which come parallel to the beam direction and are definitely muons. The events left after the muon rejection have directionality very close to zero and thus definitely originate from the target region.

The scatter plot in Figure 5.5 shows the time of arrival of photon vs directionality, for events in which the veto wall had a signal in the quadrant corresponding to the triggering EMLAC octant. Figure 5.6 shows the above plot with the require-

ment that veto wall had no signals in the quadrant corresponding to the EMLAC octant. From these two plots it is clear that the events with large directionality are also out of time and have been generated by muons travelling parallel to the beam direction. By requiring a directionality of 0.4 or less, events with large directionality which were also out of time were rejected.

The longitudinal profile of the shower deposited inside the calorimeter can also be used to discriminate against muons. The muons would emit photons with a flat distribution in depth. This will lead to muon generated showers having a much larger fraction of energy in the back section of the EMLAC. Photons in which the energy reconstructed in the front section of the EMLAC was less than 20% of the total reconstructed energy of that photon, were rejected. The cut imposed on the amount of energy deposited in the front section of the EMLAC to that of the total energy deposited in the EMLAC (E_F/E_T), also insures that shower caused by hadrons are rejected.

Vertex Cut

Events that did not have a reconstructed vertex within the target were rejected. This is necessary in order to ensure that the interaction has occurred between the incoming beam particle and the beryllium or copper target and to decide with which target the beam interacted. This provides the cross-sections for beryllium and copper targets to study the nuclear dependence of direct photon production. The reconstructed vertex position is shown in Figure 5.7. The reconstructed vertex position for twenty beryllium and two copper pieces of the target are well separated and visible.

Uncorrelated Energy Cut

Events were also checked for large amount of energy in any one view in a quadrant which did not correlate with energy from any other view to form photons. A large value of uncorrelated energy indicates that the reconstruction code did not handle the event properly. The events with triggering quadrant having more than 10 GeV of uncorrelated energy were rejected.

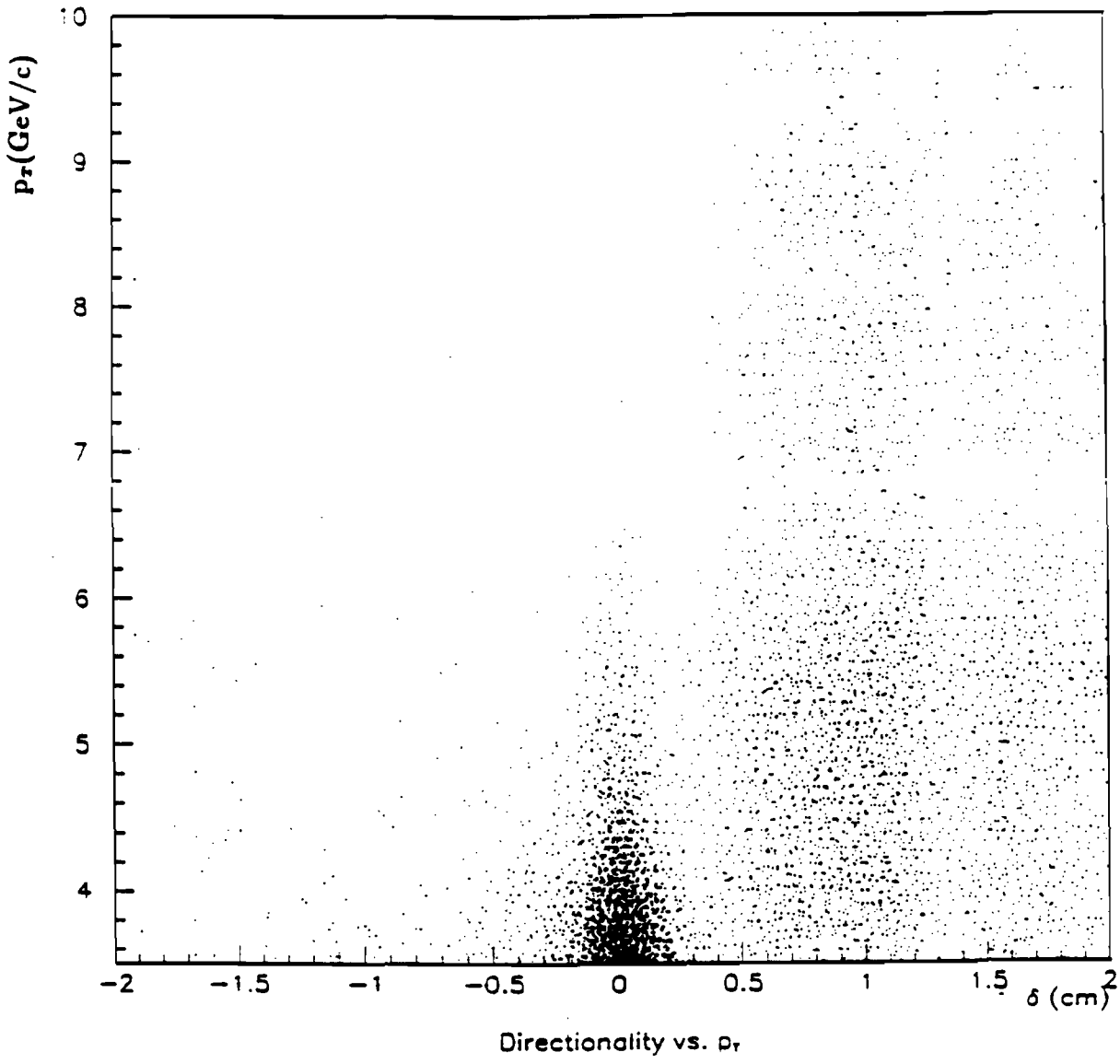

Figure 5.3: Photon directionality vs P_T. The muon events are clearly visible in the band with directionality greater than 0.4 cm, indicating that these photons did not originated in the target.

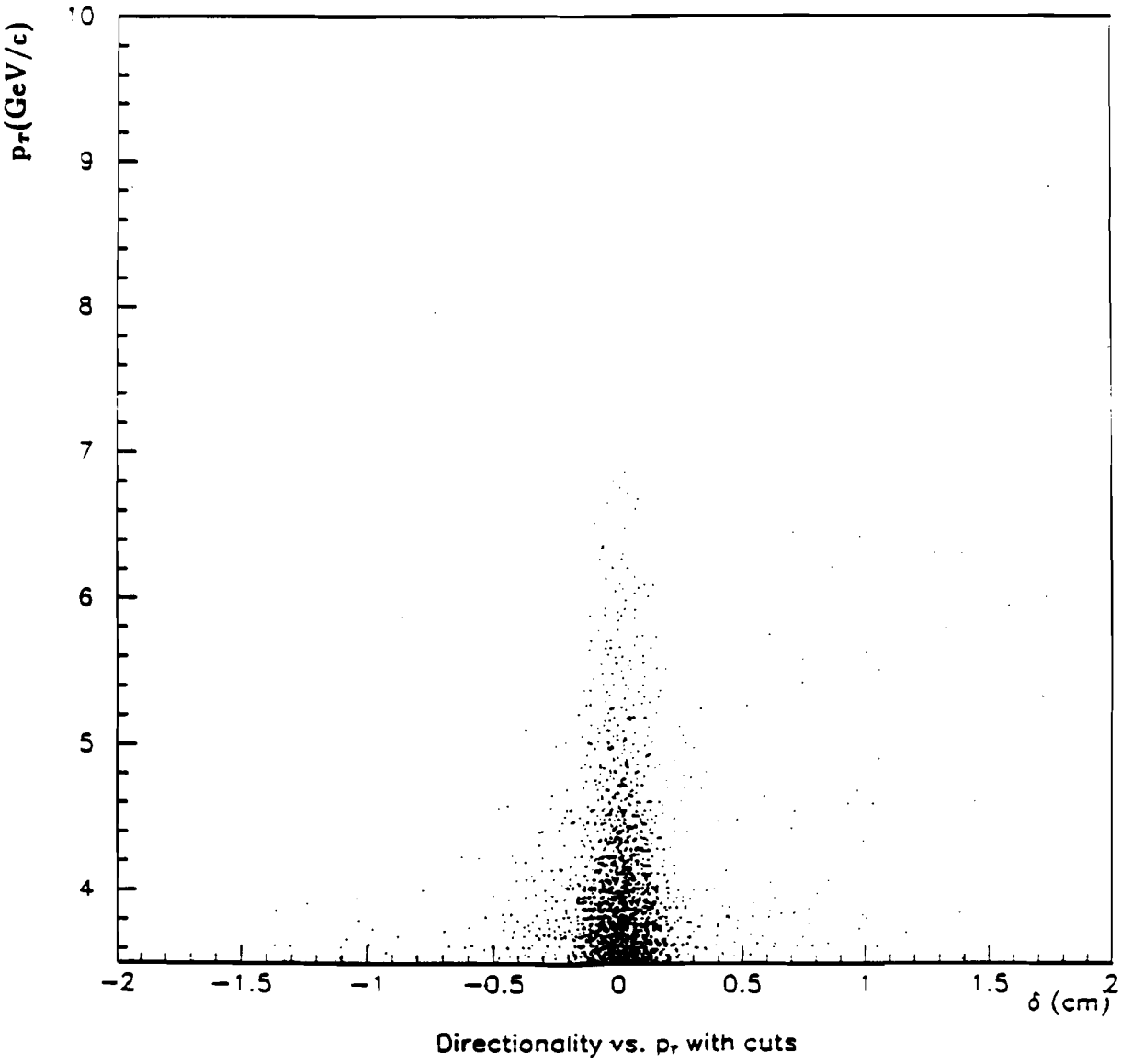

Figure 5.4: Photon directionality vs P_T. The above plot requires that the veto wall quadrant should not have a hit corresponding to the triggering EMLAC octant. The veto wall requirement removes the muon generated events with large directionality as observed in Figure 5.3.

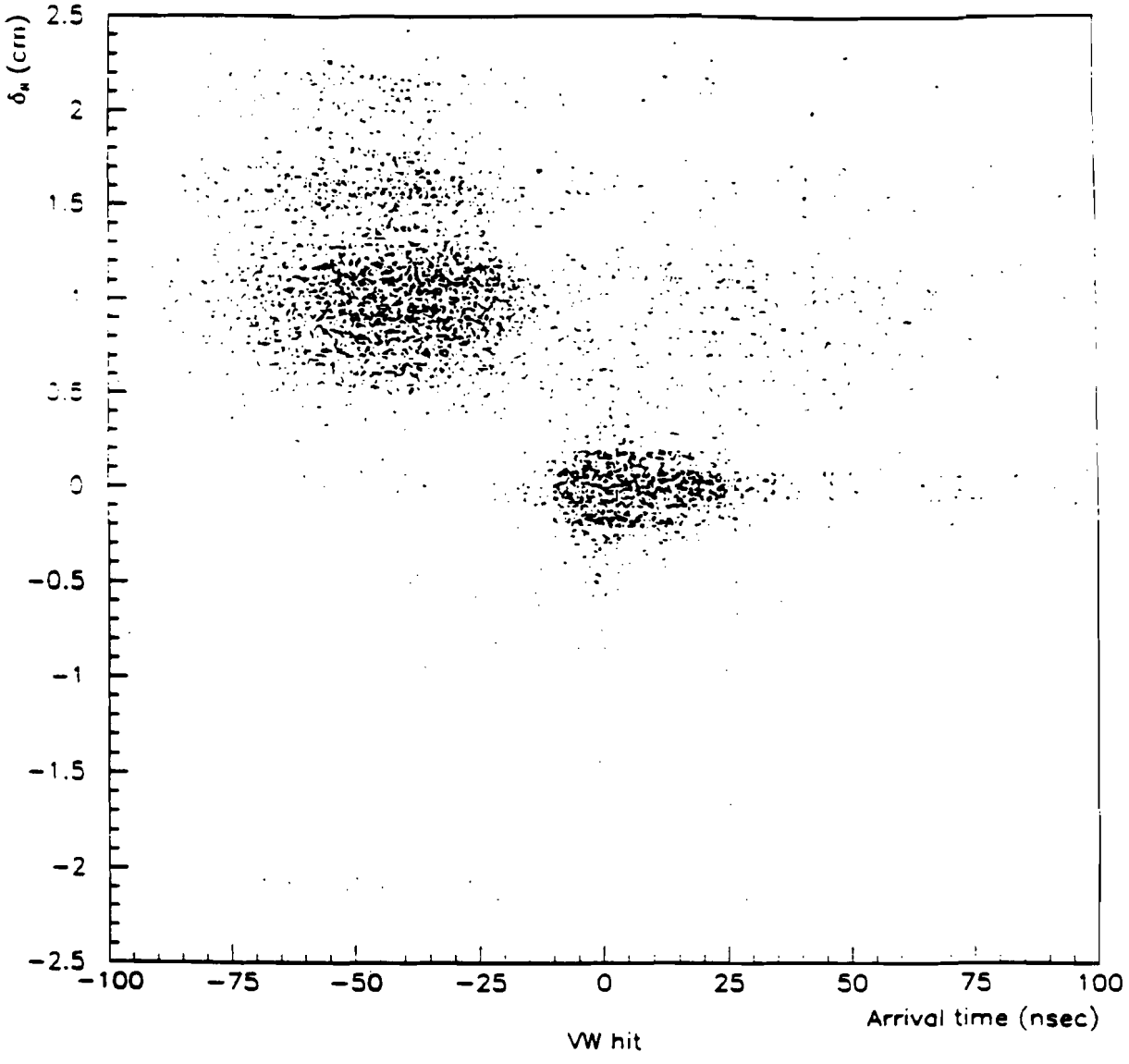

Figure 5.5: Arrival time of photon vs directionality. All events, with and without a hit in either of the veto wall quadrant corresponding to the triggering EMLAC octant have been considered.

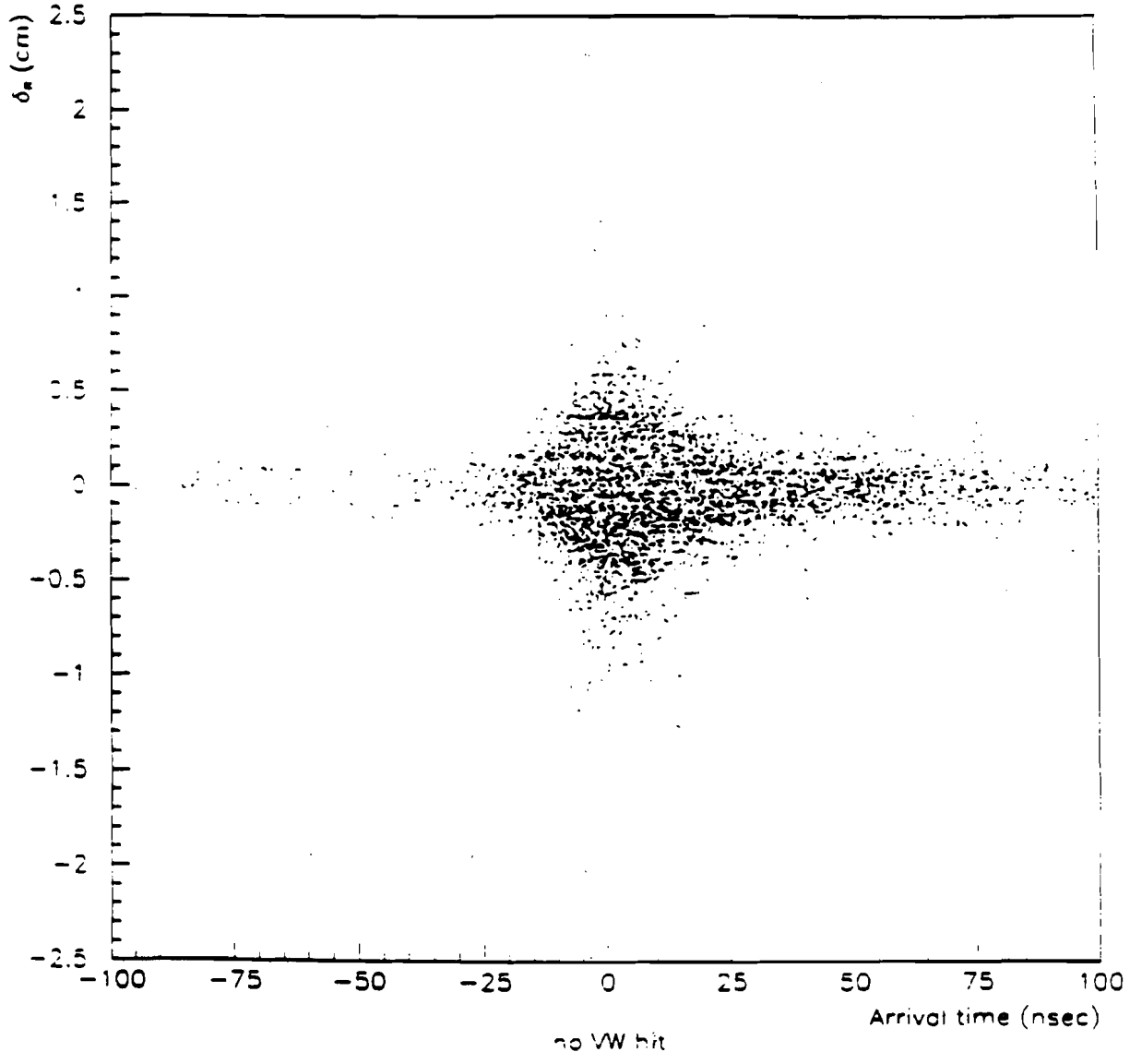

Figure 5.6: Arrival time of photon vs directionality. Only events for which veto wall quadrants corresponding to the triggering EMLAC octant having no hits have been plotted.

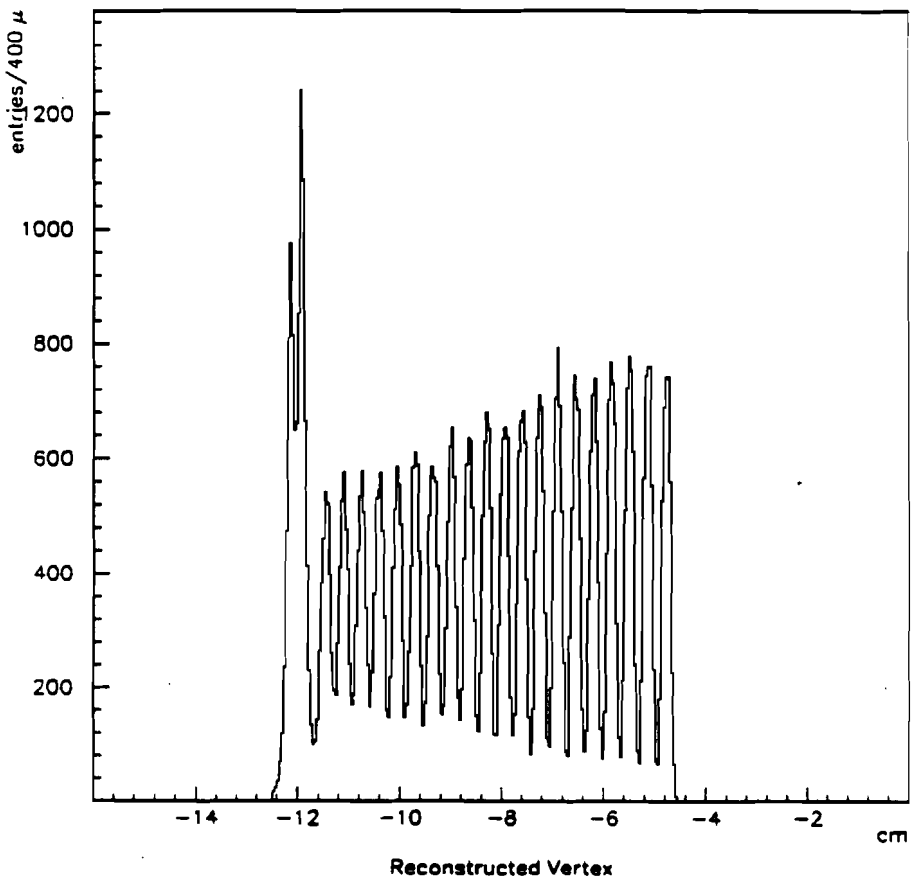

Figure 5.7: Reconstructed vertex position. The 20 beryllium and 2 copper targets are clearly visible.

Fiducial Cut

Proper reconstruction is difficult for photons which fall very close to detector boundaries. Fiducial cuts were made to eliminate such photons. If the reconstructed R position of the photons were not in the region 24 cm $<$ r $<$ 138 cm, then they were rejected. The photons were also rejected if the reconstructed Φ position was within 2 cm of the octant boundary or was within 3 strips plus 3 cm of the quadrant boundary.

Close Track Cut

Close track cut was used to insure that the shower originated from a neutral particle. If a track from a charged particle fell within 1 cm of any shower when projected to the front face of the EMLAC, then the particular shower was associated

with a charged particle. This close track cut eliminated showers associated with electrons, muons and charged hadrons.

5.3 Effect of Cuts

Table 5.3 shows the effect of veto wall, vertex and the uncorrelated energy cut in the respective order on the event reduction. The largest reduction in data sample comes from veto wall cut, which mostly eliminates the muon triggered events. It can be seen that more than half of the very high P_T events were triggered by the muons. The vertex cut ensures that very high P_T interaction occurred in the target region. The uncorrelated energy cut reflects on the inefficiency of the reconstruction code. Less than 2% of the events were rejected due to an uncorrelated energy of more than 10 GeV in the triggering quadrant.

Set	A	B	C	D	E
Total	314781	95297	198551	162554	149642
Veto Wall Cut	188632	22766	46857	57595	38863
Vertex Cut	147230	18069	37554	46643	26728
Uncorr. Energy Cut	142730	17408	36383	44924	25954

Table 5.3: Number of events surviving each successive event cut.

Table 5.4 shows the effect of cuts imposed on individual photons. Of the photons surviving the event cut, most of the photons fall below the P_T requirement of the experiment. Fiducial cuts ensure that the photons are not near the detector boundaries. The directionality cut removes showers which don't point back to the target region. Each of the above cuts led to the rejection of some good photons also. The losses were calculated and the final cross section was corrected for each of these losses.

The number of photons rejected due to veto wall, uncorrelated energy and close track requirements were measured by studying the effect of each cut on the $\gamma\gamma$ mass

Set	A	B	C	D	E
Total	2044726	512990	1027848	874194	855185
Event Cut	1157135	150212	307606	397187	239688
P_T> 3.5 GeV/c	36792	11242	24226	28400	17165
Fiducial Cut	30188	9052	19702	22818	13796
Directionality Cut	29507	8800	19116	22365	13385
Close Track Cut	25967	8191	17491	20390	12273
E_F/E_T Cut	25120	7866	16834	19851	11825
Timing Cut	25120	7866	16834	19851	11825

Table 5.4: Number of photons surviving each successive photon cut.

spectrum in the π^0mass peak (110 MeV/c^2 to 160 MeV/c^2) region. Only those events which fell into the π^0 mass region and satisfied the cuts mentioned in the Table 5.5 were selected for this study. Using these events, a π^0 ($\gamma\gamma$) mass spectrum was generated. A gaussian plus a straight line fit was made to this spectrum. The entries under the straight line gives the background to be subtracted from the total entries, to get the real number of the π^0's. After total number of real π^0's were found the entire procedure was repeated again after applying the veto wall cut. The number of good π^0's before the cut, divided by the number of good π^0's available after applying the cut gave the veto wall correction. This cut removed the events for which the veto wall quadrant fired simultaneously with the corresponding triggering octant. The correction for the uncorrelated energy cut is evaluated in the same fashion. As the close track cut acted on individual photons, its effect on direct photon signal was taken only square root times its effect on the π^0signal.

The concept of directionality for π^0 and single photon differs in the sense that a pair of photons in the front section of the EMLAC can coalesce into a single photon and can give wrong position for the back photon, thus giving wrong directionality. The directionality correction cannot be evaluated in a fashion similar to the other

Vertex Cu	-12.47 cm $\leq$ Z $\leq$ -11.66
Vertex Be	-4.58 cm $\leq$ Z $\leq$ -11.66
π^0 P_T	4 GeV/c $\leq$ P_T $\leq$ 10 GeV/c
π^0 Asymmetry	A $\leq$ 0.75
π^0 mass	0.11 $\leq$ $M_{\gamma\gamma}$ 0.16 GeV/c^2

Table 5.5: Cuts applied to data to study the effect of event level cut.

cuts. The correction for the directionality cut of 0.4 cm was estimated from the directionality distribution. The entries with negative directionality were attributed to the tail of the distribution, and assuming that the directionality distribution for photons is symmetric, the sudden increase in the entries above 0.4 cm were attributed to non-target associated showers. The effect of E_F/E_T cut was determined by studying fully simulated electromagnetic showers using GEANT and comparing them to showers in the the data sample. To understand the effect of the timing cut, timing distribution of $\gamma\gamma$ pair which formed π^0 mass was generated. The $\gamma\gamma$ pair falling in the π^0 side bands (the mass regions 75 MeV/c^2 to 100 MeV/c^2 and 170 MeV/c^2 to 195 MeV/c^2 were defined as π^0 sideband pairs) were subtracted from the $\gamma\gamma$ pair forming the π^0 mass band and the resulting loss gave the correction for the timing cut.

5.4 Corrections for Cuts Applied

Table 5.6 shows the correction[75] that must be applied to the observed single photons to correct for the good photons lost by applying various cuts. As is evident from the table the veto wall cut is dependent on the Z-position of the target. The veto wall correction for the copper target is comparatively larger than that for the events that originates in the beryllium target. This can be explained from the backscatter theory. Many π^0 events generate enough back scatter to register hits in the veto wall. The further upstream the interaction occurs the larger is the veto wall correction. As the copper target was upstream compared to the beryllium, hence

the larger correction for the former. To check the backscatter theory, the beryllium target was divided into four sections and corrections were found separately for all the four pieces. Figure 5.8 (Ref. 75) confirms that the more upstream the interaction, the higher the veto wall correction.

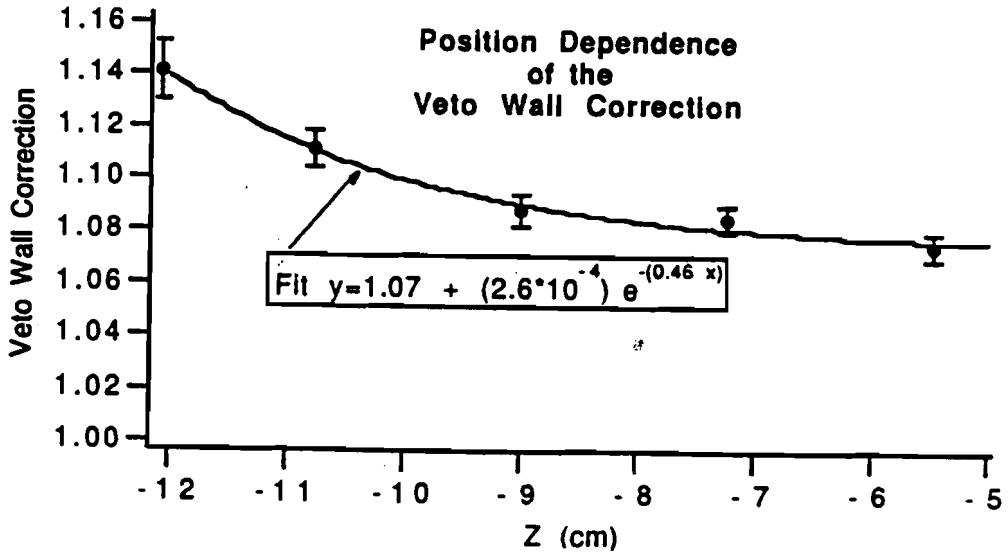

Figure 5.8: The veto wall correction as a function of the Z-coordinate position of the vertex.

Studies for other cuts were also done for separate data sets as well as target type, and the corrections observed were very close for the different sets and the target type. One more correction was applied to the photons. The photons which are products of either parton-parton hard scattering or meson decay travel about 9 meters before they deposit their energy in the EMLAC. During its flight to the EMLAC, a photon encounters various materials in which it can convert into an e^+e^-

Cut	Data Set	Target	Correction applied
Veto Wall	A,C,DE	Be,Cu	$1.07+2.6*10^{-4}e^{-0.46z}$
Uncorrelated Energy	A,C,D,E	Cu	1.0080±0.0015
Uncorrelated Energy	A	Be	1.0035±0.0010
Uncorrelated Energy	C,D,E	Be	1.0080±0.0009
Close Track	A,C,D,E	Cu	1.006±0.001
Close Track	A,C,D,E	Be	1.007±0.003
Directionality	A	Be,Cu	1.004±0.001
Directionality	C,D,E	Be,Cu	1.007±0.0009
E_F/E_T	A,C,D,E	Be,Cu	1.015±.001
Timing	A,C,D,E	Be,Cu	1.027±.004

Table 5.6: Corrections applied to the single photons to compensate for the losses due to cuts.

pair. The materials in which a photon can convert into pair before it encounters the first MWPC plane are the eight silicon planes of SSD, air and helium. Also the amount of material through which a photon will pass, depends on its production point (X, Y and Z coordinate) and production angle (θ and ϕ). Because the spectrometer elements are of finite size, they introduce θ dependence. The ϕ dependence comes from the rectangular shape of the various materials.

The photons are tracked through the first MWPC planes and the distance covered by the photon is measured in units of radiation length. Using a software program the non conversion probability of the photon is found using the relation,

$$P_{nc} = e^{-(7f/9)}$$

$$f = \sum_{i}^{n} \frac{\Delta l_i}{\lambda_i}$$

where Δl_i is the amount of the material i traversed and λ_i is the radiation length

of the material i. Each photon is corrected by the weight factor $\frac{1}{P_{nc}}$ for the photon conversion. Figure 5.9 (Ref. 75) shows the photon conversion correction for three different Z-positions in the beryllium target as a function of angle and depth. The figure shows that a larger photon conversion correction is required for the upstream interactions. Also, one can see the difference in the vertical planes for angles above and below the beam center line, due to the light guide that is below the downstream interaction counters.

It was found that the vertex determination algorithm failed to find vertex in some of the events. To correct for this inefficiency, the events in which the algorithm failed to find the vertex were visually scanned. The correction for the vertex determination algorithm was found as a function of the vertex position.[76] The correction term varies with the Z position of the vertex, V_Z, according to the equation $1.0019 - V_Z * 0.0079$, being 90.88±2.0% efficient at the upstream end of the copper target and 96.33±1.3% efficient at the downstream end of the beryllium target.

5.5 $\gamma\gamma$ Mass Spectrum: π^0 and η Definition

$\gamma\gamma$ Mass Spectrum

The detailed understanding of $\gamma\gamma$ mass pair in the π^0 and η range is very necessary because the π^0 and η are the two major sources of the background to the direct photon. During reconstruction, in each event photons were paired with other photons and their four momentum vectors calculated. Some of the direct photon cuts like directionality, close track, E_F/E_T and timing were not applied for this study. Only photons falling in the same octant were allowed to form $\gamma\gamma$ mass pairs. It was also required that the P_T of the pair was greater than 3.5 GeV/c and the rapidity lied in the range -0.7<y<0.7 .

Figure 5.10 shows the $\gamma\gamma$ mass pair spectrum. π^0 and η peaks are clearly visible. The measured mass and width for the π^0 is respectively 135.4±0.1 MeV/c^2 and 7.5±0.1 MeV/c^2 , and for η it is respectively 543.8±0.9 MeV/c^2 and 24.1±1.0 MeV/c^2. The mass region $110<M_{\gamma\gamma}<160$ MeV/c^2 was defined as the as π^0 peak region. The mass regions $75<M_{\gamma\gamma}<100$ MeV/c^2 and $170<M_{\gamma\gamma}<195$ MeV/c^2 were

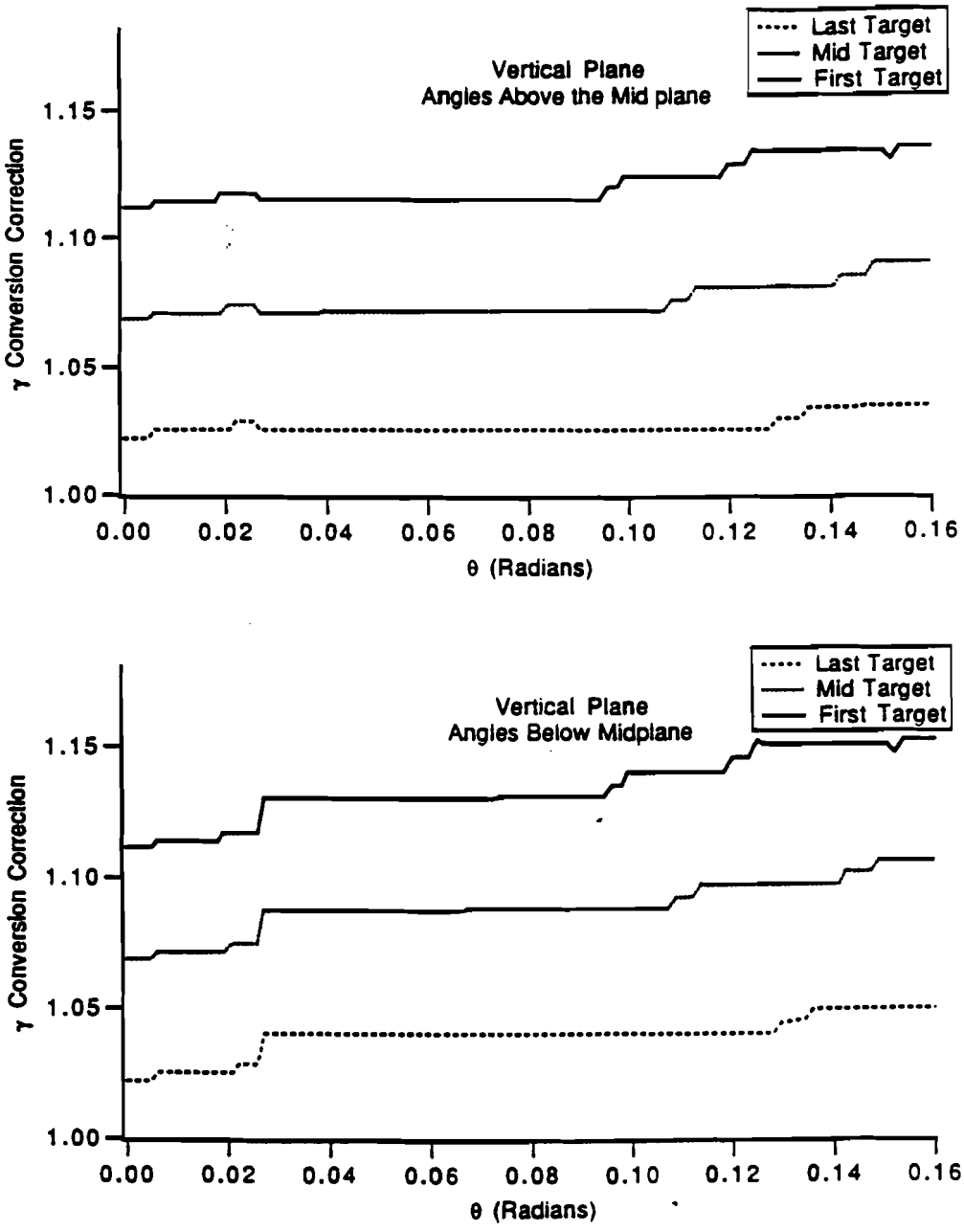

Figure 5.9: Photon conversion correction for three different Z positions in the beryllium target as a function of angle. The top plot is for angles in the vertical plane above the horizontal mid plane of the detector. The bottom plot is for angles below the mid plane. The difference in the correction is due to the interaction counter light guides.

defined as π^0 sideband pairs and were used for statistical subtraction from the peak region to get the true π^0 signal. This method was used for sideband subtraction because it was found that the background effects had a linear dependence on the mass. The mass region $500<M_{\gamma\gamma}<600$ MeV/c^2 was defined as η peak region with $400<M_{\gamma\gamma}<450$ MeV/c^2 and $650<M_{\gamma\gamma}<700$ MeV/c^2 as sidebands.

Asymmetry

The energy asymmetry for the photons from π^0 decay in the laboratory frame can be defined as:

$$A = \frac{| E_1 - E_2 |}{| E_1 + E_2 |}$$

where E_1 and E_2 are the energies of the two decay photons. As the π^0 is a pseudoscalar meson with spin zero, it will decay with a flat distribution in $|\cos\theta|$, where θ is the angle between one of the decay photons and the line of sight of the π^0 in the rest frame of the π^0. Biases in π^0 acceptance and reconstruction can produce departure from isotropy in the detected $\cos\theta$ distribution. For highly asymmetric decays, where one of the photons is produced with very low energy and at a large angle with respect to π^0 rest frame, the chances of its missing the detector is non negligible. The top and middle plots in figure 5.11 shows asymmetry distribution for the π^0 mass region and sideband regions respectively. The bottom plot shows the sideband subtracted distribution. Although one would expect this sideband subtracted energy asymmetry plot to be flat for the full asymmetry range, the plot actually shows roll off for higher asymmetries. The dotted plot in Figure 5.10 is the $\gamma\gamma$ mass plot for pairs having an asymmetry less than 0.75. It is clear that the signal-to-background ratio improves when the asymmetry cut is applied. A clean sample of π^0 was chosen with asymmetry cut of 0.75 to study the inclusive π^0 production.

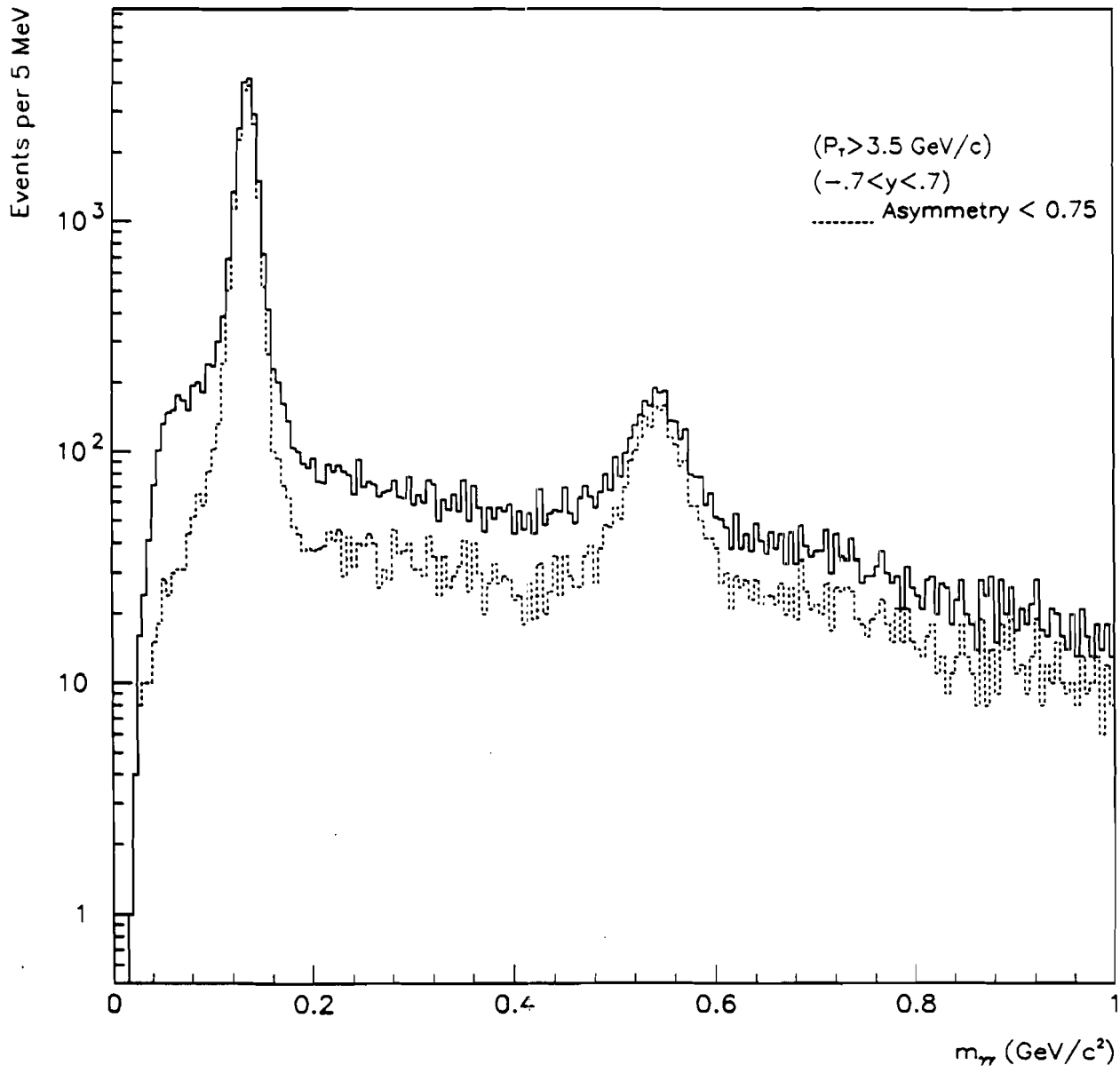

Figure 5.10: $\gamma\gamma$ mass spectrum. The π^0 and η mass peaks are clearly visible. The dotted line represents the two photon distribution with an energy asymmetry cut of 0.75.

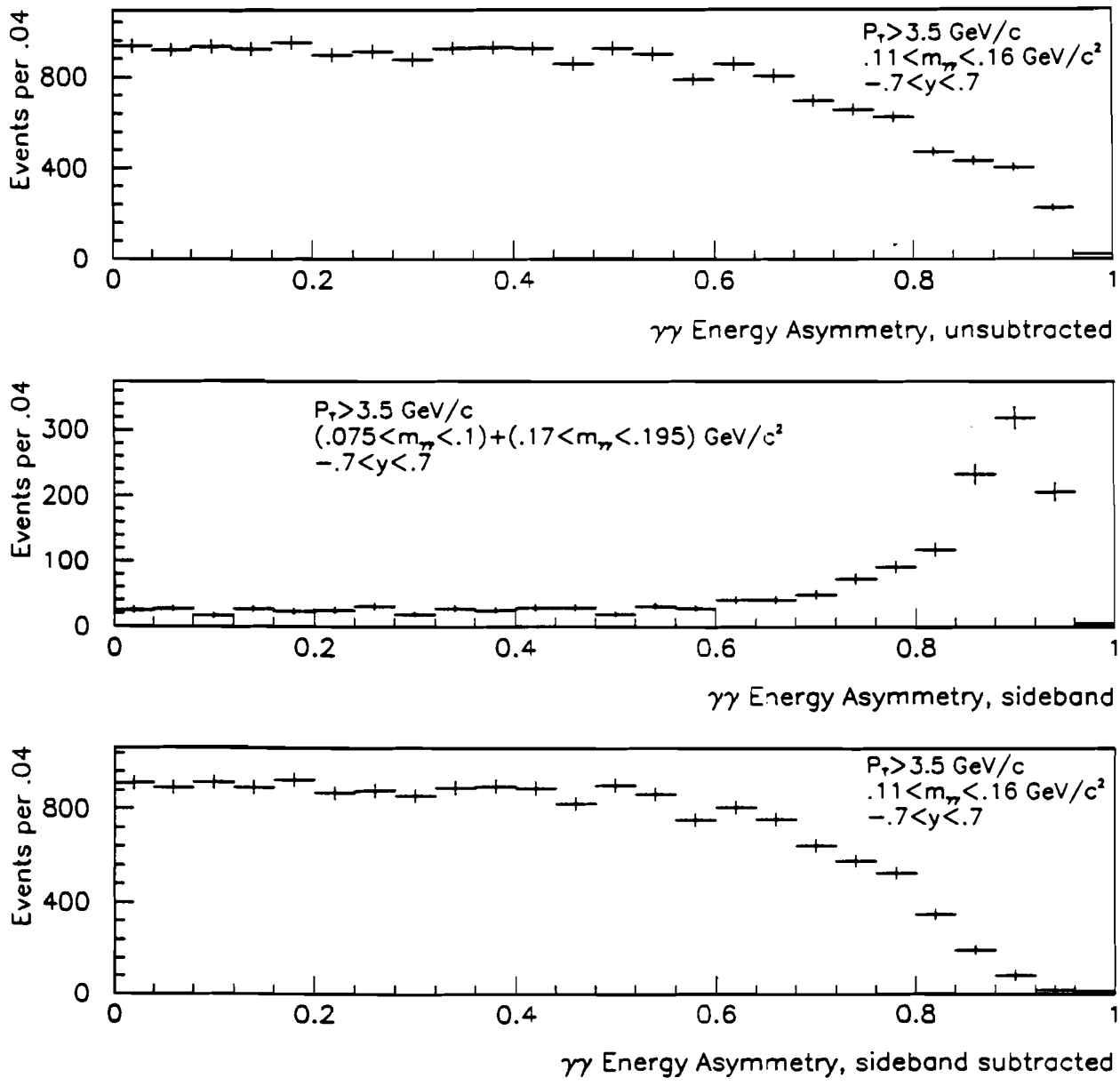

Figure 5.11: π^0 asymmetry. The asymmetry plots are shown for unsubtracted π^0 mass region, sideband region and background subtracted π^0 mass region. Asymmetry cut of 0.75 is applied for all π^0 studies because at higher asymmetry there is sharp roll off.

5.6 π^0 Cross-Section Calculation

Once the π^0 sample was selected, it must be corrected for losses to evaluate the invariant cross-section per nucleon.

Acceptance and Reconstruction Efficiency

Monte Carlo programs were used to simulate the EMLAC, and to study the geometric acceptance and the reconstruction efficiency for the π^0. Geometric acceptance of the π^0 does not only depend on the production parameters but also on the decay parameters. To calculate the acceptance, ten thousand π^0's were generated in each bin for P_T of 3.0 to 10.0 GeV/c in bin widths of 0.5 GeV/c and rapidity bins for rapidity from -1.0 to 1.0 in bin width of 0.2. These generated π^0's were allowed to decay and land in the detector volume. The ratio of the number when both the decay photons from a π^0 of given P_T and rapidity fell into a particular octant fiducial volume, to the number of π^0 events generated for that particular P_T and rapidity range gave the acceptance efficiency for the π^0's. In a similar way, using the same reconstruction code as used for the data, the reconstruction efficiency was determined for the π^0's that had both photons in the fiducial volume from the additional requirement that the two photons satisfy the π^0 definition.

Trigger Efficiency

Only events which satisfied the Single-Local trigger were used in the analysis of π^0 and direct photon production. Events which satisfied the Two-Gamma trigger were selected for studying the efficiency of the Single-Local trigger. This was done because for both of these trigger types, the P_T was summed in the same fashion. The threshold for the Two-Gamma trigger was less than that of the Single-Local trigger. The performance of Single-Local trigger was studied by finding the number of events which satisfied the Single-Local trigger in addition to Two-Gamma trigger.

Due to the image charge effect, the Single-Local trigger behaved differently in the different R-regions inside a octant. For each octant only 14 groups of 16 radial strips were used for the Single-Local trigger. Each octant was divided into three R regions for the trigger efficiency study. The three regions consisted of the first

32 radial strips, the next 64 radial strips and the next 128 radial strips inside the octant. Reconstructed photon momentum was used to estimate the P_T deposition in each of the triggering octant. The efficiency ϵ, for each region, was obtained from the ratio

$$\epsilon = \frac{Single - Local \bullet Two - Gamma}{Two - Gamma}$$

for the group of 16 strips with the highest P_T. The ratio gives the performance of the Single-Local trigger compared to the Two-Gamma trigger.

To determine the correction, the reconstructed R-view energy of all the photons in the octant of interest were deposited back in the corresponding EMLAC strips. The energy in each strip was weighted by the radial position of the strip and P_T for each group of 16 was calculated. The probability for each group firing the trigger octant was evaluated and the probabilities were combined. The trigger weight assigned to the event is the inverse of the calculated efficiency.

To evaluate the trigger* efficiency, malfunctioning octants and group of dead strips were taken into account. For cross-section calculation, each region was also assigned a minimum P_T threshold below which the trigger was not considered reliable and the events were not accepted. The minimum threshold was set such that average π^0's trigger efficiency was $\geq 50\%$. As the thresholds and trigger efficiency varied from region to region the contribution to the data from different octants also varied with P_T. This effect was especially pronounced near the threshold.

Live Beam Count

The number of beam particles incident when the trigger system was able to perform the event selection, called live triggerable beam (LTB), is determined from the information stored in the trigger scalers. The following quantities must be taken into account to define the live triggerable beam:

1. Pretrigger dead time i.e. time required to decide whether the pretrigger conditions were satisfied or not.

⋆ Octants 1 and 7 were not in the Single-Local trigger for a large portion of the run due to trigger hardware problems.

2. Clean interaction i.e. the interaction has no other interaction within ± 60 ns. If there is another interaction within ± 60 ns of the first one, then the trigger must reset itself.

3. The loss of clean interaction signal due to transmission problem in traversing a distance of about 50 ft to the LAC Faraday room.

4. Veto wall dead time i.e. time lost due to a hit in any set of both the veto wall quadrants when the event triggered, electronic noise or by early deposition of residual P_T from a previous event.

5. Sometimes the RUN CONTROL program ended the run during the spill. If the run ended before the spill finished, the scalers did not get written to the tape. This required correction for the lost spill events.

6. Computer ready time i.e. the number of beam particles which went through the hole in the BH counter when all the computers were ready for the event selection.

7. Backscatter veto, when an event was vetoed because the veto wall fired due to backscatter particles from the interaction.

Because P_T cuts were imposed according to the Single-Local trigger threshold, the LTB has a P_T dependence. Accordingly, for a given P_T range, the value of LTB was integrated only for runs for which the P_T threshold was above the minimum allowed value.

The beam count $B(P_T)$ used for determining the cross-section is defined as

$$B(P_T) = LTB \times \eta_{abs} \times B_f$$

where η_{abs} is the probability that a beam particle was not absorbed between the beam counters and the target. B_f gives the number of beam particles not tagged as minority particles (the helium pressure in the Cherenkov was set to tag the minority particle in negative/positive beam).

π^0 Cross-Section Calculation

The invariant cross-section per nucleon for π^0 production is given by the expression:

$$\frac{1}{A}E\,\frac{d\sigma}{d^3p} = \frac{1}{2\,\pi\,\mathrm{P_T}\,\triangle\,\mathrm{P_T}\,\triangle y}\,\frac{1}{\rho l N_a}\mathrm{C}_{\pi^0}\,\frac{N^{corr}(\mathrm{P_T},\mathrm{y})}{B(\mathrm{P_T})}(ABS) \qquad (5.2)$$

where

$$ABS = e^{\frac{d}{\lambda}} \approx 1 + \frac{d}{\lambda}$$

is the correction due to beam attenuation from interactions in the thin target, and

$$N^{corr} = N^{obs}\frac{(trig)(conv)(vrteff)(accpt)(C_{oct})}{(rec)}$$

is the corrected differential $\mathrm{P_T}$ distribution,
A is the atomic weight of the target material,
$\triangle\mathrm{P_T}$ is the $\mathrm{P_T}$ range ,
$\triangle y$ is the rapidity range,
ρ is the density of the target material in gm/cm^3,
l is the thickness of the target material in cm,
N_a is the Avogadro's number expressed in nucleon/gm,
C_{π^0} is an overall correction factor for π^0's to be described below,
$B(\mathrm{P_T})$ is the the beam count for each $\mathrm{P_T}$ bin,
d is the the average distance traveled by a beam particle in the target,
λ is the beam attenuation coefficient,
N^{corr} is the corrected number of π^0,
N^{obs} is the observed number of π^0,
trig is the trigger correction calculated event by event,
conv is the correction for lost π^0's due to conversion of the decay photons while still in the target region,
vrteff is the vertex efficiency correction,
accpt is the π^0 acceptance correction,
rec is the reconstruction efficiency.

and, C_{oct} is the correction for the malfunctioning trigger octants. This is given by $C_{oct} = 8 \ / \ N_{live}$, where N_{live} is the number of octants for which the trigger was reliable at the given P_T and radius at the time the event occurred.

The overall correction factor C_{π^0} is a combination of the following corrections: (1)the double occupancy which takes into account the case when two beam particles arrive simultaneously, (2) the asymmetry correction of 4/3 is applied because no $\gamma\gamma$ mass pair with asymmetry greater than 0.75 is included in this sample, (3) the correction for loss of good events due to the veto wall, vertex and uncorrelated energy cut, (4) the correction for the conversion of the decay photons downstream of the target, and (5) the correction for losses due to the mass cuts imposed in the π^0 mass definition, called the tail loss correction.

Figures 5.12 and 5.13 show respectively the inclusive invariant cross-sections per nucleon as a function of P_T integrated over the rapidity range $-0.7<y<0.7$, for the reactions π^-+Be$\rightarrow\pi^0$+X and p+Be$\rightarrow\pi^0$+X. Figures 5.14 and 5.15 show the inclusive invariant cross-sections per nucleon as a function of P_T for these reactions in three separate rapidity ranges, $-0.7<y<-0.2$, $-0.2<y<0.2$ and $0.2<y<0.7$. Figures 5.16 and 5.17 shows the inclusive invariant cross-sections per nucleon as a function of rapidity integrated over the P_T for these reactions.

5.7 Direct Photon Cross-Section Calculation

As mentioned earlier, only candidates satisfying the Single-Local trigger were used for this analysis. The candidate events also must have a P_T greater than some minimum value as discussed in the trigger efficiency section and were required to fall in the fiducial volume of the calorimeter. These direct photon candidates were selected only if they satisfied the muon cuts, uncorrelated energy cut, close track cut and had a vertex in the target. The candidate events were also required not to combine with any other photon in the event to form a $\gamma\gamma$ mass pair with any asymmetry which fell into π^0 mass region and with asymmetry less than 0.75 which fell into the η mass region. Photons not satisfying these requirements were removed from the direct photon sample. For the photons which formed a $\gamma\gamma$ mass pair in

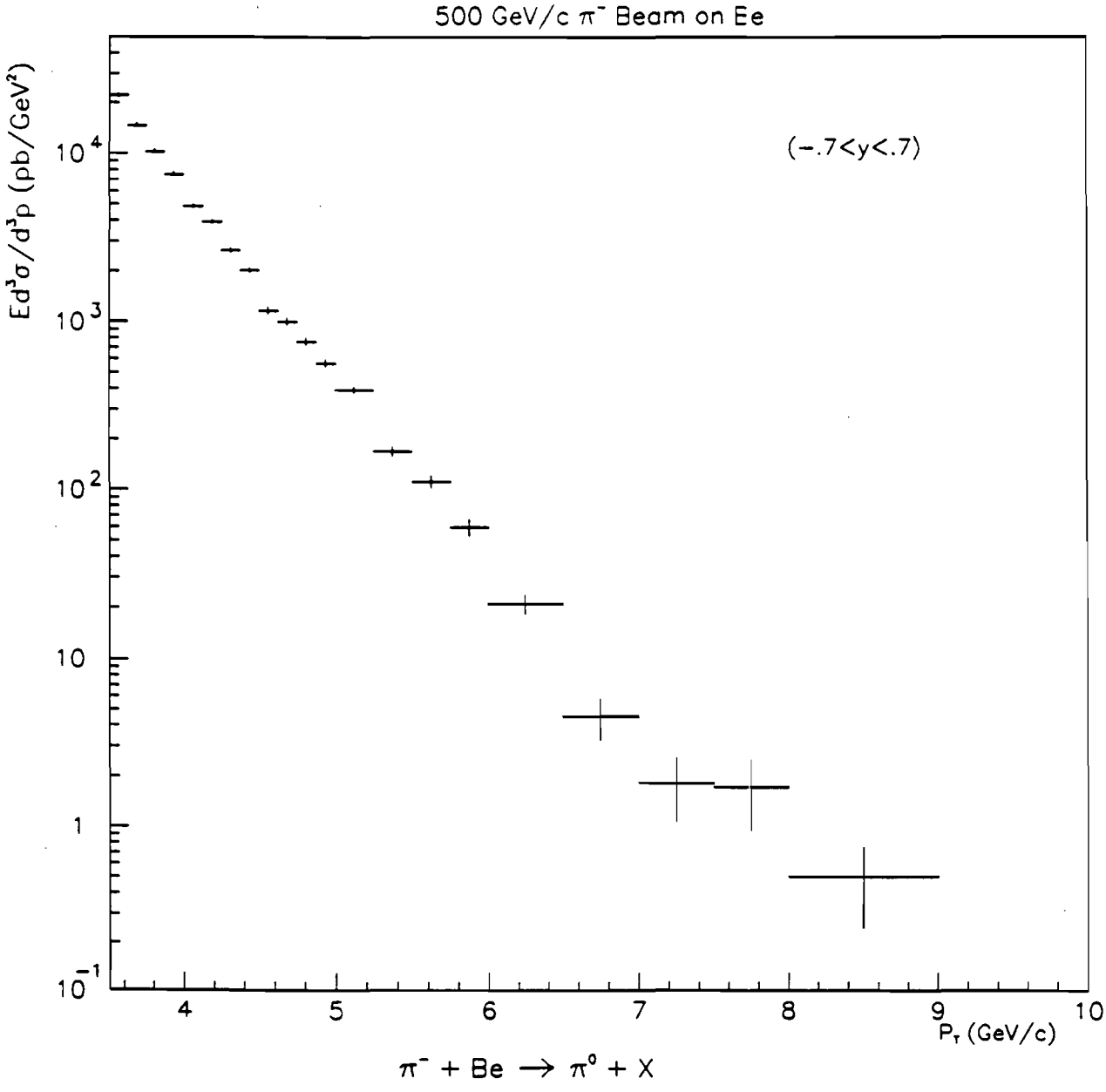

Figure 5.12: π^0 inclusive invariant cross-section per nucleon as a function of P_T integrated over -0.7<y<0.7 for π^- + Be $\rightarrow$ π^0 + X.

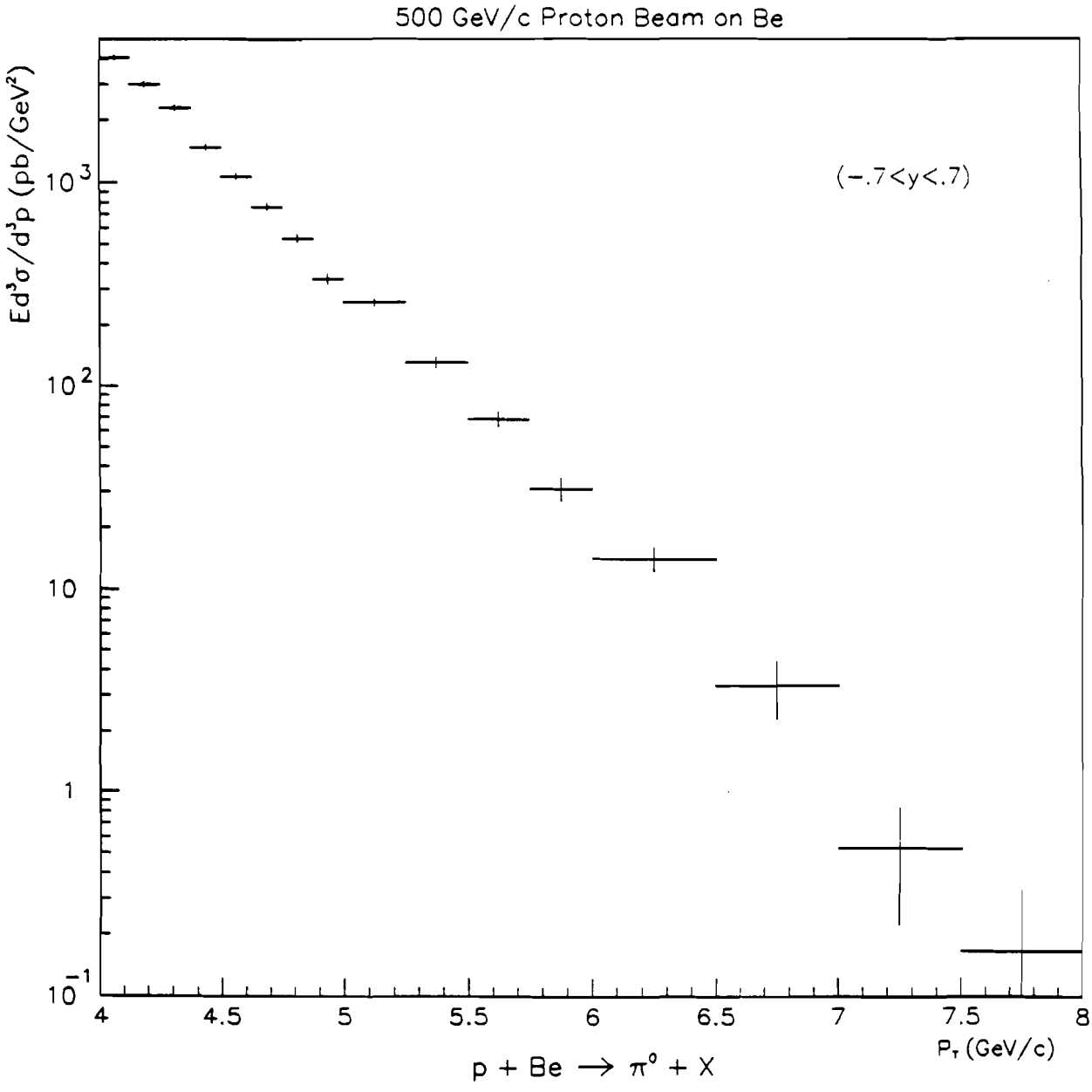

Figure 5.13: π^0 inclusive invariant cross-section per nucleon as a function of P_T integrated over -0.7<y<0.7 for p + Be → π^0 + X.

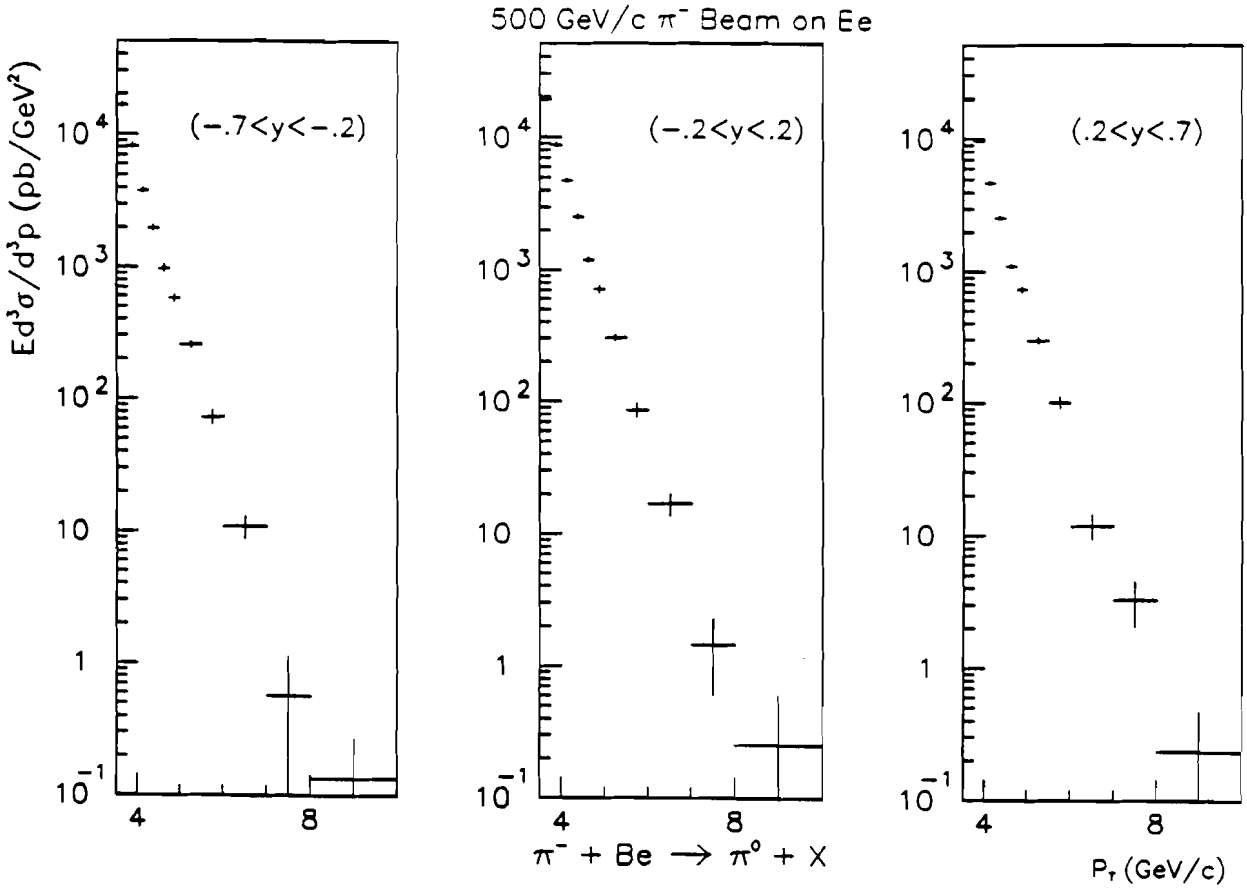

Figure 5.14: π^0 inclusive invariant cross-section per nucleon as a function of P_T in rapidity bins -0.7<y<-0.2, -0.2<y<0.2 and 0.2<y<0.7 for $\pi^- + Be \rightarrow \pi^0 + X$.

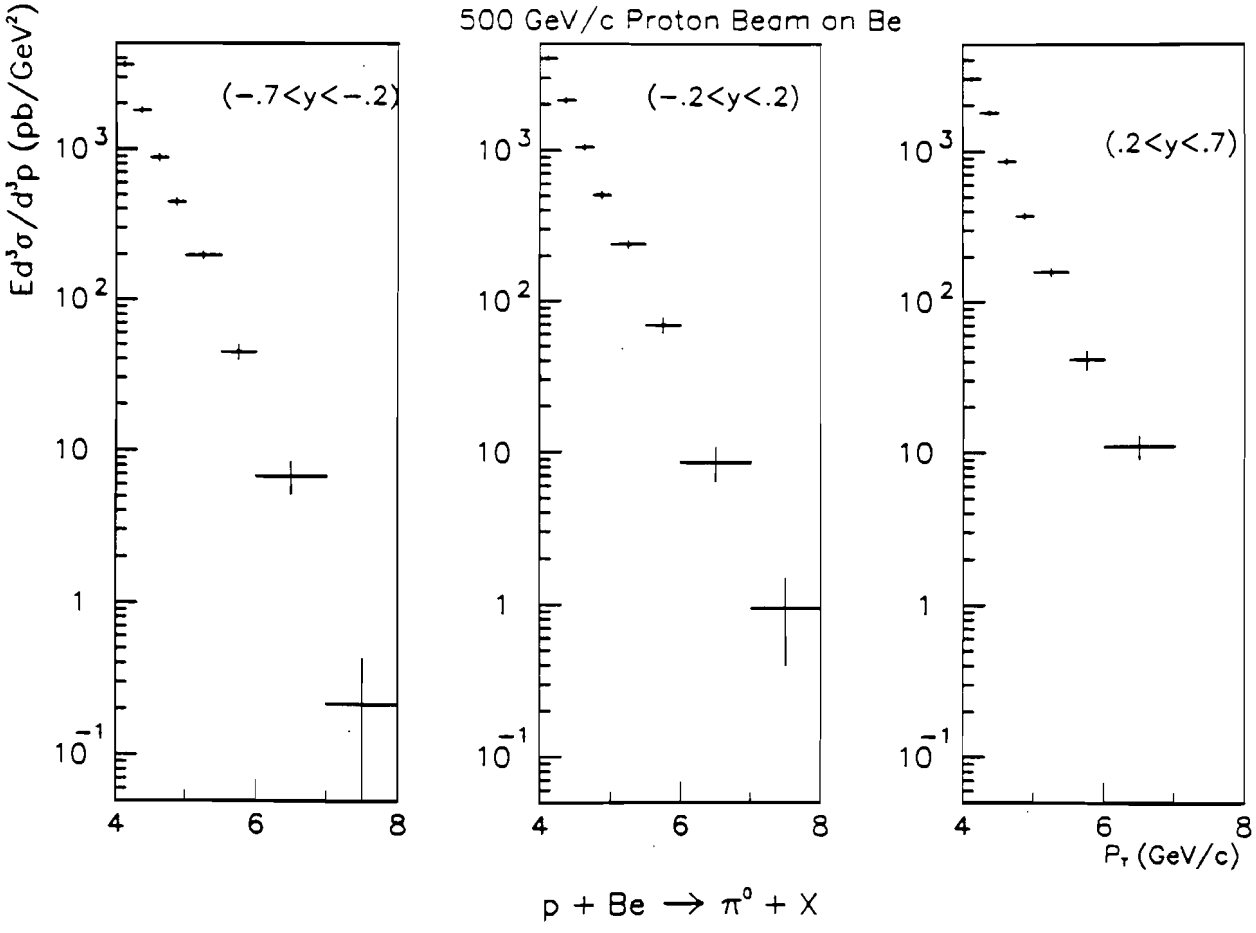

Figure 5.15: π^0 inclusive invariant cross-section per nucleon as a function of P_T in rapidity bins -0.7<y<-0.2, -0.2<y<0.2 and 0.2<y<0.7 for p + Be $\rightarrow \pi^0$ + X.

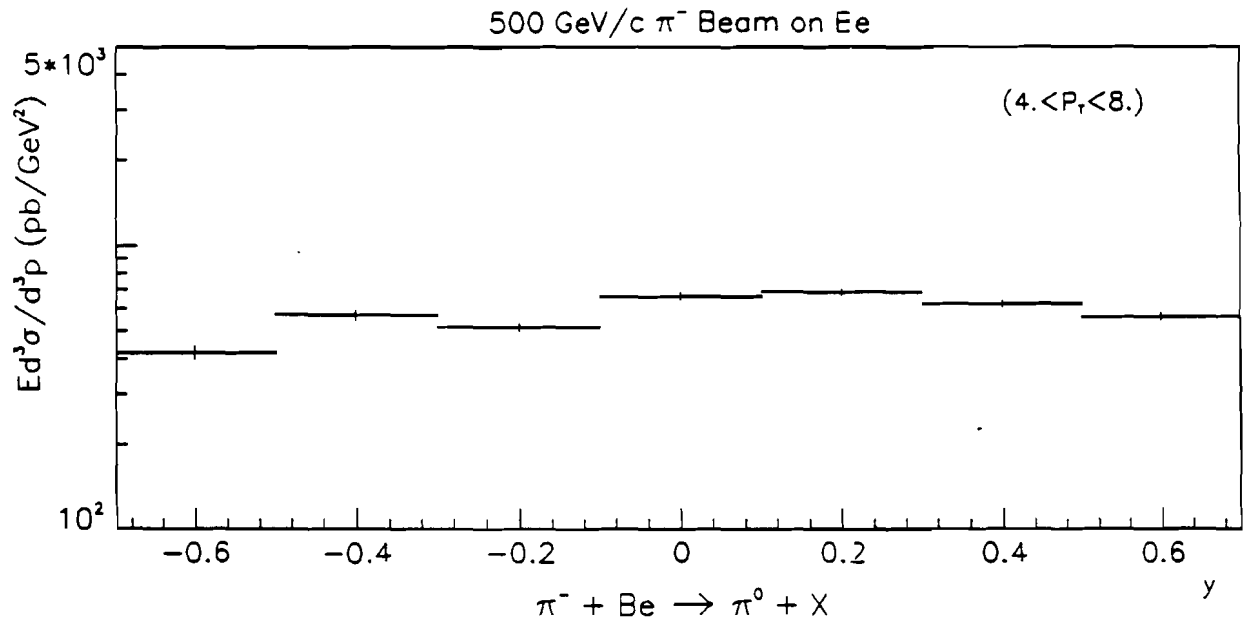

Figure 5.16: π^0 inclusive invariant cross-section per nucleon as a function of rapidity integrated over P_T range for $\pi^- + Be \rightarrow \pi^0 + X$.

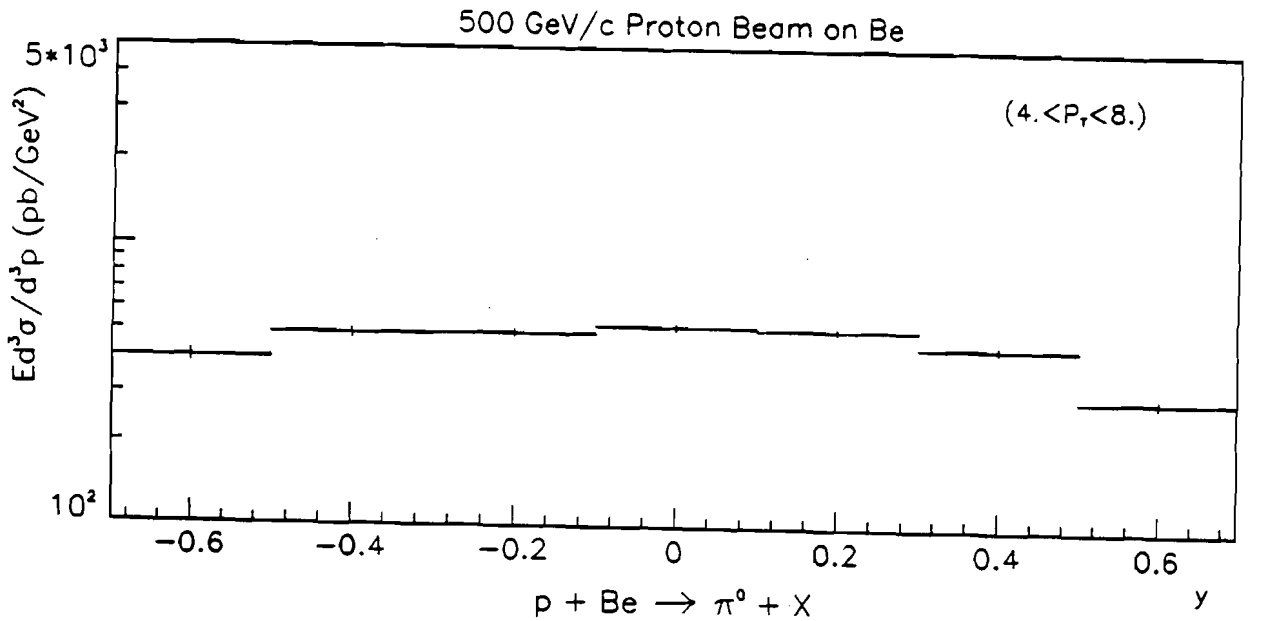

Figure 5.17: π^0 inclusive invariant cross-section per nucleon as a function of rapidity integrated over P_T range for $p + Be \rightarrow \pi^0 + X$.

the π^0 or η sideband region, the photons were counted to statistically correct for the accidental combinations in the π^0 and η mass region.

Figure 5.18 shows an illustration of a direct photon candidate event. The direct photon in the event is represented by the dashed line. The lengths of the line represents the relative magnitude of the particle transverse momenta. The circle represents in radius P_T equivalent to 10 GeV/c. The charged particles in the event are represented by the solid lines. Most of the charged particles seem clustered back to back with the direct photon candidate nearly balancing the P_T of the photon. It also illustrates the possible jet like structure of the high transverse momentum events.

The invariant cross-section per nucleon for direct photon production is given by the expression:

$$\frac{1}{A}E\,\frac{d\sigma}{d^3p} = \frac{1}{2\,\pi\,\mathrm{P_T}\,\triangle\,\mathrm{P_T}\,\triangle y}\frac{1}{\rho l N_a}\mathrm{C}_\gamma\frac{N^{corr}(\mathrm{P_T},\mathrm{y})}{B(\mathrm{P_T})}(ABS) \tag{5.3}$$

where

$$ABS = e^{\frac{d}{\lambda}} \approx 1 + \frac{d}{\lambda}$$

is the correction due to beam attenuation from interactions in the thin target, and

$$N^{corr} = N^{obs}(trig)(conv)(vrteff)(accpt)(C_{oct})$$

is the corrected differential P_T distribution,
A is the atomic weight of the target material,
$\triangle P_T$ is the P_T range,
$\triangle y$ is the rapidity range,
ρ is the density of the target material in gm/cm^3,
l is the thickness of the target material in cm,
N_a is the Avogadro's number expressed in nucleon/gm,
C_γ is an overall correction factor for the direct photons to be described below,
$B(P_T)$ is the the beam count for each P_T bin,

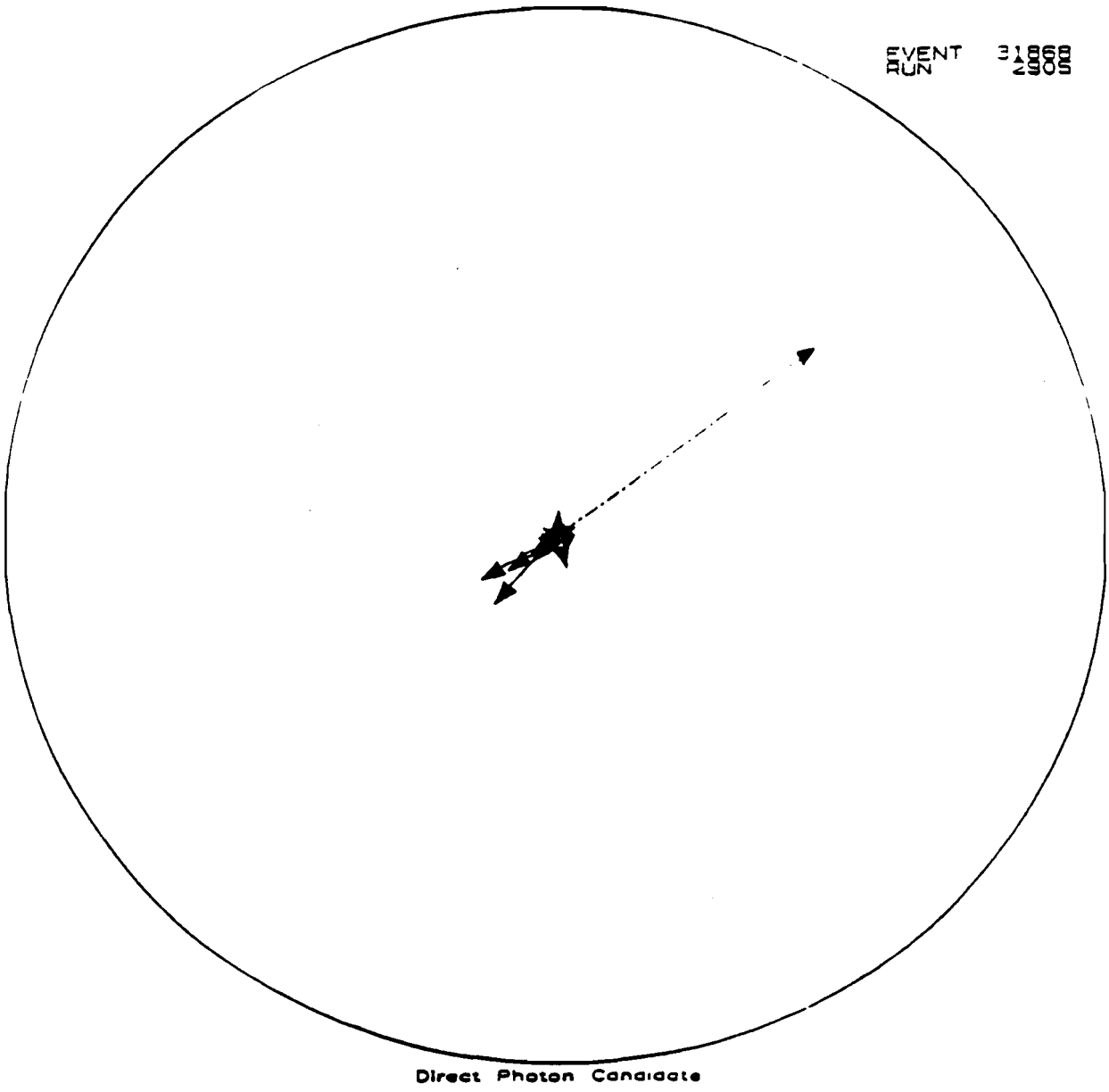

Figure 5.18: Illustration of a direct Photon candidate event. The circle represents in radius P_T equivalent to 10 GeV/c. The dashed line represents the direct photon candidate and the solid lines represent the charged particles. The lengths of the line represent the relative magnitude of the particle transverse momenta. The picture also illustrates possible jet like structure in the event.

d is the the average distance traveled by a beam particle in the target,
λ is the beam interaction length,
N^{corr} is the corrected number of direct photons,
N^{obs} is the observed number of direct photons,
trig is the trigger correction calculated event by event for Single-Local trigger,
conv is the correction for lost direct photons due to pair conversion of the photon between the vertex and the second MWPC station.
$vrteff$ is the residual vertex efficiency correction,
accpt is the single photon acceptance correction,
and, C_{oct} is the correction for the malfunctioning trigger octants. This is given by $C_{oct} = 8 \ / \ N_{live}$, where N_{live} is the number of octants for which the trigger was reliable at the given P_T and radius at the time the event occurred.

The overall correction factor C_γ is a combination of the following corrections: (1)the double occupancy which takes into account the case when two beam particles arrive simultaneously, (2) the correction for loss of good events due to the veto wall, vertex and uncorrelated energy cut.

5.8 Monte Carlo Studies

The direct photon cross-section observed above has to be corrected for backgrounds from the electromagnetic and hadronic showers accepted and reconstructed. For this purpose the response of the detector has to be simulated and studied on the events of interest. GEANT3, a Monte Carlo simulation from CERN was used to study the response of the detectors on the events of interest.

The most accurate method of event simulation is called the 'full shower' method, where all the particles are tracked through the different parts of the spectrometer until their energies fall below certain user defined limit. By this method one can find the energy deposition in every sensitive part of the calorimeter. But to fully track all the particles in the events through the detector, requires a large amount of CPU time. It took 3 hrs per event on VAX780 to fully simulate a high P_T event of interest. The timing for each event was found to be most sensitive to the momentum

cut applied on the charged particle tracks. To get a faster response for the Monte Carlo studies, various parts of the spectrometer can also be parametrized using GEANT. For our high statistics Monte Carlo studies the parametrized response to the detectors was developed by using the full shower simulation.

Direct Photon Background The major source of the background for the candidate direct photon events, are the photons from the π^0 and η decays. If one of the photons from the decay either missed the detector, or landed into the insensitive region of the detector or could not be reconstructed because of very low energy, the other photon will be interpreted as a direct photon candidate. The Monte Carlo studies were done to account for backgrounds arising from the electromagnetic decays of π^0, η, η', ω, K_S^0 and hadronic interactions of K_L^0 and neutrons.

The event topologies can be generated in several ways. Different event topologies were studied and it was decided to use the observed π^0 spectrum from the data to be put through GEANT. The π^0 events were selected from the data summary tape (DST) files. The events were checked for uncorrelated energy cut, veto wall cut, vertex cut and triggering octant. The photons in the event were paired with each other to get the highest P_T π^0. For the purpose of this selection the π^0 was defined as any $\gamma\gamma$ pair with $P_T > 3.0$ GeV/c, mass less then 175 MeV/c^2 and asymmetry up to 1. For each event, only the highest P_T π^0 was selected. The reconstructed π^0's were corrected for trigger correction and non conversion in the target. The π^0's were checked for trigger weight greater than 10 and events with π^0 weight greater than 10 were rejected. The momentum vectors of all the π^0's and photons were calculated.

These π^0's selected from the DST's, were redecayed randomly using GEANT routines and tracked through the spectrometer, and the parametrized response of the EMLAC was recorded. Keeping the event topology the same, each event was rotated five times with random azimuthal rotation to gain in the statistics. The photons were allowed to convert into pairs. They were also allowed to pass through the extra material in front of the calorimeter. The effect of the extra material in front of the calorimeter led to the parametrized response to the energy loss. To

get the response of the photons only EMLAC was simulated. These events were then reconstructed using EMREC. As the Monte Carlo events were reconstructed twice, once to get the data DST and again when they were tracked through GEANT and reconstructed, the input events to the GEANT were corrected for photons lost due to reconstruction. This was done by studying the P_T and rapidity distribution of events before and after it was put through GEANT. Also, the event energy spectrum was studied and was interpolated at lower energy to compensate for the softer photons lost. The events were also corrected for photons lost due to event rotation when a good photon from the unrotated event fell into the non-fiducial region due to rotation. Finally, only the photons which fell into $\pm 45^0$ of the π^0 Φ position were processed through GEANT to save the processing time.

Before these Monte Carlo events were finally reconstructed, they were pre-processed to account for the hardware and software related problems that were found during the extensive study of the data. The corrections applied were:

1. The events were modified for amplifier and EWE gain in groups of 16 strips, once per event, to simulate card by card variation.

2. Every channel in the firing octant was checked for being alive or dead. Typical reason for a channel being dead are shorts in the detector or open connections somewhere along the path. For the purpose of Monte Carlo, these channels were determined by looking at histograms containing the number of times a channel had more than 1 GeV of energy in the front section or 0.5 GeV of energy in the back section. Channels that had zero or very low energy were declared dead. The channels affected tended to vary in time.

3. Every channel was modified for the pedestal shift from studying the non zero suppressed data.

4. Energy in each channel was also smeared by some gaussian noise to simulate the electronic noise.

5. Each channel was also modified for the energy resolution term. The energy resolution term used for the Monte Carlo was $16\%/\sqrt{E}$.

6. Modification was also applied for the cross-talk effect[77] among the amplifier channels. The electromagnetic shower shape was studied in the EMLAC using the beam calibration data and the standard data. It was found that the chi-square distribution for the standard data were larger than that for the calibration data and also larger than expected from the statistical distribution. The reason for this difference was found to be the cross-talk effect among the amplifier channels which changes slightly the energy in the neighbouring channels thus changing the shape of the distribution. Study was done to mimic for this energy sharing among the channels.

7. In the end, the signal assigned to each channel was checked to determine whether it was above or below the zero suppression cut, which was set separately for each channel based on the quadrant, section, view and strip information.

The above mentioned effects were applied, and the Monte Carlo generated events were reconstructed to study the background. For studying the η, η', ω, K_S^0, K_L^0 and neutron contribution to the background, the observed π^0 spectrum was used to model their production. This was done because the production cross-section for these particles is known to be approximately a constant fraction of the π^0 cross-section and so this was a valid model for the background calculations. The procedure followed for η was identical to the one followed for the π^0's, except that the π^0 was replaced by an η before the event was tracked through GEANT. The resulting events were weighted by the η to π^0 production ratio[78] of 45% and by the branching ratio for $\pi^0 \rightarrow \gamma\gamma$ (=98.8%) and $\eta \rightarrow \gamma\gamma$ (=38.9%). The weighted events were then added into the sample.

The η sample was also checked for its non $\gamma\gamma$ ($\eta \rightarrow 3\pi^0$) neutral decay mode. Events were generated where all the measured neutral decay modes of η were simulated and the decay modes were flagged. It was found that the non $\gamma\gamma$ decay mode does contribute to the background in a very small amount and this was included in the correction term for the cross-section.

The η' and ω were assumed to have the same production ratio (=45%) as η

to π^0. The method followed to generate these events was identical to the one followed for π^0's, except that the π^0 was replaced by η' and ω respectively before being tracked through GEANT. η' was studied for two of its decay modes, $\eta' \rightarrow \gamma\gamma$ (=2.16%) and $\eta' \rightarrow \rho^0\gamma$ (=30.0%) which had the maximum chances to contribute some background to the direct photon signal. Other neutral decay modes were not investigated because of their decay characteristics. The contribution from $\eta' \rightarrow \rho^0\gamma$ decay was found to be negligible. Only weighted events from $\eta' \rightarrow \gamma\gamma$ decay were added into the background sample. ω was studied for its neutral decay into $\omega \rightarrow \pi^0\gamma$ (=8.5%) and the weighted events were added to the background sample.

The spectrum for K_S^0 was also generated. The production ratio of K_S^0 to π^0 was estimated[79] to be 40% from the ratio of $K^{\pm}/\pi^{\pm}$ in proton-proton collisions. Decay of $K_s^0 \rightarrow \pi^0\pi^0$ (=31.39%) was studied and the weighted events were added to the rest of the background sample. The spectrum for K_L^0 and neutron was also simulated in the same fashion, and the number of photons found after reconstruction was less than 0.01%. Thus the contribution from K_L^0 and neutron were not taken into consideration for background calculations.

The Monte Carlo data was reconstructed and analysed with exactly the same code as used for the data. The trigger efficiency was replaced by the trigger weight associated with each event and the true $\pi^0+\eta+\eta'+\omega+K_S^0$ spectrum was simulated. As this whole sample contained no real direct photons, any direct photon candidate identified by the direct photon analysis code represented a background contribution due to these neutral decays. This background was represented as a fraction of the π^0 cross-section, measured from the same Monte Carlo sample.

Studies were also done to see the relative contribution to the direct photon background from the different sources. As the samples for Monte Carlo generated events had no real direct photons, the number of direct photons found in each sample scaled by their production cross-section and branching ratio with respect to the other source of the background, will give the relative measure for the background contribution. η background was found with respect to the π^0 and for η', ω and K_S^0 the relative contribution was found with respect to η. This was done because of rel-

atively small contribution to the background due to η', ω and K^0_S. The contributions to the background as found are:

1. $\eta \rightarrow \gamma\gamma / \pi^0 \rightarrow \gamma\gamma = 17.59 \pm 0.37$ %
2. $\eta' \rightarrow \gamma\gamma / \eta \rightarrow \gamma\gamma = 7.17 \pm 0.18$ %
3. $\omega \rightarrow \pi^0\gamma / \eta \rightarrow \gamma\gamma = 13.21 \pm 0.41$ %
4. $K^0_S \rightarrow \pi^0\pi^0 / \eta \rightarrow \gamma\gamma = 16.9 \pm 1.4$ %
5. $\eta \rightarrow$non $\gamma\gamma / \eta \rightarrow \gamma\gamma = 3.1 \pm 1.0$ %

Comparison of Data and Monte Carlo

For a direct photon experiment, the sensitivity of the Monte Carlo can be best studied by how well it reproduces the π^0 asymmetry distribution. The π^0 asymmetry distribution is sensitive to the detection resolution of the calorimeter for low asymmetry photon pairs from highly energetic π^0 decay. The asymmetry distribution is also very sensitive to the acceptance of the calorimeter for highly asymmetric decays of the π^0's. Figure 5.19 shows the π^0 energy asymmetry distribution for the full sample of data compared to the Monte Carlo for unsubtracted, sideband and the sideband subtracted distributions. The agreement is quite good. Figure 5.20 shows the sideband subtracted $\gamma\gamma$ energy asymmetry distribution for the η mass region. Although the statistics for this mass range is limited, the agreement between the data and the Monte Carlo is quite good. The Monte Carlo information for both the above plots have been area normalized to be compared with the data.

Figure 5.21 and 5.22 shows the $\gamma\gamma$ mass plots for data and Monte Carlo when no asymmetry and A<0.75 cut have been applied. The agreement in Figure 5.21 is very good except that there is some discrepancy on the lower mass side of the π^0 tail. When asymmetry cut is applied the difference in the tail for the data and the Monte Carlo is very distinct. Most of the effects simulated in the Monte Carlo, were assumed to have gaussian distribution which may not be completely true for the data. In consequence, our Monte Carlo corrections for π^0 reconstruction efficiency did not fully correct the data. π^0 mass spectrum for data and Monte Carlo were

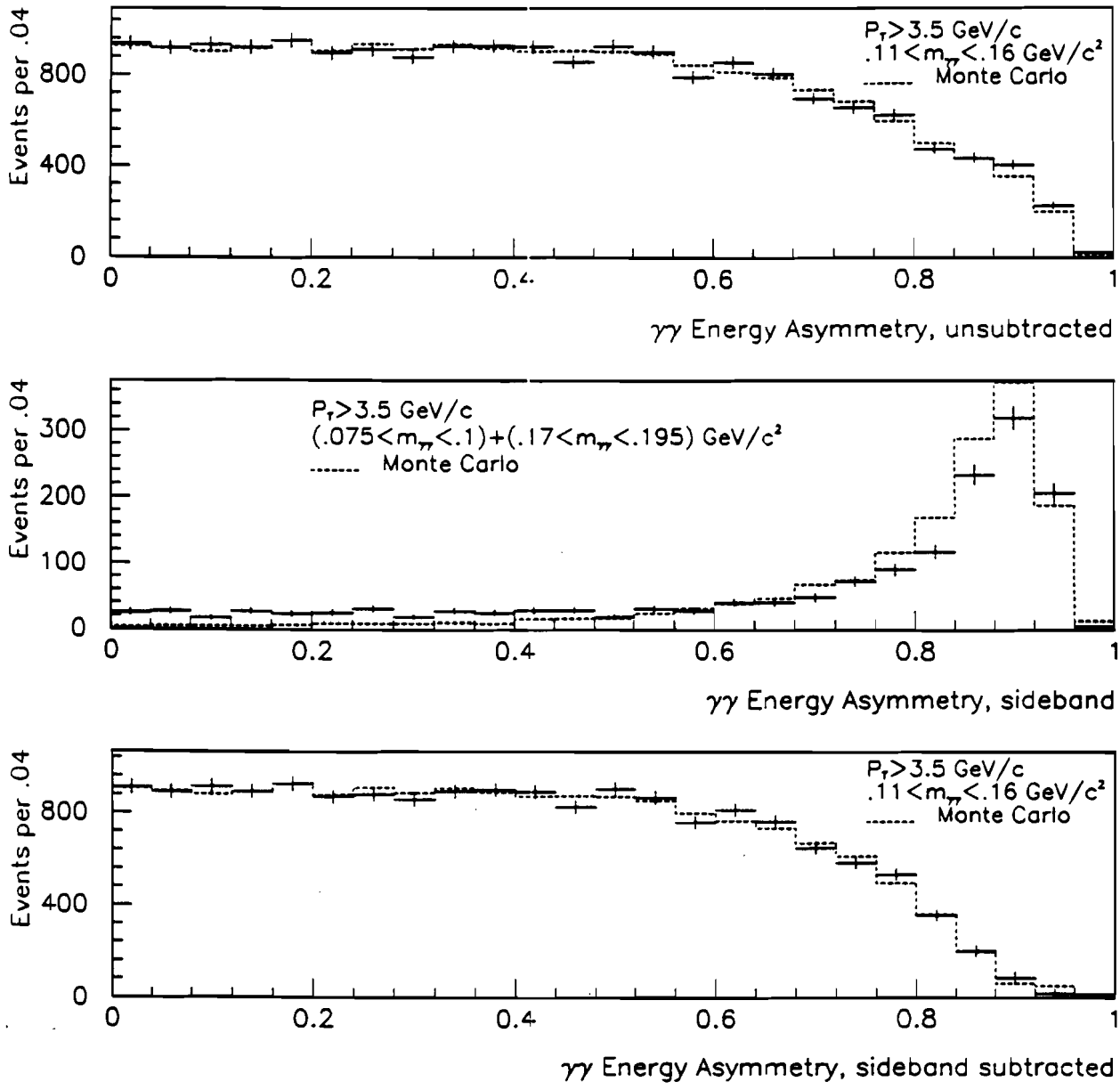

Figure 5.19: Distribution for unsubtracted, sideband and the sideband subtracted π^0 energy asymmetry. The solid points represent the data sample and the dashed points represents the distribution predicted by the Monte Carlo.

compared for different energy and rapidity ranges and based on the study, the π^0 cross-section had to be scaled up by 3.2±0.4 %.

The Monte Carlo and data were also compared for the π^0 mass distribution as a function of the radial position of the π^0 in the calorimeter, the measured energy of the π^0, the measured P_T of the π^0 and the energy asymmetry of the photon pairs forming the π^0. Figure 5.23 shows the comparison of the π^0 mass with respect to these variables for data and Monte Carlo. Except for inner radius where the π^0 mass for data comes consistently higher than Monte Carlo by about 0.2 MeV, the agreement is quite good. This difference in mass is also obvious at energy greater than 150 GeV. This difference can be attributed in the position and energy resolution of two overlapping showers.

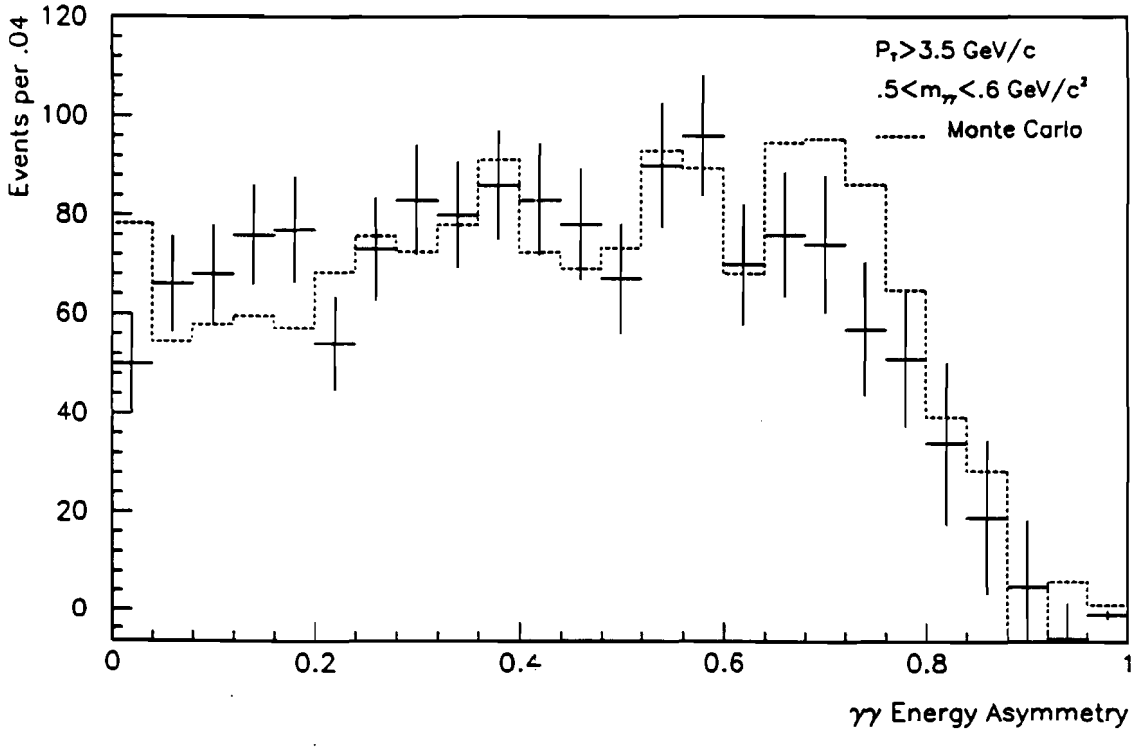

Figure 5.20: η energy asymmetry for the sideband subtracted distribution. The points represent the data sample and the dashed line represents the Monte Carlo distribution.

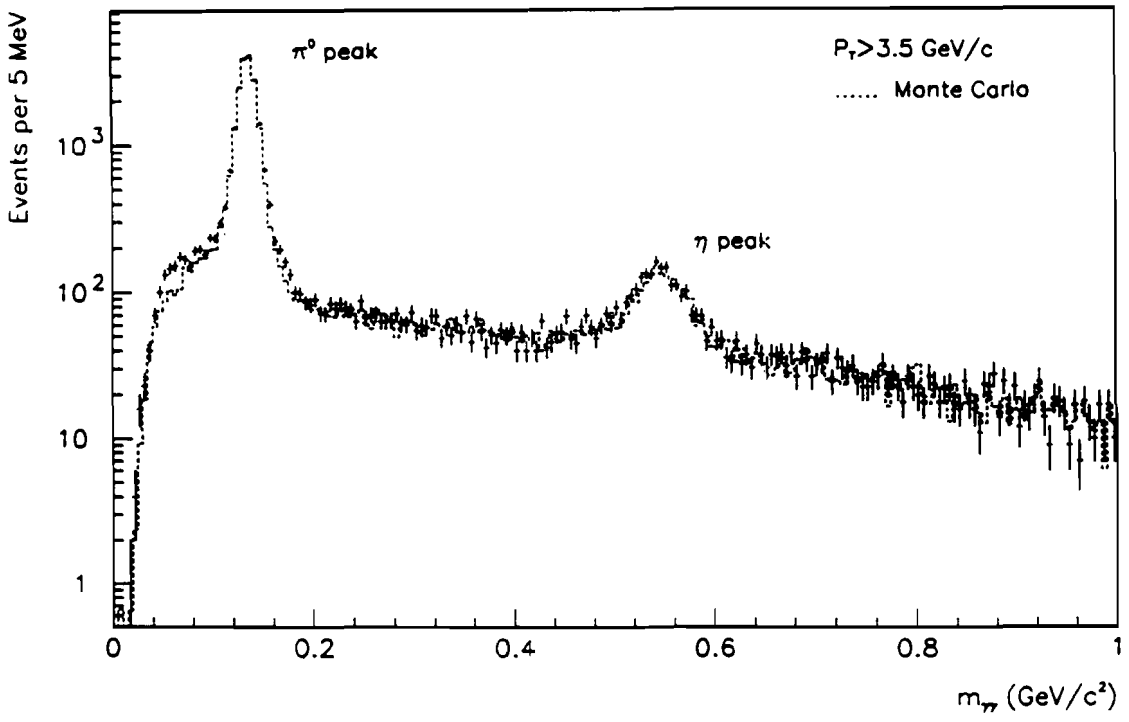

Figure 5.21: $\gamma\gamma$ Mass distribution comparison for Data and Monte Carlo. No asymmetry cut has been applied.

Figure 5.24 shows the comparison of χ^2 fit to the shower shape for different energy ranges for the data and the Monte Carlo. The data and the Monte Carlo compares well except for the tail of the distribution on higher χ^2 side for 60<E<80 GeV. Figure 5.25 shows the E_F/E_T (defined in chapter 4) distribution compared for data and Monte Carlo in different energy ranges. Although the distribution for E_F/E_T agrees over most of the energy range some difference between the data and the Monte Carlo exists for the energy range 5<E<10 GeV. The data has more energy in the front section compared to the Monte Carlo distribution. E_F/E_T value of the distribution was studied for Monte Carlo with different zero suppression values and it was found that the E_F/E_T graph for 5<E<10 GeV is very sensitive to the zero suppression cut applied. It was also found that the E_F/E_T ratio is very sensitive to the amount of the material in front of the LAC. As parametrized showers were used for the Monte Carlo studies, the difference in the particular plot suggests either

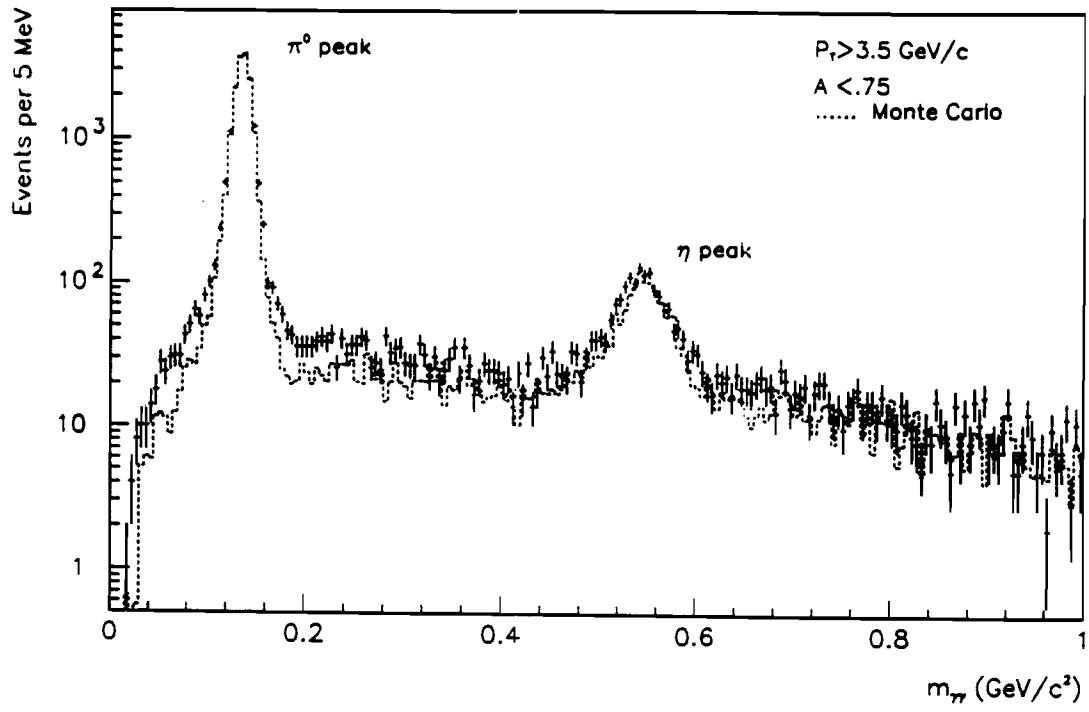

Figure 5.22: $\gamma\gamma$ Mass plot comparison for data and Monte Carlo. An asymmetry cut of A<0.75 has been applied.

some difference in zero suppression implementation between data and the Monte Carlo or some small correction needed for the parametrized shower studies.

Figure 5.26 shows the comparison between data and Monte Carlo for low and high energy photons forming π^0. The agreement is quite impressive over all the energy ranges. Figure 5.27 shows the comparison for photon multiplicity per half octant for the data and the Monte Carlo. The graphs are peak normalized. We compare the multiplicity for the half octant in which the π^0 was found. This was done because when the event was passed through GEANT all other photons which were not within $\pm 45^0$ of the π^0 azimuthal position were disregarded. The comparison does give a feel how successfully the extra photons were added for the photons lost due to the reconstruction and for the photons lost in the non-fiducial volume.

Figure 5.28 and 5.29 shows the distribution of the width of all the showers in centimeters in various rapidity and energy bins. The data and Monte Carlo predic-

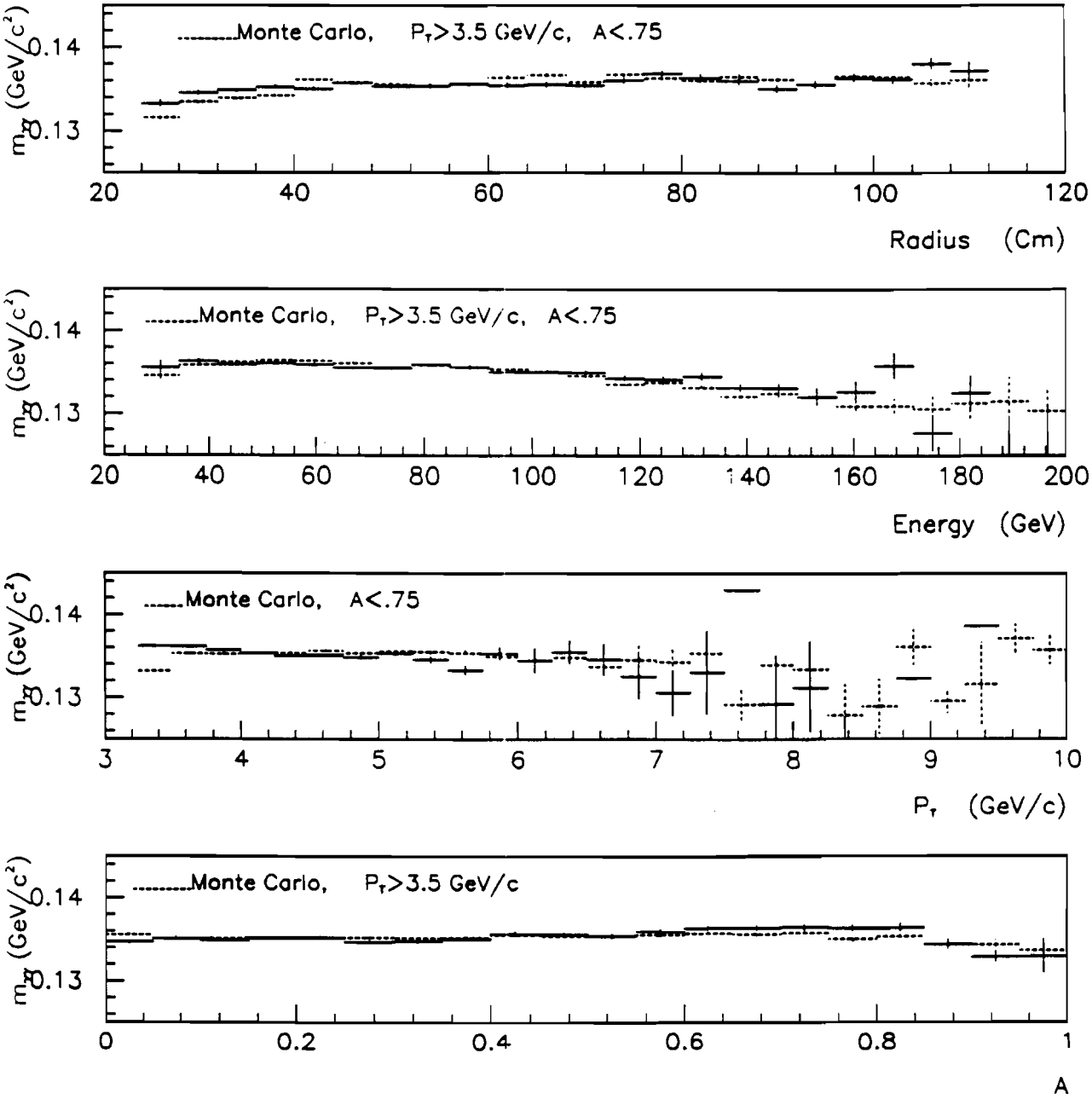

Figure 5.23: Data and Monte Carlo comparison for π^0 mass distribution as a function of radius, energy, P_T and energy asymmetry of the π^0.

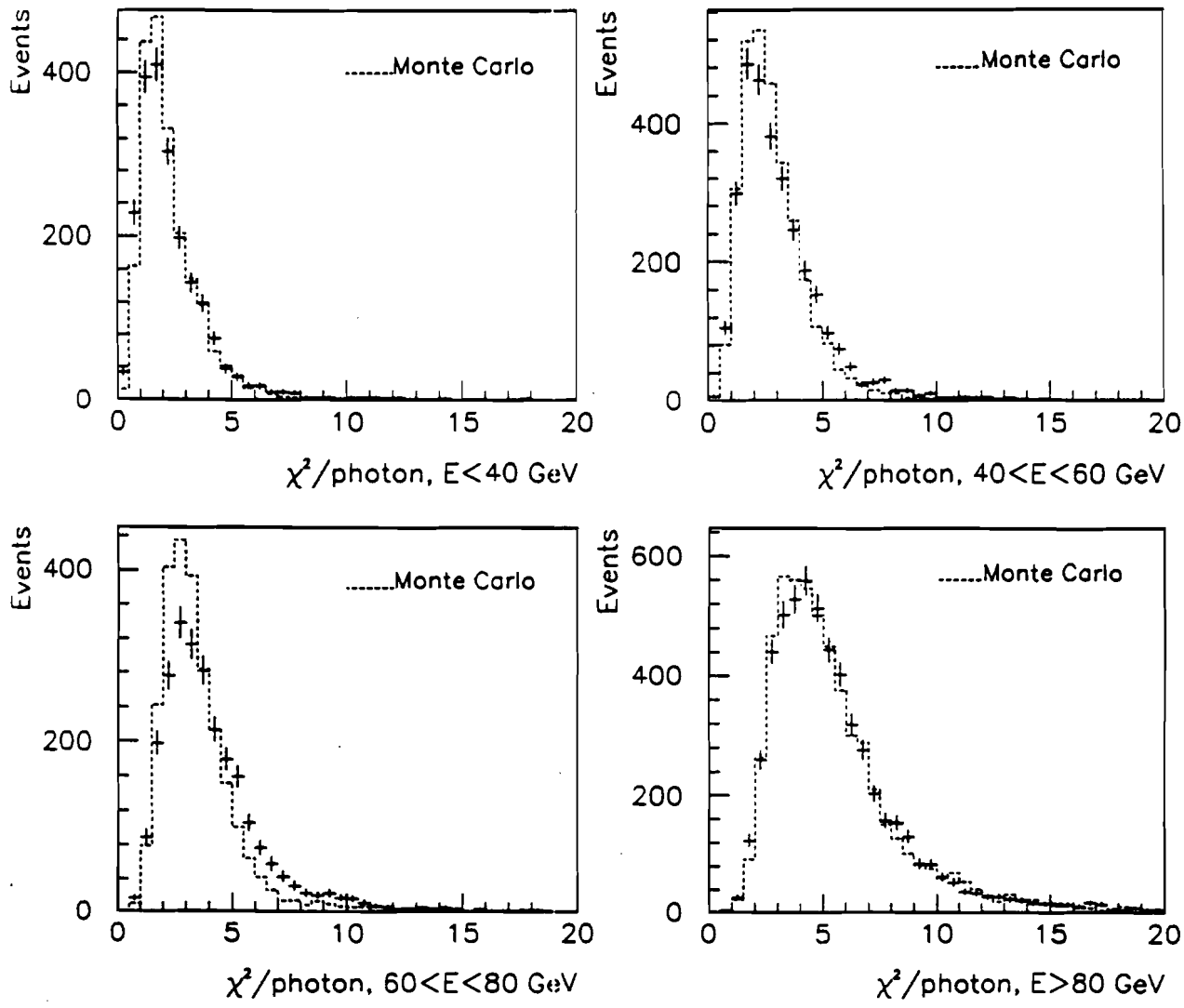

Figure 5.24: Chisquare per photon for different photon energy ranges. The data and Monte Carlo compares well. There are some differences in tail of the distribution on higher χ^2 side for 60<E<80 GeV.

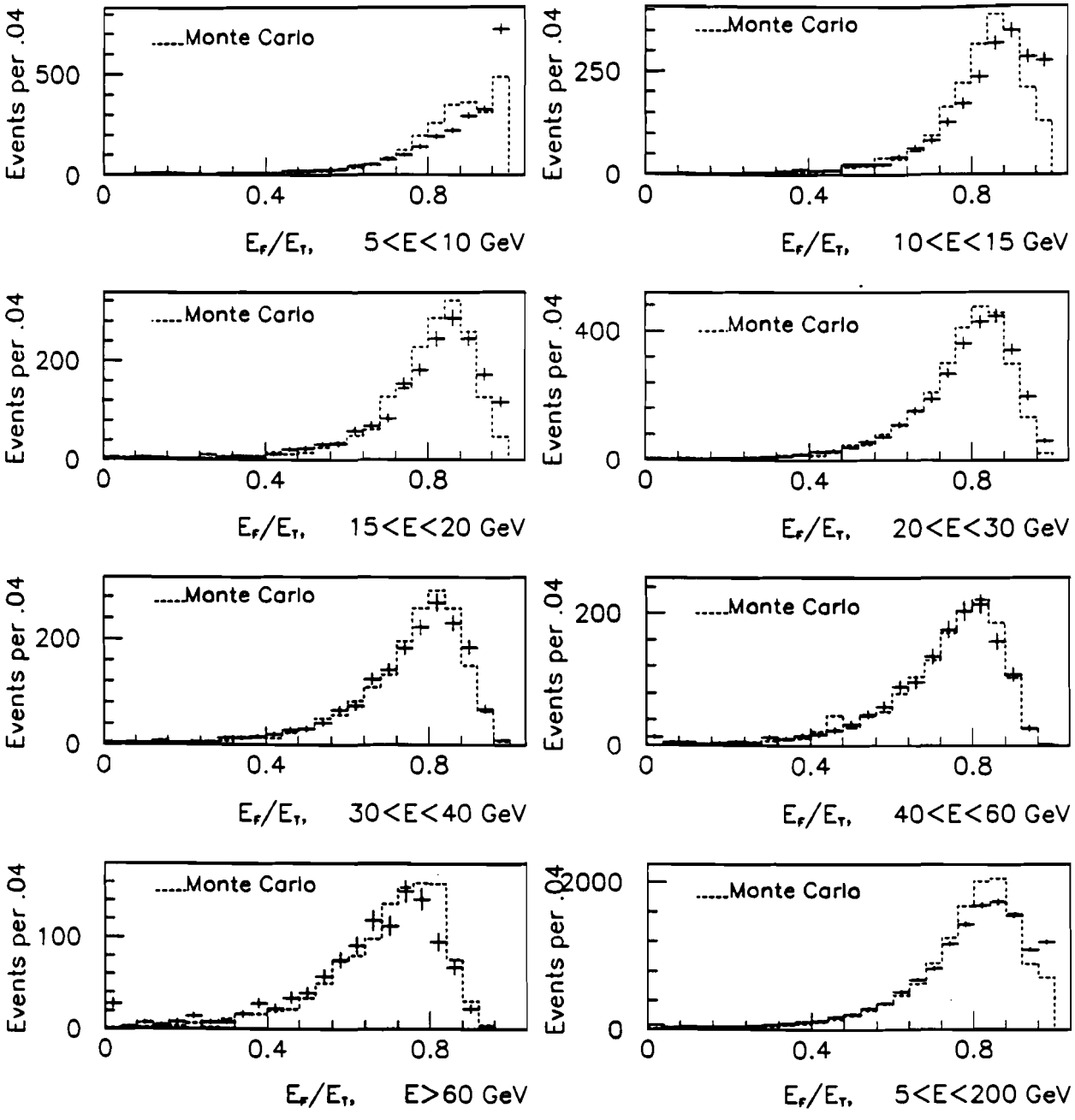

Figure 5.25: E_F/E_T distribution for shower deposition compared for data and Monte Carlo for different energy ranges. Although they agree for most of the energy ranges, some difference in data and Monte Carlo can be seen for 5<E<10 GeV.

tions agree very well for forward rapidity and for higher energies. The agreement is not so great at the backward rapidity or lower energy.

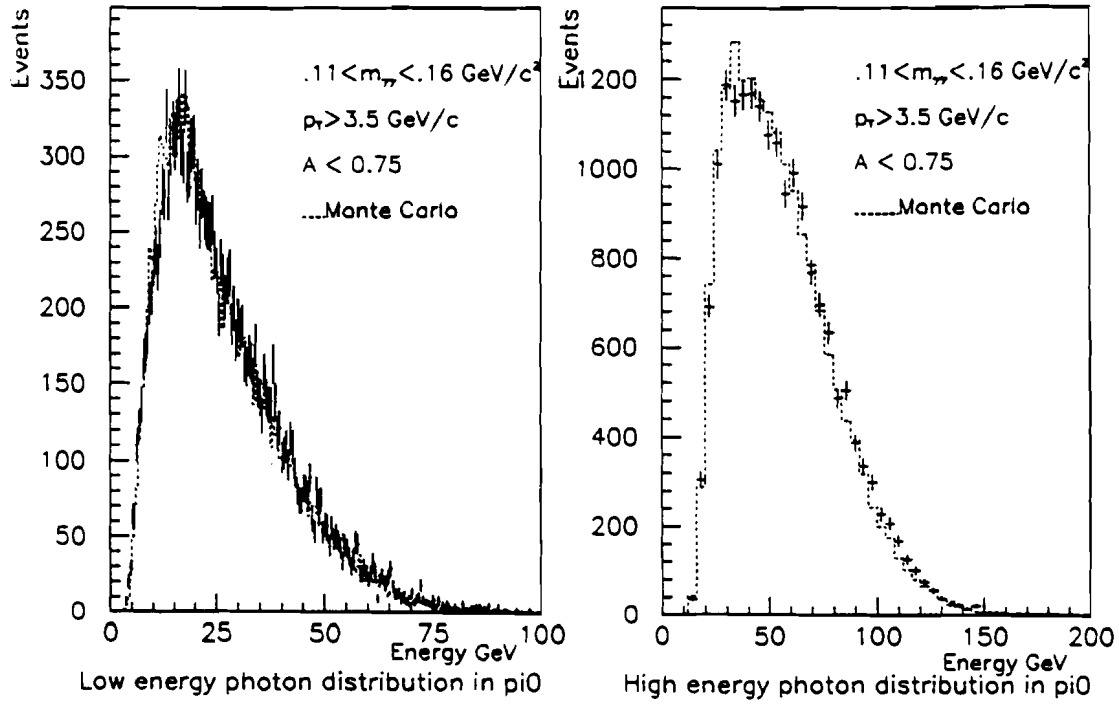

Figure 5.26: Comparison of data and Monte Carlo for low and high energy photon distribution in π^0 mass band. The agreement is quite impressive.

From above comparison between the data and Monte Carlo it is obvious that we can trust our Monte Carlo results. The direct photon cross section is found from the data. To correct for the background, the Monte Carlo gives us the fake γ/π^0 ratio which is multiplied by the π^0 cross-section and subtracted from the observed direct photon candidate cross-section to get the final direct photon cross-section.

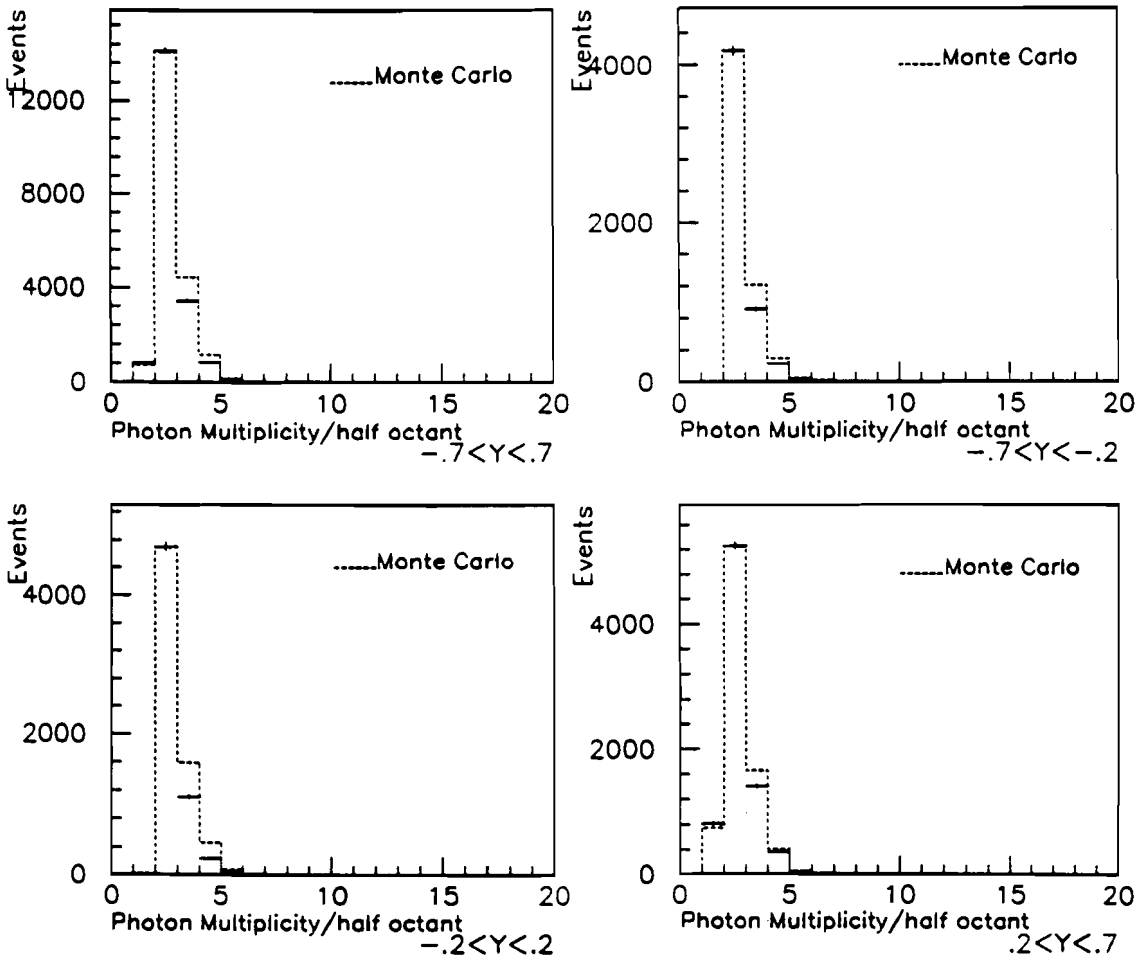

Figure 5.27: Photon multiplicity per half octant. The half octant considered here is the azimuthal space around the π^0 phi position. There is small difference between data and Monte Carlo at higher multiplicity.

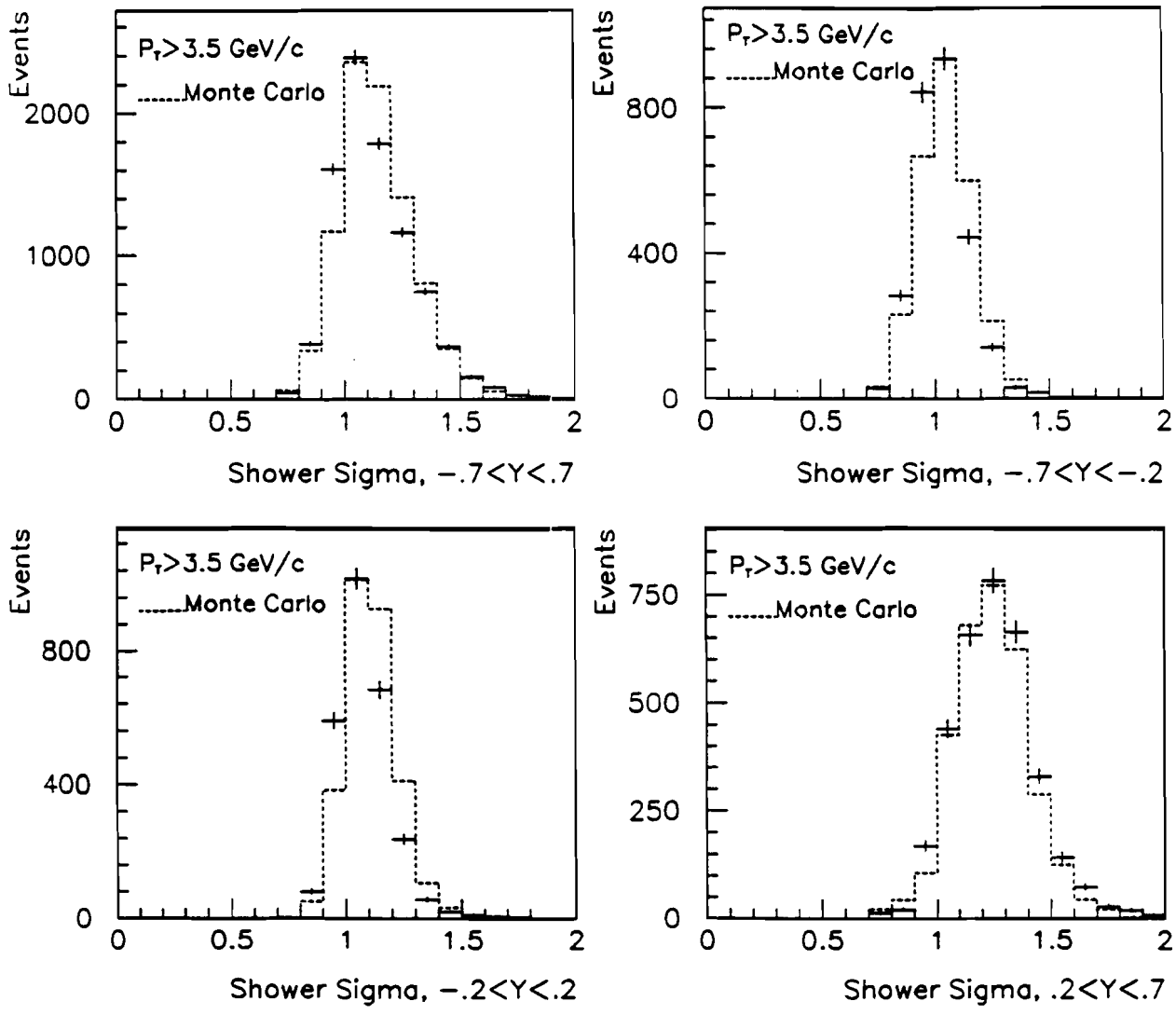

Figure 5.28: Shower sigma (in cms) compared for data and Monte Carlo in different rapidity bins. The agreement for backward rapidity (i.e low energy showers) is not as good as the agreement for the forward rapidity range (i.e high energy showers).

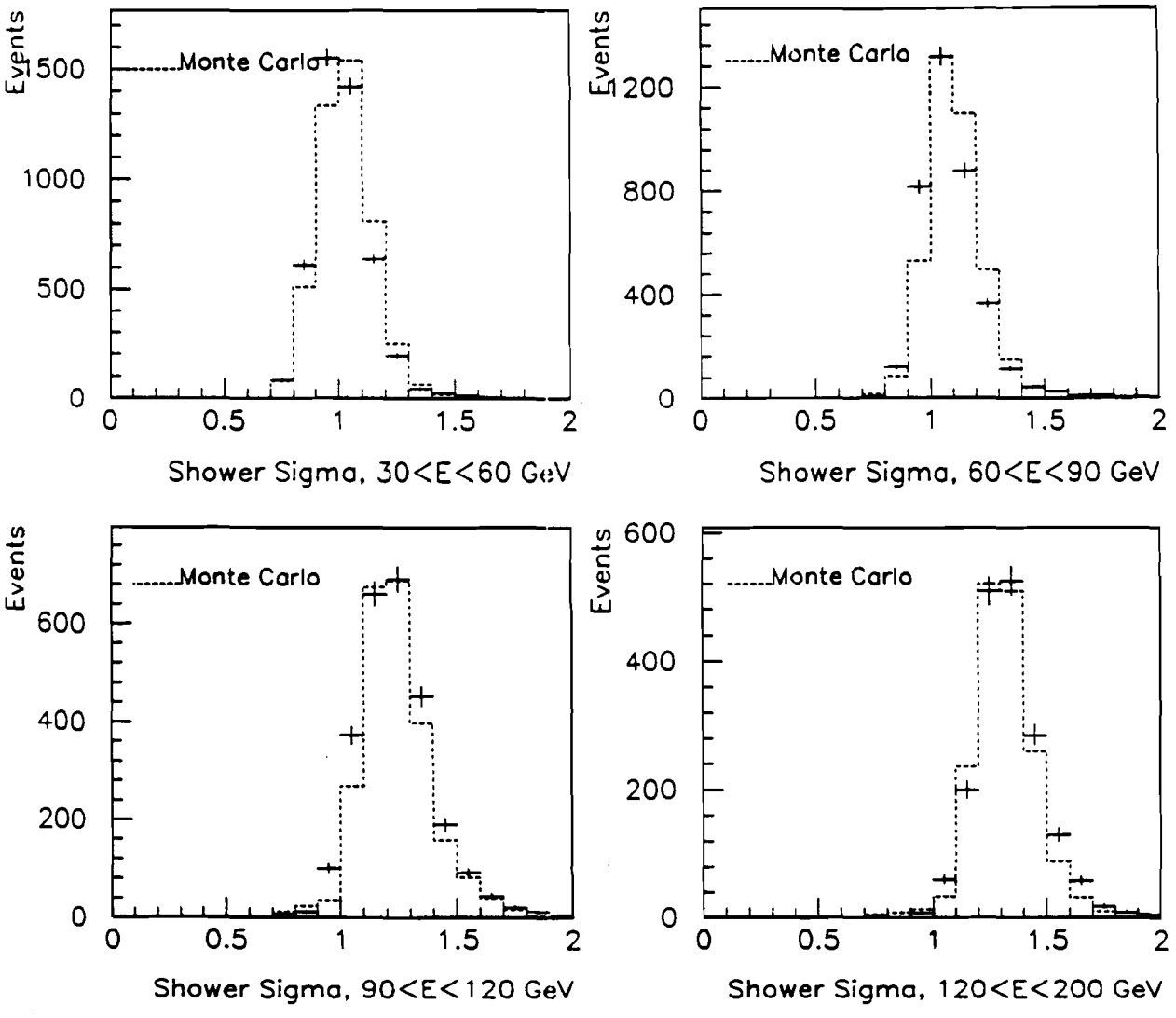

Figure 5.29: Shower sigma (in cms) compared for data and Monte Carlo in different energy bins. The agreement for higher energy is better than the ones for the lower energy.

5.9 Energy Scale Determination

The determination of precise energy scale is very important for experiments like E706 where particle (π^0, η, γ) production cross section falls off very rapidly with increasing P_T. An error of 1% in the measurement of the energy scale can result in an uncertainty of about 10% in the measured cross section value. The energy scale can be determined by normalizing the mass of particles like π^0 or η to their standard mass. The earlier direct photon experiments like WA70 (Ref. 42) and UA6[80] has used this method. But as π^0 and η are formed of two photons, the overlapping of the showers inside the electromagnetic calorimeter can create problems. Due to overlapping of shower pairs the calculated mass of the particle may change while the energy of the pair will essentially remain unchanged.

The energy scale for this experiment was determined with an entirely different scheme. Only those events, where one of the photons from the π^0 or η converted into an e^+e^- pair in the target downstream of the primary vertex, were used for this study. The electrons (e^+ and e^-) from photon conversion leave a distinct signal in the charged particle tracking system. Upstream of the analysis magnet, they appear as a single track in the SSD system, but downstream of the magnet they appear as a pair of widely separated tracks in the MWPC system. These oppositely charged electron-positron form a zero mass pair (ZMP, Ref. 52). The momentum of the e^+e^- pair was measured by the tracking system while the EMLAC was used to measure their energy. Tracks were also matched with electromagnetic type showers in the EMLAC having $E_F/E_T > 0.5$. The resultant E/P distribution is shown in Figure 5.30 for electrons with $E > 15$ GeV. E is the energy of the electron as measured in the EMLAC and P is the measured momentum from the tracking system. The mean and standard deviation for the peak are respectively 0.999 ± 0.003 and 7.6%. Figure 5.31 shows the corrected γe^+e^- mass distribution using the measured momentum for the electrons and the energy of the isolated photons. It is also required that this isolated photon satisfies the requirement that it is formed from GAMMAS with only one-to-one correlation.* As one of the photons

* One GAMMA in the R-view correlates with only one GAMMA in the Φ-view to form a photon.

from the π^0 or η decay converts in the e^+e^- pair, the other photon will be isolated in the EMLAC and the shower reconstruction for the particular photon will be much simpler. The mass and width of π^0 evaluated from the γe^+e^- plot is respectively 135.1±0.6 Mev/c^2 and 13.5±0.7 Mev/c^2. Using the γe^+e^- combination the mass and width of η comes to be respectively, 551.1±3.3 Mev/c^2 and 20.3±6.1 Mev/c^2. Using only the information available from the electromagnetic calorimeter the mass and width of π^0 comes respectively, 134.1±1.0 Mev/c^2 and 15.2±0.9 Mev/c^2. The calculated value of the mean and the standard deviation for the E/P distribution, and the mass and width of π^0 and η shows the consistency with which the energy scale has been determined.

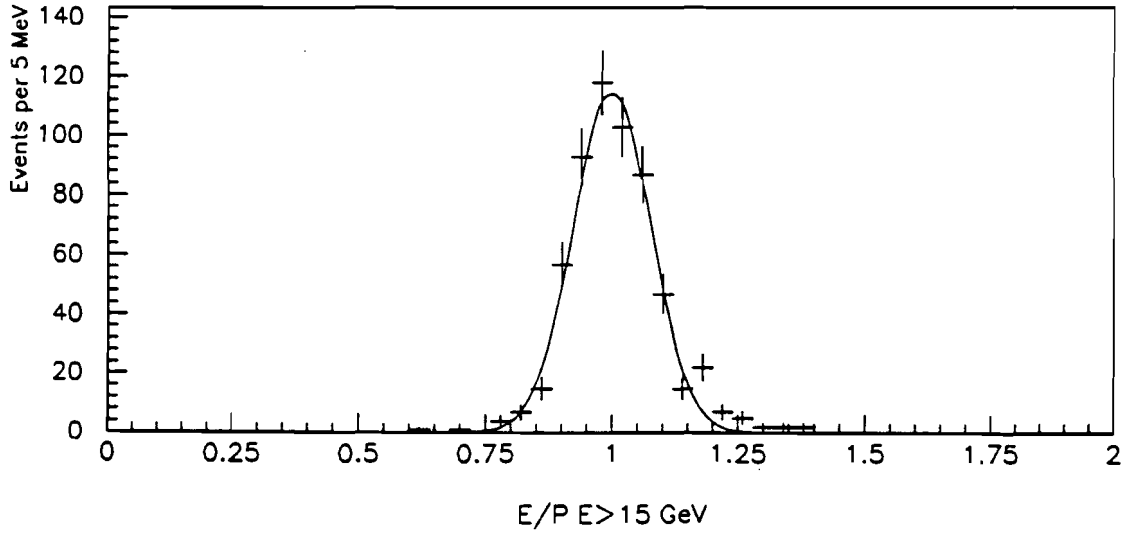

Figure 5.30: The ratio of E/P for all conversion electrons with E > 15 GeV. E is from EMLAC and P is from the tracking system.

The charged particle tracking system momentum scale was calibrated via the decays of $K^0_S \rightarrow \pi^+\pi^-$, $J/\psi \rightarrow e^+e^-$ and $J/\psi \rightarrow \mu^+\mu^-$. The measured mass for the J/ψ and K^0_S decays are within 0.5% of the standard particle mass. The electron energy measurement from the EMLAC was corrected for showering in the additional material in the front of the EMLAC. The correction for the photon showers was

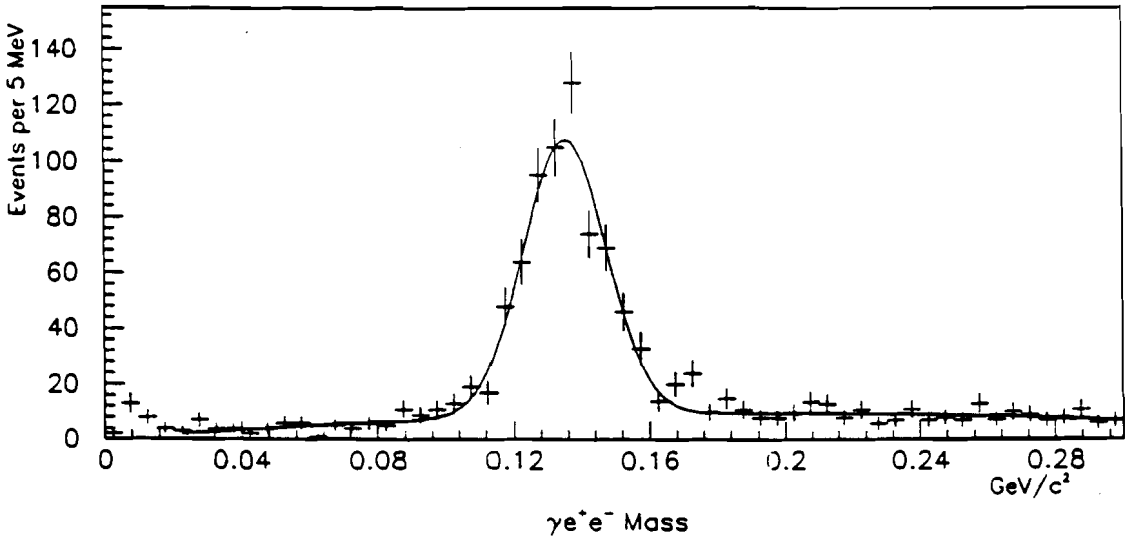

Figure 5.31: The γe^+e^- mass distribution. The π^0 peak is apparent. For electron momentum measurement, the charged particle tracking system is used while the photon energy is determined from the EMLAC.

estimated after running full-GEANT Monte Carlo showers which converted the electron correction to the one valid for the photons. This suggests that the calibration of the EMLAC is totally dependent on our tracking calibration.

Using the scale arrived from the above method the data was also checked for the energy dependent effects. Figure 5.32 shows the corrected mean E/P ratio for the conversion electrons as a function of the electron energy. No systematic variation in E/P ratio as a function of the electron energy is seen over the entire range. Figure 5.33 shows the variation with photon energy of the mean values of fits to γe^+e^- mass distribution. Within the limits of errors on the fitted value to γe^+e^- mass, only very minimal energy variation is apparent.

The energy scale obtained from the method described above was used to determine π^0 and η mass in the $\gamma\gamma$ events. Photon pairs ($\gamma\gamma$) were reconstructed for π^0's mass range with P_T>4.0 GeV/c, A<0.75, and an additional cut was applied that required the separation between the two γ's to be greater than 3 cm. The separation cut reduced the problem of the overlapping showers. As shown in Figure 5.34, the π^0 mass is 135.8±0.1 MeV/c^2. For $\gamma\gamma$ mass in the η mass region, as the

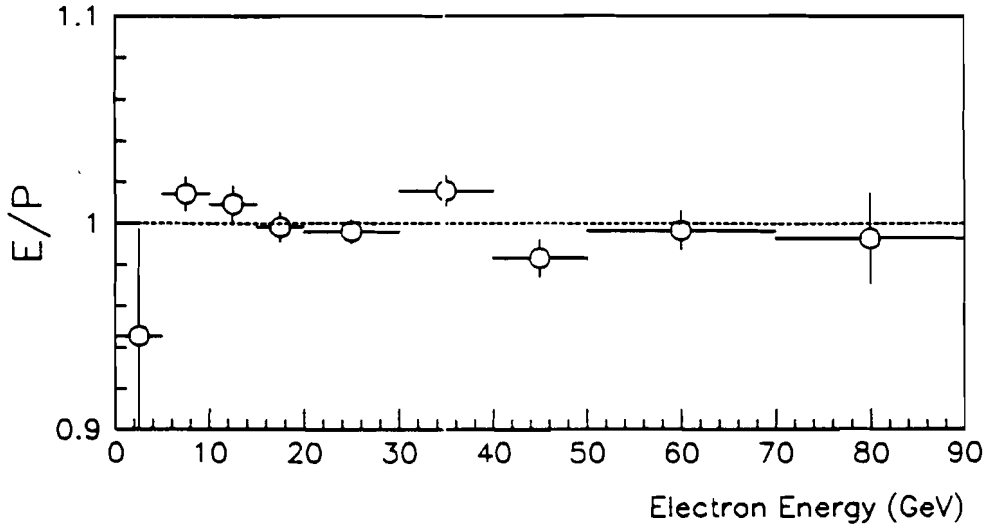

Figure 5.32: E/P ratio for conversion electrons as a function of electron energy. No systematic variation is apparent.

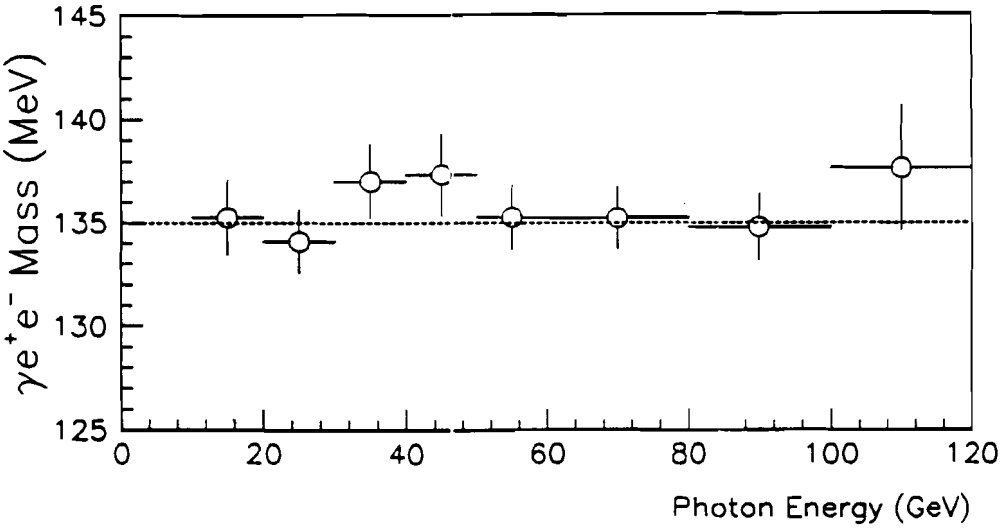

Figure 5.33: γe^+e^- mass distributions shown as a function of the photon energy.

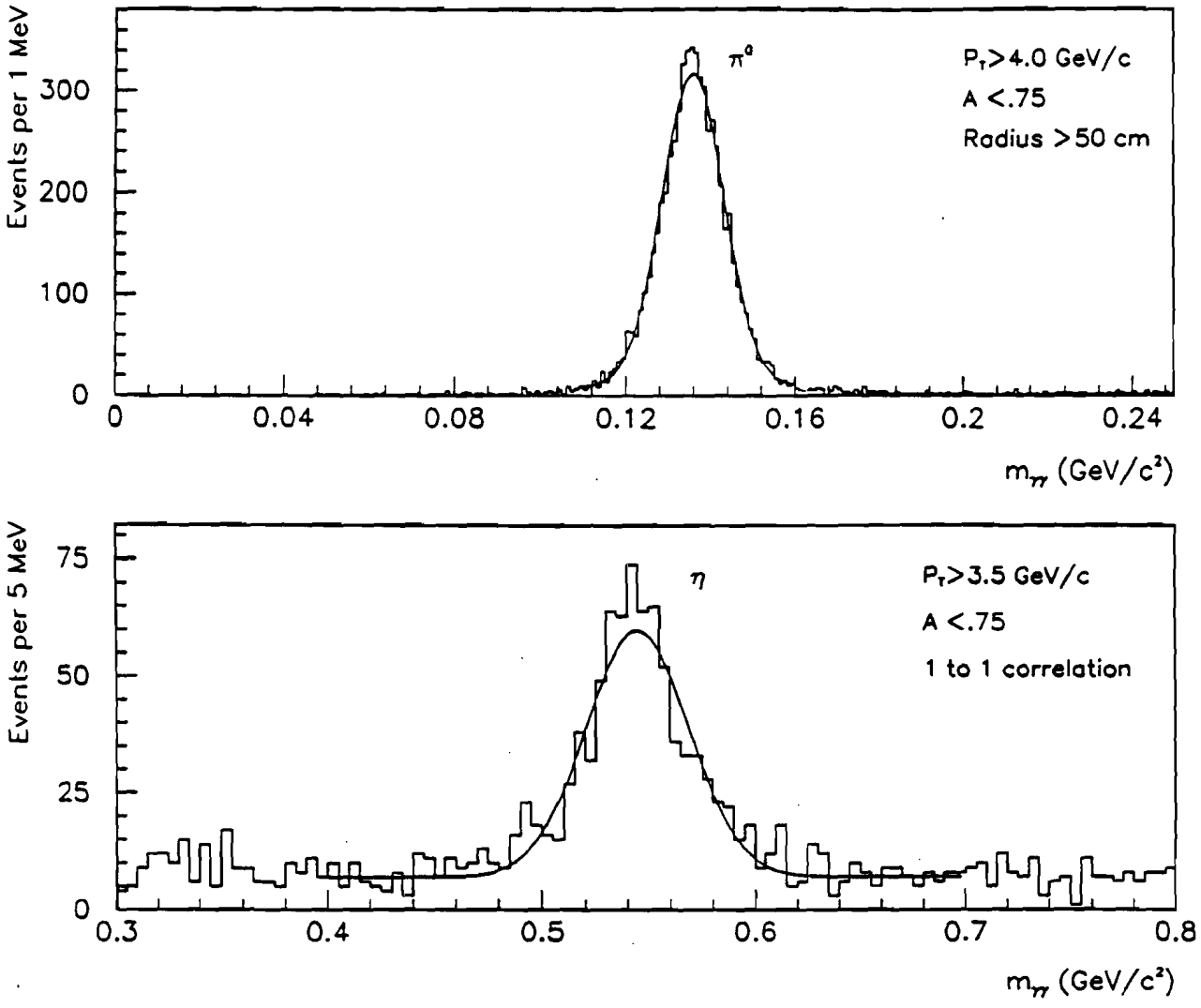

Figure 5.34: π^0 and η mass plot obtained by using the earlier mentioned energy scale. The measured π^0 mass is 135.8$\pm$0.1 MeV/c^2 and η mass is 544.7$\pm$1.2 MeV/c^2.

photons are already well separated, no separation cut was applied. But an additional requirement was imposed that the photons which have one to one correlation are used. The measured η mass is 544.7$\pm$1.2 MeV/c^2. We see that the π^0 mass is 0.6% higher than the standard π^0 mass and η mass is 0.7% lower than the standard η mass. Figure 5.21 and 5.22 shows that our Monte Carlo analysis also reproduces the mean and the width for both π^0 and η, with and without an asymmetry cut of 0.75. The difference in π^0 and η mass from their standard values reflects on the uncertainty in the determination of our energy scale, which we estimate to be no larger than $\pm$0.9%.

6. Results

6.1 Direct Photon Cross Section

The direct photon production cross section is evaluated by subtracting the background contribution from the unsubtracted direct photon cross section. Figure 6.1 shows the unsubtracted γ/π^0 ratio for π^-Be in the P_T range $3.5<P_T<10$ GeV/c integrated over rapidity $-0.7<y<0.7$. The background contribution to the γ/π^0 ratio as evaluated from the meson decays (π^0, η, η', ω, K^0_S) is shown by the curves. Although the figure shows that the major source of the background is π^0; η also contributes significantly to the background. Other neutral mesons (η', ω, and K^0_S) contribute to the background in a much smaller proportion. Even after background subtraction, a reasonable direct photon signal can be seen for all the P_T values. Figure 6.2 shows the unsubtracted γ/π^0 for π^-Be in the P_T range $3.5<P_T<10$ GeV/c divided into three rapidity regions $-0.7<y<-0.2$, $-0.2<y<0.2$ and $0.2<y<0.7$. Figure 6.3 shows the inclusive invariant cross section per nucleon for $\pi^- + Be \rightarrow \gamma + X$ in the P_T range $3.5<P_T<10$ GeV/c integrated over rapidity range $-0.7<y<0.7$. Figure 6.4 shows the inclusive invariant cross section per nucleon for $\pi^- + Be \rightarrow \gamma + X$ in the P_T range $3.5<P_T<10$ GeV/c integrated over rapidity regions $-0.7<y<-0.2$, $-0.2<y<0.2$ and $0.2<y<0.7$ respectively. Figure 6.5 and 6.6 shows the γ/π^0 value and the cross section respectively for π^-Be in the rapidity range $-0.7<y<0.7$ integrated over the P_T range $4<P_T<8$ GeV/c.

Figures 6.7 and 6.8, show respectively the unsubtracted γ/π^0 ratio for pBe interactions in the P_T range $4<P_T<8$ GeV/c integrated over rapidity $-0.7<y<0.7$ and also in three rapidity regions $-0.7<y<-0.2$, $-0.2<y<0.2$ and $0.2<y<0.7$. Figures 6.9 and 6.10 shows the direct photon cross section for pBe collisions as a function of P_T in different rapidity ranges. Figures 6.11 and 6.12 show respectively the γ/π^0 ratio and the invariant cross-section for pBe interactions as a function of rapidity integrated over the P_T range $4<P_T<8$ GeV/c.

The γ/π^0 ratio rises with increasing P_T. As the direct photons are produced in the parton-parton interaction and the π^0's are the product of parton fragmentation,

one would expect the γ/π^0 ratio to increase with P_T. For pBe data there is also a rising trend, but statistics are limited at the higher P_T. The sharper rising trend in the γ/π^0 for π^-Be data compared to the pBe data can be explained because the annihilation term dominates at higher P_T in π^-Be data and also the fractional momentum carried by the individual valence constituents in π^- beam is larger compared to that in the proton beam for the same incident beam energy.

Table 6.1 gives the inclusive direct photon cross section per nucleon in P_T bins for π^-Be and pBe interactions, integrated over rapidity -0.7<y<0.7. Tables 6.2 and 6.3, present the respective cross sections in P_T bins for π^-Be and pBe interactions for rapidity ranges -0.7<y<-0.2, -0.2<y<0.2 and 0.2<y<0.7. Table 6.4 presents the cross sections in rapidity for π^-Be and pBe integrated over $4<P_T<8$ GeV/c.

P_T range (GeV/c)	π^-+Be$\rightarrow\gamma$+X (pb/GeV^2)	p+Be$\rightarrow\gamma$+X (pb/GeV^2)
3.50 to 3.75	617.9±136.4	—
3.75 to 4.00	308.9±86.1	—
4.00 to 4.25	258.3±38.7	187.6±29.6
4.25 to 4.50	95.2±25.0	105.3±19.8
4.50 to 4.75	127.3±15.4	66.0±10.7
4.75 to 5.00	53.1±10.1	35.4±7.2
5.00 to 5.50	33.2±4.8	7.4±2.7
5.50 to 6.00	14.5±2.6	6.2±1.6
6.00 to 7.00	5.1±0.9	1.4±0.4
7.00 to 8.00	0.36±0.22	0.039±0.079
8.00 to 10.00	0.174±0.091	0.005±0.019

Table 6.1: Direct photon cross sections per nucleon for π^-Be and pBe collisions integrated over rapidity -0.7<y<0.7. The background due to meson decays has been subtracted.

P_T range (GeV/c)	π^-+Be$\rightarrow\gamma$+X (pb/GeV^2) -0.7<y<-0.2	π^-+Be$\rightarrow\gamma$+X (pb/GeV^2) -0.2<y<0.2	π^-+Be$\rightarrow\gamma$+X (pb/GeV^2) 0.2<y<0.7
3.50 to 4.00	—	726.4±147.0	580.7±124.5
4.00 to 4.50	210.6±43.6	234.7±43.7	101.0±33.2
4.50 to 5.00	82.0±16.2	123.5±18.3	73.6±13.9
5.00 to 5.50	29.7±8.3	46.9±9.5	26.8±7.2
5.50 to 6.00	12.6±4.3	21.8±5.5	10.9±4.1
6.00 to 7.00	4.3±1.4	6.2±1.8	5.1±1.4
7.00 to 10.00	0.32±0.17	0.25±0.18	0.17±0.15

Table 6.2: Direct photon cross sections per nucleon for π^-Be collisions for rapidity ranges -0.7<y<-0.2, -0.2<y<0.2 and 0.2<y<0.7. The background due to meson decays has been subtracted.

P_T range (GeV/c)	p+Be$\rightarrow\gamma$+X (pb/GeV^2) -0.7<y<-0.2	p+Be$\rightarrow\gamma$+X (pb/GeV^2) -0.2<y<0.2	p+Be$\rightarrow\gamma$+X (pb/GeV^2) 0.2<y<0.7
4.00 to 4.50	130.2±34.8	168.1±33.7	130.7±24.9
4.50 to 5.00	51.6±12.1	69.1±12.3	34.2±9.2
5.00 to 6.00	6.00±2.7	7.3±3.1	7.5±2.4
6.00 to 7.00	1.00±0.66	2.51±0.96	0.84±0.67
7.00 to 10.00	0.091±0.079	—	—

Table 6.3: Direct photon cross sections per nucleon for pBe collisions for rapidity ranges -0.7<y<-0.2, -0.2<y<0.2 and 0.2<y<0.7. The background due to meson decays has been subtracted.

Rapidity range	π^-+Be$\rightarrow\gamma$+X (pb/GeV^2)	p+Be$\rightarrow\gamma$+X (pb/GeV^2)
-0.7 to -0.5	40.7±8.4	18.8±6.7
-0.5 to -0.3	46.9±10.1	36.9±8.0
-0.3 to -0.1	47.9±8.8	29.4±6.7
-0.1 to 0.1	44.7±9.1	29.3±6.7
0.1 to 0.3	56.1±8.1	33.1±6.1
0.3 to 0.5	39.1±7.4	27.0±5.5
0.5 to 0.7	29.0±6.6	18.6±4.3

Table 6.4: Direct photon cross sections per nucleon for π^-Be and pBe collisions integrated over the P_T range $4<P_T<8$ GeV/c. The background due to meson decays has been subtracted.

6.2 Systematic Uncertainties

The uncertainties quoted in the cross sections, in Tables 6.1 through 6.4 are statistical only. Contributions due to systematic uncertainties are discussed below.

As mentioned in the previous chapter, the uncertainty in the energy scale is ±0.9%. This uncertainty in the energy scale leads to a systematic uncertainty of the order of 8∼9% in the measured cross section.

The energy loss correction applied to the photons was based on Monte Carlo studies for the energy loss for electrons. Also a zero mass pair like correction was studied[81] assuming additional material in the detector (for example argon leakage into the excluder vessel). The total systematic uncertainty to the cross section from these effects was found to be of the order 10%.

To evaluate sensitivity to the trigger corrections, the cross section was compared for data sets with different trigger thresholds. Also the trigger thresholds and widths used in the calculation of trigger efficiency corrections (from turn-on fits) were varied by one standard deviation and the results were compared to the standard result.

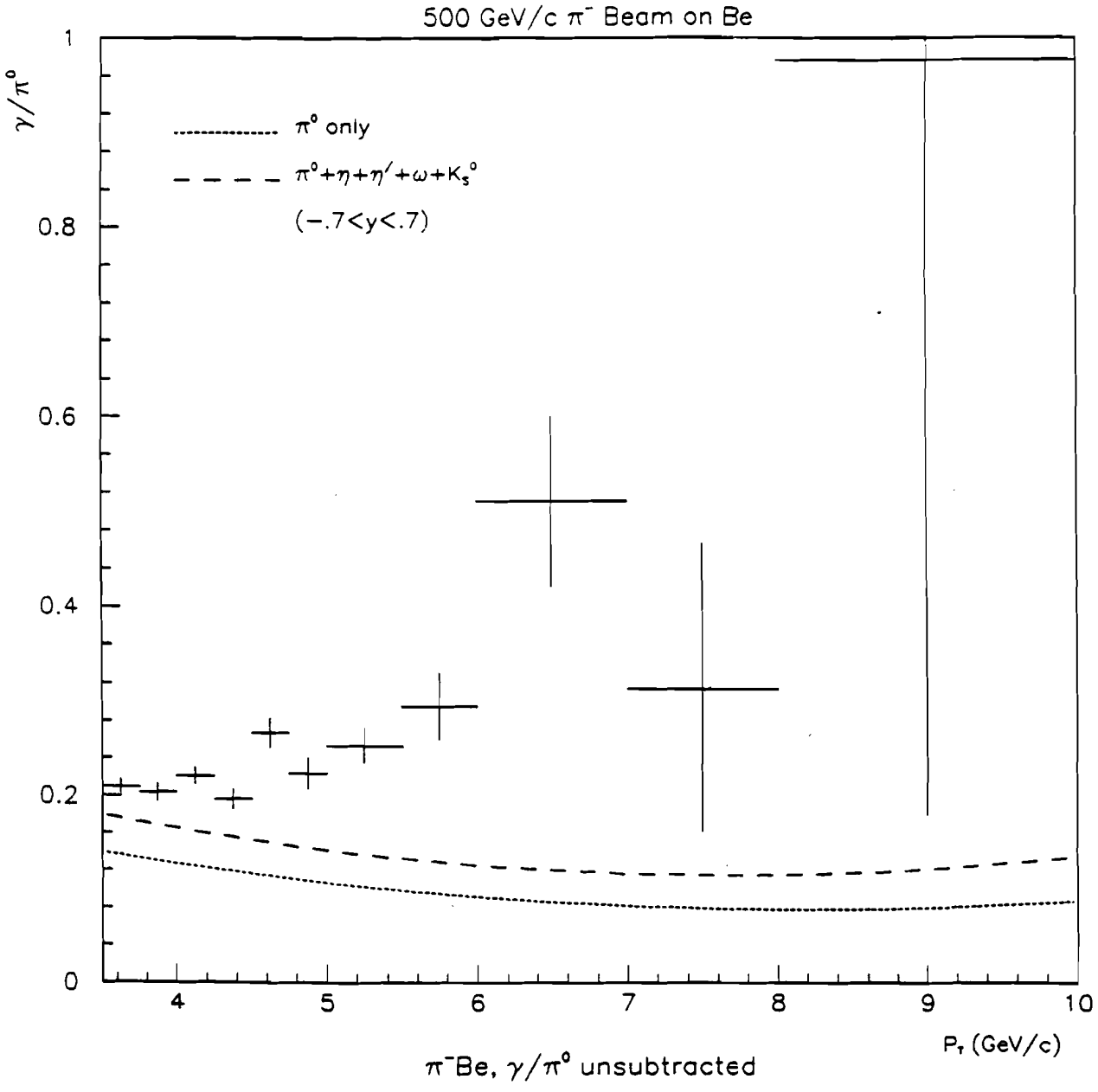

Figure 6.1: The unsubtracted ratio of direct photon production cross section to π^0 cross section for π^-Be collisions at 500 GeV/c in the P_T range $3.5<P_T<10$ GeV/c integrated over the rapidity range $-0.7<y<0.7$. The background contribution from π^0 and $\pi^0+\eta+\eta'+\omega+K^0_S$ decays are shown separately by dashed curves.

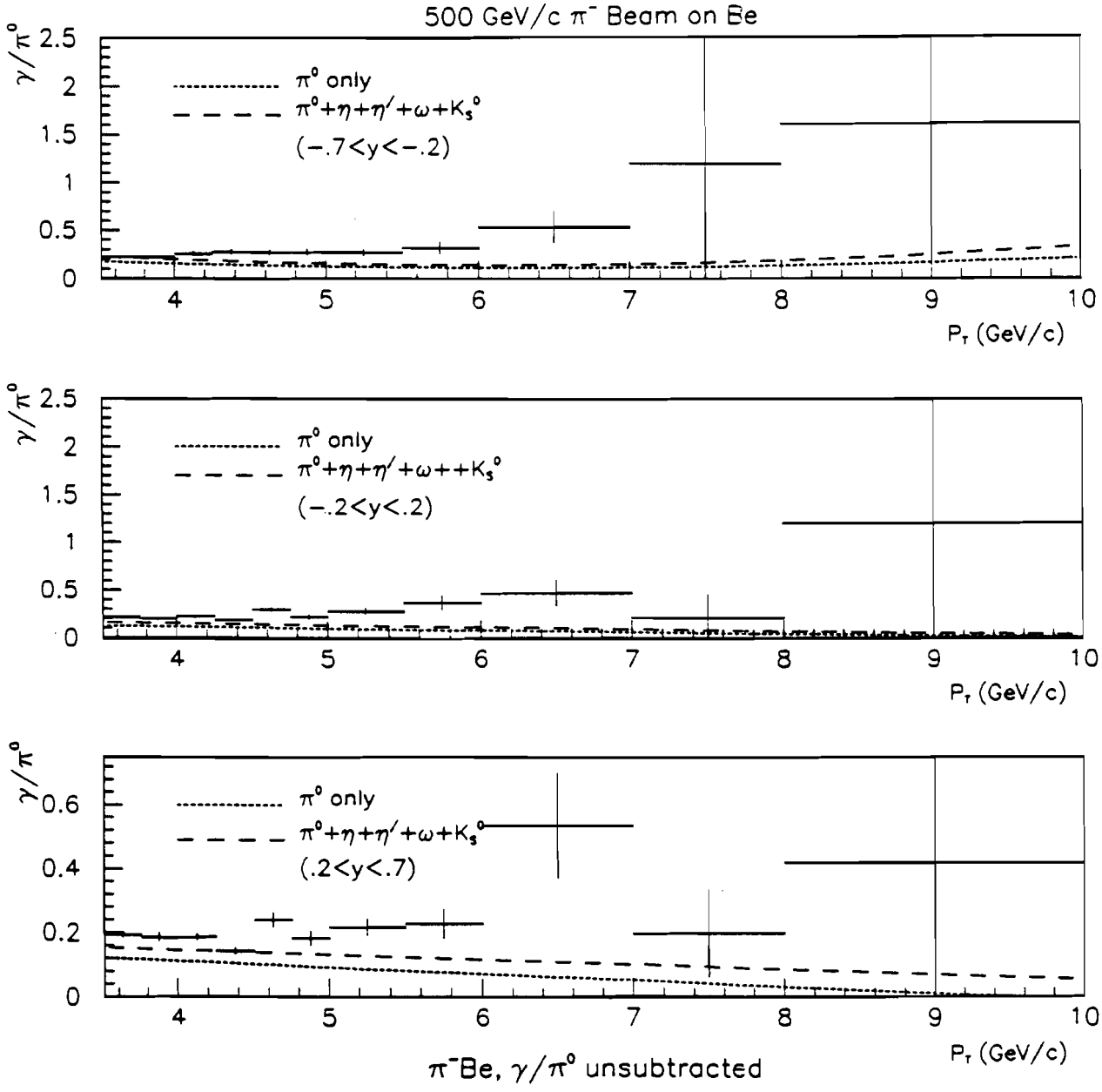

Figure 6.2: The unsubtracted ratio of direct photon production cross section to π^0 cross section for π^-Be collisions at 500 GeV/c in the P_T range $3.5<P_T<10$ GeV/c integrated over rapidity ranges $-0.7<y<-0.2$, $-0.2<y<0.2$ and $0.2<y<0.7$. The background contribution from π^0 and $\pi^0+\eta+\eta'+\omega+K^0_S$ decays are shown separately by dashed curves.

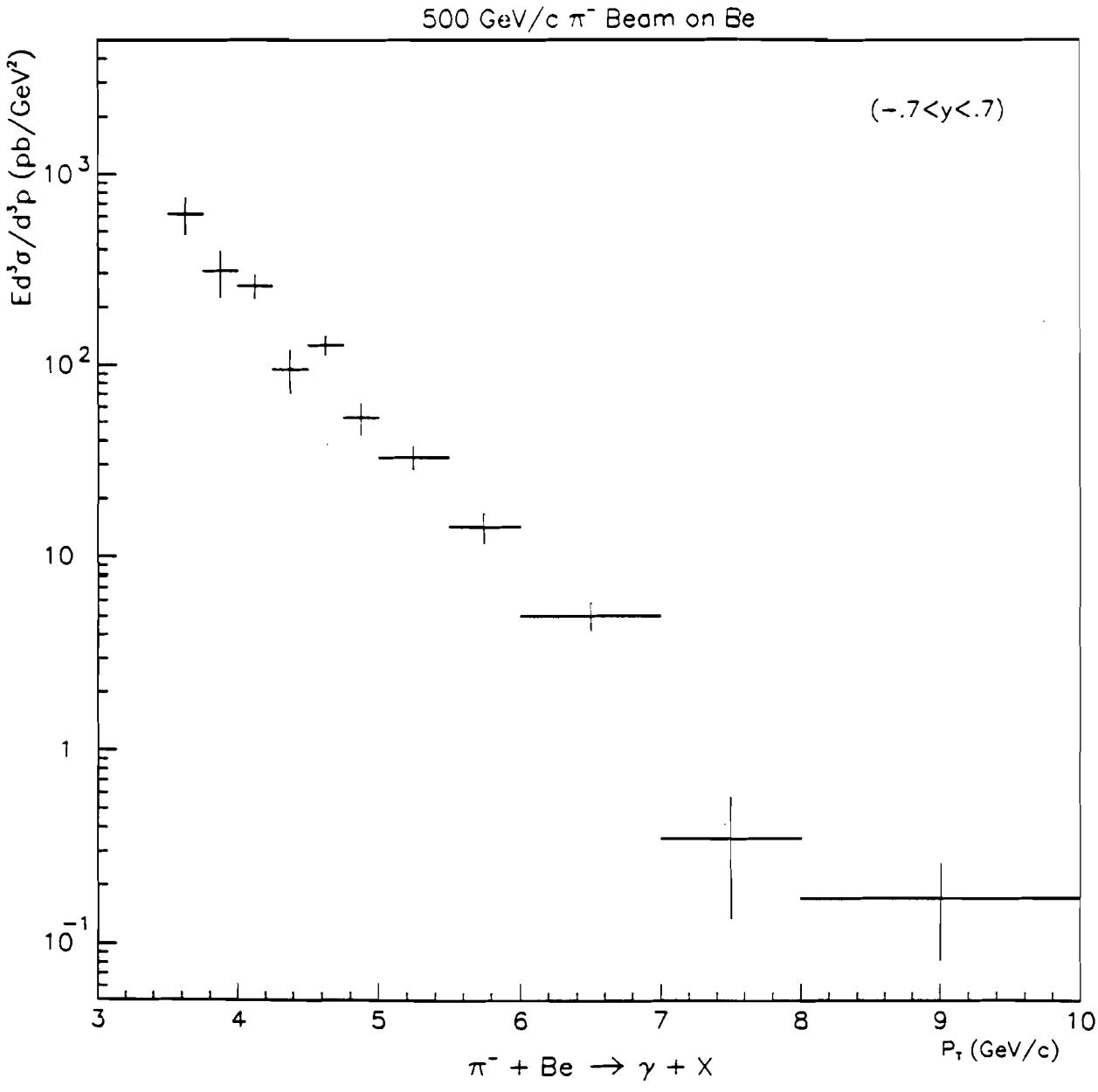

Figure 6.3: Direct photon inclusive invariant cross section per nucleon for π^-Be collisions at 500 GeV/c in the P_T range $3.5<P_T<10$ GeV/c integrated over the rapidity range $-0.7<y<0.7$.

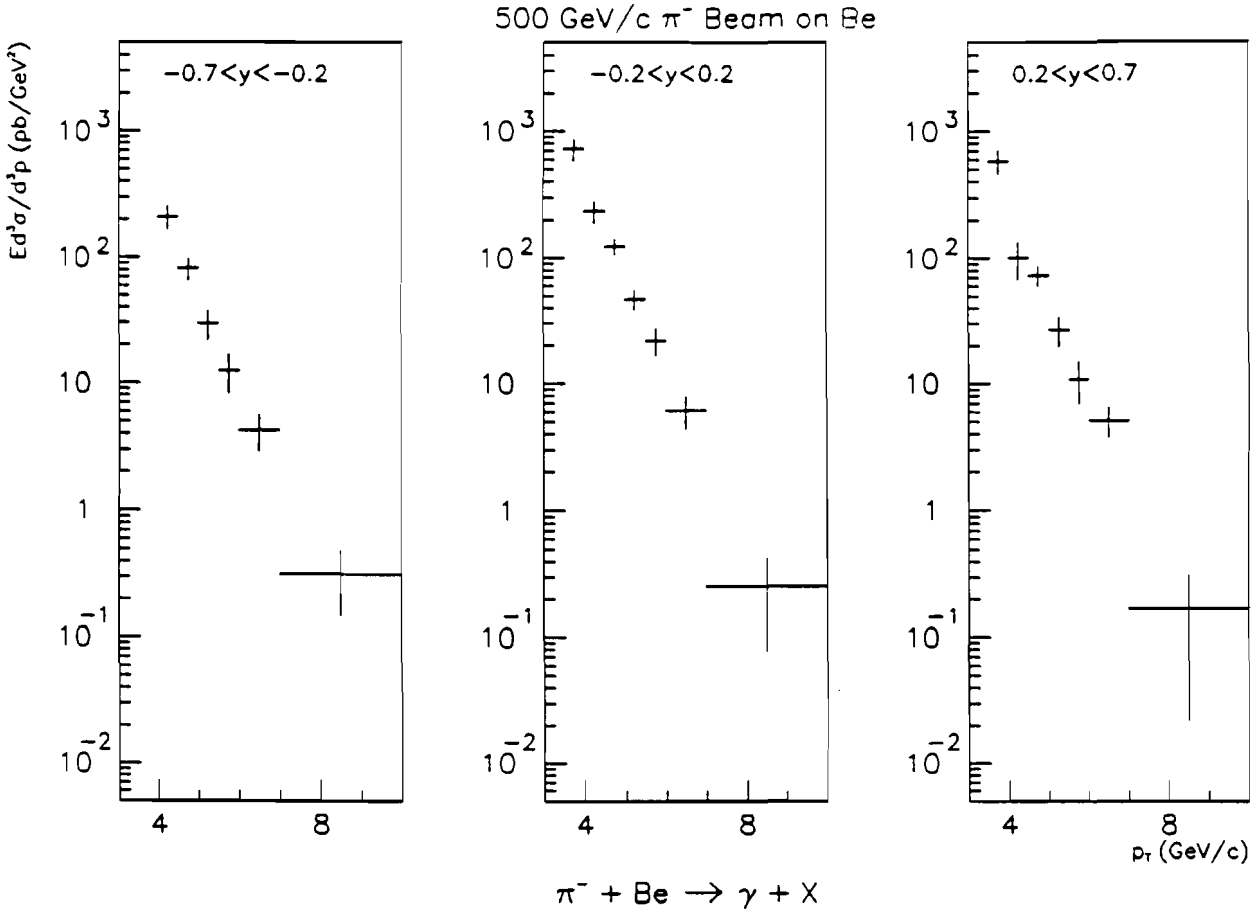

Figure 6.4: Direct photon inclusive invariant cross section per nucleon for π^-Be collisions at 500 GeV/c in the P_T range $3.5<P_T<10$ GeV/c integrated over rapidity $-0.7<y<-0.2$, $-0.2<y<0.2$ and $0.2<y<0.7$.

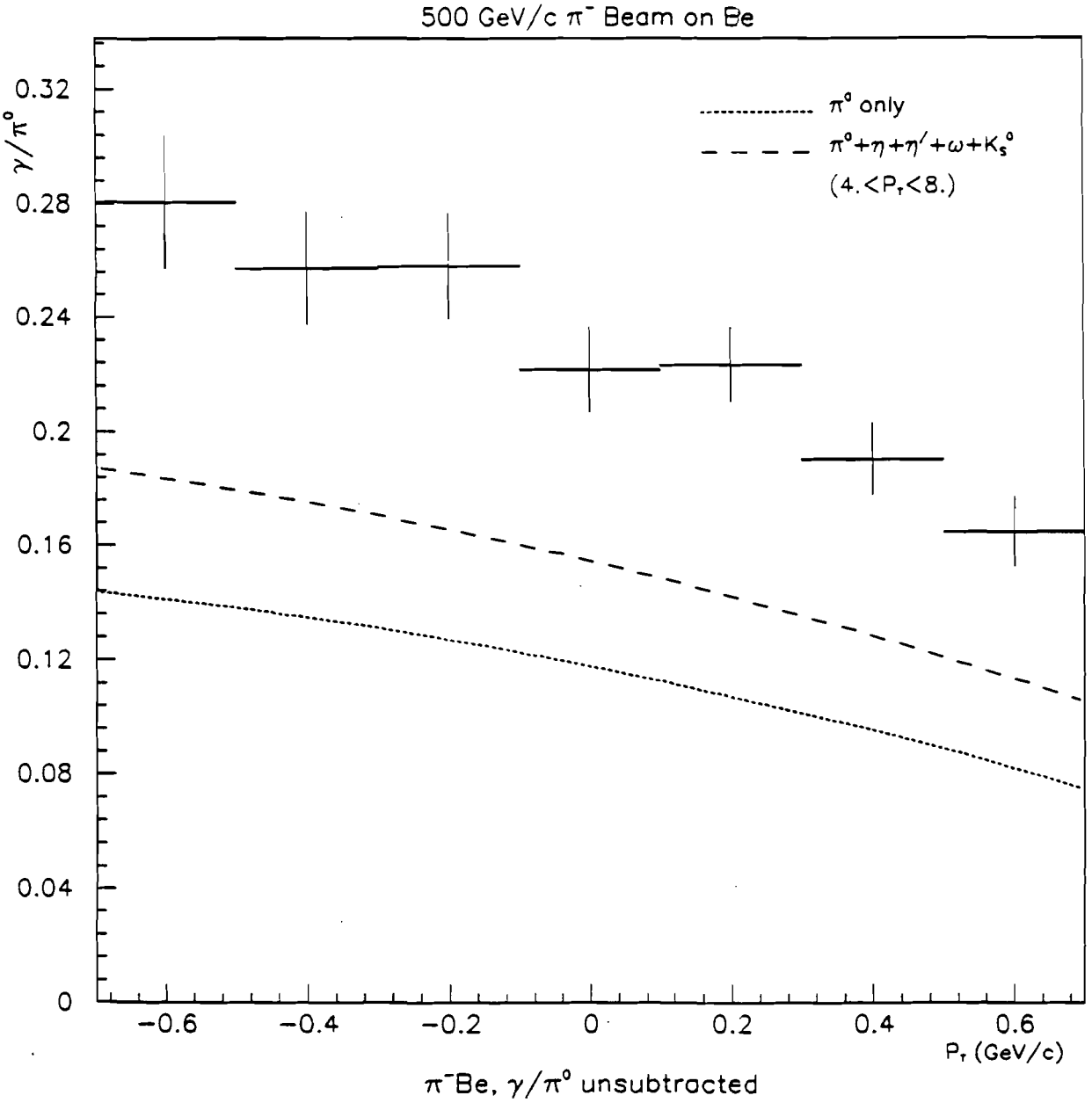

Figure 6.5: The unsubtracted ratio of direct photon production cross section to π^0 cross section for π^-Be collisions at 500 GeV/c in rapidity range -0.7<y<0.7 integrated over $4<P_T<8$ GeV/c. The background contribution from π^0 and $\pi^0+\eta+\eta'+\omega+K^0_S$ decays are shown separately by dashed curves.

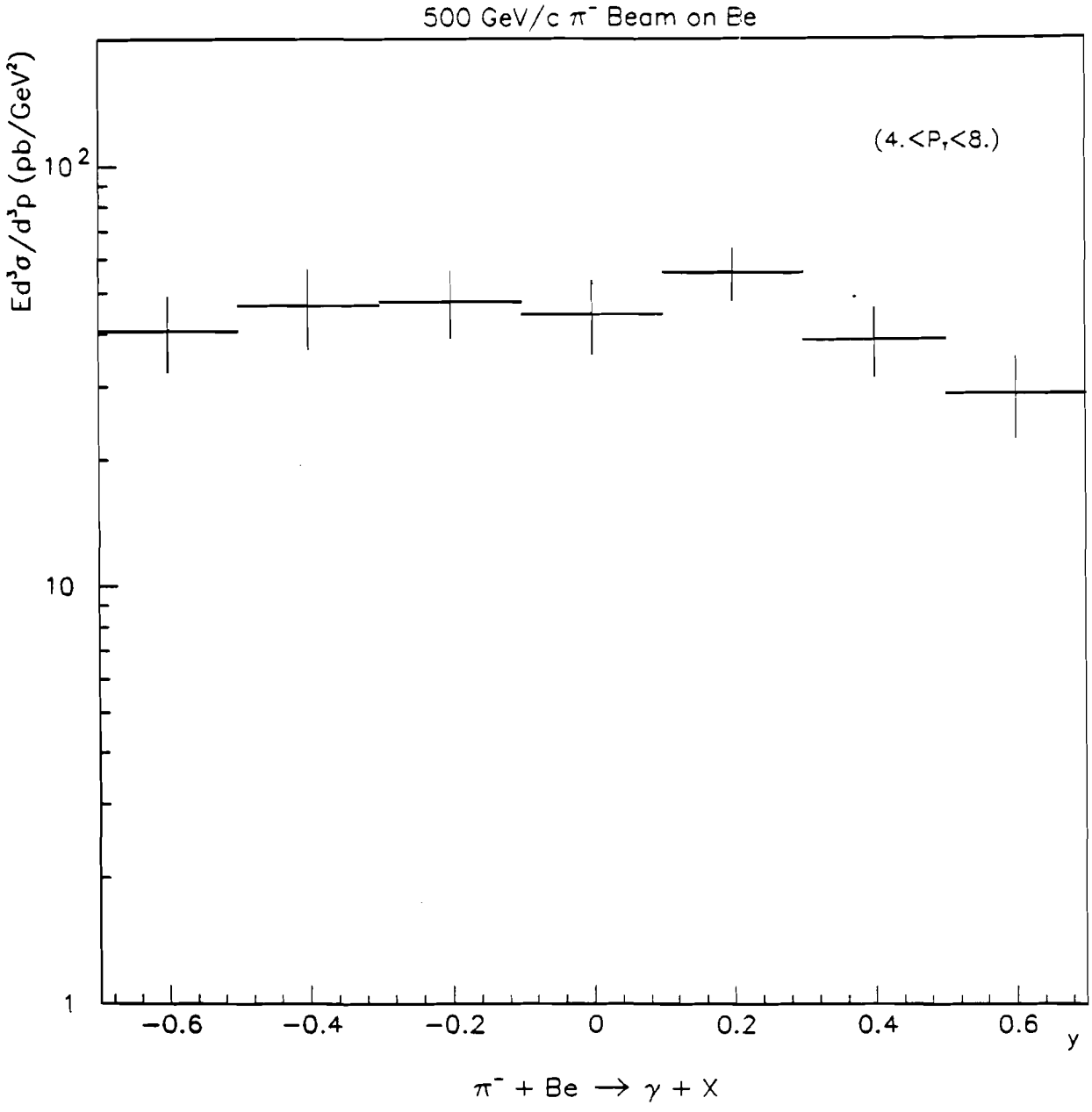

Figure 6.6: Direct photon inclusive invariant cross section per nucleon for π^-Be collisions at 500 GeV/c in the rapidity range -0.7<y<0.7 integrated over $4<P_T<8$ GeV/c.

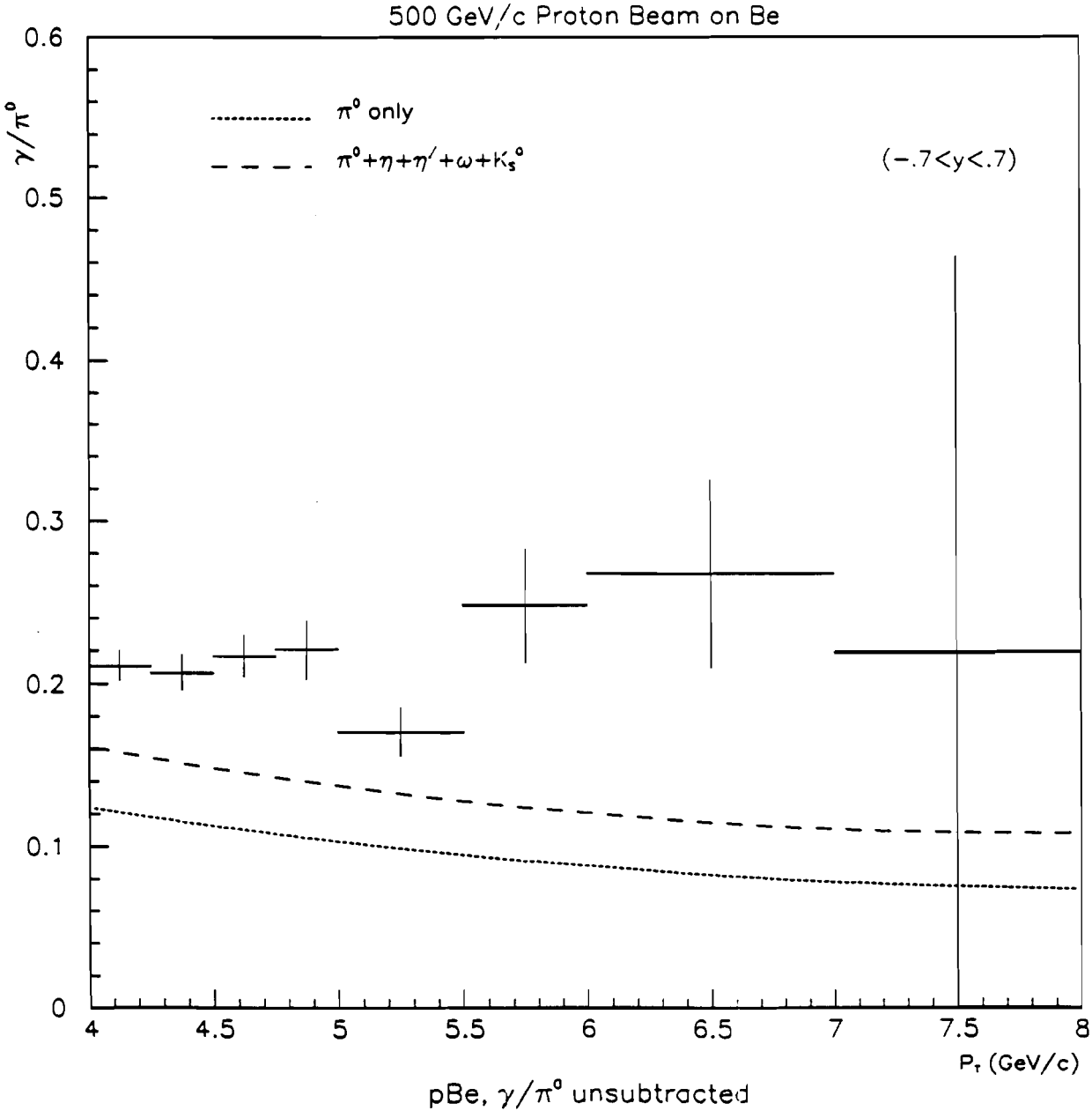

Figure 6.7: The unsubtracted ratio of direct photon production cross section to π^0 cross section for pBe collisions at 500 GeV/c in the P_T range $4<P_T<8$ GeV/c integrated over rapidity range $-0.7<y<0.7$. The background contribution from π^0 and $\pi^0+\eta+\eta'+\omega+K^0_S$ decays are shown separately by dashed curves.

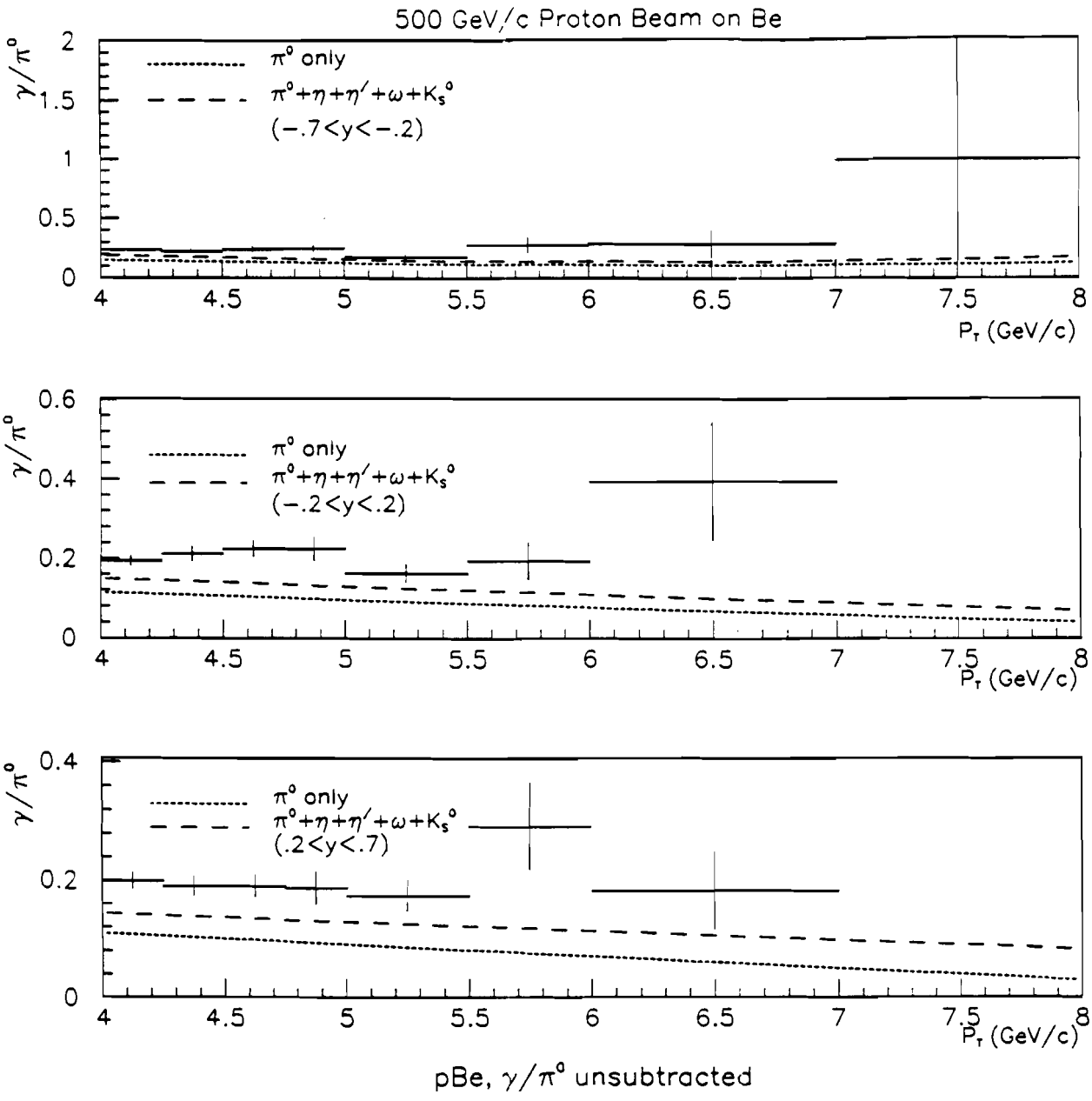

Figure 6.8: The unsubtracted ratio of direct photon production cross section to π^0 cross section for pBe collisions at 500 GeV/c in the P_T range $4<P_T<8$ GeV/c integrated in rapidity regions $-0.7<y<-0.2$, $-0.2<y<0.2$ and $0.2<y<0.7$. The background contribution from π^0 and $\pi^0+\eta+\eta'+\omega+K_S^0$ decays are shown separately by dashed curves.

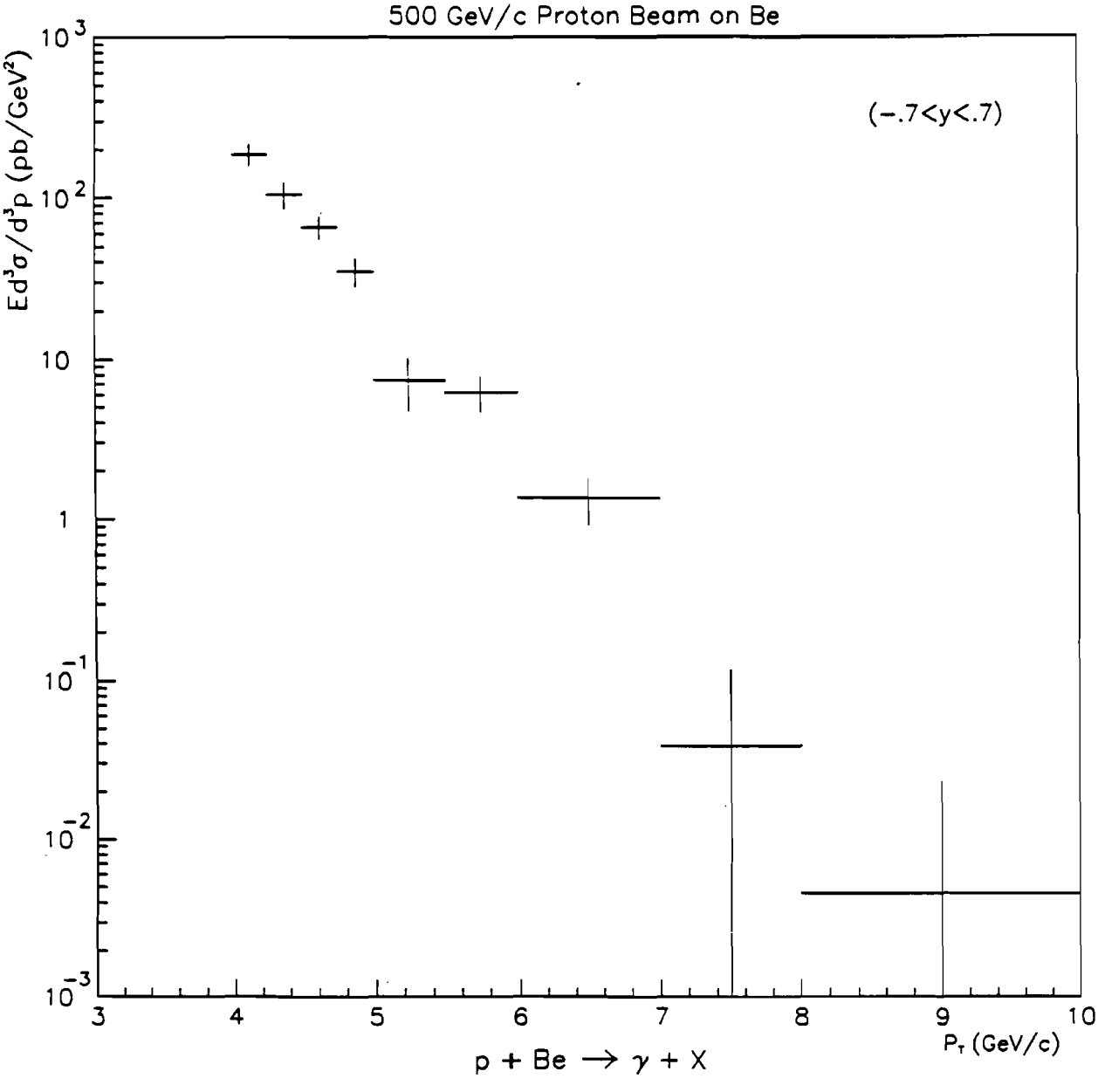

Figure 6.9: Direct photon inclusive invariant cross section per nucleon for pBe collisions at 500 GeV/c in the P_T range $4<P_T<8$ GeV/c integrated over the rapidity range $-0.7<y<0.7$.

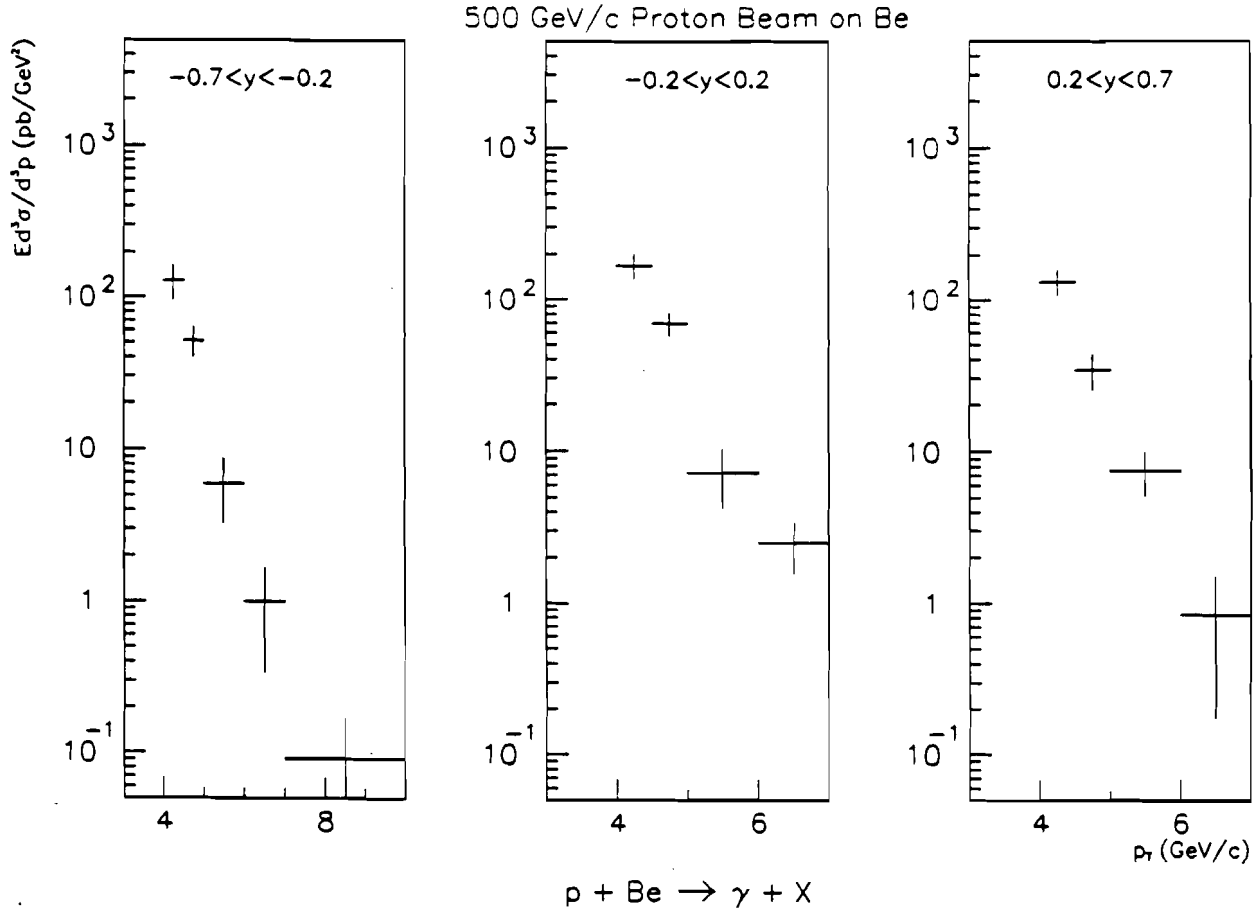

Figure 6.10: Direct photon inclusive invariant cross section per nucleon for pBe collisions at 500 GeV/c in the P_T range $4<P_T<8$ GeV/c integrated over rapidity ranges $-0.7<y<-0.2$, $-0.2<y<0.2$ and $0.2<y<0.7$.

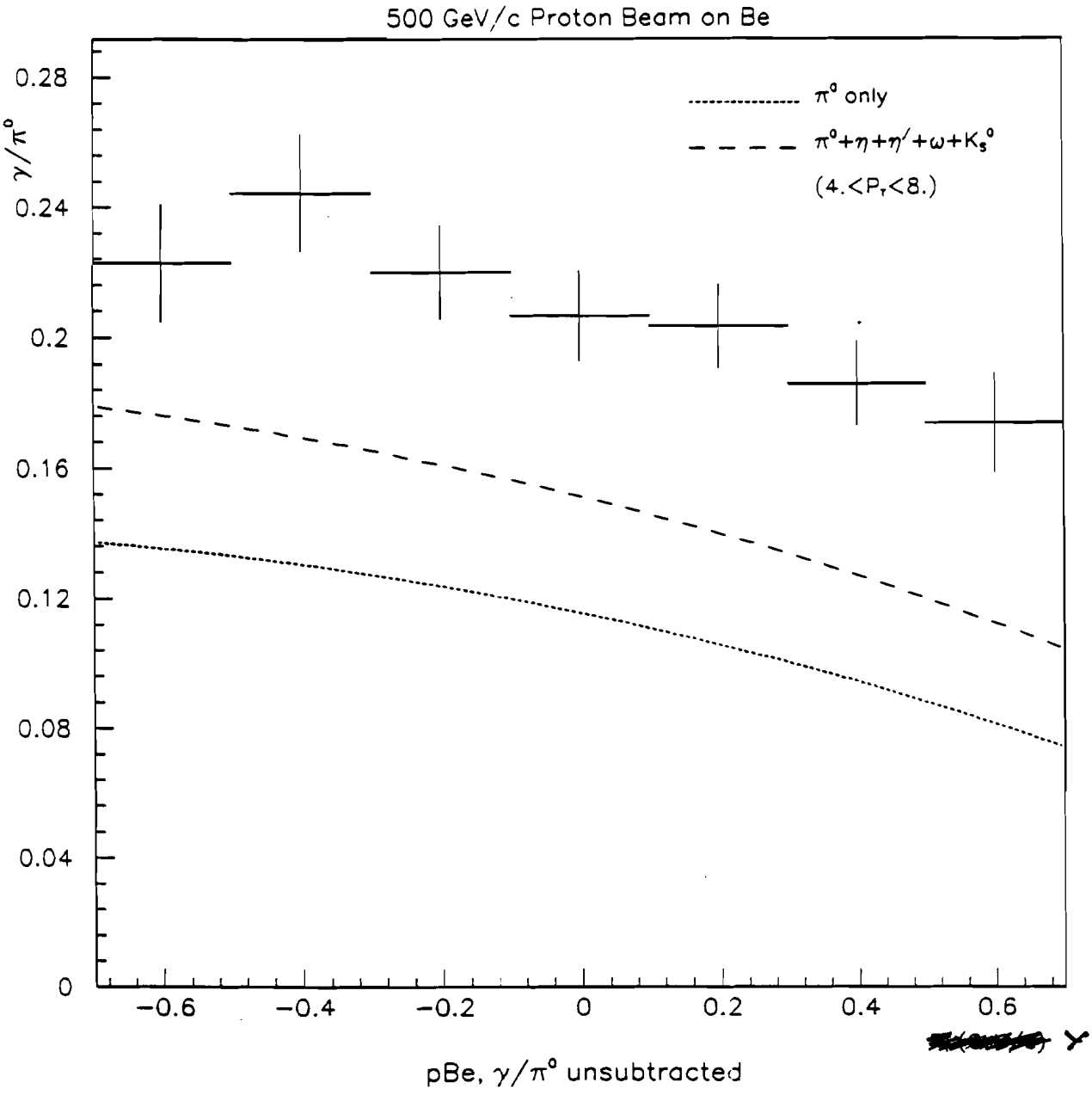

Figure 6.11: The unsubtracted ratio of direct photon production cross section to π^0 cross section for pBe collisions at 500 GeV/c in the rapidity range -0.7<y<0.7 integrated over $4<P_T<8$ GeV/c. The background contribution from π^0 and $\pi^0+\eta+\eta'+\omega+K_S^0$ decays are shown separately by dashed curves.

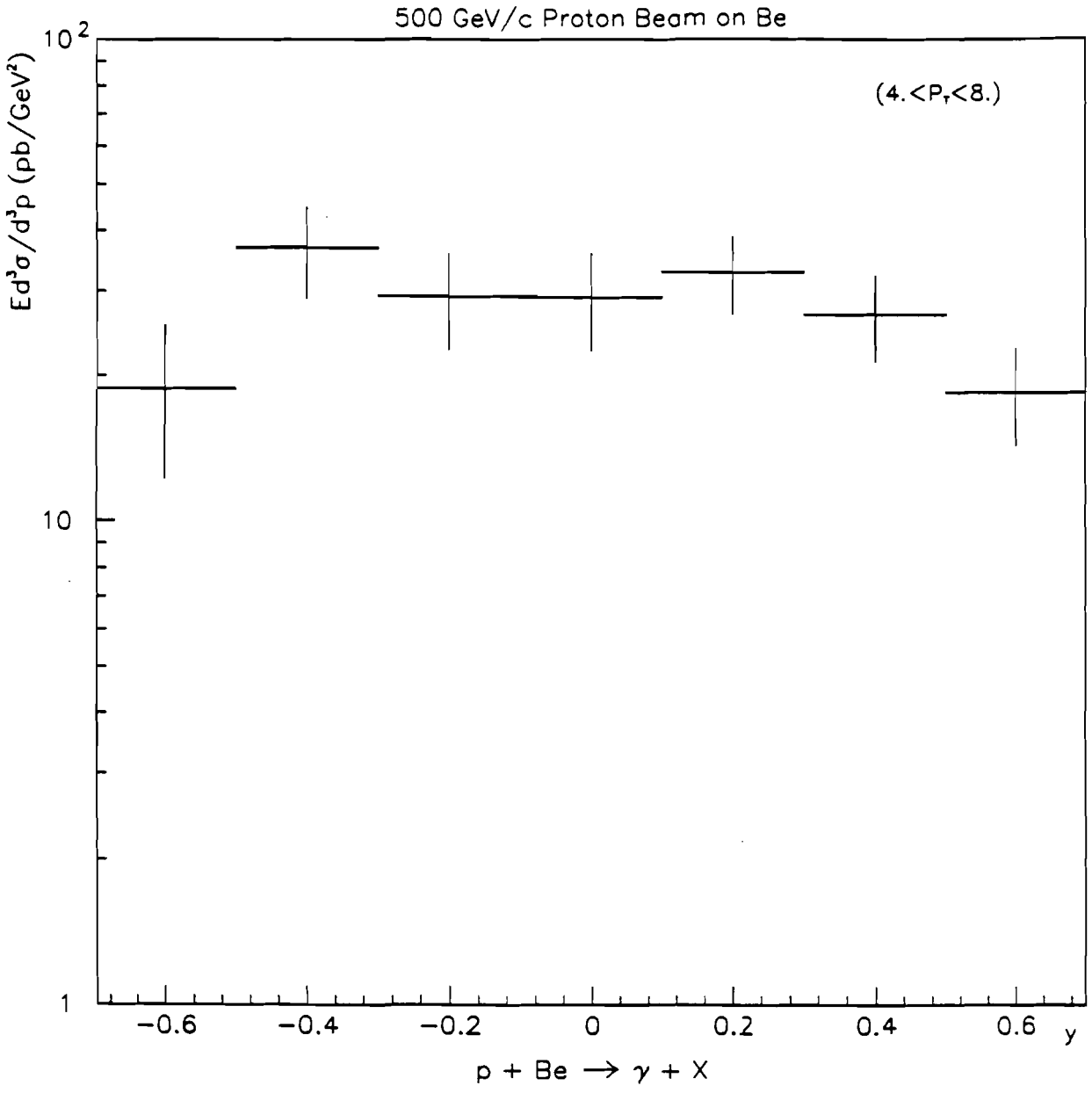

Figure 6.12: Direct photon inclusive invariant cross section per nucleon for pBe collisions at 500 GeV/c in the rapidity range -0.7<y<0.7 integrated over $4<P_T<8$ GeV/c.

Uncertainty on pretrigger efficiency was also estimated. The overall uncertainty for trigger correction was estimated to be 10% at P_T of 4 GeV/c diminishing to 2% at P_T of 8 GeV/c.

Proper background subtraction is very important for the direct photon cross section evaluation. The sensitivity of the background subtraction (γ/π^0 ratio) in the Monte Carlo was studied by changing some parameter values. The energy resolution of the EMLAC was changed from $16\%/\sqrt{E}$ to $15\%/\sqrt{E}$ and the gain term was changed from 2.2% to 2.0%. The effect of cross-talk between the amplifiers were reduced and the zero suppression value for each channel was changed by one standard deviation. This led to a 2.3% change in the γ/π^0 value. Using this combined effect of Monte Carlo parameter variation, we estimate this contribution to systematic uncertainty on cross section to be 8.5% at 4 GeV/c P_T and 2% at 8 GeV/c P_T.

A one standard deviation uncertainty on γ/π^0 fit, using the uncertainty on the fit parameters and covariance matrix gave a systematic uncertainty of 5% at P_T of 4 GeV/c and 1.5% at P_T of 8 GeV/c. The uncertainty in the η production rate of $45\pm4\%$ relative to the π^0 production rate (for studying background to direct photon sample from η and π^0) gave a systematic uncertainty of 10% at 4 GeV/c P_T and 2% at 8 GeV/c P_T. The uncertainty due to the difference between data and Monte Carlo in the tail part of the π^0 mass distribution led to a systematic uncertainty in the cross section of 5% at P_T of 4 GeV/c and 1.5% at P_T of 8 GeV/c.

Uncertainties were also estimated for veto wall, vertex, timing, directionality, track cut and one photon conversion. The combined systematic uncertainty introduced due to these effects was 1.5% at the lower end of the P_T spectrum and 0.5% at the higher end of the P_T spectrum. The residual muon contamination was found to be negligible.

The overall systematic uncertainty when added in quadrature was 25% at the lower end of the P_T (4 GeV/c) spectrum and 15% at the higher end of the P_T (8 GeV/c) spectrum.

The direct photon cross section was evaluated using two methods. In the first

method, it was required that the direct photon candidate should not form a $\gamma\gamma$ pair in the π^0 mass band with asymmetry<0.75. In the second method it was required that the direct photon candidate should not form a $\gamma\gamma$ pair in a wider π^0 mass band (100-170 MeV) with any asymmetry. Monte Carlo events were processed with both the requirements to evaluate the backgrounds. In addition, in both the methods direct photon candidates were not allowed to form a $\gamma\gamma$ combination in the η mass band with A<0.75. The cross section determined by the second method compared to the first one was found to be 1% higher for the negative data and 19% higher for the positive data. As the cross section presented in this thesis are based upon the second method only, the difference in the measured cross section between these two methods will add an additional 10% systematic error.

6.3 Nuclear Dependence Result

As the statistics available for the copper data was an order of magnitude less than the data available on the beryllium target, the nuclear dependence was studied for π^- beam in the P_T range $4<P_T<7$ GeV/c and for proton beam in the P_T range $4<P_T<8$ GeV/c integrated over the rapidity -0.7<y<0.7. Assuming a scaling for the cross section per nucleus of the form A^α, the ratio of the cross section per nucleus for the targets Cu and Be will be given as

$$\frac{\sigma_{\mathrm{Cu}}}{\sigma_{\mathrm{Be}}} = \left(\frac{A_{\mathrm{Cu}}}{A_{\mathrm{Be}}}\right)^{\alpha} \tag{6.1}$$

where σ_{Cu} and σ_{Be} is the cross section per nucleus for target Cu and Be and A_{Cu} and A_{Be} are the atomic numbers of Cu and Be. α can be evaluated from the cross section per nucleon by

$$\alpha = \frac{\log(\sigma_{\mathrm{Cu}}^{nucleon}/\sigma_{\mathrm{Be}}^{nucleon})}{\log(A_{\mathrm{Cu}}/A_{\mathrm{Be}})} + 1 \tag{6.2}$$

where $\sigma_{\mathrm{Cu}}^{nucleon}$ and $\sigma_{\mathrm{Be}}^{nucleon}$ is the cross section per nucleon for Cu and Be targets. The ratio of the cross sections per nucleon for copper compared to beryllium was

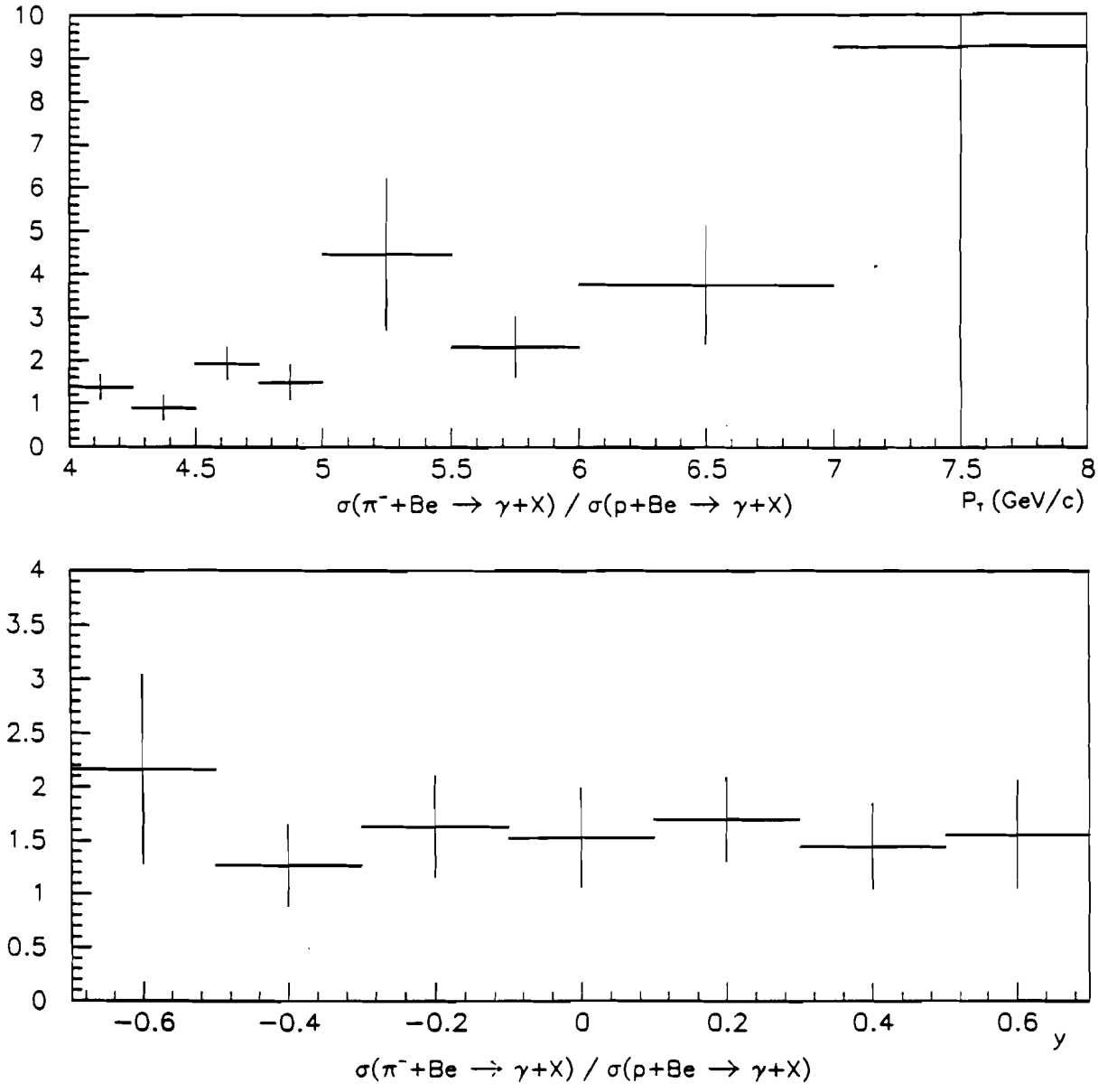

Figure 6.13: The ratio of direct photon production cross section for π^-Be to pBe interactions as a function of P_T and rapidity.

Rapidity	$\frac{\pi^- + Be \to \gamma + X}{p + Be \to \gamma + X}$
-0.7 to -0.5	2.16 ± 0.88
-0.5 to -0.3	1.27 ± 0.39
-0.3 to -0.1	1.63 ± 0.48
-0.1 to 0.1	1.53 ± 0.47
0.1 to 0.3	1.70 ± 0.40
0.3 to 0.5	1.45 ± 0.40
0.5 to 0.7	1.56 ± 0.50

Table 6.5: Ratio of direct photon production cross section for π^- and proton beam in different rapidity bins.

P_T (GeV/c)	$\frac{\pi^- + Be \to \gamma + X}{p + Be \to \gamma + X}$
4.00 to 4.25	1.38±0.30
4.25 to 4.50	0.90±0.29
4.50 to 4.75	1.93±0.39
4.75 to 5.00	1.50±0.42
5.00 to 5.50	4.5±1.8
5.50 to 6.00	2.32±0.72
6.00 to 7.00	3.76±1.37
7.00 to 8.00	9.3±19.7
8.00 to 10.00	37.9±155.1

Table 6.6: Ratio of direct photon production cross section for π^- and proton beam in different P_T bins.

E706 can be attributed to the higher center of mass energy. For positive data the E706 results falls between earlier fixed target experiments which have $\sqrt{S}$ around 20 GeV and the ISR collider experiments which have $\sqrt{S}$ around 60 GeV. Different

experiments also cover different rapidity region. At large P_T, E706 cross section fall faster than other experiments.

6.6 Comparison with QCD

The E706 results are also compared to the next-to-leading log ($O(\alpha\alpha_s^2)$) (NLL) direct photon cross section calculations. The momentum transfer Q^2, can be related to the transverse momentum P_T measured in the experiments as, Q = constant × P_T. The Q^2 scale can also be defined by the method of Principle of Minimum Sensitivity[82-85] (PMS). In the PMS method the factorization scale (M), which is used for the evaluation of the structure function, and the renormalization scale (μ), which is used in the argument of α_s, are chosen at each point such that the sensitivity of the result to the choice of the scale is minimized. If the calculation is carried to all orders it will predict a result insensitive to the choice of scale. As the calculation to all orders is not possible, the series is truncated, and it is required to satisfy the condition

$$\mu\frac{\partial\sigma}{\partial\mu} = 0 \quad and \quad M\frac{\partial\sigma}{\partial M} = 0$$

and μ and M are so chosen at every point that this condition is satisfied.

Figure 6.16 and 6.17 shows the comparison between the measured direct photon cross section per nucleon for π^- and proton on beryllium respectively for the rapidity range -0.7<y<0.7 and the theoretical predictions using Q = 0.5P_T and Q = P_T and Q obtained from the optimized PMS scale. The latest parametrization of Owens[86,87] for the nucleon structure functions, called Owens 1.1, use the value of Λ = 212 MeV. The theoretical predictions by Aurenche et al[88,89] for Q = 0.5P_T and Q = P_T and Q from the PMS scale, was estimated using the nucleon structure function sets of ABFOW[90] with Λ = 231 MeV and the pion structure functions of ABFKW[91] with Λ = 230 MeV. We see that Aurenche's parametrization with Q = 0.5P_T comes closer to data than Q = P_T for both π^- and proton. We also see that the data is closer to Q = 0.5P_T parametrization of Aurenche than that of the Owens 1.1 NLL QCD predictions with the same Q scale, except for high P_T where they are in

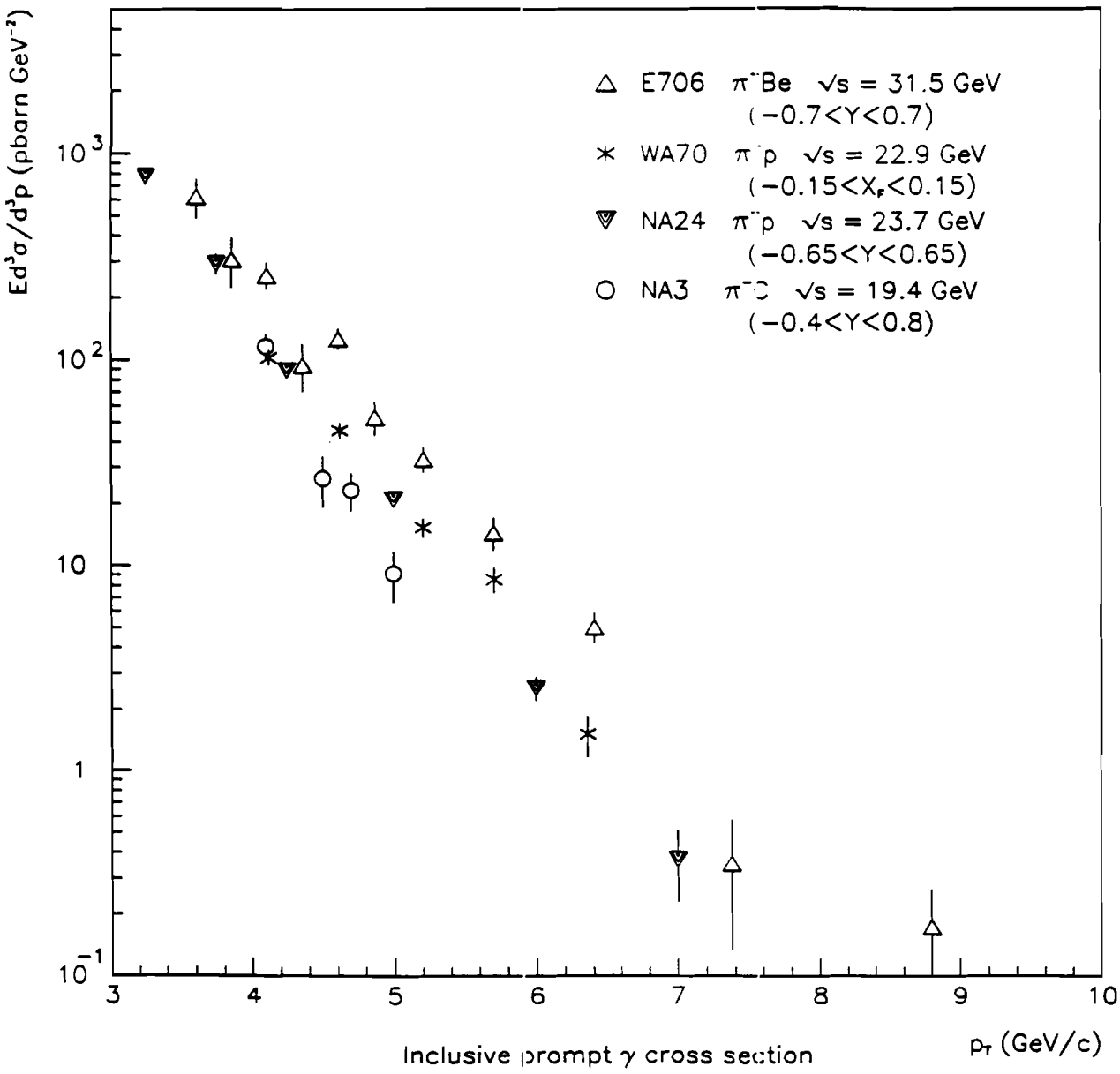

Figure 6.14: Direct photon inclusive invariant cross section per nucleon for π^- data for E706 compared with results from other experiments.

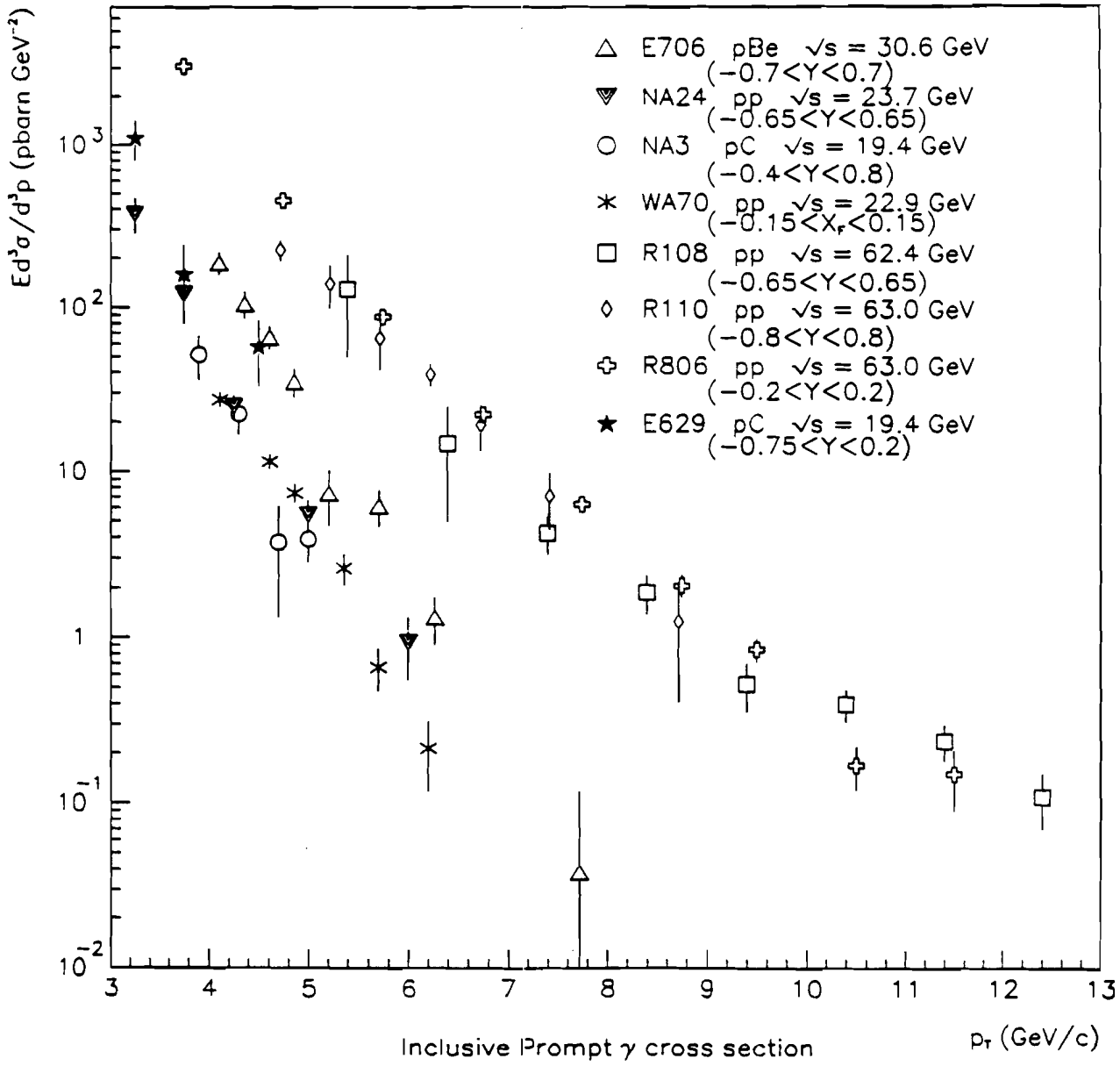

Figure 6.15: Direct photon inclusive invariant cross section per nucleon for proton data for E706 compared with results from other experiments.

agreement. Both these plots also show that the data points are consistently higher than the QCD curves for Q = $0.5P_T$ but agrees better with the PMS results.

Figure 6.18 shows the pBe data points compared to the PMS scale for several different η_G values in the gluon structure function $xG(x) \simeq (1-x)^{\eta_G}$ for protons. The value of Λ used in the structure function for η_G=3 is 248.5 MeV, for η_G=4 is 231.5 MeV and for η_G=5 is 221 MeV. We see that the data points compare well with the QCD predictions for η_G=3 at low P_T and for η_G=4 at high P_T. Using η_G=4 for protons and η_G=2 for pions in the gluon structure function, the π^-Be data is compared to the theoretical curves using Q = $0.5P_T$, Q = P_T and Q from the PMS scale of Aurenche et al. Figure 6.19 shows that the data points compare very well with the PMS scale.

Results for π^- and proton data were also compared with Owens 1.1 NLL predictions and Aurenche et al PMS results in three separate rapidity ranges of -0.7<y<-0.2, -0.2<y<0.2 and 0.2<y<0.7. The results for π^- and proton data are shown respectively in the figures 6.20 and 6.21. We see that the data agree well with the PMS predictions for all rapidity ranges. The data points are higher than the Owens 1.1 predictions for both the positive and the negative beam.

The data in separate rapidity ranges are also compared to calculations using Q = $0.5P_T$ and PMS scaling of Aurenche et al. Figures 6.22 and 6.23 show the data for π^- and proton compared to QCD results for both choices of scale. The agreement between data and QCD predictions at lower P_T is much better for the PMS scale compared to Q = $0.5P_T$ scale. At higher P_T (above 6 GeV/c) both the theoretical predictions, the PMS and the Q = $0.5P_T$ scale results are almost identical for π^- and very close to each other for proton data. From above comparisons one can conclude that in general the data agrees with the NLL theoretical predictions and the PMS results comes closest to the data.

Figures 6.24 and 6.25 show respectively the unsubtracted γ/π^0 ratio for π^-Be and pBe compared with the leading log γ/π^0 calculation from the theory. The theoretical calculation for both the γ and π^0 cross sections was based on the Owens Set 1.1 structure function. Also shown in both the diagrams are the background

expected from meson decays. The sum of the background and the QCD maps the data very well for both positive and negative beam. Figure 6.26 shows the ratio of the cross sections for direct photon production for π^-Be over pBe interactions. The result has been compared with leading log and next-to leading log QCD calculations using the momentum transfer scale of Q=0.5P_T and Owens Set 1.1 structure functions. The experimental result and the theory are consistent with each other.

6.7 Summary

The experiment has measured the direct photon production cross section per nucleon for π^-Be and pBe interactions for the P_T range 3.5<P_T<10 GeV/c and 4<P_T<10 GeV/c respectively in the rapidity interval -0.7<y<0.7. The γ/π^0 ratio was found to be of the order of 5% for the lower P_T values, rising slowly to a value of the about 1 at 9 GeV/c for π^- beam. For the proton beam, a rising trend in γ/π^0 ratio can also be seen with P_T (not as sharp as π^- data) but the statistics available at higher P_T are limited. The γ/π^0 ratio for π^-Be and pBe in P_T bins also agrees with the leading log QCD calculations using the scale Q = 0.5 P_T and Duke Owens Set 1.1 structure function.

Nuclear dependence of direct photon production was studied with beryllium and copper targets averaged over rapidity -0.7<y<0.7 and 4<P_T<7 GeV/c for π^- beam and 4<P_T<8 GeV/c for the proton beam. The ratio of the invariant cross section per nucleon for copper compared to beryllium was found to be 0.67$\pm$0.28 for π^- data and 0.87$\pm$0.25 for proton data. Assuming no P_T dependence and an atomic number dependence of the form A^α, α is 0.79$\pm$0.33 for the π^- data and 0.93$\pm$0.29 for the proton data. Within the limit of errors, these results are consistent with α=1.0, and consequently with a simple parton parton scattering.

The beam dependence of direct photon production was also studied. The ratio of the cross section for π^-Be to pBe which is around 1 at P_T of 4 GeV/c rises to around 4 at P_T of 7 GeV/c. This result is in agreement with the theoretical predictions for leading log and next to leading log calculations using Q = 0.5 P_T and Owens Set 1.1 structure functions. As discussed in chapter 1, the same behaviour was also

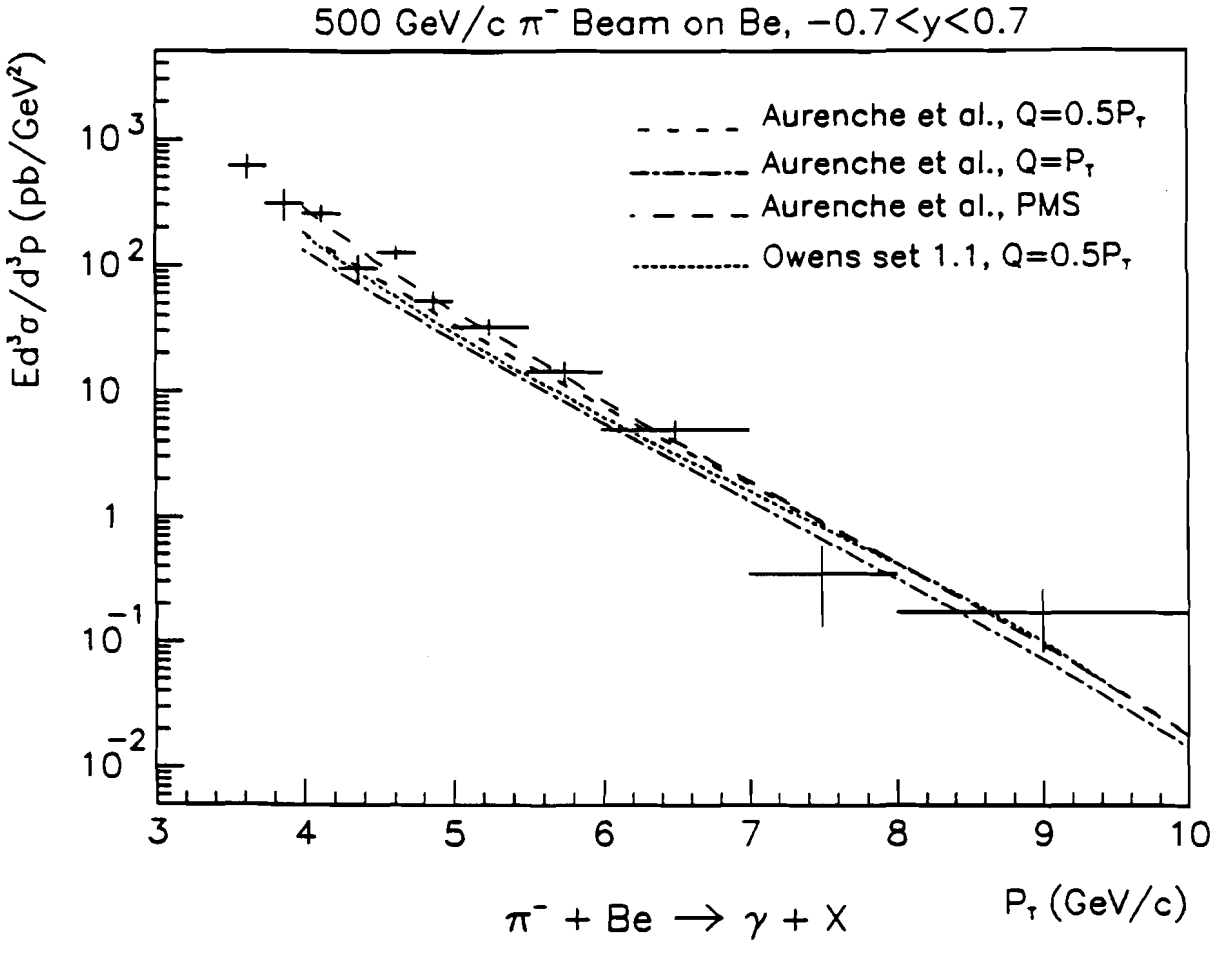

Figure 6.16: Cross section per nucleon for π^-+Be$\rightarrow\gamma$+X compared to QCD predictions with Q=0.5P_T of Owens 1.1 and Q=0.5P_T, Q=P_T and Q from the optimized PMS scaling of Aurenche et al. for data in the rapidity range -0.7<y<0.7.

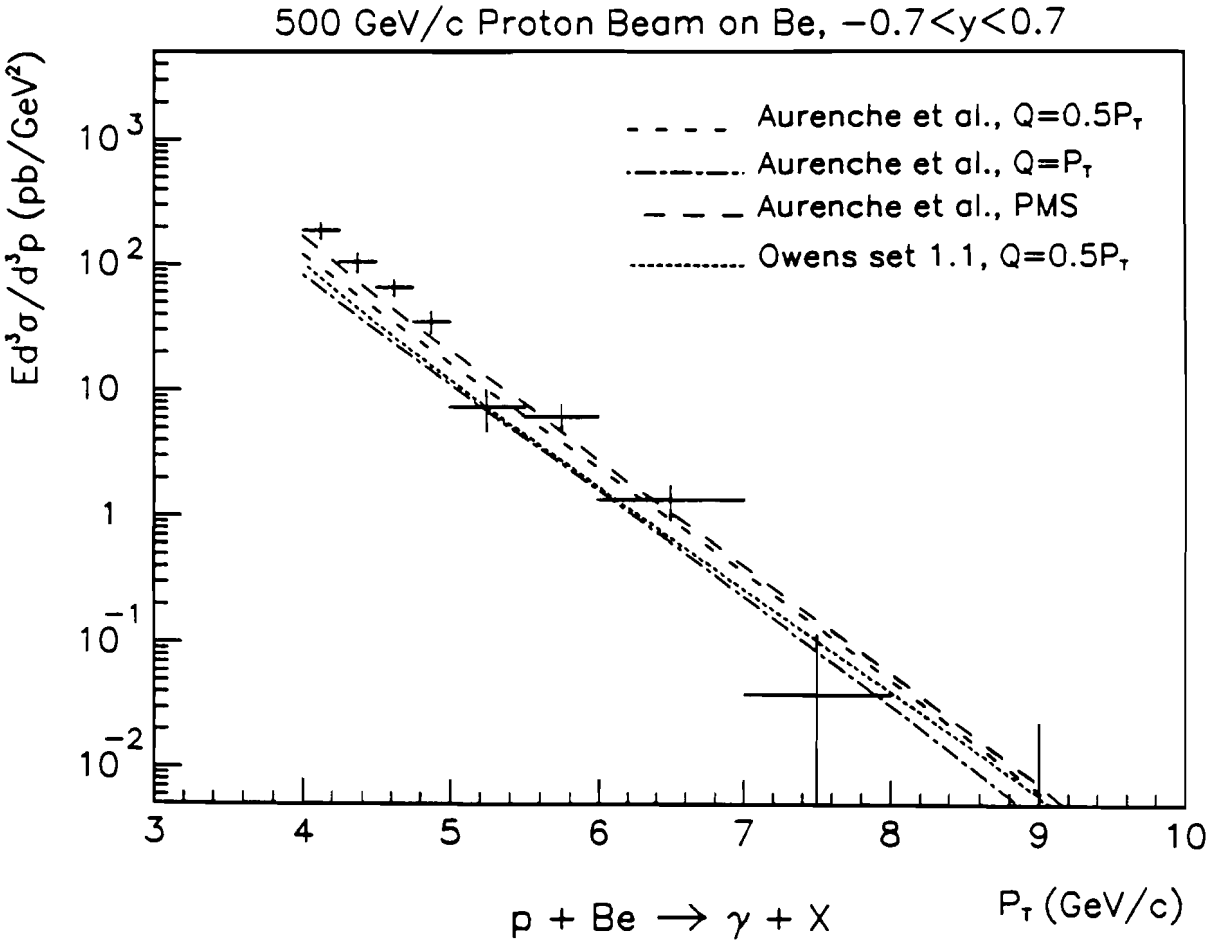

Figure 6.17: Cross section per nucleon for p+Be→γ+X compared to QCD predictions with Q=0.5P_T of Owens 1.1 and Q=0.5P_T, Q=P_T and Q from the optimized PMS scaling of Aurenche et al. for data in the rapidity range -0.7<y<0.7.

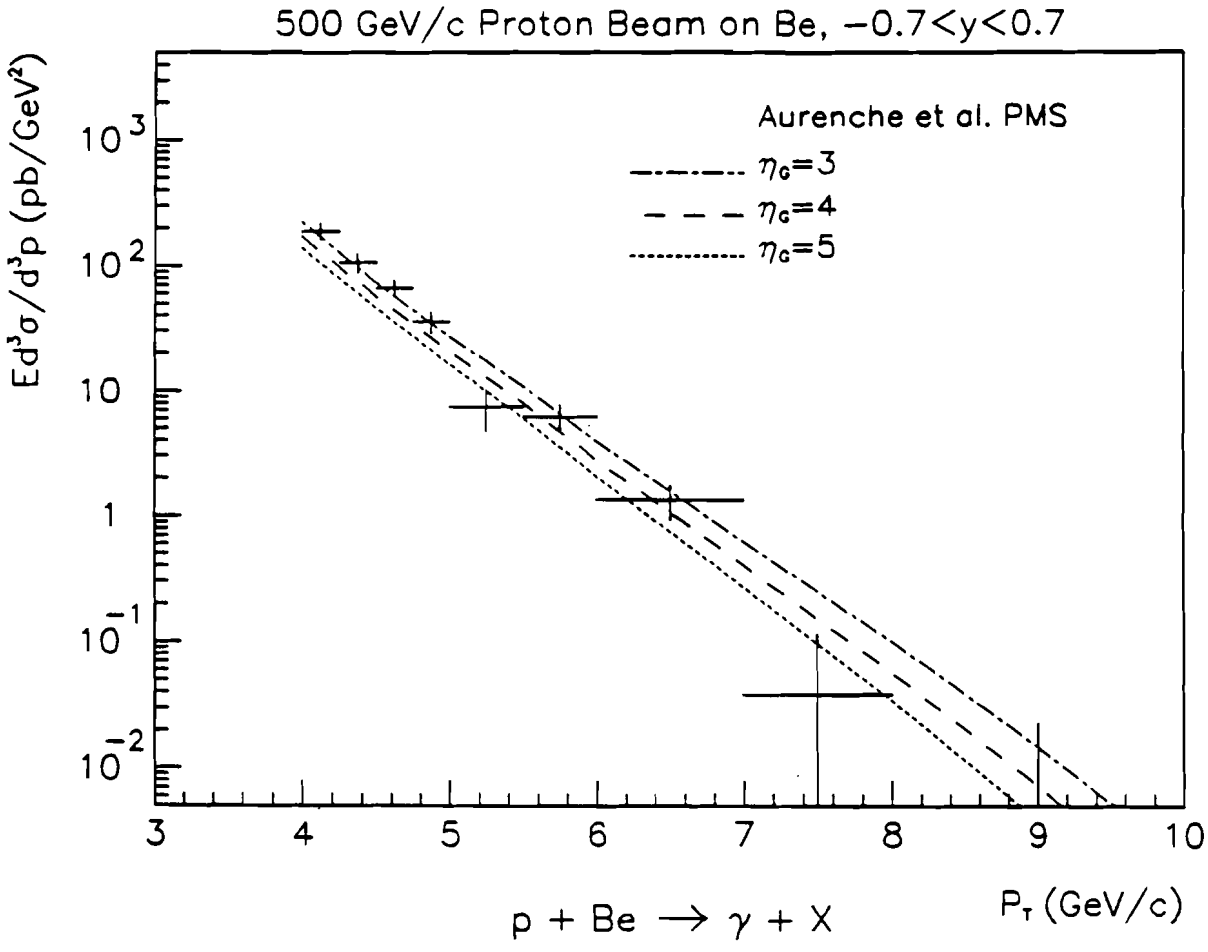

Figure 6.18: Cross section per nucleon for p+Be→γ+X compared to QCD predictions using PMS scale with η_G=3 , η_G=4 and η_G=5 for data in the rapidity range -0.7<y<0.7.

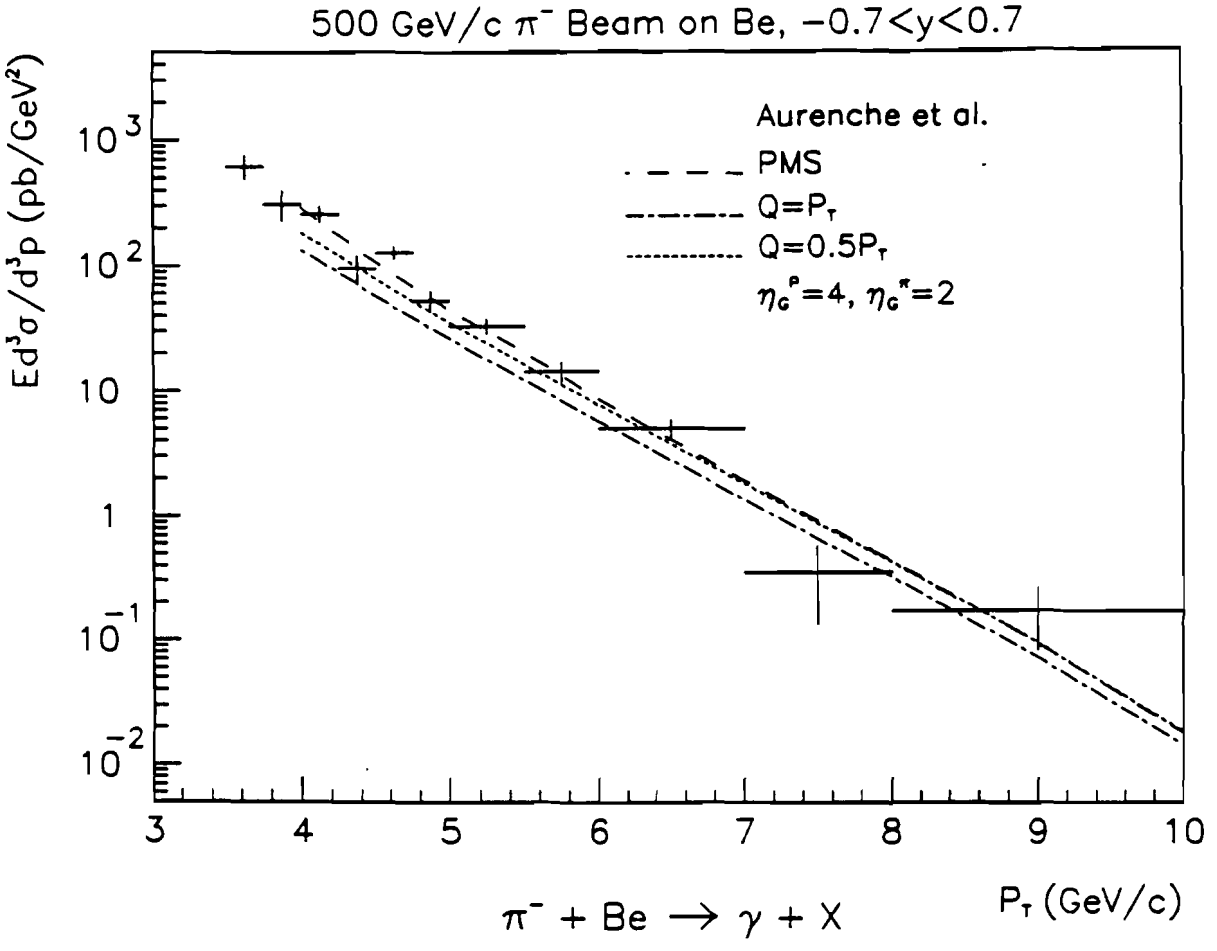

Figure 6.19: Cross section per nucleon for π^-+Be$\rightarrow\gamma$+X compared to QCD predictions with Q=0.5P_T, Q=P_T and Q from the PMS scale of Aurenche et al. for η_G=4 for proton and η_G=2 for pions, for data in the rapidity range -0.7<y<0.7.

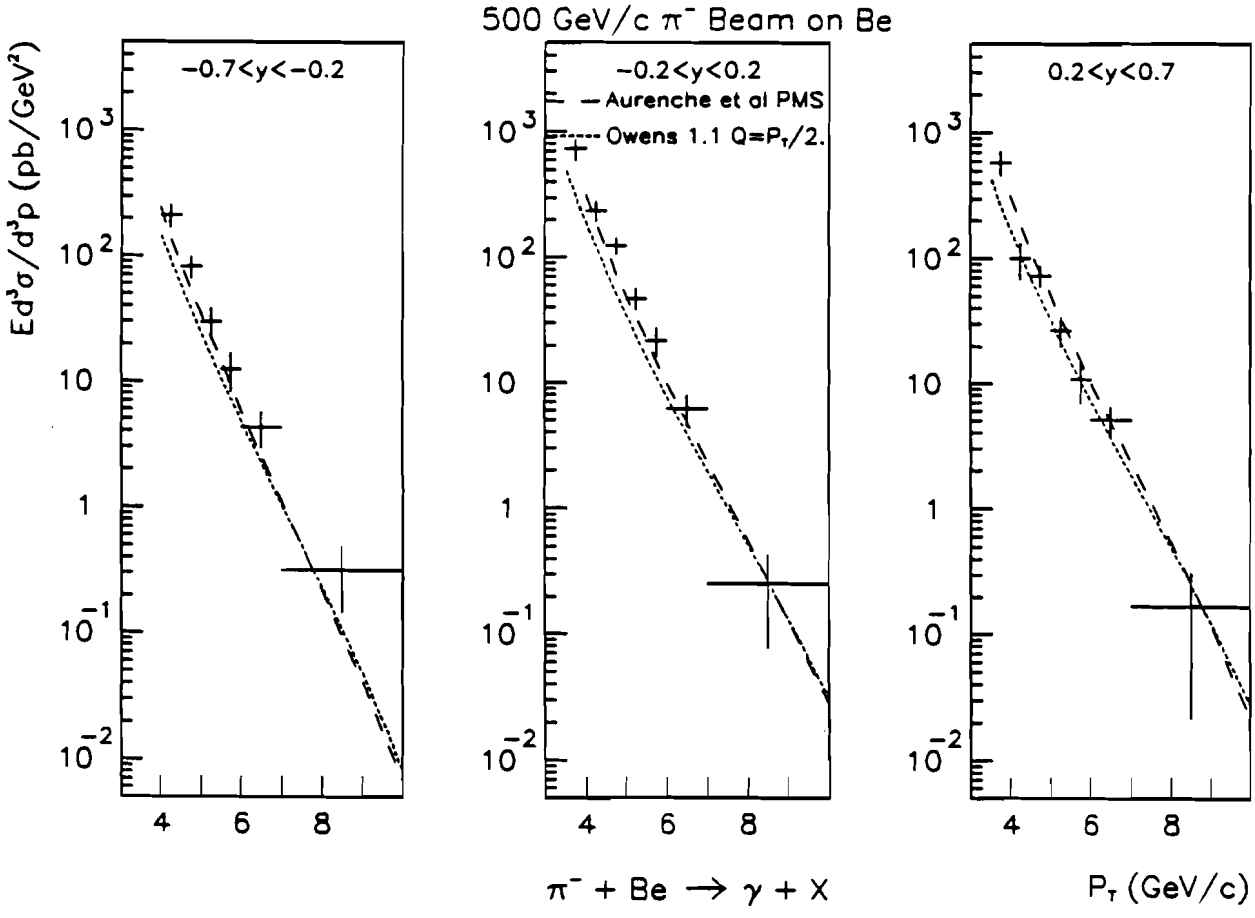

Figure 6.20: Cross section per nucleon for π^-+Be$\rightarrow\gamma$+X compared to QCD predictions with Q=0.5P_T of Owens 1.1 and optimized PMS scaling of Aurenche et al. for data in rapidity ranges -0.7<y<-0.2, -0.2<y<0.2 and 0.2<y<0.7.

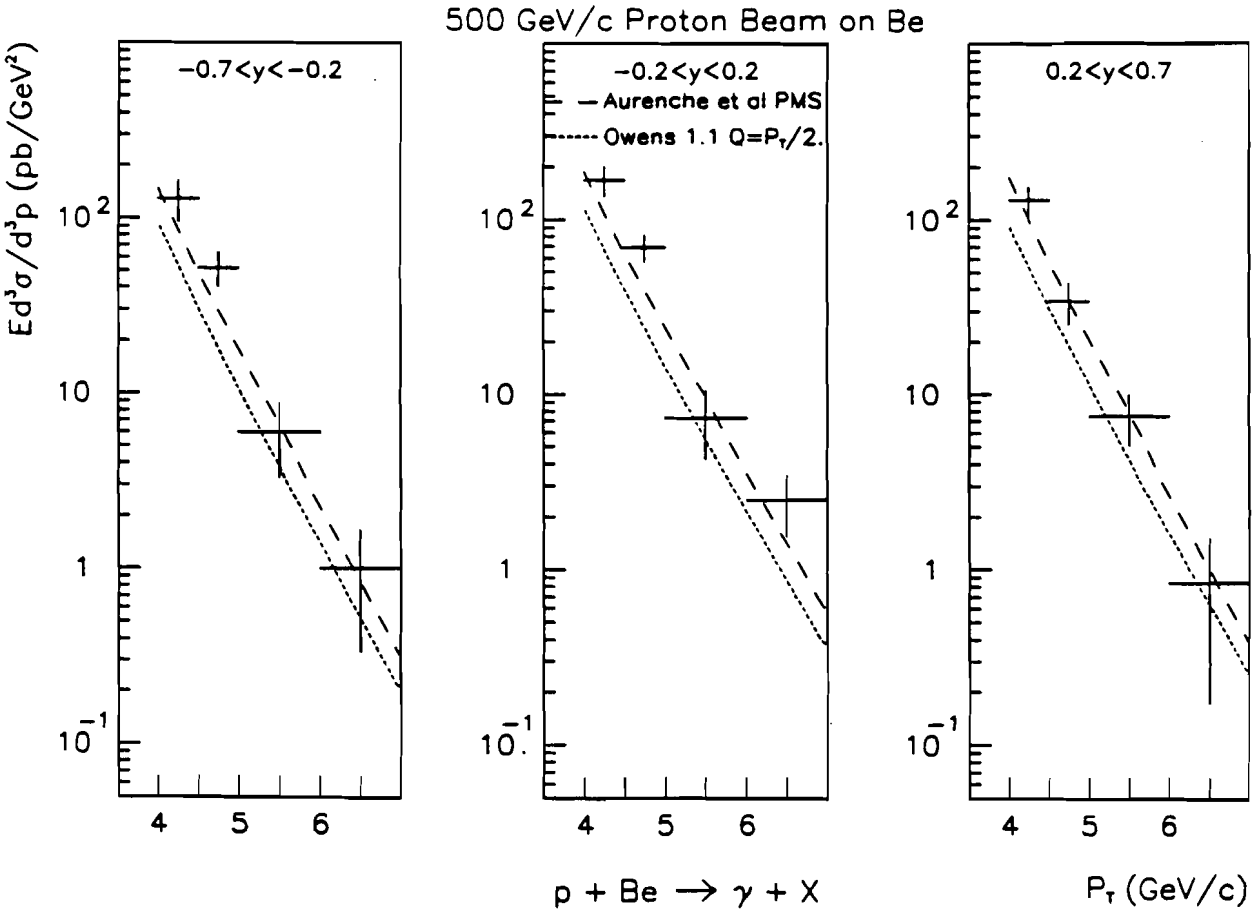

Figure 6.21: Cross section per nucleon for p+Be→γ+X compared to QCD predictions with Q=0.5P_T of Owens 1.1 and optimized PMS scaling of Aurenche et al. for data in rapidity ranges -0.7<y<-0.2, -0.2<y<0.2 and 0.2<y<0.7.

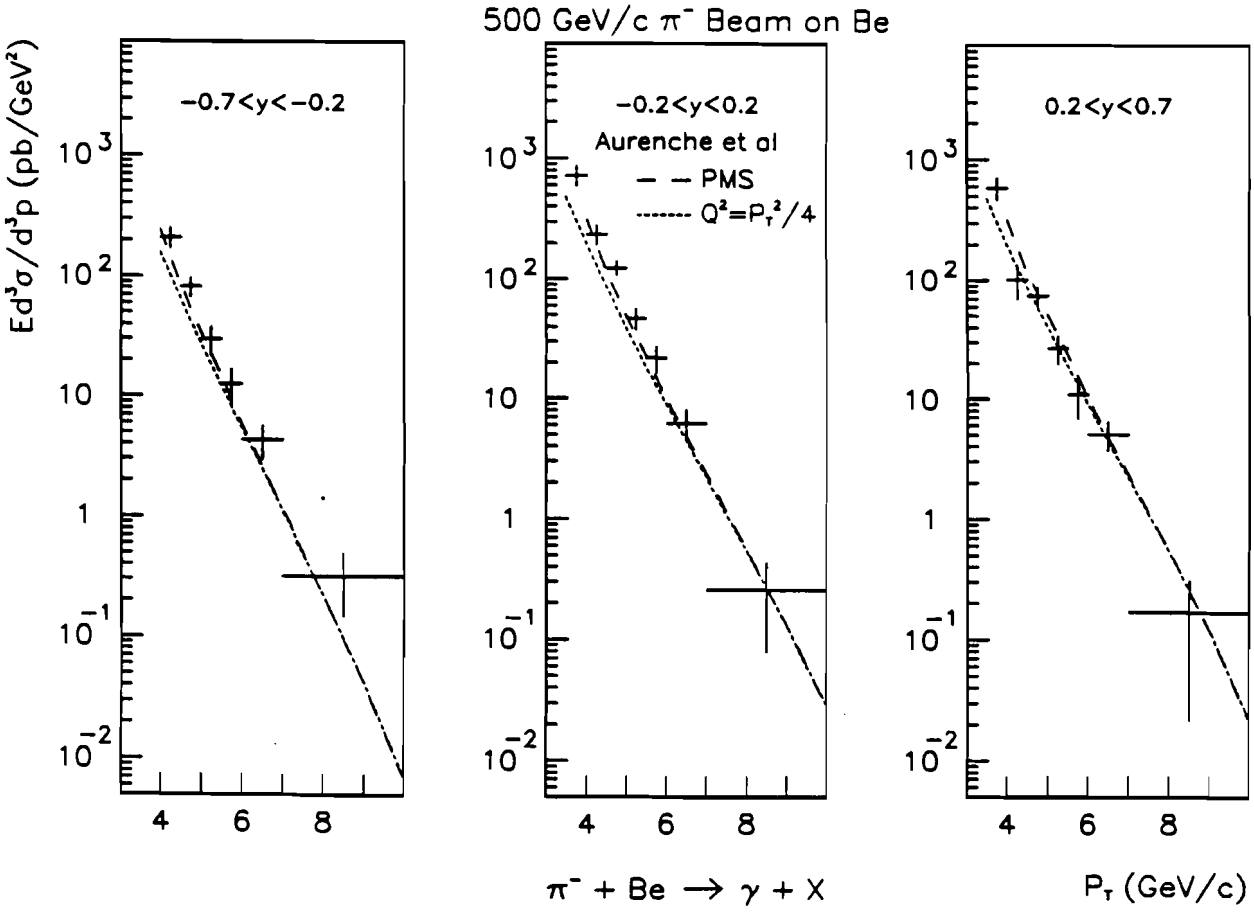

Figure 6.22: Cross section per nucleon for π^-+Be$\rightarrow\gamma$+X compared to QCD predictions with Q=0.5P_T and optimized PMS scaling of Aurenche et al. for data in rapidity ranges -0.7<y<-0.2, -0.2<y<0.2 and 0.2<y<0.7.

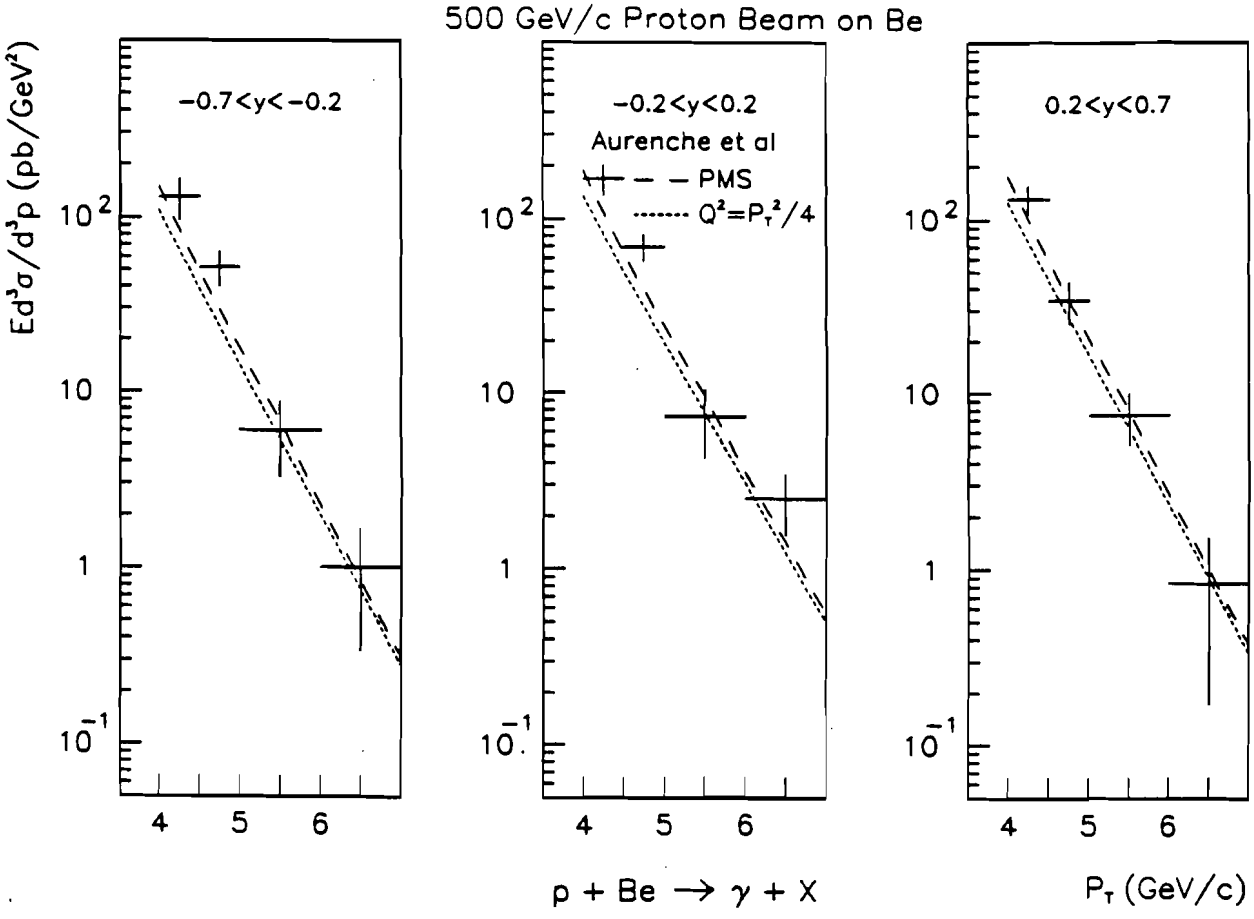

Figure 6.23: Cross section per nucleon for p+Be→γ+X compared to QCD predictions with Q=0.5P_T and optimized PMS scaling of Aurenche et al. for data in rapidity ranges -0.7<y<-0.2, -0.2<y<0.2 and 0.2<y<0.7.

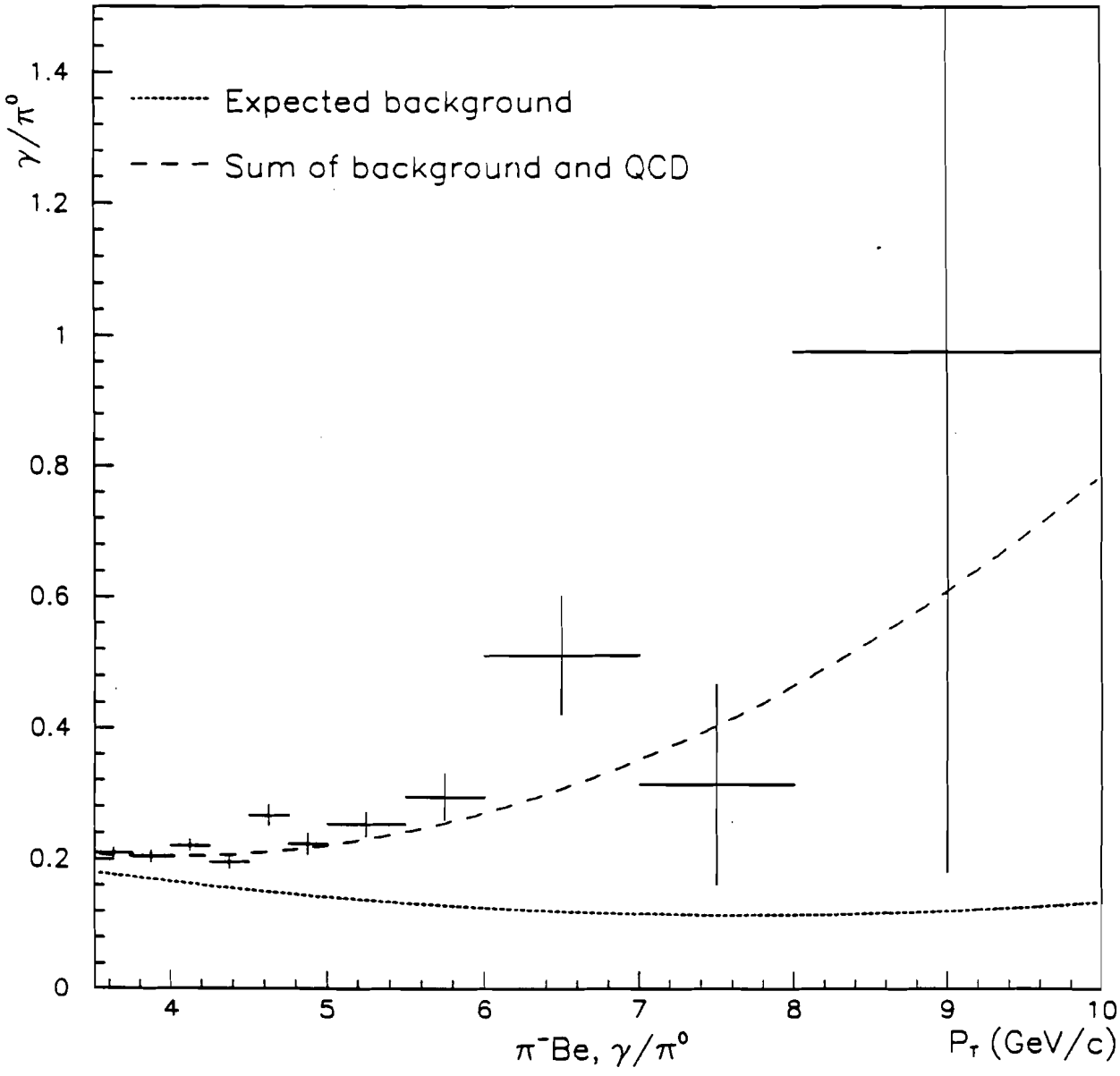

Figure 6.24: The unsubtracted γ/π^0 ratio for π^-Be interaction at 500 GeV/c. Monte Carlo estimate of the background from meson decay is shown. Also shown is the sum of background and the leading log QCD calculation using Owens 1.1 structure functions with $Q = 0.5P_T$.

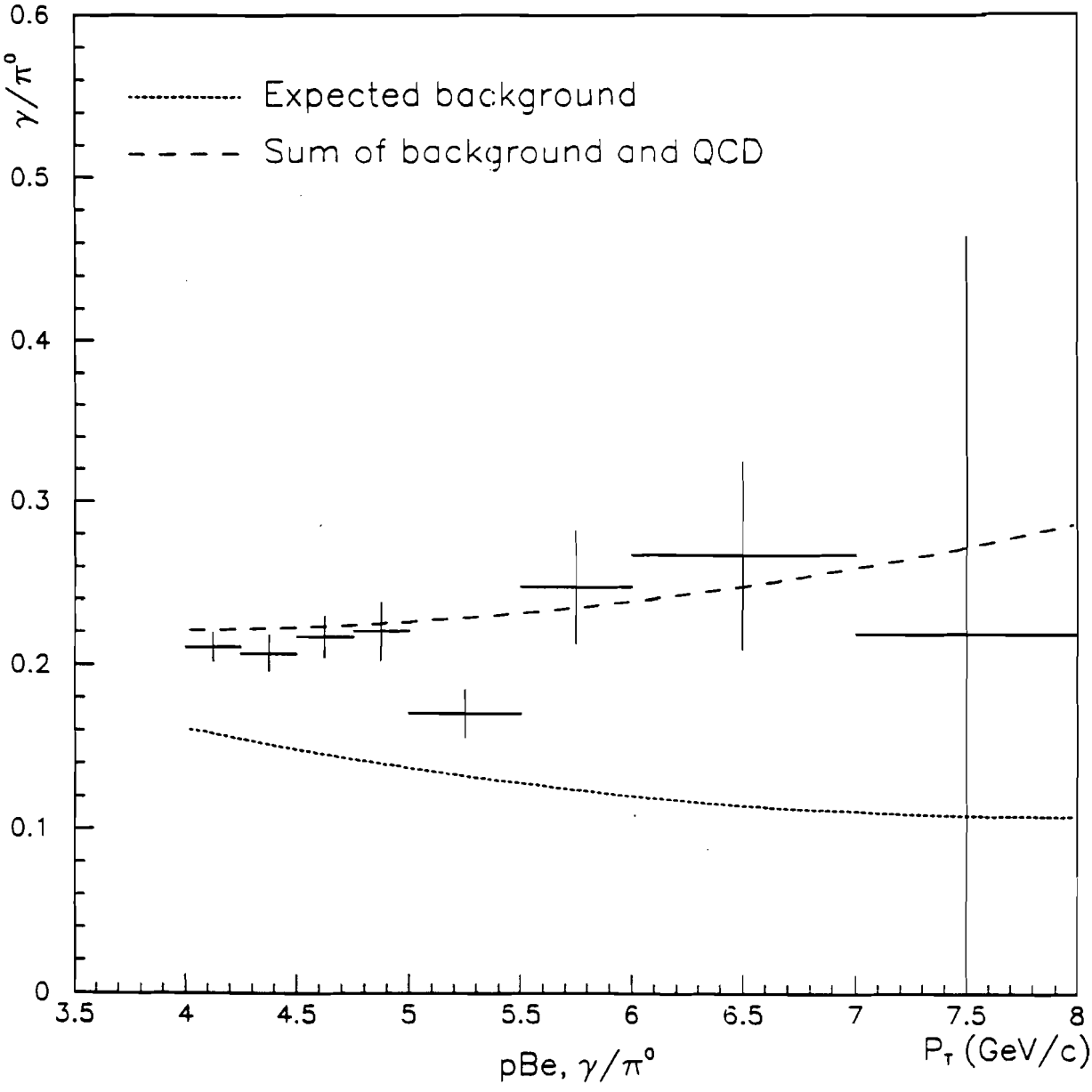

Figure 6.25: The unsubtracted γ/π^0 ratio for pBe interaction at 500 GeV/c with Monte Carlo estimate of the background from meson decay shown. Also shown is the sum of background and the leading log QCD calculation using Owens 1.1 structure function with Q = $0.5P_T$.

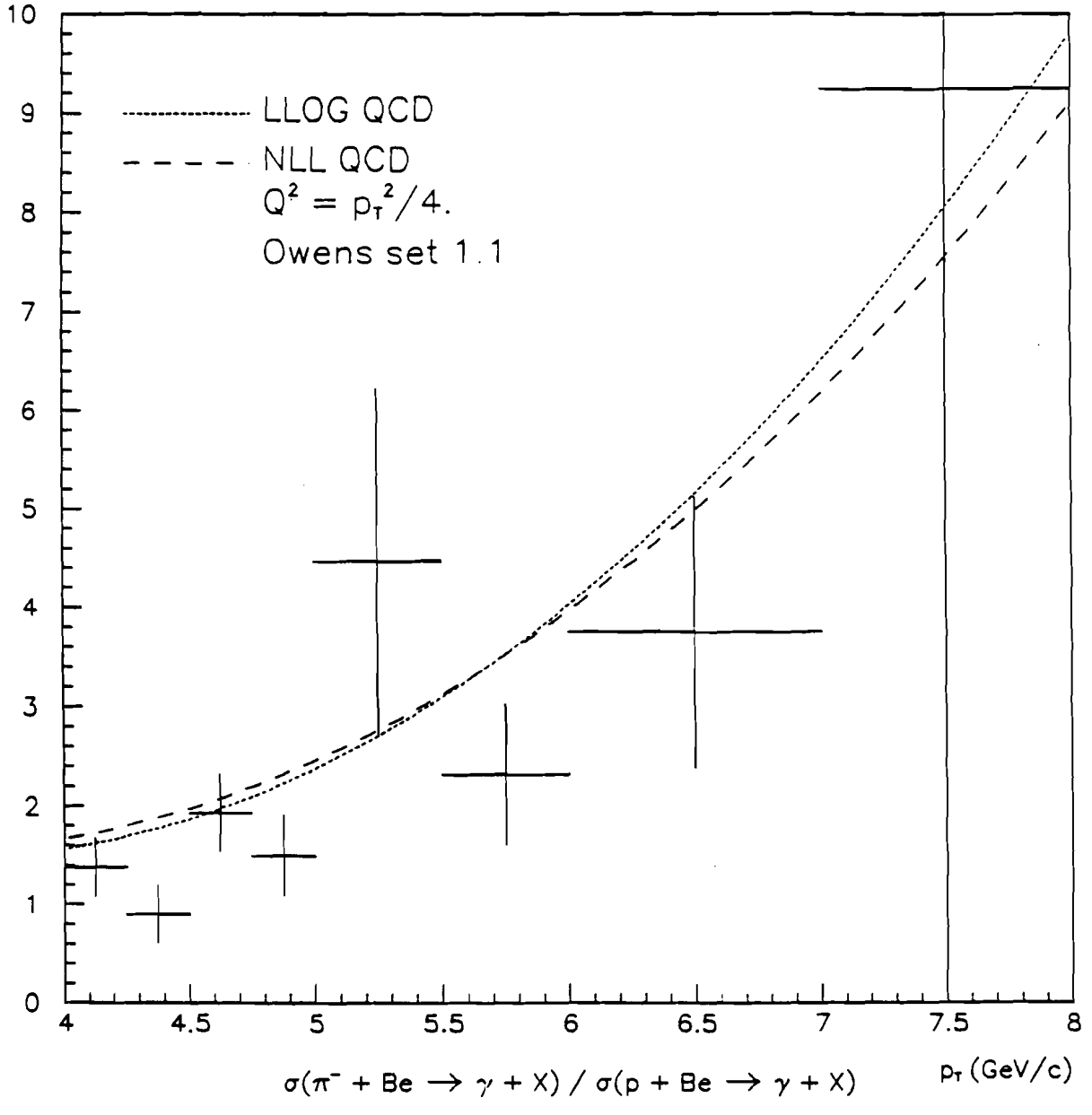

Figure 6.26: The ratio of the direct photon production cross section for π^- and proton beam on Be target. The dashed curves are leading log and next to leading log theoretical predictions with $Q=0.5P_T$, using Owens Set 1.1 structure functions.

seen for other experiments like NA24 and WA70. The ratio of the cross section for π^-Be to pBe as a function of rapidity was found to be almost flat with an average value of 1.54±0.17.

The data for π^-Be and pBe were also compared with next-to-leading log predictions for optimized Q^2 scaling (PMS) and $Q = 0.5P_T$ and $Q = P_T$ using calculations of Aurenche et al. structure functions and $Q = 0.5P_T$ using Owens 1.1 structure function. The agreement between data and PMS optimized scale is quite satisfactory.

To conclude, the cross section measured in E706 covers the $\sqrt{S}$ and x_T region not measured by the earlier fixed target and ISR experiments. The results are compatible with theoretical predictions.

REFERENCES

1. M. Gell-Mann, Phys. Lett. 8, 214(1964).
2. G. Zweig, CERN Rep. TH 401, 412 unpublished, 1964.
3. D. H. Perkins, Introduction to High Energy Physics, Third Edition, Addison-Wesley Publishing Company, Inc. 1987.
4. Howard Georgi, A Unified Theory of Elementary Particles and Forces, Scientific American, Vol 244, 48(1981).
5. D. J. Gross and F. Wilczek, Phys. Rev. Lett. 30, 1334(1973).
6. D. J. Gross and F. Wilczek, Phys. Rev. D8, 3633(1973).
7. H. D. Politzer, Phys. Rev. Lett. 30, 1346(1973).
8. M. R. Pennington, Rep Prog. Phys. 46, 393(1983).
9. R. K. Ellis, 1987 Theoretical Advanced Study Institute, Santa Fe, New Mexico, July 1987. Fermilab preprint 79507.
10. S. D. Ellis, 1987 Theoretical Advanced Study Institute, Santa Fe, New Mexico, July 1987. Fermilab preprint 79507.
11. E. Reya, Lectures given at the Herbstschale fur Hochenergiephysik, Maria Laach, Sept 1978, DESY 79/88 DO-TH 79/20.
12. J. F. Owens, Rev of Mod. Phys. 59, 465(1987).
13. T. Ferbel and W. R. Molzon, Rev. of Mod. Phys. 56, 181(1984).
14. T. Ferbel, Physics in Collision, Capri, Italy 1988. P Strolin ed. University of Rochester preprint 1097.
15. L. Camilleri, 19th Symposium on Multiparticle Dynamics, Arles, France, June 1988, World Scientific Pub. Co., D. Schiff and J. Tran Thanh Van eds.
16. E. L. Berger, E. Braaten and R. D. Field, Nucl. Phys. B239, 52(1984).
17. J. P. Rutherford, Proceeding of 1985 International Symposium on Lepton and Photon Interactions at High Energies, Kyoto.

18. J. Huston, Proceedings of 1989 International Symposium on Lepton and Photon Interactions at High Energies, SLAC, Palo Alto, California, USA.

19. P. Aurenche, R. Baier, M. Fontanaaz and D. Schiff, Phys. Lett. 140B, 87(1984).

20. M. Fritzsch and P. Minkowski, Phys. Lett. B69, 316(1977).

21. R. K. Ellis, H. Georgi, M. Machacek, H. D. Politzer and G. C. Ross, Phys. Lett. B78, 281(1978).

22. R. K. Ellis, H. Georgi, M. Machacek, H. D. Politzer and G. C. Ross, Nucl. Phys. B152, 285(1979).

23. S. Gupta and A. H. Mueller, Phys. Rev. D20, 118(1979).

24. Aguilar-Benitez, et al. (Particle Data Group), Particle Properties Data Booklet 17(1990).

25. D. M. Kaplan et al., Phys Rev. Lett. 40, 435(1978).

26. E. Anassontzis et al., Z. Phys. C13, 277(1982).

27. A. L. S. Angelis et al., Phys. Lett. B94, 106(1980).

28. V. Burkett, 1983, in Gluons and Heavy Flavor, Proceedings of the Hadronic Session of the Eighteenth Recontre de Moriond, edited by J. Tran Thanh Van (Editions Frontieres, Gif-sur-Yvette), Vol. I. p. 189.

29. T. Akesson et al., 1985, paper presented at the 1985 European Physical Conference in Bari(unpublished); Direct Photon plus Away side jet production at $\sqrt{S}$ = 63 GeV and a Determination of the Gluon Distribution, CERN Report No. CERN-EP 186-195.

30. C. DeMarzo et al., 1985, In the Proceedings of the 16th International Symposium on Multiparticle Dynamics, edited by J. Grunhaus. (Editions Frontiers, Gif-sur-Yvette), p.149.

31. J. Badier et al., Phys Lett. B164, 184(1985).

32. E. Bonvin et al, Phys. Lett. B 236, 523-527(1990).

52. K. Hartman, Hadronic Production of π°Pairs and Associated Event Structure, PhD Thesis in Physics, Pennsylvania State University, 1990.

53. W. E. DeSoi, Construction and Performance of a Liquid Argon Calorimeter for Use in Experiment E-706 at the Fermi National Accelerator Laboratory, PhD Thesis in Physics, University of Rochester, 1990.

54. F. Lobkowicz, "Superlad", E-706 Internal Note #002.

55. C. B. Lirakis, A Study of High Transverse Momentum η Production in 530 GeV/c Hadronic Interactions, PhD Thesis in Physics, Northeastern University, 1990.

56. R. Benson, Characteristics of Forward Energy Production in Proton-Nucleus and Pion-Nucleus Collisions as $\sqrt{S}$=31.5 GeV, PhD Thesis in Physics, University of Minnesota, 1990.

57. Carlos M. Yosef, Production of High Transverse Momentum π°Mesons in Interactions of 530 GeV/c Proton and π^{-} Beams on Beryllium and Copper Targets, PhD Thesis in Physics, Northeastern University, August 1990.

58. VAXONLINE system, FNAL Computing Division publication PN 252.

59. R. Brun, M. Goossens and J. Zoll, ZEBRA User's Guide, CERN Computer Center Program Library, DD/EE/85-6, Q100. Fermilab Library, PU0046.

60. J. Zoll, ZEBRA Reference Manual, CERN Computer Center Program Library. Fermilab Library, PU0046.

61. H. J. Klein and J. Zoll, PATCHY Reference Manual, CERN Computer Center Program Library, Oct. 1983. Fermilab Library, PU0013.

62. R. Brun, R. Hagelberg, J. C. Lasalle, G. Misuri and J. Vobrueggen, FFREAD User's Guide and Reference Manual, CERN Computer Center Program Library, DD/US/71, I302. Fermilab Library, SU0026.

63. DI-3000 User's Guide, copyright 1984 by Precision Visuals, Inc. Boulder, Colorado. Also Fermilab SP0018 to run DI-3000 at Fermilab.

64. R. Brun and D. Lienart, HBOOK User's Guide, Cern Computing Center Program Library, Y250. Fermilab Library, PM0082.

65. R. Brun and N. Cremel Somon, HPLOT User's Guide, Cern Computing Center Program Library, Y251. Fermilab Library, SP0028.

66. R. Brun, O. Couet, N. Cremel Somon and P. Zanarini, PAW - Physics Analysis Workstation, Cern Computing Center Program Library, Q121. Fermilab Library, SP0027. Also SP0027A to run PAW at Fermilab.

67. R. Bock, R. Brun, O. Couet, R. Nierhaus, N. Cremel-Somon, C. Vandoni and P. Zanarini, HIGZ- High level Interface to Graphics and Zebra, Cern Computing Center Program Library, Q120. Fermilab Library, SP0026.

68. R. Brun, F. Bruyant, M. Maire, A. C. McPherson and P. Zanarini, GEANT3 User's Guide, CERN Data Handling Division, DD/EE/84-1. Fermilab Library, PM0062.

69. ACP Software User's Guide for Event Oriented Processing, FNAL Computing Division publication #GA0001.

70. ACP User's Guide for Utilities, FNAL Computing Division publication #GA0002.

71. ACP User's Guide for Luni, FNAL Computing Division publication #GA0003.

72. S. Easo, Structure of Events Containing a Direct Photon or Neutral Pion in Hadronic Interactions, PhD Thesis in Physics, Pennsylvania State University, December 1989.

73. J. P. Mansour, High Transverse Momentum π° Production from π^- and p Beams at 530 GeV/c on Be and Cu, PhD Thesis in Physics, University of Rochester, 1989.

74. A. P. Sinanidis, Particle Produced in Association with High Transverse Momentum Single Photons and π° in Hadronic Collisions, PhD Thesis in Physics, Northeastern University, October 1989.

75. Phillip Gutierrez, Cross-Section Corrections, E706 internal note, Draft march 23, 1991.

76. P. D. D. S. Weerasundara, private communication.

77. Takahiro Yasuda, The χ^2 of the EM Shower Fit in the E706 Liquid Argon Calorimeter, E706 internal node186, September 1990.

78. M. Bonesini et. al., Z. Phys., C42, 527-532(1989).

79. A. Breakstone et. al., Phys. Lett., B135, 510(1984).

80. G. R. Snow, Recent Results and Status of CERN Experiment UA6, Presented at FNAL Direct Photon Workshop, May 17, 1991.

81. K. Hartman, private communication

82. P. M. Stevenson, Phys. Rev. D23, 2916(1981).

83. H. D. Politzer, Nucl. Phys. B194, 493(1982).

84. P. M. Stevenson, Nucl. Phys. B203, 472(1982).

85. P. M. Stevenson and H. D. Politzer, Nucl. Phys. B277, 758(1986).

86. J. F. Owens, Florida State Preprint FSU-HEP-910606(June 1991).

87. J. F. Owens, Phys. Rev. D30, 943(1984).

88. P. Aurenche et al., Phys. Lett., 140B, 87(1984).

89. P. Aurenche et al., Nucl. Phys., B286, 509(1987).

90. P. Aurenche et al., Phys. Rev. D39, 3275(1989).

91. P. Aurenche et al., Phys. Lett. B233, 517(1989).

Nuclear Instruments and Methods in Physics Research A279 (1989) 272–276
North-Holland, Amsterdam

PERFORMANCE CHARACTERISTICS AND RADIATION DAMAGE RESULTS FROM THE FERMILAB E706 SILICON MICROSTRIP DETECTOR SYSTEM *

E. ENGELS, Jr., S. MANI, D. ORRIS, P.F. SHEPARD and P.D. WEERASUNDARA
University of Pittsburgh, Pittsburgh, PA 15260, USA

B.C. CHOUDHARY, U. JOSHI, V. KAPOOR and R. SHIVPURI
Delhi University, Delhi, India

W. BAKER, D. BERG, D. CAREY, C. JOHNSTONE and C. NELSON
Fermilab, Batavia, IL 60510, USA

C. BROMBERG, D. BROWN, J. HUSTON, R. MILLER and A. NGUYEN
Michigan State University, East Lansing, MI 48824, USA

R. BENSON, P. LUKENS and K. RUDDICK
University of Minnesota, Minneapolis, MN 55455, USA

G. ALVERSON, W. FAISSLER, D. GARELICK, M. GLAUBMAN, I. KOURBANIS, C. LIRAKIS, E. POTHIER, A. SINANIDIS, G.-H. WU, T. YASUDA and C. YOSEF
Northeastern University, Boston, MA 02115, USA

S. EASO, K. HARTMAN, B.Y. OH, W. TOOTHACKER and J. WHITMORE
Pennsylvania State University, University Park, PA 16802, USA

G. BALLOCCHI, L. DEBARBARO, W. DESOI, G. FANOURAKIS, T. FERBEL, G. GINTHER, P. GUTIERREZ, A. LANARO, F. LOBKOWICZ, J. MANSOUR, G. PEDEVILLE, E. PREBYS, D. SKOW, P. SLATTERY, N. VARELAS and M. ZIELINSKI
University of Rochester, Rochester, NY 14627, USA

A charged particle spectrometer containing a 7120-channel silicon microstrip detector system, one component of Fermilab experiment E706 to study direct photon production in hadron–hadron collisions, was utilized in a run in which 6 million events were recorded. We describe the silicon system, provide early results of track and vertex reconstruction, and present data on the radiation damage to the silicon wafers resulting from the narrow high intensity beam.